Department of Imaging and Applied Physics
Centre for Marine Science and Technology

Benthic Habitat Mapping using Multibeam Sonar Systems

Iain Michael Parnum

This thesis is presented for the Degree of
Doctor of Philosophy
of
Curtin University of Technology

December 2007

DECLARATION

To the best of my knowledge and belief this thesis contains no material previously published by any other person except where due acknowledgement has been made.

This thesis contains no material which has been accepted for the award of any other degree or diploma in any university.

Signature: _____

Date: 18/7/08

This thesis is dedicated to Bethan.

ABSTRACT

The aim of this study was to develop and examine the use of backscatter data collected with multibeam sonar (MBS) systems for benthic habitat mapping. Backscatter data were collected from six sites around the Australian coastal zone using the Reson SeaBat 8125 MBS system operating at 455 kHz. Benthic habitats surveyed in this study included: seagrass meadows, rhodolith beds, coral reef, rock, gravel, sand, muddy sand, and mixtures of those habitats.

Methods for processing MBS backscatter data were developed for the Coastal Water Habitat Mapping (CWHM) project by a team from the Centre for Marine Science and Technology (CMST). The CMST algorithm calculates the seafloor backscatter strength derived from the peak and integral (or average) intensity of backscattered signals for each beam. The seafloor backscatter strength estimated from the mean value of the integral backscatter intensity was shown in this study to provide an accurate measurement of the actual backscatter strength of the seafloor and its angular dependence. However, the seafloor backscatter strength derived from the peak intensity was found to be overestimated when the sonar insonification area is significantly smaller than the footprint of receive beams, which occurs primarily at oblique angles.

The angular dependence of the mean backscatter strength showed distinct differences between hard rough substrates (such as rock and coral reef), seagrass, coarse sediments and fine sediments. The highest backscatter strength was observed not only for the hard and rough substrate, but also for marine vegetation, such as rhodolith and seagrass. The main difference in acoustic backscatter from the different habitats was the mean level, or angle-average backscatter strength. However, additional information can also be obtained from the slope of the angular dependence of backscatter strength.

It was shown that the distribution of the backscatter strength derived from the integral intensity can be accurately approximated by the gamma distribution model. Both scale and shape parameters of the gamma model were found to be dependent on

incidence angle. The scale parameter changes with the angle of incidence in accordance with the angular dependence of backscatter. The shape parameter was shown to relate to the ratio of the insonification area (which can be interpreted as an elementary scattering cell) to the footprint size rather than to the angular dependence of backscatter strength. When this ratio is less than 5, the gamma shape parameter is very similar for different habitats and is nearly linearly proportional to the ratio. Above a ratio of 5, the gamma shape parameter is not significantly dependent on the ratio and there is a noticeable difference in this parameter between different seafloor types.

A new approach to producing images of backscatter properties, introduced and referred to as the angle cube method, was developed. The angle cube method uses spatial interpolation to construct a three-dimensional array of backscatter data that is a function of X-Y coordinates and the incidence angle. This allows the spatial visualisation of backscatter properties to be free from artefacts of the angular dependence and provides satisfactory estimates of the backscatter characteristics. Using the angle-average backscatter strength and slope of the angular dependence, derived by the angle cube method, in addition to seafloor terrain parameters, habitat probability and classification maps were produced to show distributions of sand, marine vegetation (e.g. seagrass and rhodolith) and hard substrate (e.g. coral and bedrock) for five different survey areas.

Ultimately, this study demonstrated that the combination of high-resolution bathymetry and backscatter strength data, as collected by MBS, is an efficient and cost-effective tool for benthic habitat mapping in costal zones.

ACKNOWLEDGEMENTS

There are many people I would like to acknowledge and thank for their assistance throughout this study.

Firstly I would like to thank my principal supervisor Prof. Alexander (Sasha) Gavrilov for his invaluable help and guidance doing this work. Sasha always had time for me whether it was to discuss my work, explain concepts or advise on problems with my car. I am greatly indebted to him and I could not ask for a better supervisor. Sasha was also the main contributor to the development of the CMST multibeam sonar Matlab® toolbox and the calibration experiment.

My co-supervisor Dr. Alec Duncan was a great help with statistical analysis and underwater acoustics. Alec also contributed to the development of the CMST multibeam sonar Matlab® toolbox. My associate supervisor Dr. Paulus (Justy) Siwabessy taught me how to operate multibeam sonar systems in the field and was a great source of information on a range of topics in acoustic seabed classification. Justy also contributed to the development of the CMST multibeam sonar Matlab® toolbox, the calibration experiment and the collection of multibeam sonar data. Dr. Tim Pauly (SonarData) was an associate supervisor who provided useful commercial insight into the project.

This PhD project was funded by the Coastal Water Habitat Mapping (CWHM) project of the Cooperative Research Centre for the Coastal Zone, Estuarine and Waterway Management (Coastal CRC). Special thanks to Mrs Theresa Leijten from the Coastal CRC for her support as the student coordinator. Other sources of funding came from the International Postgraduate Research Scholarship from Curtin University of Technology, and the Endeavour Australia-Europe Postgraduate Student Award from the Department of Education, Science and Training (DEST).

I would like to thank everyone at the Centre for Marine Science and Technology. In particular, Prof. John Penrose and Dr. Rob McCauley for project management as part of the CWHM project and useful discussions; Mr Mal Perry for his help with the

fieldwork; Mrs Ann Smith for keeping me on budget and getting me to conferences; Mr Frank Thomas and Mr Amos Maggi for IT support; and Mr Miles Parsons and Dr. Susan Rennie for their assistance and useful discussions.

Thanks to the following people that helped with the collection of ground-truth information used in this study: Mr. Andy Bickers (University of Western Australia), Dr. Brendon Brooke and Mr. Dave Ryan (Geoscience Australia), Mr. Les Hamilton (Defence Science and Technology Organisation), Dr. Thomas Stieglitz (James Cook University) and Miss Bethan Thompson.

Thanks to Mr. Paul Kennedy (Fugro Pty.) who provided the Reson SeaBat 8101 multibeam sonar data from Marmion Marine Park.

I would like to thank my family for their support and understanding. My parents Jane and John Parnum, my brothers and sister Alan, James and Kate Parnum, my nan, Eileen Tydeman, and my uncle, Alan Tydeman.

Finally, I would like to thank the most important person in my life, Bethan Thompson, for her constant love and support. From helping with fieldwork, to checking drafts and generally being wonderful I cannot thank her enough.

TABLE OF CONTENTS

Abstract i

Acknowledgements iii

Table of contents v

List of figures x

List of tables xviii

Chapter 1. Introduction 1

1.1 Overview 1

1.2 The need for acoustic remote sensing tools 1

1.3 Coastal Water Habitat Mapping project 2

1.4 Benthic habitats 3

1.5 Aim and objectives of the study 3

1.6 Outline of the thesis 4

Chapter 2. Theoretical and experimental background 6

2.1 Overview 6

2.2 Scattering of sound from the seafloor 6

2.2.1 Wave scattering from rough surfaces 6

2.2.2 Seafloor backscatter strength 9

2.2.3 Modelling seafloor backscatter strength 10

2.2.4 Statistics of seafloor backscatter 15

2.3 Multibeam sonar systems 18

2.3.1 Operation of multibeam sonar systems 18

2.3.2 Processing of multibeam sonar backscatter data 22

2.3.3 Correcting multibeam sonar backscatter images for angular dependence 23

2.4 Acoustic seafloor classification 24

2.4.1 Classification methodologies 24

2.4.2 Classification of multibeam sonar data 26

2.4.2.1 Seafloor terrain characteristics 27

2.4.2.2 Analysis of backscatter mosaics 27

2.4.2.3 Angular dependence of backscatter 28
2.5 Implications for the approach of this study 30
Chapter 3. Multibeam sonar backscatter measurements 32
3.1 Overview 32
3.2 Reson SeaBat 8125 system description 33
3.2.1 General description 33
3.2.2 System settings 33
3.2.2.1 Transmit signal 33
3.2.2.2 Receive signal 34
3.2.3 Dynamic focusing 35
3.3 Logging multibeam sonar backscatter data 36
3.3.1 Introduction 36
3.3.2 Data description 37
3.3.3 Complete acoustic waveforms (snapshots) 37
3.3.4 Sidescan logging mode 39
3.3.5 Seafloor backscatter envelopes (snippets) 40
3.3.6 Choice of backscatter logging method 45
3.4 Calibration of the Reson SeaBat 8125 system 46
3.4.1 Introduction 46
3.4.2 Equipment and set-up 47
3.4.3 Transmit beam 47
3.4.4 Receive Beams 50
3.4.4.1 Theoretical predictions 50
3.4.4.2 Measurements 53
3.5 Algorithm development for processing Reson SeaBat 8125 data 56
3.5.1 Introduction 56
3.5.2 Conversion of data from the XTF format to Matlab 57
3.5.3 Calculation of X, Y, Z position and incidence angle (θ) 57
3.5.4 Calculation of peak and average intensity corrected for system settings 59
3.5.5 Removal of system Time Varied Gain 61

3.5.6 Calculation of surface scattering strength 61

3.6 Multibeam sonar system effects on backscatter data 65

3.6.1 Introduction 65

3.6.2 Effect of beam pattern on backscatter 65

3.6.3 Effect of saturation on backscatter strength 67

3.6.4 Effect of pulse duration on backscatter 68

3.6.5 Guidelines for collecting backscatter data for benthic habitat mapping 72

Chapter 4. The effects of incidence angle on the intensity and statistics of seafloor backscatter data collected with high-frequency multibeam sonar 73

4.1 Overview 73

4.2 Dependence of backscatter envelopes on incidence angle and seafloor type 74

4.3 Dependence of the peak backscatter intensity on incidence angle 76

4.4 Dependence of the mean backscatter strength on incidence angle and seafloor habitat 81

4.4.1 Model predictions 81

4.4.2 Field measurements 82

4.5 Statistical distribution of the average backscatter intensity 85

4.5.1 Introduction 85

4.5.2 Theoretical predictions 86

4.5.3 Data description 88

4.5.4 Results 90

4.6 Implications for benthic habitat mapping 98

Chapter 5. Processing techniques for visualisation and classification of backscatter strength data collected with multibeam sonar 100

5.1 Overview 100

5.2 Correcting backscatter images for angular dependence 101

5.2.1 Methodology 102

5.2.2 Results of different angular corrections 102

5.3 Visualising backscatter properties: Angle cubes 108

5.3.1 Methodology 108

5.3.2 Track spacing, grid size, and interpolation algorithm 111
5.3.3 Case Study 1: Keppel Bay, Queensland 115
5.3.4 Case Study 2: Marmion Marine Park, Western Australia 117
5.4 Seafloor classification using multibeam sonar data 119
5.4.1 Methodology 119
5.4.1.1 Extracting useful features of the backscatter strength versus incidence angle 120
5.4.1.2 Unsupervised and supervised classification 121
5.4.2 Case Study: Esperance Bay, Western Australia 123
5.4.2.1 Study area and methods 123
5.4.2.2 Analysis of backscatter features 123
5.4.2.3 Classification of features 129
5.5 Implications for benthic habitat mapping 137
Chapter 6. Analysis of multibeam sonar data from different seafloor habitats 138
6.1 Overview 138
6.2 Data description 138
6.3 Owen Anchorage, Western Australia 139
6.3.1 Site description 139
6.3.2 Results 140
6.4 Moreton Bay, Queensland 146
6.4.1 Site description 146
6.4.2 Results 146
6.5 Esperance Bay, Western Australia 155
6.5.1 Site description 155
6.5.2 Results 156
6.6 Morinda Shoal, Queensland 163
6.6.1 Site description 163
6.6.2 Results 162
6.7 Implications for benthic habitat mapping 174
Chapter 7. Discussion 177
7.1 Overview 177

7.2 Achievements of the study 177
7.3 Summary of recommendations for further work 186
7.4 Conclusions 188
References 189
Appendix A. Data description 199
A1. Morinda Shoal, Queensland 199
A2. Esperance Bay, Western Australia 200
A3. Owen Anchorage, Western Australia 203
A4. Moreton Bay, Queensland 204
A5. Keppel Bay, Queensland 205
Appendix B. The effect of beam pattern on backscatter intensity measurements 206
Appendix C. Acronyms 213

LIST OF FIGURES

Figure 1.1:	Location of study areas involved in this study and as part of the CWHM project.	3
Figure 2.1:	Schematic representation of the reflection, transmission and scattering of acoustic energy at a rough boundary and the effect of impedance contrast and surface roughness on the scattered field (after Urick,(1983)).	7
Figure 2.2:	Geometric arrangement for measuring backscatter strength.	10
Figure 2.3:	Generic representation of backscatter strength versus incidence angle (after Augustin *et al.* (1996)).	14
Figure 2.4:	Schematic representation of the operation of MBS systems. Blue represents the transmit beam, red the receive array and green the footprint formed by the intersection of the two.	18
Figure 2.5:	Typical beam geometry of multibeam sonar systems (a) sideview, (b) plan view and (c) graphical representation of the beam areas versus incidence angle/across track distance.	20
Figure 3.1:	Reson SeaBat 8125 sonar head mounted on a side pole: (a) photograph of it out of the water, and (b) diagram of its position in the water.	34
Figure 3.2:	Beam patterns of the Reson 8125 receive array modelled with (green) and without (blue) dynamic focusing and shown projected onto the seafloor for different sea depths and steering angles. Red vertical lines show the footprint edges determined at the –3 dB level for the far field.	36
Figure 3.3:	An example ping of signal level (relative dB) from BGB_57: (a) all beams and (b) some selected beams - 5 (red), 60 (pink) and 121 (black). Vertical dotted lines in plot (b) represent the snippet locations.	38
Figure 3.4:	Comparison of snapshot, with (a) sidescan and (b) snippet data.	39
Figure 3.5:	Multibeam sonar data collected from line BGB_57: (a) bathymetry (m), (b) sidescan simulated from full water column data, (c) snippets - peak beam intensity and (d) sidescan simulated from snippets.	40
Figure 3.6:	Location of the snippet fragments extracted from the signal envelope as recorded in snapshots for beams 21 and 22.	41
Figure 3.7:	Example of inadequate snippet location, solid lines are the waveforms and dashed lines are the start and finish positions of the snippets. Beams 135 and 136 start at same position.	42
Figure 3.8:	Percentage of matches in maximum amplitude between snippets and snapshots for each beam of the Reson SeaBat 8125 along line BGB 57.	43
Figure 3.9:	Experiment set-up for calibration experiment.	48

Figure 3.10: Transmission loss modelled along beam axis in the near field of the Reson SeaBat 8125 transmit array (blue) compared to spherical spreading loss (red). 49

Figure 3.11: Along-track transmit beam pattern measured at 6.4 m from the transmit array (stars) and modelled for the same distance for a transmit power of 220 dB re 1 µPa at 1m. 49

Figure 3.12: The across-track directivity pattern of the transmit beam (-*) of the Reson SeaBat 8125. The -3 dB limit is indicated by the black dashed line. 50

Figure 3.13: Modulus of the reflection and transmission coefficients from a 10 mm thick aluminium plate at 455 kHz (acoustic characteristics of aluminium: density 2700 kg m^{-3}; compressional wave speed 6320 m s^{-1}; shear wave speed 3130 m s^{-1}; compressional wave attenuation 0.01 dB $wavelength^{-1}$; shear wave attenuation 0.02 dB $wavelength^{-1}$). 51

Figure 3.14: (a) Amplitude and (b) phase of the Reson transmit signal along the receive array, after reflection from an aluminium plate 40 by 40 cm wide and 10 mm thick. The amplitude is shown corrected for spherical spreading. The blue line is the result of numerical modelling using the Kirchhoff approximation. The red line shows a simple spherical spreading approximation for reflection from an infinite surface. 53

Figure 3.15: Average backscatter strength of sonar signals reflected from the aluminium plate (-) and backscattered from the sand paper plate (--) and concrete slab (-) for each beam expressed in dB relative system ADC units. 55

Figure 3.16: Bathymetry (m) images (a) before and (b) after compensation for ship's motion (data collected from Esperance Bay). 58

Figure 3.17: Typical sound velocity profiles from the different sites surveyed. 58

Figure 3.18: Backscatter images not corrected (top) and corrected (bottom) for changes in power (middle). 60

Figure 3.19: Backscatter intensity collected at an incidence angle of 30º with and without system TVG and the backscatter strength $BS_{integral}$ derived after all corrections versus (a) range and (b) footprint size. 64

Figure 3.20: The Reson SeaBat 8101 (a) relative across-track sensitivity as measured by Foote *et al.* (2003), (b) the relative mean backscatter strength from a flat sandy seafloor (different 8101 system). 66

Figure 3.21: Backscatter image (top) corrected for changes in gain (middle) and the mean beam response (bottom) for fixed operator gain (dB) of 5 (blue), 11 (red), 20 (black) and 30 (green). 67

Figure 3.22: Mean (a) $BS_{integral}$ and (b) BS_{peak} versus incidence angle from an area of flat sand for a range of pulse durations 31-292µs. 69

Figure 3.23: Pulses reflected from an aluminum plate for different pulse durations of the Reson SeaBat 8125. 70

Figure 4.1: Backscatter envelopes from sand (black) and rhodolith (grey) for beams (a) 120, (b) 60 and (c) 5 of the Reson 8125. 75

Figure 4.2: Numerically modelled mean value of the peak intensity versus the number of samples (scattering cells) for a mean intensity assumed to be unity. 79

Figure 4.3: Mean backscatter strength (determined from the peak and integral intensity), sonar receive footprint and transmit insonification areas versus incidence angle. 80

Figure 4.4: APL model (APL 1994) predictions as determined for generic sediment types at 455kHz by Anstee (2001). 82

Figure 4.5: Mean backscatter strength ($BS_{integral}$) versus incidence angle for a variety of benthic habitats from around the Australian coast measured using a Reson SeaBat 8125 MBS system. 83

Figure 4.6: The mean footprint and insonification areas versus incidence angle for the different seafloor habitats analysed in this section. 88

Figure 4.7: Transects used for statistical analysis (Backscatter images are not corrected for angular dependence). 89

Figure 4.8: (a) Mean backscatter strength and (b) coefficient of variation versus incidence angle for the different habitats. 91

Figure 4.9: Skewness squared versus kurtosis of backscatter intensity in different angular domains for the different habitats. The dependence predicted from the gamma model is shown as a black line along with the positions of a normal (●) and exponential (●) distribution. 93

Figure 4.10: Probability density for normalised backscatter intensity for a variety of habitats for incidence angles 5 º (- solid lines), 30 º (-- lines) and 55º (···lines). Black line shows the gamma model fit. 94

Figure 4.11: Probability density for normalised backscatter intensity for a variety of habitats for incidence angles (a) 5 º, (b) 30 º and (c) 55º. Black dashed line shows the gamma model fit for sand (Esperance Bay). 95

Figure 4.12: The gamma shape parameter β versus (a) incidence angle (deg.) and (b) the ratio of the insonfication area to footprint size. 97

Figure 5.1: Backscatter strength from line Esperance 309 with the results of various corrections for angular dependence. 104

Figure 5.2: (a) Mean and (b) standard deviation of backscatter strength versus beam number for sand before and after various angular corrections. Plot (b) also shows the effects of gridding (blue lines) on the results of correction (c) as a function of across track distance. 105

Figure 5.3: The production of an angle cube (2m x 2m x 1˚), and the resulting angle-average backscatter strength over 5-60° (dB) compared to the bathymetry (m). Data from a MBS survey north of Thomas Island in Esperance Bay, Western Australia. 109

Figure 5.4: The results of applying four methods of angular correction to 4 lines of backscatter strength data (dB) with subsequent gridding to 2m. Data were collected north of Thomas Island in Esperance Bay, Western Australia. 110

Figure 5.5: The effect of track spacing (ship's tracks shown in black) and interpolation algorithm on the angle-average backscatter strength over 5-60° (dB) for a 5m grid size. 112

Figure 5.6: The effect of spatial grid size on the angle-average backscatter strength over 5-60° (dB) and the distribution of the number of samples in the 30° grid cells for (a) 1 m, (b) 5 m and (c) 10 m grid sizes (all for 1° angle bins). Cells with no values are omitted from the histograms. 113

Figure 5.7: The effect of angle bin size used to create an image of angle-average backscatter strength over 5-60° (dB): data gridded to a 2m grid and angle bin size of (a) 5, (b) 10, (c) 15 and (d) 20 degrees. 114

Figure 5.8: (a) Bathymetry, (b) average backscatter strength and (c) slope of its angular dependence with corresponding grab samples of sediment and (d) density plot of mean backscatter strength versus incidence angle using data collected in the Centre Banks area of Keppel Bay, Queensland. 116

Figure 5.9: Marmion Marine Park, Western Australia survey: (a) aerial photo with MBS survey lines, (b) angle-average backscatter strength from 5 to 80˚ collected with Reson SeaBat 8101 (relative dB). UTM zone 50 south. 118

Figure 5.10: The process used in this study for seafloor classification using multibeam sonar data. 119

Figure 5.11: (a) Bathymetry, (b) terrain slope (deg.), (c) angle-average backscatter strength over 40-60º (dB) and (d) slope of the backscatter angular dependence over 5-40º (dB/deg.). Data comes from a MBS survey between Thomas and Woody Island in Esperance Bay, Western Australia. 124

Figure 5.12: Mean backscatter strength (dB) versus incidence angle (deg.) for: (a) all data in the angle cube shown as a density plot (colour represents number of data points), and (b) areas of sand, rhodolith and rock habitats (error bars represent +/- one standard deviation). Data were gathered from part of a MBS survey between Thomas and Woody Islands in Esperance Bay, Western Australia. 125

Figure 5.13: Results of analysis of the angle cube produced from backscatter data obtained from a MBS survey between Thomas and Woody Islands in Esperance Bay, Western Australia. 127

Figure 5.14: Loading coefficients from PCA and LDA of mean backscatter strength from MBS data collected between Thomas and Woody Islands in Esperance Bay, Western Australia. 128

Figure 5.15: Two dimensional histogram (colour displays number of samples) of the terrain slope (deg.) versus the angle-average backscatter strength over 40-60° (dB). Data are from part of a MBS survey of Esperance Bay, Western Australia. 131

Figure 5.16: The terrain slope versus the mean backscatter strength averaged over 40-60° for all data and for the training areas, segmented through (a) supervised and (b) unsupervised classification. The training areas were also used to assess the accuracy of the classification results. 133

Figure 5.17: Posterior probabilities for (a) sand, (b) rock and (c) rhodolith classes determined through the multivariate probability density model derived from the training data. 134

Figure 5.18: Results of seafloor classification into sand (**blue**), rhodolith (**red**) and rock (**black**) classes. Data segmented with (a) supervised classification; (b) same as (a) but after contextual editing, (c) k-means clustering and (d) same as (c) but after contextual editing. 135

Figure 6.1: Mean backscatter strength (dB) versus incidence angle (deg.): (a) two dimensional histogram for all of the data; and (b) the mean value for sand and seagrass found in Owen Anchorage (error bars show the standard deviation measured at different angles). 141

Figure 6.2: (a) Bathymetry (m), (b) angle-average (dB) and (c) slope of angular dependence (dB/deg.) of backscatter strength for incidence angles from 5 to 60º. Data from a MBS survey in Owen Anchorage, Western Australia. Representative still images from the towed video transects are also shown. 142

Figure 6.3: Two-dimension histogram of slope of the angular dependence (dB/deg.) versus angle-average backscatter strength (dB) over 5-60º incidence angles. Data from a MBS survey in Owen Anchorage, Western Australia. 143

Figure 6.4: Slope of angular dependence (dB/deg.) versus angle-average (dB) of the mean backscatter strength over 5-60º incidence angles: (a) sand (●) and seagrass (●) classes determined by supervised classification (sand (●) and seagrass (●) training data also shown); (b) sand, seagrass and an unknown acoustic class (●) determined by k-means clustering. Data from a MBS survey in Owen Anchorage, Western Australia. 144

Figure 6.5: Results of seafloor classification from the MBS survey in Owen Anchorage, Western Australia: (a) seagrass and (b) sand class posterior probabilities; (c) class map derived from supervised classification using a linear multivariate normal density model; and (d) classification assigned by the k-means algorithm assuming the presence of an additional unknown class. 145

Figure 6.6: Mean backscatter strength (dB) versus incidence angle (deg.): (a) a two-dimensional histogram for all of the data and (b) for muddy sand, sand and seagrass found in Moreton Bay, Queensland (error bars show the standard deviation measured at different angles). 146

Figure 6.7: (a) Bathymetry (m), (b) angle-average (dB) and (c) slope of the angular dependence (dB/deg.) of backscatter strength over 5-60º from the MBS survey in Moreton Bay, Queensland. Circles represent seafloor classification based on towed video: muddy sand (●), sand (●) and seagrass (o). 149

Figure 6.8: Seafloor acoustic features from MBS data along towed video tracks: (a) Depth (m); (b) angle-average (dB) and the (c) slope of angular dependence (dB/deg.) of backscatter strength (dB) over 5-60º from the MBS survey in Moreton Bay, Queensland. Video classification shown: muddy sand (●), sand (●) and seagrass (●). Still images from the underwater video labelled with record number and class assigned. 150

Figure 6.9: Feature space of the slope of angular dependence (dB/deg.) versus angle-average backscatter strength (dB): (a) two dimensional histogram and (b) scatter plot segmented by supervised classification into sand, seagrass and muddy sand classes with the training areas shown by darker dots. Data from a MBS survey in Moreton Bay, Queensland. 151

Figure 6.10: The posterior probabilities of the (a) sand, (b) seagrass and (c) muddy sand classes. Data from a MBS survey in Moreton Bay, Queensland. 152

Figure 6.11: The results of supervised classification without (a) and with (b) contextual editing. Data from a MBS survey in Moreton Bay, Queensland. 153

Figure 6.12: Distribution of depth values for the seagrass class segmented into 3 subclasses as shown in Figure 6.11(b). Data from a MBS survey in Moreton Bay, Queensland. 155

Figure 6.13: Mean backscatter strength (dB) versus incidence angle (deg.): (a) a two dimensional histogram for all of the data and (b) mean value from sand, seagrass, rhodolith and rock from east of Woody Island in Esperance Bay, Western Australia (error bars show the standard deviation measured at different angles). 157

Figure 6.14: (a) Bathymetry (m), (b) terrain slope (deg.), (c) angle-average (dB) and (d) slope of the angular dependence (dB/deg.) of backscatter strength over 5-60º for MBS data collected east of Woody Island in Esperance Bay, Western Australia. Grab sample data and underwater video images of: rhodolith (●), sand (●), seagrass (●) and rock (●) are also shown. 158

Figure 6.15: Terrain slope (deg.) versus the angle-average backscatter scatter (dB): (a) two dimensional histogram and (b) scatter plot segmented by supervised classification into sand, seagrass, rhodolith and rock classes. Data from a MBS survey east of Woody Island in Esperance Bay, Western Australia. 159

Figure 6.16: Results of supervised classification of MBS data collected east of Woody Island in Esperance Bay, Western Australia: posterior probabilities of (a) sand, (b) seagrass, (c) rock and (d) rhodolith classes, and resulting class map without (e) and with (f) contextual editing of the seagrass class using the k-means algorithm. 161

Figure 6.17: Distribution of depth values of the seagrass class east of Woody Island in Esperance Bay. The two colours represent subclasses segmented by depth using k-means clustering. The spatial distribution of these subclasses can be seen in Figure 6.16(f). 162

Figure 6.18: Mean backscatter strength (dB) versus incidence angle (deg.): (a) a two-dimensional histogram for all of the data and (b) the mean angular dependence with standard deviation (error bars) for different habitats. Data from a MBS survey of Morinda Shoal, Queensland. 164

Figure 6.19: (a) Bathymetry (m), (b) terrain slope (deg.), (c) angle-average (dB) and (d) slope of the angular dependence (dB/deg.) of backscatter strength with video tracks colour-coded according to the following classification: Coral Reef (●), Coral Rubble (●), Seagrass – dense (●), Seagrass – sparse (●), Sand (●) and Mixed coral and seagrass (●). Data from a MBS survey of Morinda Shoal, Queensland. 166

Figure 6.20: Seafloor acoustic features from MBS data along the northern Morinda Shoal towed underwater video: (a) Depth (m), (b) terrain slope (deg.), (c) angle-average (dB) and (d) slope of angular dependence (dB/deg.) of backscatter strength. Video classification: Coral Reef (●) and Mixed coral and seagrass (●). 167

Figure 6.21: Seafloor acoustic features from MBS data along the southern Morinda Shoal towed underwater video: (a) Depth (m), (b) terrain slope (deg.), (c) angle-average (dB) and (d) slope of angular dependence (dB/deg.) of backscatter strength. Video classification: Coral Reef (●), Coral Rubble (●), Seagrass – dense (●), Seagrass – sparse (●), Sand (●). 168

Figure 6.22: (a) Two- dimensional histogram of terrain slope (deg.) versus angle-average backscatter strength over 5-60º (dB). Data collected from a MBS survey of Morinda Shoal, Queensland. 169

Figure 6.23: Plot of slope of angular dependence of backscatter strength (dB/deg.) versus angle-average backscatter strength (dB) (both over 5-60º) versus terrain slope (deg.) for training data used for supervised classification of Morinda Shoal, Queensland. Coral (●), coral and seagrass (●), seagrass (●) and sand (●). 171

Figure 6.24: Posterior probabilities for the four acoustic classes Morinda Shoal: (a) Sand, (b) Seagrass (c) Coral and (d) Mixed coral and seagrass. 172

Figure 6.25: Class maps of Morinda Shoal using (a) supervised classification and (b) the addition of two subclasses determined by terrain slope. 173

Figure 6.26: Slope of angular dependence of backscatter strength (dB/deg.) versus angle-average backscatter strength (dB) over 5-60º for selected training areas used in Chapter 6. 174

Figure 7.1: Backscatter strength (dB) draped over bathymetry (m) from a MBS survey of Morinda Shoal, Queensland. Representative still images from the underwater video show major habitats found. 184

Figure A1.1: Track lines from the Morinda Shoal survey. UTM zone 55 south. 199

Figure A2.1: Track lines from east of Woody Island survey. UTM zone 51 south. 200

Figure A2.2: Track lines from north Thomas Island survey. UTM zone 51 south. 201

Figure A2.3: Track lines for the survey between Thomas and Woody Islands. UTM zone 51 south. 202

Figure A3.1: Track lines from the Owen Anchorage survey. UTM zone 50 south. 203

Figure A4.1: Track lines from the Owen Anchorage survey. UTM zone 56 south. 204

Figure A5.1: Track lines from the Keppel Bay survey. UTM zone 56 south. 205

Figure B1 Distortion of backscatter signal envelope due to receive beam pattern shown for odd beams 121 – 239 (a) and 121 – 141 (b) for sea depth of 20 m and pulse width of 100 μs. 209

Figure B2 Angular dependence of the backscatter strength estimates derived from the peak intensity (a) and energy (b) for sea depth of 20 m and different pulse width. 210

Figure B3 Angular dependence of the backscatter strength estimates derived from the peak intensity (a) and energy (b) measured at the sampling frequency of 28 kHz and different pulse width and sea depth of 20 m. 212

LIST OF TABLES

Table 1.1:	Summary of thesis chapters.	5
Table 2.1:	Typical values of density, sound speed and resulting acoustic impedance for various grades of sediment (APL 1994; Lurton 2002).	8
Table 2.2:	Input parameters used in the APL model (APL 1994).	13
Table 3.1	List of data structures created after conversion of XTF to Matlab data format.	57
Table 4.1:	Gamma scale (λ) and shape (β) parameters for the distributions shown in Figure4.10.	92
Table 5.1:	Matrix of correlation coefficients for different features derived from data collected from part of a MBS survey of Esperance Bay, Western Australia.	130
Table 5.2:	Fisher criterion for a variety of features derived from the angle cubes and the seafloor (terrain) slope. Highest values for each combination of habitat are shown in bold.	131
Table 5.3:	Confusion matrix for the training dataset from results of supervised classification.	136
Table 5.4:	Confusion matrix for training data from results of unsupervised classification.	136
Table 6.1:	Case studies, their benthic habitats and angle cube cell size used in Chapter 6.	138
Table 6.2:	FC values for different backscatter parameters of the seagrass, muddy sand and sand classes. Data from the MBS survey in Moreton Bay, Queensland.	154
Table 6.3:	Confusion matrix for the coarse sand, seagrass and muddy sand classes. Data from a MBS survey in Moreton Bay, Queensland.	155
Table 6.4:	The FC calculated for different pairs of habitat classes and compared for different backscatter properties and terrain slope. The highest value for each habitat pair is shown in bold. Data from a MBS survey east of Woody Island in Esperance Bay, Western Australia.	160
Table 6.5:	The correlation coefficient for the backscatter parameters and terrain slope. Data from a MBS survey east of Woody Island in Esperance Bay, Western Australia.	160

Table 6.6: Confusion matrix for the training data from a MBS survey east of Woody Island in Esperance Bay, Western Australia. 160

Table 6.7: Fisher criterion values for the different acoustic properties of the habitat classes identified by analysis of video recordings. Data collected from a MBS survey of Morinda Shoal, Queensland. 169

Table 6.8: Correlation matrix of the different properties derived from the MBS data collected over Morinda Shoal, Queensland. 170

Table 6.9: Confusion matrix for the training datasets from the classification of acoustic data collected from a MBS survey of Morinda Shoal, Queensland. 171

Table A1.1: Lines and rotation used for gridding data along with the settings of the Reson Seabat 8125 for Morinda Shoal survey. 199

Table A2.1: Lines and rotation used for gridding data along with the settings of the Reson Seabat 8125 for east of Woody Island survey. 200

Table A2.2: Lines and rotation used for gridding data along with the settings of the Reson Seabat 8125 for north Thomas Island survey. 201

Table A2.3: Lines and rotation used for gridding data along with the settings of the Reson Seabat 8125 for the survey between Thomas and Woody Islands. 202

Table A3.1: Lines and rotation used for gridding data along with the settings of the Reson Seabat 8125 for Owen Anchorage survey. 203

Table A4.1: Lines and rotation used for gridding data along with the settings of the Reson Seabat 8125 for Moreton Bay survey. 204

Table A5.1: Lines and rotation used for gridding data along with the settings of the Reson Seabat 8125 for Keppel Bay survey. 205

CHAPTER 1

INTRODUCTION

1.1 Overview

The aims of this chapter are to introduce and give an overview of the thesis, and to put the work in context. The chapter begins with the motivation for the study and provides details of the Coastal Water Habitat Mapping (CWHM) project, of which this work was a part, then the definition of habitat used, followed by the objectives of the study, and concludes with an outline of the thesis.

1.2 The need for acoustic remote sensing tools

The motivation behind this study into benthic habitat mapping using multibeam sonar (MBS) systems came from the need to further develop acoustic remote sensing tools. This is a result of the increasing pressure on the marine environment, which requires a greater need for effective coastal zone management (Holdgate 1994; Reichelt & McEwan 1999). In particular, successful management of coastal seafloor habitats is of great social, economic and environmental importance (Turner et al. 2004). Hence, there is an increasing need for a greater understanding of the natural resources present in the coastal zone and an ability to subsequently monitor changes over time or measure the effect of anthropogenic and natural impacts (Reichelt & McEwan 1999). These issues can only be addressed fully using survey methods and equipment that can produce high-resolution maps of biological resources. However, due to the economic and technical difficulties in mapping benthic habitats (compared with their terrestrial counterparts) many areas of coastal zone remain poorly investigated.

Remote sensing techniques are one of the most cost-effective methods of resource mapping, particularly in the coastal zone (Malthus & Mumby 2003). The use of acoustic remote sensing techniques in seabed mapping and monitoring has proven to be a useful tool in contemporary marine resource management (Kenny et al. 2003; Pickrill & Todd 2003), particularly in turbid and deep water areas, where aerial and satellite remote sensing based on measuring the electromagnetic spectra is of limited use.

Sonar systems (including MBS) have been used for many years to help map the seafloor, however, it is the recent (in the last decade) advancement and widespread use of MBS mapping technology, in combination with traditional survey techniques, that has provided the ability to map relatively large areas of seafloor at a resolution comparable to that of terrestrial maps (Augustin et al. 1996; Hughes-Clarke, Mayer & Wells 1996; Pickrill & Todd 2003). Nevertheless, benthic habitat mapping is still an underdeveloped field and requires further research work to realise the potential of the currently available technology, particularly MBS systems. This was the reason that further development of acoustic remote sensing tools was part of the Coastal Water Habitat Mapping project's objectives.

1.3 Coastal Water Habitat Mapping project

The Coastal Water Habitat Mapping (CWHM) project was an initiative of the Cooperative Research Centre for Coastal Zone, Estuary and Waterway Management (Coastal CRC) and its partner organizations. To date it has been the largest single program related to shallow water benthic habitat mapping in Australia (Penrose 2007). A joint venture between universities, government agencies and private enterprise, the CWHM project aimed to develop and examine technologies, including sonar tools, for rapid and cost effective assessment of shallow water marine habitats. Acoustic and ground-truth data have been collected from 10 sites around the Australian coast. Data from Owen Anchorage, Marmion Marine Park and Esperance Bay in Western Australia and Moreton Bay, Keppel Bay and Morinda Shoal in Queensland (Figure 1.1) were primarily used in this study. These sites represent a wide range of the coastal-benthic habitats found in Australia, including coral reefs, seagrass, rocky reefs and various grades of sediment. This thesis presents the results of the development of acoustic techniques for mapping based, in particular on using MBS systems. The primary MBS system used for this study was the Reson SeaBat 8125, which operates at 455 kHz. The Matlab® toolbox used to process MBS data was developed by a team at the Centre for Marine Science and Technology (CMST), Curtin University of Technology. This team included the candidate, Prof. Alexander Gavrilov, Dr Alec Duncan and Dr. Paulus Siwabessy. The calibration of the Reson SeaBat 8125 was conducted by the candidate, Prof. Alexander

Gavrilov and Dr. Paulus Siwabessy. All other work reported in this thesis was carried out by the candidate.

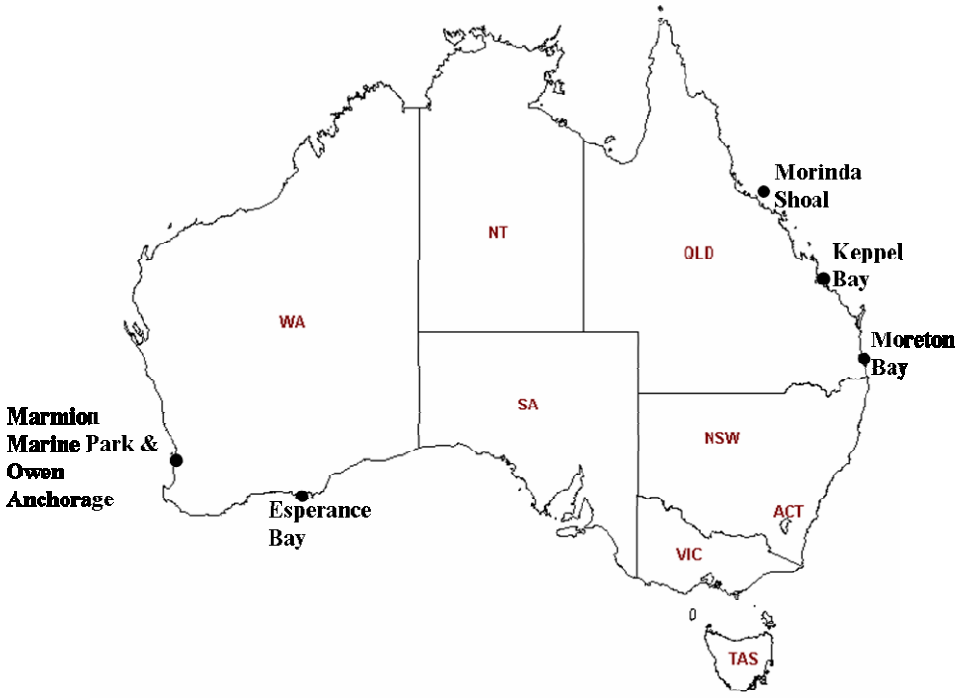

Figure 1.1: Location of study areas involved in this study and as part of the CWHM project.

1.4 Benthic habitats

The term "habitat" is defined for the purposes of this study as the combination of physical, geomorphological and biological properties of the seafloor. Specifically, the substrate, morphology and (if present) epi-benthic formations of the seafloor. This study is focused on broad-scale mapping over large areas (~10-1000 km^2) using MBS, as such, it is large-scale changes in habitat type that are of the most interest.

1.5 Aim and objectives of the study

MBS systems are recognised as one of the most effective tools available to map and characterise the seafloor as they can provide co-located high-resolution bathymetry and acoustic backscatter characteristics from a wide swath across a vessel's track. Bathymetry gives the relief of the seafloor and acoustic backscatter imagery can relate to morphological and composition characteristics of the seabed surface. Combined, these

two different sets of data can effectively describe the spatial variations of physical seafloor properties. While the production of bathymetry maps from MBS is well developed, processing and analysis of MBS backscatter data has not yet reached its full potential (Diaz 1999; Kostylev et al. 2001; Lurton 2002; Mayer 2006; Whitmore 2003). Hence, the need for enhanced techniques of MBS backscatter analysis was evident. This called forth the primary aim of this study, which was to examine and develop new methodologies for using MBS backscatter data for benthic habitat mapping.

This study had the following objectives:

1. Collect MBS backscatter data from a variety of shallow water habitats around the Australian coast.
2. Develop methods for processing backscatter data collected with high-frequency MBS systems.
3. Examine any MBS system effects on collection of backscatter data.
4. Investigate the relationship between seafloor backscatter characteristics and the angle of incidence in high-frequency MBS systems.
5. Evaluate the ability of various backscatter characteristics to discriminate between different seafloor types and identify key backscatter parameters that characterize the seafloor at high frequencies of hundreds of kHz.
6. Create methods to visualise the spatial distribution of seafloor backscatter properties (i.e. backscatter intensity images).
7. Demonstrate the use of MBS data in seafloor classification.

The results achieved towards fulfilling these objectives are presented in this thesis.

1.6 Outline of the thesis

The thesis is divided into 7 chapters, a summary of which is given in Table 1.1. The next chapter (2) gives some key elements of relevant theory and a review of literature in the field of acoustic seafloor classification. Chapter 3 aims to fulfil Objectives 2 and 3 by presenting the results of the calibration experiments and an outline of processing methods used in the work. Objective 4 is the focus of Chapter 4, where the effects of incidence angle on high-frequency backscatter from various seafloor types are

analysed. Chapter 5 is devoted to the methods for visualising and classifying MBS data (Objectives 5 and 6). Chapter 6 demonstrates and assesses the capabilities of the methods developed in Chapters 3 and 5 using a variety of case studies. The thesis ends with a discussion of the key findings and makes recommendations for future work in this research area.

Table 1.1: Summary of thesis chapters.

Chapter	Title	Summary
1	Introduction	Introduction to the study and to put the work in context.
2	Theoretical and experimental background	Gives key elements of background theory relevant to the subject and a review of progress made and problems encountered with using MBS for seafloor mapping.
3	Multibeam sonar backscatter measurements	Describes MBS system used in this study, the Reson SeaBat 8125, the results from a calibration experiment the method developed for processing MBS backscatter and some system effects.
4	The effects of incidence angle on the intensity and statistics of seafloor backscatter data collected with high-frequency multibeam sonar	Examines the effects of incidence angle on high-frequency backscatter and the implications of those effects for habitat mapping.
5	Techniques for visualisation and classification of the seafloor using multibeam sonar data	Describes an algorithm developed for visualising the spatial distribution of backscatter properties, and demonstrates the application of classification methods on MBS data.
6	Analysis of MBS data from different seafloor habitats	Applies the methods considered in the previous chapters to case studies in order to examine the capabilities of MBS data in benthic habitat mapping.
7	Discussion	Discussion of findings and recommendations

CHAPTER 2

THEORETICAL AND EXPERIMENTAL BACKGROUND

2.1 Overview

The aim of this chapter is to describe the theoretical and experimental background of this study and to review relevant work in the field of benthic habitat mapping using high-frequency multibeam sonar (MBS) systems. The chapter is divided into 4 main sections. Section 2.2 outlines theory and studies on the scattering of sound from the seafloor. This is followed by a description of the operation of MBS systems and processing of bathymetry and backscatter measurements (Section 2.3). How the bathymetry and backscatter measurements are used for the classification of the seafloor is the focus of Section 2.4. The chapter concludes with implications of the theoretical predictions and results of previous works for this study (Section 2.5). The literature in the field of bottom-interacting ocean acoustics is substantial, and the author is indebted to the many useful texts, including: Brekhovskikh & Lysanov (2001); J.E. Hughes Clarke *et al.* (2004); Lurton (2002); Medwin & Clay (1998); and Oglivy (1991).

2.2 Scattering of sound from the seafloor

2.2.1 Wave scattering from rough surfaces

The seafloor is a highly complex boundary, and is considered a rough surface for acoustic wavelengths used for the purposes of seafloor mapping. When sound waves encounter a rough boundary between two media with different impedances, waves are reflected, transmitted and scattered (Figure 2.1). This study is primarily concerned with the portion of energy scattered back towards the source, i.e. monostatic scattering, referred to in this study as backscatter. The proportion of energy backscattered from a rough surface is determined by the impedance contrast, sometimes referred to as 'hardness' and apparent surface roughness scale (i.e. roughness scale relative to the acoustic wave length. In general, as the impedance contrast or roughness of a surface increases so does the intensity of backscatter (Figure 2.1).

Typical values of density, sound speed and resulting acoustic impedance for selected sediment types are given in Table 2.1. The reflection coefficient from the different

sediment types at vertical incidence is also given in this table. In general, as the logarithmic parameter Φ of grain size decreases the acoustic impedance increases and, consequently, the scattering strength increases.

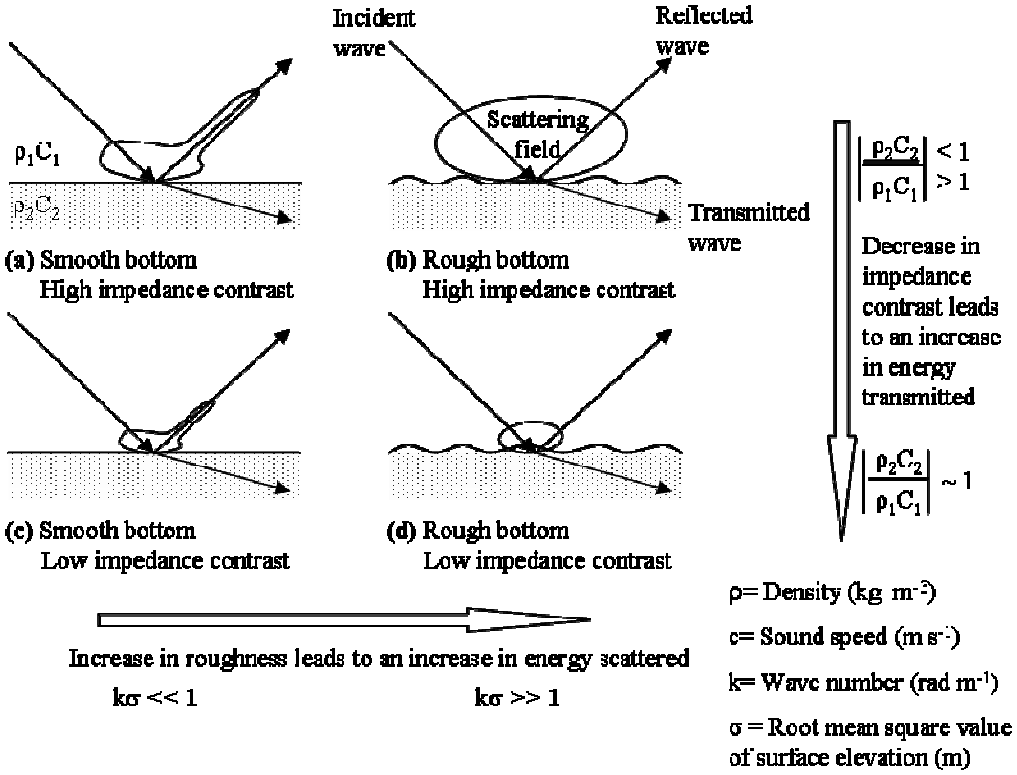

Figure 2.1: Schematic representation of the reflection, transmission and scattering of acoustic energy at a rough boundary and the effect of impedance contrast and apparent surface roughness scale on the scattered field (after Urick (1983)).

Sound waves scattered from a stochastically rough surface of the seafloor contain both coherent (s_{coh}) and incoherent (s_{inc}) components (Equation 2.1). The coherent component represents the backscatter signal averaged over the ensemble of statistically independent realisations of the rough surfaces. This component usually corresponds to specular reflection from the mean surface derived from spatial averaging of the roughness. The incoherent component represents waves scattered from the surface roughness and inhomogeneities within the volume of the seafloor, which have randomly varying amplitudes and phases.

$$s_{total} = s_{coh} + s_{inc} \qquad (2.1)$$

Table 2.1: Typical values of density, sound speed and resulting acoustic impedance for various grades of sediment (APL 1994; Lurton 2002).

Media	Grain size (Φ)	Density (kg m^{-3})	Sound Speed (m s^{-1})	Acoustic Impedence (rayls)	Reflection coefficient (R_θ)
Seawater	N/A	1000	1500	1.5 x10^6	N/A
Clay	9	1200	1470	1.764 x10^6	0.0809
Clayey silt	7	1500	1515	2.496 x10^6	0.2492
Very fine sand	3	1900	1680	3.192 x10^6	0.3606
Course Sand	1	2000	1800	3.6 x10^6	0.4118
Rock	N/A	2500	3750	9.375 x10^6	0.7241

The relative contribution of coherent and incoherent components depends on the incidence angle and apparent surface roughness scale. The Rayleigh parameter Γ (Equation 2.2) is commonly used to quantify the vertical scale of surface roughness. It characterises the root mean square (RMS) variation of the phase of a plane wave reflected from a surface with Gaussian distributed elevation differences:

$$\Gamma = 2k\sigma \cos\theta_1 \qquad (2.2)$$

where: $k = 2\pi/\lambda$ is the wave number, σ is the root mean square value of the surface elevation, and θ_1 is the incidence angle. A surface that appears smooth relative to the wavelength (i.e. $k\sigma << 1$) will impart the same phase shift and so the normal incidence wave is reflected coherently. When the surface is rough (i.e. $k\sigma >> 1$), sound waves are highly scattered because the elevation differences impart random phase shifts on the reflected wave causing constructive and destructive interference between the waves returning from the surface. The cos θ_1 term accounts for the effect of the incidence angle on the vertical component of the wavenumber. For a homogeneous surface at small incidence angles, Γ is nearly $2k\sigma$, whereas at small grazing angles, Γ tends to zero.

2.2.2 Seafloor backscatter strength

According to Medwin and Clay (1998), the surface scattering coefficient can be defined by Equation 2.3, which is illustrated in Figure 2.2:

$$\sigma_{bs} = \frac{I_s R_1^2 R_2^2}{I_i R_{\mathrm{Re}f}^2 A} \tag{2.3}$$

where: I_i is source intensity at a reference distance R_{ref} (usually 1m), $I_s = \langle p_s p_s^* \rangle / \rho c$ is the mean intensity of the scattered signal at the receiver (p_s is the acoustic pressure in the received signal), R_1 is the range from the source to the seafloor, R_2 is the range from the seafloor to the receiver, and A is the area of the scattering surface (<… > means statistical averaging). In this study, the scattering coefficient is measured in a monostatic arrangement, and thus $R_1=R_2$. Loss of energy through absorption in the water column must be taken into consideration at high frequencies. The absorption loss is usually defined as βR (dB), where β is the absorption coefficient (dB/m). Consequently, for this study the surface scattering coefficient is calculated as:

$$\sigma_{bs} = \frac{I_s R^4 \exp(2\alpha R)}{A I_i}, \quad \alpha = \beta / 20\log(e). \tag{2.4}$$

The surface scattering coefficient is a dimensionless quantity that accounts for the intensity (power) ratio of the incident and scattered waves determined per unit area at a reference distance of 1m. When expressed in dB, it is commonly called the backscatter strength (BS):

$$BS = 10\log_{10}(\sigma_{bs}) \tag{2.5}$$

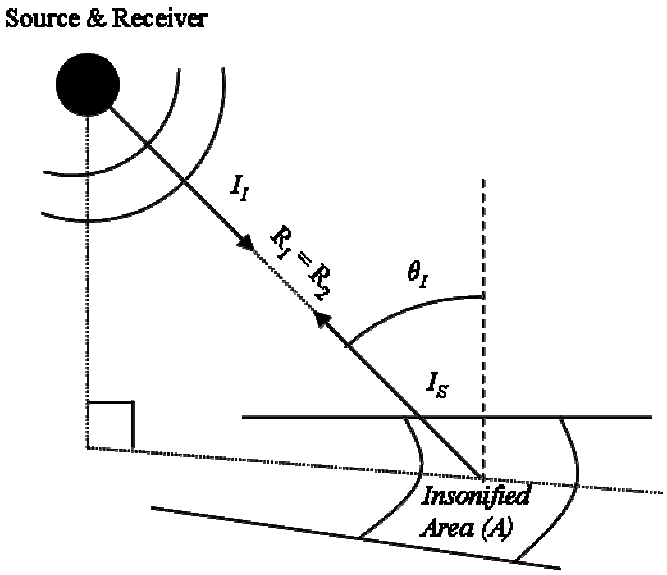

Figure 2.2: Geometric arrangement for measuring backscatter strength.

2.2.3 Modelling seafloor backscatter strength

The modelling of seafloor backscatter strength has been the subject of numerous papers and studies over the last 40 years. Models developed are either empirical, based on physical models, or a composite of the two. Physical models of acoustic scattering are usually based on methods of small perturbation, Kirchhoff theory or small slope approximation. One of the empirical models is the well-known Lambert's law commonly used to describe backscatter strength as a function of incidence angle θ_I (Urick 1983):

$$\sigma_{bs} = \mu \cos^2 \theta_I \ , \qquad (2.6)$$

where μ is the Lambert constant. For example, Mackenzie (1961) estimated μ = –27. For seafloor surfaces, Lambert's law appears to be a good approximation of backscatter data for incidence angles of 50-85º (Urick 1983). For incidence angles less than 50º, backscattering strength values show a significant rise with decreasing angle, which is in accordance with perturbation theory, but not with Lambert's law (Essen 1994).Various modifications to Equation 2.6 have been developed, such as combinations with near-specular and/or volume scattering components (Hellequin, Boucher & Lurton 2003;

Novarini & Caruthers 1998). Although some models based on Lambert's law have had success for specific applications (e.g. sonar signal processing), the lack of a physical premise is its shortcoming.

The method of small perturbation (MSP) is based on formulating the scattering mechanism as a boundary value problem expressed via partial differential equations. This involves finding a solution in terms of plane waves that match the surface boundary conditions, which state that the tangent component of the acoustic field must be continuous across the boundary. The boundary conditions at a rough surface $z = \zeta(r)$ can be transferred to the mean surface by expanding them in a power series of ζ (Brekhovskikh & Lysanov 2001; Oglivy 1991). The main drawback of the MSP is that it is only valid for surfaces with small slopes and roughness heights much smaller than the wavelength. It has also been shown that the MSP approach is not satisfactorily accurate at near-specular angles (Jackson, Winebrenner & Ishimaru 1986).

Conversely to the MSP, the Kirchhoff theory is valid for large roughness, when the RMS slope of roughness is small, and provides a more accurate prediction of scattering at near-specular angles than the MSP approximation. The Kirchhoff theory approximates the scattered field at the interface by assuming the scattering to be a result of a series of reflections from facets with random tilt angles. The Kirchhoff approximation assumes that: 1) the coherent reflection coefficient is valid at each point of these facets, 2) the radius of curvature is much larger than the wavelength and 3) effects of shadowing and contribution from multiple scattering are negligible. The Kirchhoff approximation is robust at modelling backscattering close to the vertical incidence on smooth sediment surfaces at sufficiently high frequencies (Brekhovskikh & Lysanov 2001; Oglivy 1991). Talukdar *et al.* (1995) developed a model specifically for backscatter intensity measured by an MBS system based on the Kirchhoff theory. This model provides a reasonably accurate prediction of backscatter from the seafloor for incidence angle less than 20º at relatively low frequencies.

To overcome the shortcomings of both the MSP and the Kirchhoff approximation, there have been a variety of compositions of these models developed by various authors, e.g. Kur'yanov (1962), Brekhovskikh and Lysanov (2001), which are referred to as composite (or two scale) roughness models. The general approach is to calculate the total scatter coefficient as the summation of the scattering coefficient (σ_{MSP}) from small-scale roughness as calculated by the MSP and the scattering coefficient (σ_{Kirch}) from large-scale roughness calculated using the Kirchhoff approximation:

$$\sigma_{bs} = \sigma_{Kirch} + \sigma_{MSP} \qquad 2.7$$

Equation 2.7 only considers scattering from the interface. The composite roughness model developed by Jackson *et al.* (1986) and further developed at the Applied Physical Laboratory at the University of Washington (USA) (APL 1994), hereafter referred to as the 'APL model', considers the scattering coefficient to be the sum of the surface ($\sigma_{Surface}$) and volume (σ_{Volume}) components (Equation 2.8):

$$\sigma_{bs} = \sigma_{Surface} + \sigma_{Volume} \qquad 2.8$$

The APL model uses six input parameters, which are listed along with their limitations for use in the model in Table 2.2. The first 5 of the parameters listed in Table 2.2 are used for estimating $\sigma_{Surface}$ and only the volume parameter is used to model σ_{Volume}. The APL model is intended for backscatter prediction between 10 and100 kHz. However, Anstee (2001) obtained reasonable results for backscatter strength from different seafloor types at 455 kHz, using the APL model.

The APL model distinguishes three domains (Figure 2.3):

- Near-vertical incidence;
- Moderate incidence angles;
- Small Grazing angles.

At near vertical incidence, backscattering from slowly varying large-scale roughness dominates backscattering from small-scale roughness and the volume scattering. At moderate incidence angles, scattering from small-scale roughness and volume inhomogeneities are the primary mechanisms. At small grazing angles below the critical angle, the volume scattering becomes negligible, which reduces the backscatter intensity especially at lower frequencies. For smooth and moderately rough surfaces (e.g. clay, silt and sand), $\sigma_{Surface}$ is modelled using the Kirchhoff approximation for near vertical incidence, and the MSP approach is used for all other angles. For rough bottoms (e.g. gravel and rock), an empirical expression is used to calculate $\sigma_{Surface}$ (APL 1994). The main challenge in the composite models is determining the boundaries between different angular domains for different approximation methods to be applied.

Table 2.2: Input parameters used in the APL model (APL 1994).

Symbol	Definition	Short name	Limitations
ρ	Ratio of sediment mass density to water mass density	Density ratio	1-3
ν	Ratio of sediment sound speed to water sound speed	Sound speed ratio	0.8-3
δ	Ratio of imaginary wavenumber to real wave number for the sediment	Loss parameter	0-0.1
γ	Exponent of the bottom relief spectrum	Spectral exponent	2.4-3.9
W2	Strength of bottom relief spectrum (cm^4) at a wavenumber $2\pi/\lambda$/ of 1 cm^{-1}	Spectral strength	0-1
σ2	Ratio of sediment volume scattering coefficient to sediment attenuation coefficient	Volume parameter	0-1

Lyons *et al.* (1994) extended the APL model to include interfaces within the sediment body. However, as the system used for this study operates at 455 kHz, the penetration of acoustic waves into the sediment is limited to a few centimeters due to high absorption in the sediment. Therefore, the underlying interfaces between different layers of the sediment are unlikely to influence the seafloor backscatter strength. Moreover, the majority of seafloor backscatter models, including those by the APL (1994) and Talukdar *et al.* (1995), are intended for backscatter measured at much lower frequencies (and Rayleigh numbers) than those used in this study.

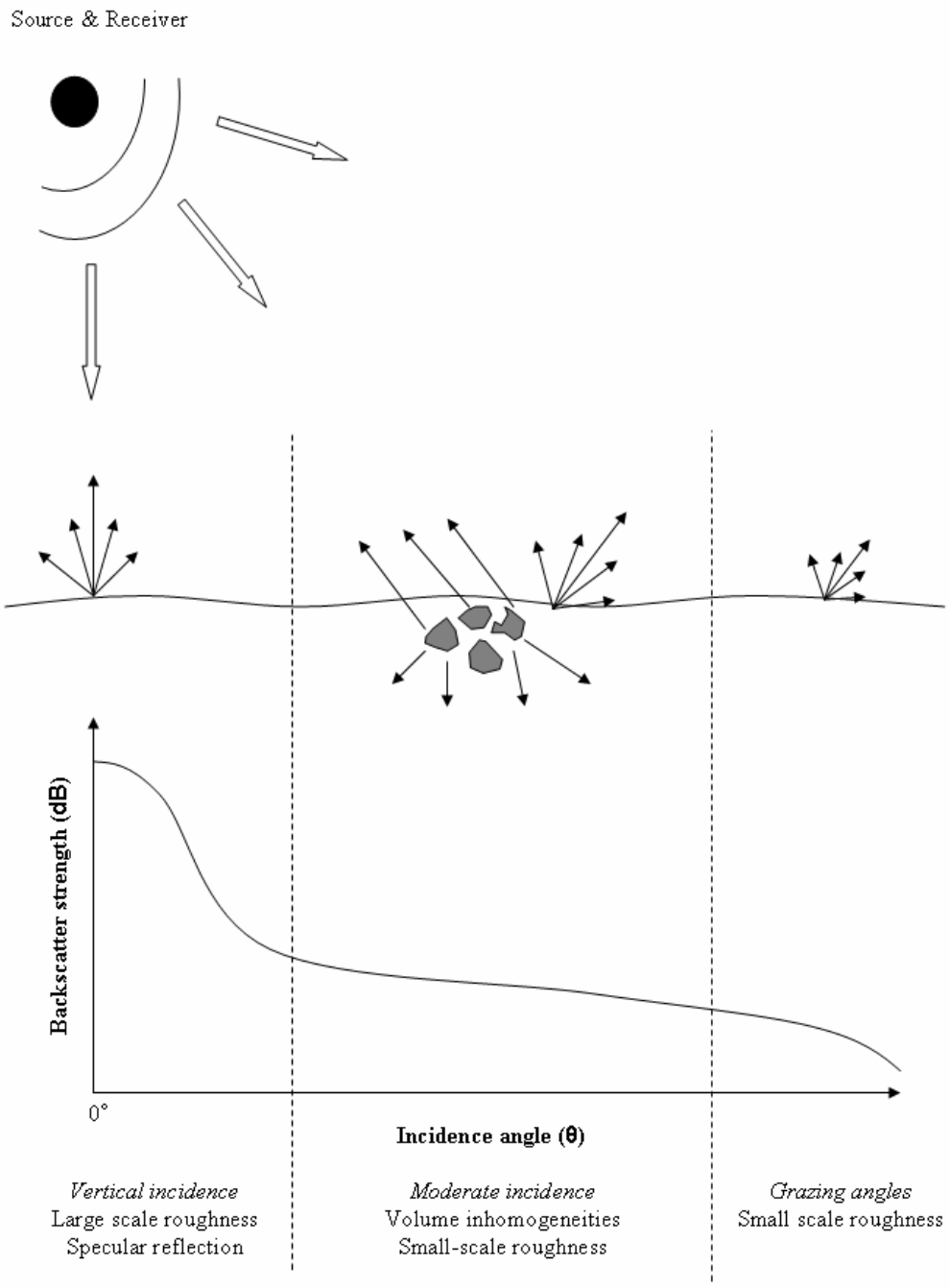

Figure 2.3: Generic representation of backscatter strength versus incidence angle (after Augustin et al. (1996)).

Some studies have tried to predict backscatter strength at high Rayleigh numbers ($\Gamma >> 1$) using high order small slope approximation (SSA) introduced by Voronovich (1985), and further developed in various studies (Broschat & Thorsos 1997; Gragg, Wurmser & Gauss 2001). The SSA is based on the assumptions that the scattered field can be represented by a superposition of plane waves propagating away from the surface, and that the acoustic field can be represented as a series in powers of the surface slope (Brekhovskikh & Lysanov 2001). The SSA overcomes the problem of determining boundaries between angular domains. It is limited, however, to situations in which shadowing and multiple scattering are unimportant, and does not include contributions from volume inhomogeneities.

There are some problems with applying current theoretical models to seafloor backscatter collected with MBS. For instance, most of the models discussed above, except for that by Talukdar *et al.* (1995) and some other methods based on the Kirchhoff approximation, are developed for plane wave scattering, and it appears to be very difficult to develop them into a model of backscatter measured by high-frequency MBS systems, especially in shallow water conditions where the plane wave approximation is no longer valid. In addition, there is a lack of models suitable for backscatter from seafloor habitats surveyed in this study, such as marine vegetation.

2.2.4 Statistics of seafloor backscatter

Acoustic backscattering from the seafloor is a stochastic process. The scattered acoustic field (ψ) is the sum of many elementary waves scattered by facets ('scattering cells') along the seafloor surface, which can be expressed as:

$$\psi = \sum_{j=1}^{N} A_j e^{i\phi_j} \tag{2.9}$$

where: A_j represents the amplitudes of the elementary scattered waves and ϕ_j their phases. When N tends to infinity and variations of A_j and ϕ_j are statistically independent, the complex amplitude of the scattered field ψ tends to be a Gaussian process in

accordance with the central limit theorem (CLT) (Oglivy 1991). If coherent scattering dominates in ψ, i.e. there is a constant term in Equation 2.9 much larger than the other randomly varying terms, then the distribution of the instantaneous absolute amplitudes $|\psi|$ will tend to Gaussian. When incoherent scattering dominates, the distribution of the instantaneous amplitude will tend to the Rayleigh distribution. The Ricean distribution, sometimes referred to as a generalised Rayleigh distribution, can be used to describe both these situations (Lurton 2002). In this study, the peak and average backscatter intensity were used to calculate the backscatter strength. The distribution of squared instantaneous amplitudes (i.e. intensity) of a Gaussian process is an exponential distribution. For a Gaussian scattering process, the statistical distribution of the average backscatter intensity was demonstrated theoretically by Middleton (1999) to follow a gamma distribution. Middleton (1999) used an approach different from the standard statistical models of scattering, which was based on an equivalent statistical structure instead of the explicit physical one.

When the number N of statistically independent scattering elements is small, the CLT is not applicable. In that case, the scattering process is not Gaussian, leading the amplitudes to exhibit non-Rayleigh statistics (Oglivy 1991). The study of non-Gaussian scattering is an active research area. Various aspects of non-Gaussian scattering are considered in papers of the special edition of the IEEE Journal of Oceanic Engineering (vol. 29(2), 2004). Recent studies have noted a non-Rayleigh character of backscatter statistics for shallow water seafloors and suggested different models, such as the Rayleigh mixture and K-distribution models (Dunlop 1997; Gallaudet & de Moustier 2003; Hellequin, Boucher & Lurton 2003; Jakeman 1988; Lyons & Abraham 1999; Stewart *et al.* 1994), and log-normal distribution models (Gensane 1989; Stanic & Kennedy 1992; Trevorrow 2004)

The Rayleigh mixture distribution model is a multimodal Rayleigh distribution, which is considered to be a result of a superposition of a number of independent Rayleigh scattering processes originating from different types of scattering mechanism (Gallaudet & de Moustier 2003; Stewart *et al.* 1994). The Rayleigh mixture model has been shown

to be robust at fitting backscatter amplitude data from a variety of seafloor habitats (Gallaudet & de Moustier 2003; Lyons & Abraham 1999; Stewart *et al.* 1994). Although a 2-3 component Rayleigh mixture model could be considered a logical choice for modelling seafloor backscatter, higher component models have many parameters so that they could fit experimental backscatter data no matter whether there is a physical premise or not.

The *K*-distribution, first used to describe the statistics of sea surface clutter in radar by Jakeman and Pusey (1976), is the product of a rapidly-fluctuating Rayleigh distributed component and a slowly-varying chi-distributed component (Lyons & Abraham 1999). The *K*-distribution has been shown to fit instantaneous seafloor backscatter amplitude and intensity data (Hellequin, Boucher & Lurton 2003; Le Chenadec *et al.* 2005; Lyons & Abraham 1999). The theoretical basis for the K-distribution representing the instantaneous seafloor backscatter amplitude and intensity data has been developed by Abraham and Lyons (2002) and Middleton (1999) respectively. According to Hellequin *et al.* (2003), the average backscatter intensity can be approximated by a "generalized *K*-distribution" which represents a product of two independent gamma-distributed processes. Similar to the logic behind multimodal Rayleigh distributions for backscatter amplitudes, if a gamma distribution does not fit the average backscatter intensity, then a multimodal gamma model could be a better approximation.

While the Rayleigh-mixture and *K*-distributions may be related to certain physical scattering mechanisms through their association with the Rayleigh models, the log-normal distribution model has not yet been analytically related to physical scattering processes. Many studies of seafloor acoustic backscatter, however, have observed a good fit of the log-normal distribution to variations of backscatter intensity data e.g. (Chotiros *et al.* 1985; Stanic & Kennedy 1992; Trevorrow 2004). Possible reasons why seafloor backscatter variations could be approximated by the log-normal distribution were considered by Gallaudet and de Moustier (2003).

2.3 Multibeam sonar systems

2.3.1 Operation of multibeam sonar systems

Some general design principles of modern MBS systems beam geometry are illustrated in Figure 2.4. MBS are mounted on a vessel (or AUV/ROV) and emit acoustic pulses with a beam pattern that is wide across-track and narrow along-track (shown in blue in Figure 2.4). The receive array is directed perpendicularly to the transmit array and forms a large number of receive beams that are narrow across track and steered simultaneously in different across-track directions by a beamforming process (shown in red in Figure 2.4). Thus the system performs spatial filtration of acoustic signals backscattered from different portions of the seafloor along the swath, referred to as beams footprints. From each beam, a co-located bathymetry and backscatter measurement can be made. Modern shallow-water MBS systems, such as Simrad EM 3000 and Reson SeaBat 8125, operate at hundreds of kHz, transmit short pulses of several tens of microseconds, and form hundreds of beams about 0.5 to 1 degree wide. Because they employ short transmit pulses and narrow-beams, such systems are capable of resolving small features a few decimetres wide in the seafloor relief.

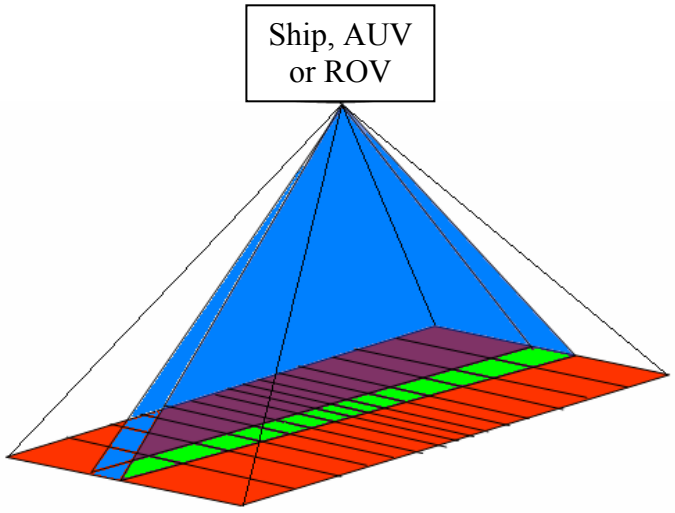

Figure 2.4: Schematic representation of the operation of MBS systems. Blue represents the transmit beam, red the receive array and green the footprint formed by the intersection of the two.

The typical beam geometry of a MBS system is shown in Figure 2.5. The area $A_{insonif}$ of the seafloor insonified by the sonar is usually approximated using Equation 2.10 (Lurton 2002):

$$A_{insonif} = \varphi R \frac{cT_w}{2\sin(\theta_I)} \tag{2.10}$$

where: φ is the along-track beam width, R is the range to the seafloor, c is the sound speed, T_w is duration of the transmit pulse, and θ_I is the incidence angle. The problem with using Equation 2.10, is that the insonified area tends to infinity as θ_I tends to 0º, which is not true. A more accurate equation for the insonification area can be easily derived from beam geometry for all incidence angles, which gives:

$$A_{insonif} = \varphi R^2 \left\{ \cos(\theta_I) \tan\left[\cos^{-1}\left(\frac{\cos(\theta_I)}{1+\frac{cT_w}{2R}} \right) \right] - \sin(\theta_I) \right\}, \tag{2.11}$$

and which was used in this study. Equation (2.10) is a good approximation for (2.11) when $\theta_I >> 0$. Intersection of the insonified area and the footprint of the receive beam results in the seafloor area for which the bathymetry measurement is made. This will be referred to as the footprint area (A_{fpa}) and is calculated using the following equation:

$$A_{fpa} = \frac{R^2 \varphi \sin(\Phi)}{\cos(\theta_I)} \tag{2.12}$$

where: Φ is the across track beam width of receive beams. The acoustic signals received within each beam of a MBS system are backscattered from the insonified area limited by the beam footprint. This area will be referred to as the insonification area for simplicity.

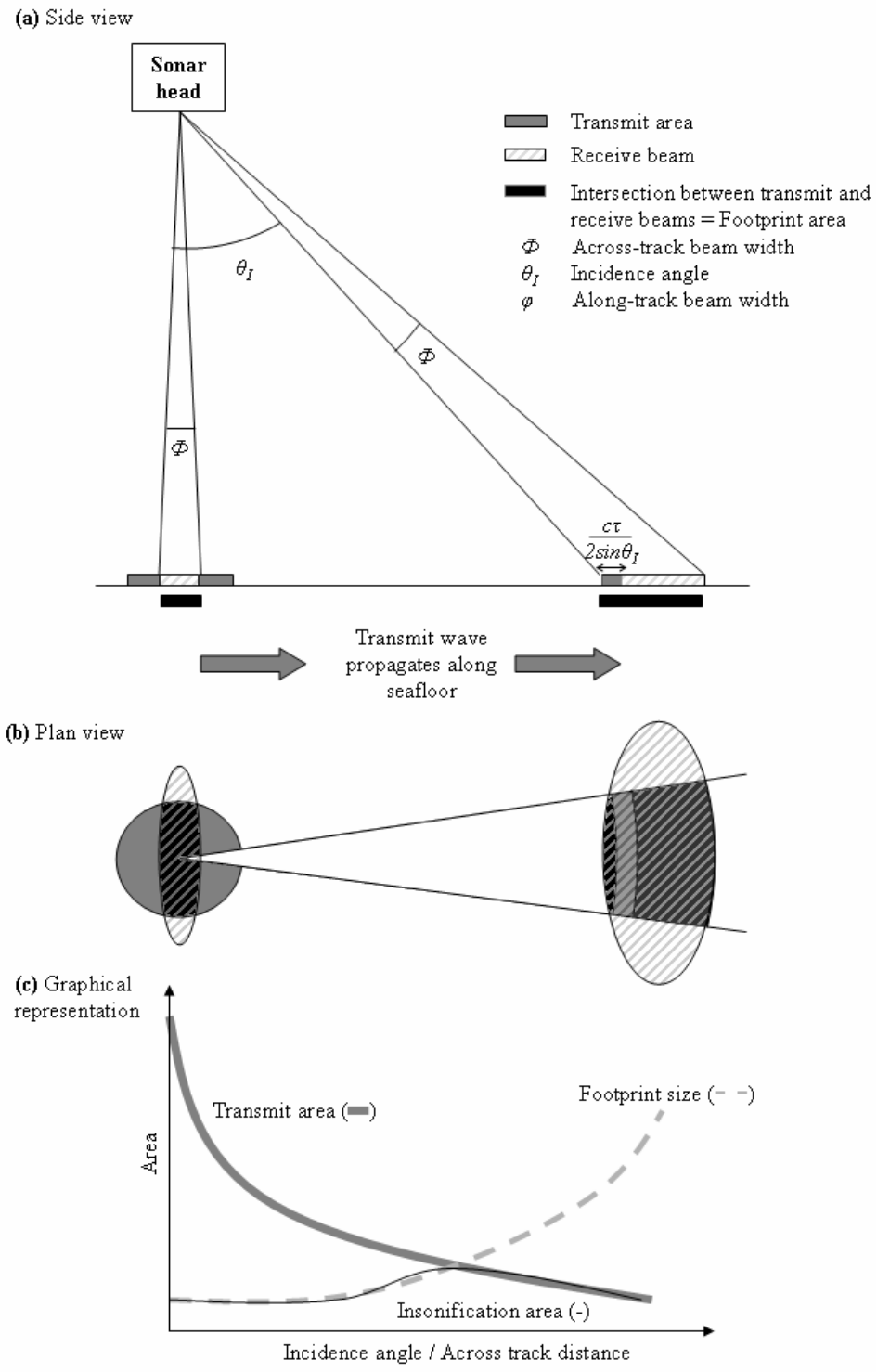

Figure 2.5: Typical beam geometry of multibeam sonar systems (a) sideview, (b) plan view and (c) graphical representation of the beam areas versus incidence angle/across track distance.

When the sonar signal returns to the receive array, the range along each beam to the bottom is calculated from the travel time and the sound speed. There are two basic ways in which the bottom is detected. At near vertical incidence, where the footprint is small and consequently the echo signal is short and has a single prominent peak, the travel time is measured by the maximum backscatter amplitude. At oblique angles, the footprint increases and the echo signal may have several peaks of comparable amplitudes. In this regime, phase detection of the bottom is commonly applied. To determine the signal travel time in this regime, a MBS system forms pairs of nearly coincident beams using receive subarrays formed, for example, from odd and even elements of the whole array, and then calculates the phase difference between the signals received along beams of each pair. The moment of time at zero phase difference is assumed to correspond to the two-way signal travel time. The bathymetry is calculated from the range, beam launch angle and the sound speed.

The operational principles of MBS systems give evident advantages for seafloor mapping. However, they require much stricter requirements for ship's navigation and motion compensation than that for single-beam systems. If ignored, ship's roll, pitch, heave and yaw may distort the bathymetry and backscatter images. Therefore MBS surveys must be accompanied with simultaneous tracking of ship's attitude. The procedure for compensating for a ship's attitude for swath seafloor mapping is well developed and described in the literature (US Army Corps of Engineers 2002).

Another serious problem specific to MBS seafloor mapping is acoustic refraction in the water column due to a depth dependent sound speed, which distorts the acoustic ray trajectories and hence the footprint location and depth cannot be accurately calculated using a simple triangulation model. If the sound speed profile is known, however, then swath data can be corrected using the ray approximation for sound propagation (Lurton, Dugelay & Augustin 1994).

2.3.2 Processing of multibeam sonar backscatter data

The initial purpose of MBS systems was to obtain high-resolution bathymetry maps, but recent research, including this study, has focused on utilising MBS backscatter data for benthic habitat mapping. de Moustier (1986) was one of the first to demonstrate the potential of MBS systems as a seafloor characterisation tool. He used backscatter data collected from a Sea Beam system to calculate and map the seafloor backscatter strength. Research works by Talukdar *et al.* (1995), Mitchell (1996), Augustin *et al.* (1996), and Hughes-Clarke *et al.* (1996) have further developed the methods for processing MBS backscatter data. These methods were developed for and examined primarily with low-frequency systems most common at that time. The basic principles of measuring the seafloor backscatter strength are similar for low and high frequency systems. However, the measurement geometry and physical conditions, such as the insonification and footprint areas relative to the seafloor roughness scale, Rayleigh parameter, etc., are significantly different. More recently, processing and analysis methods purposely designed for modern high-frequency narrow-beam MBS systems have been proposed (Beaudoin *et al.* 2002; Hellequin, Boucher & Lurton 2003).

At present, there are a limited number of software products available to process MBS backscatter data. Some of the most notable software packages are: SwathEd (J.E. Hughes Clarke *et al.* 1993), MB systems (Caress & Chayes 1995), SonarScope (J.-M. Augustin & Lurton 2005) and Geocoder (Fonseca & Calder 2005). Of these packages only, MB systems, developed by Caress and Chayes (1995), is a free and open source software. Moreover, of the software available at the start of this study, none were considered appropriate to achieve the objectives of this work, which involved examining different approaches to the processing and analysis of backscatter data collected from MBS. Hence, Matlab® was used by the acoustics research group at the Centre for Marine Science and Technology (CMST) to develop a toolbox which would implement various processing and analysis algorithms for MBS data. Matlab® was considered the most appropriate programming platform as it allowed building open-source codes, which gives much more flexibility in designing, modifying, and examining different algorithms for processing backscatter data. Moreover, a number of powerful and useful analysis

tools, such as the Signal Processing, Statistics, and Mapping toolboxes, are implemented in Matlab®, which simplified considerably the development of special programs for MBS data processing.

2.3.3 Correcting multibeam sonar backscatter images for angular dependence

As backscatter strength is dependent on the incidence angle, trying to mosaic seafloor backscatter images from multi-swath backscatter datasets requires correcting for angular dependence. An improper correction will result in artefacts in backscatter mosaics. Some of the main approaches used for angular correction are described below.

Models based on the Lambert's law have been used to correct backscatter strength images for angular dependence. For instance, Hellequin *et al.* (2003) employed a simple composite model that treated the angular dependence of backscattering using the Kirchhoff approximation term dominating at near-nadir incidence angles and a Lambert-like term dominating at off-specular angles (Equation 2.13):

$$BS(\theta) = 10\log\left[A\exp\left(-\alpha\theta^2\right) + B\cos^{\beta}\theta\right]_l, \qquad (2.13)$$

where BS is the backscattering strength and θ_l is the angle of incidence. The coefficients A, B, α and β are estimated by least-mean-square fitting of the model function to the average angular dependence of backscatter intensity observed across representative (or training) areas. As discussed previously (Section 2.2.3), the Lambert law is not robust enough for accurate numerical prediction of the angular dependence for all seafloor types. For instance, this model considers no contribution from volume inhomogeneities which, even at high-frequency, can influence the angular dependence (Jackson & Briggs 1992).

Other approaches include removing the mean angular dependence based on a series of pings from a homogeneous area (Beaudoin *et al.* 2002). A similar approach is taken by QTC's Multiview software for MBS data processing. The QTC algorithm for correction

of the angular dependence of backscatter intensity data consists basically of two steps (Preston & Christney 2003):

1. The mean angular dependence of the backscatter level is calculated for all sonar pings, i.e. for the entire seafloor area observed by the sonar system, and then this mean angular dependence is subtracted from the backscatter data obtained with each ping.
2. Standard deviation of the backscatter level relative to the mean angular dependence is calculated for each angle using all pings, and then the backscatter data corrected for the mean angular dependence are normalized (divided) by the angular dependence of standard deviation.

Both these approaches assume the slope of the angular dependence of backscatter strength for all seafloor types is uniform, although this has been found to not be the case (Urick 1983). However, these methods used to correct for angular dependence will be investigated to determine the best way to produce backscatter images.

2.4 Acoustic seafloor classification

2.4.1 Classification methodologies

Acoustic seafloor classification (ASC) segments the seafloor into discrete classes based on sonar data. The motivation for such work has been outlined in Chapter 1. There are two main methodologies in ASC:

1. Geoacoustic modelling or inversion of sonar data
2. Phenomenological approach

Geoacoustic modelling transforms the acoustic data to actual physical properties of the seafloor, such as grain size, porosity, etc. (Bentrem, Avera & Sample 2006; Chakraborty, Kodagali & Baracho 2003; Fonseca, Mayer & Kraft 2005; Talukdar, Tyce & Clay 1995). This requires an adequate model of backscatter and usually the input of additional geoacoustic parameters and a calibrated sonar system. For example, Bentrem *et al.* (2006) employed the APL model where the backscatter data and input parameters are used to estimate the mean-grain size.

A phenomenological approach assumes a correlation between morphological and physical properties of the seafloor and acoustic data, but divides data into acoustically different regions without inverting backscatter data into actual physical properties of the seafloor. Ground-truth information should then be used to infer how those regions relate to different seafloor types. For example, the commercial software QTC-Multiview derives 132 features from MBS bathymetry and backscatter images, then performs principal component analysis (PCA) and clusters the first three principal components into acoustic classes (Preston 2004; Preston *et al.* 2004; Preston *et al.* 2001).

The classification process can be broken down into three steps:

1. Feature extraction
2. Feature selection or reduction
3. Segmentation

Feature extraction is the determination of univariant descriptors of acoustic data that can be used to discriminate between seafloor classes or to infer geoacoustic parameters. Features can be either individual measures, such as the peak intensity, or more sophisticated descriptors, such as results of statistical and spectral analyses. Determining what features are useful for classification is an important objective of this study.

If the number of features extracted is very large, some sort of feature selection or reduction is recommended before segmenting data (Duda, Hart & Stork 2001). Feature selection ranks features through some discrimination criteria, e.g. Fishers' criterion (Duda, Hart & Stork 2001) and the most effective features are used in the segmentation routine. Feature reduction involves combining all original features into a smaller number of their combinations which are used as new features. This can be done, for example, through PCA and linear discriminate analysis (LDA) (Duda, Hart & Stork 2001).

With geoacoustic modelling, the features that characterise the backscatter model are fitted to those derived from backscatter measurements, which is usually performed using

various least mean squares algorithms. In a phenomenological approach, after features have been derived, they are segmented using either supervised or unsupervised classification algorithms. Supervised classification is where ground-truth information is used to train a classifier with a certain number of known classes, which is then applied to all of the dataset. Unsupervised classification involves clustering data of unknown classes into statistically similar groups. The number of groups to classify can be either specified before clustering or determined after clustering.

There are various algorithms for segmentation of data described in the pattern recognition literature. The main ones that have been applied to acoustic seafloor classification include *k*-means clustering (Diaz 1999; Preston 2004; Siwabessy 2001), decision trees (Dartnell & Gardner 2004; Ierodiaconou *et al.* 2006), statistical-distance/maximum-likelihood (J.M. Augustin *et al.* 1997; Canepa & Pace 2000; Foster-Smith & Sotheran 2003) and neural-networks (Chakraborty, Kodagali & Baracho 2003; Stewart 1994).

2.4.2 Classification of multibeam sonar data

Of the different steps in seafloor classification using MBS data, this study is most interested in determining the best features to extract from MBS data in order to realise the maximum potential of MBS data in seafloor discrimination. Features extracted from MBS data for seafloor classification can be in general divided into three types:

1. Seafloor terrain characteristics (i.e. bathymetry and derivatives)
2. Backscatter characteristics corrected for the angular dependence (i.e. analysis of backscatter mosaics)
3. Angular dependence of backscatter.

There have also been combinations of these features examined in some studies. The following highlights some of the most interesting and relevant works.

2.4.2.1 Seafloor terrain characteristics

From analysis of bathymetry, it is possible to identify many geomorphologic features of the seafloor, such as sand waves, bioturbation, rocky outcrops, etc. Moreover, depth is an important factor influencing the distribution of benthic communities, both through affecting the amount of light that reaches the seafloor and governing wave exposure. However, using depth alone as a feature is not sufficient for seafloor classification as it produces depth contours rather than habitat boundaries. Derivatives of depth, e.g. standard deviation, slope, etc., are measures of large-scale roughness of the seafloor surface and are useful for identifying areas of high or rapidly changing relief. However, care must be taken when using terrain derivatives, because these parameters suffer considerably from ship motion artefacts. There are a variety of terrain analysis tools employing bathymetry derivatives described in the literature (Rinehart *et al.* 2004). It has been shown that applying ecological principles to seafloor terrain features can be successful in predicting the presence of some benthic organisms through modelling (Holmes *et al.* 2005). Although terrain analysis is effective in identifying geomorphologic features, it does not help in discriminating between different habitat classes, if there is no significant difference in the topography of those habitats.

2.4.2.2 Analysis of backscatter mosaics

The analysis of MBS backscatter mosaics/images for seafloor classification follows on from classification of sidescan sonar images. For example, the use of grey-level co-occurrence matrices (GLCMs) (Blondel, Parson & Robigou 1998; Reed & Hussong 1989) based on work by Haralick *et al.* (1973), Fourier analysis (Pace & Gao 1988) and wavelet analysis (Atallah, Smith & Bates 2002) have been shown to be successful in the classification of sidescan sonar images. The aim of these image analysis algorithms is to recreate recognition principles in human vision which distinguish and quantify different tones and texture. As a result, the features derived can often be hard to relate to physical features of the seafloor, but for the purposes of classification this may not be critical. Of the few software products commercially available for seafloor classification using MBS data, most use image analysis techniques. For example, QTC-Multiview utilises both GLCMs and the spectral features

described by Pace and Gao (1988) along with some other parameters derived from image analysis (Preston & Christney 2003).

To apply image analysis to MBS backscatter data for classification, the backscatter values and their statistical characteristics derived from MBS data must be only dependent on seafloor type, and hence be adequately corrected for the incidence angle and the method of backscatter measurements. Methods for angular correction were reviewed in Section 2.3.3, but at present there is no universally accepted method. Seafloor classification based on analysis of MBS backscatter images often contains artefacts due to inadequate correction for angular dependence (Dartnell & Gardner 2004; Houziaux *et al.* 2007; Whitmore 2003). For the purposes of spatial visualisation of backscatter strength (backscatter mosaicing), correcting for incidence angle is worthwhile, whereas for seafloor classification, analysis of the relationship of backscatter intensity with the incidence angle offers an additional means not just to discriminate between different seafloor classes, but also to determine some seafloor properties.

2.4.2.3 Angular dependence of backscatter

Exploiting curves of the backscatter angular dependence for seafloor classification can be done using either model-based (Bentrem, Avera & Sample 2006; Fonseca, Mayer & Kraft 2005) or empirical approaches (Canepa & Pace 2000). The advantage of model-based approaches is that they can be used with little or no ground-truth information. The end goal of model-based methods is geoacoustic inversion. For example, the amplitude versus offset (AVO) model developed by Fonseca *et al.* (2005) extracts features from mean backscatter curves (derived from a series of stacked pings), which are correlated to seafloor properties, such as the acoustic impedance and grain size, by comparison with the model prediction. For sedimentary habitats, the AVO model shows some promising results. However, there are some problems with using MBS backscatter data for geoacoustic inversion. At present, there is not a universal high-frequency model available that can adequately describe the backscatter angular response from all seafloor habitats, such as those investigated in this study (e.g. seagrass,

coral reef, etc). Also, most MBS systems are not calibrated and hence do not give absolute values of seafloor backscattering strength. Moreover, the beam pattern of some systems (e.g. the Reson Seabat 8101) is not uniform across track, so that the measured angular dependence must be corrected for the actual beam pattern of both transmit and receive beams (Foote *et al.* 2003).

The relationship between backscatter strength and incidence angle can be exploited empirically, i.e. using the relative difference between angular responses to distinguish seafloor types. Hughes Clarke (1994) identified and used ten features of angular dependence curves, including the mean and slope from 3 different angular domains, that could be used for seafloor classification. Canepa and Pace (2000) empirically derived the median backscatter strength versus incidence angle curves for all known seafloor types in the survey area. Data from unknown areas were then compared to each reference curve and the shortest statistical distance for each beam and ping was used as the criterion for classification. The main problem with using the angular dependence curves for seafloor classification is segmentation of heterogeneous areas of seafloor and around boundaries between habitats (J. E. Hughes Clarke 1994).

Utilising the angular dependence of backscatter in addition to the mean backscatter strength (or backscatter level at a reference angle) is a better approach to seafloor classification, because it provides more information about morphological and physical properties of the seafloor. This was also concluded in the study by Diaz (1999), where the seafloor classes determined from the textural analysis (using GLCMs) of a backscatter mosaic did not always distinguish sediments of different grain sizes. However, using the method developed by Hughes Clarke (1994) that exploits the angular dependence of backscatter strength, Diaz (1999) was able to distinguish those seafloor classes.

2.5 Implications for the approach of this study

Scattering models

- In the absence of fully adequate high-frequency (i.e. > 100kHz) seafloor backscatter models, theoretical predictions made by Anstee (2001) using the APL model for backscatter strength from different seafloor types at 455 kHz will be used for general comparison.
- Statistical variations of backscatter should first be compared to the simplest model based on Gaussian mechanism for backscatter. For instance, the applicability of the gamma model to approximate the distribution and statistics of variations of the average backscatter intensity from different seafloor habitats will be examined. If the gamma distribution is not a sufficiently accurate approximation, then non-Rayleigh statistical models, such as the generalised *K*-distribution, should be investigated.

Processing MBS data

- Methods to determine seafloor backscatter strength data from MBS data developed at the Centre for Marine Science and Technology (CMST), Curtin University of Technology will be presented. Backscatter strength data will be assessed for adequate correction for system settings, beam geometry and oceanic conditions.
- When investigating the production of backscatter mosaics from multiple swaths, consideration will be given to previous methods used to correct backscatter strength images for incidence angle.

Seafloor classification

- Based on previous studies, a phenomenological approach will be used when developing an acoustic seafloor classification system based on MBS data, as this was considered to be the most robust.
- Features of MBS backscatter to be investigated for their ability to discriminate between different seafloor types include: statistical distributions of backscatter

and properties of the angular dependence of backscatter strength on different seafloor habitats found in different coastal shelf areas around Australia.

- Seafloor terrain analysis will be used to identify areas of high-relief.
- Established methods for feature reduction and selection, and unsupervised and supervised segmentation routines will be used.

CHAPTER 3

MULTIBEAM SONAR BACKSCATTER MEASUREMENTS

3.1 Overview

Multibeam sonar (MBS) systems are one of the most effective tools available to map the seafloor (Kenny *et al.* 2003). This is because MBS systems are capable of collecting data from a wide swath of the seafloor. The MBS backscatter signals are primarily used to derive high-resolution bathymetry, however, in recent years research has concentrated on utilising the backscatter intensity to infer certain physical properties of the seafloor (Augustin *et al.* 1996; de Moustier 1986; Hughes Clarke, Mayer & Wells 1996; Talukdar, Tyce & Clay 1995). The general operation of MBS systems was outlined in Chapter 2. The aim of this chapter is to describe in more detail the principal MBS system used for this study, the Reson SeaBat 8125 (referred to as the Reson 8125), and the methods used for backscatter measurements and processing. The methods for data processing and analysis developed are also applicable to many other MBS systems.

This chapter is broken into a further five sections. First a description of the Reson SeaBat 8125 system is given (Section 3.2), which is important for understanding the geometry and scheme of measurements, including signal transmission, reception and preliminary processing. This is followed by a description of the different methods available in the Reson 8125 to log backscatter data (Section 3.3), which provides the rationale for the further data analysis. Section 3.4 details a calibration experiment that aimed to verify known and estimate unknown system parameters. Section 3.5 gives a step-by-step explanation of a program developed to calculate the backscatter strength from the data collected with the Reson 8125, which could also be applied to other systems. The final section (3.6) examines the effects system configuration and settings have on backscatter data. Where appropriate, the implications for benthic habitat mapping are outlined.

3.2 Reson SeaBat 8125 system description

3.2.1 General description

The Reson SeaBat 8125 is a 455-kHz high-resolution MBS system with dynamic focusing of receiving beams. Figure 3.1 shows a picture of the sonar head out of the water and a diagram showing the orientation in the water. The Reson 8125 system insonifies a swath on the seafloor that is 120º across track by 1º along track. The receive array forms 240 individual beams with 0.5° spacing of the beam centres across track. The along-track width of the receive beams is 20°. Because the receive array is flat, the across-track beamwidth varies with the steering angle from 0.5° for the innermost beams to 1.0° for the outermost beams. As a result, the sonar beams formed by the intersection of the transmitted and received beams are 0.5 x 1° wide in the centre and 1 x 1° wide at the outer edges. The Reson 8125 has a 16-bit dynamic range and a sampling rate of 28437.5 samples per second, which provides approximately one amplitude measurement for every 2.5 centimetres in terms of transmission range (RESON Inc. 2002b). The amplitude measurements are proportional to the acoustic pressure (Bridge[1], *pers. comm.*).

Although information on the actual beamforming scheme realised in the Reson 8125 receive array was not available, it was assumed, based on the calibration results (see below) that a Chebyshev shading filter was applied to the amplification factor of array elements in order to reduce the level of side-lobes to about –30 dB relative to the main lobe.

3.2.2 System settings

3.2.2.1 Transmit signal

The Reson 8125 system allows control of signal power emitted into the water. The selections of power settings are 1 through 14, with each increment being 3 dB. The full power setting yields a source level of 220 dB re 1 μPa at 1 m. The system also allows various settings of the pulse duration of the transmitted signal. The pulse

A1. [1] Burr Bridge was a Reson Engineer during the period of study

durations available for the Reson 8125 system are from 11 to 292 μs in increments of 2 μs.

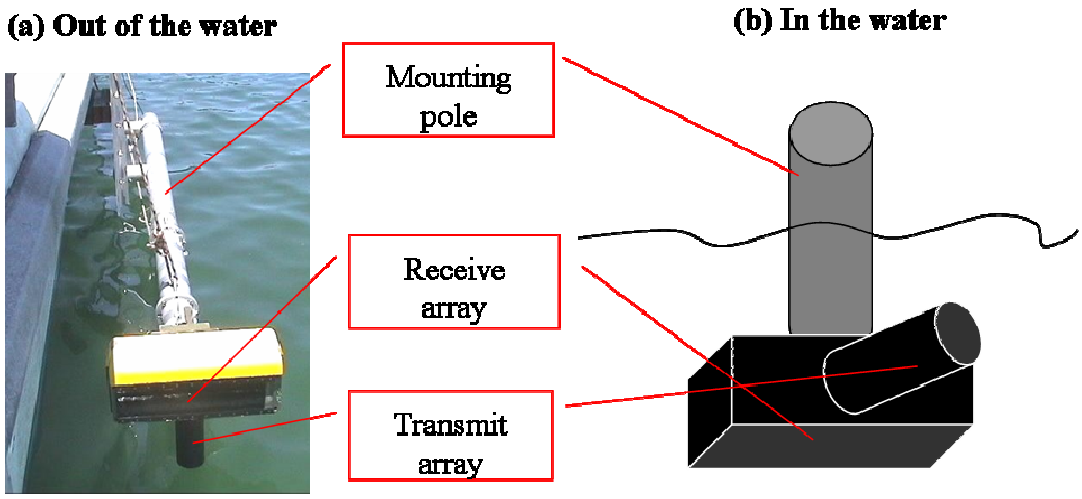

Figure 3.1: Reson SeaBat 8125 sonar head mounted on a side pole: (a) photograph of it out of the water, and (b) diagram of its position in the water.

3.2.2.2 Receive signal

The Reson 8125 system allows for the receiver gain to be controlled and applied in two modes: Fixed and Time Varied Gain (TVG). For all of the surveys performed during this study, the TVG mode was chosen. This means that the total receiver gain (G_{total}) applied by the system had 3 components (in linear scale):

$$G_{total} = G_p \, G_o \, G_{TVG} \qquad (3.1)$$

where: G_p is a fixed processor gain and G_o is extra gain selected by the operator (in the log scale) from 1 to 45 dB. TVG is introduced to correct for transmission loss:

$$TVG = 10\log G_{TVG} = 2\alpha R + Sp\,\mathrm{Log}_{10} R \qquad (3.2)$$

where: α is the absorption loss coefficient in dB/m, R is the along-beam range in m, and Sp is the spreading loss coefficient. Both α and Sp are set by the operator. Also the

AutoGain mode is available to allow the receive system to automatically adjust the variable gain G_o based on the amplitude of the returned signal. The G_o values selected by the processor are automatically stored in the data files. The fixed system gain (G_p) is usually unknown for end-users, and hence, unless the sonar is fully calibrated (see Section 3.4), backscatter values can only be measured in relative units.

3.2.3 Dynamic focusing

Dynamic focusing is implemented in the beamforming scheme of the Reson 8125 to reduce distortion of the array beam pattern in the near field, *i.e.* when the sea depth is relatively small. The algorithm of beamforming with dynamic focusing can be expressed as follows (Lurton 2002):

$$P_a = \sum_n p_n A_n \exp\{-ikx_n \sin(\theta)\} \exp\left\{ikx_n^2 \cos(2\theta)/cT\right\} \qquad (3.1)$$

where P_a is the output signal of the array, p_n are acoustic signals on the array elements, x_n are distances from the receive elements to the centre of the linear array, A_n are coefficients of the side-lobe shading window, k is the wavenumber, θ is the beam steering angle, c is the sound speed, and T is the time elapsed from the transmission moment. The first exponential term in Equation 3.1 denotes conventional beamforming for the far field, while the second exponential term implements time varying, i.e. dynamic focusing of the array. Figure 3.2 demonstrates the effect of dynamic focusing for different sea depths and steering angles of the Reson 8125 receive array. The modelled beam patterns are shown projected onto the seafloor, which is assumed to be flat. At small sea depths and steep steering angles, the beam pattern without dynamic focusing is noticeably distorted (Figure 3.2), so that the actual footprint size measured at the –3 dB level is considerably larger than that predicted for the far field (shown by red lines). Dynamic focusing corrects the beam pattern, making it similar to that expected for the far field. At oblique angles and in deeper water, when the array length becomes negligibly small compared to the slant range to the bottom, the beam patterns and the footprint size with and without dynamic focusing are similar.

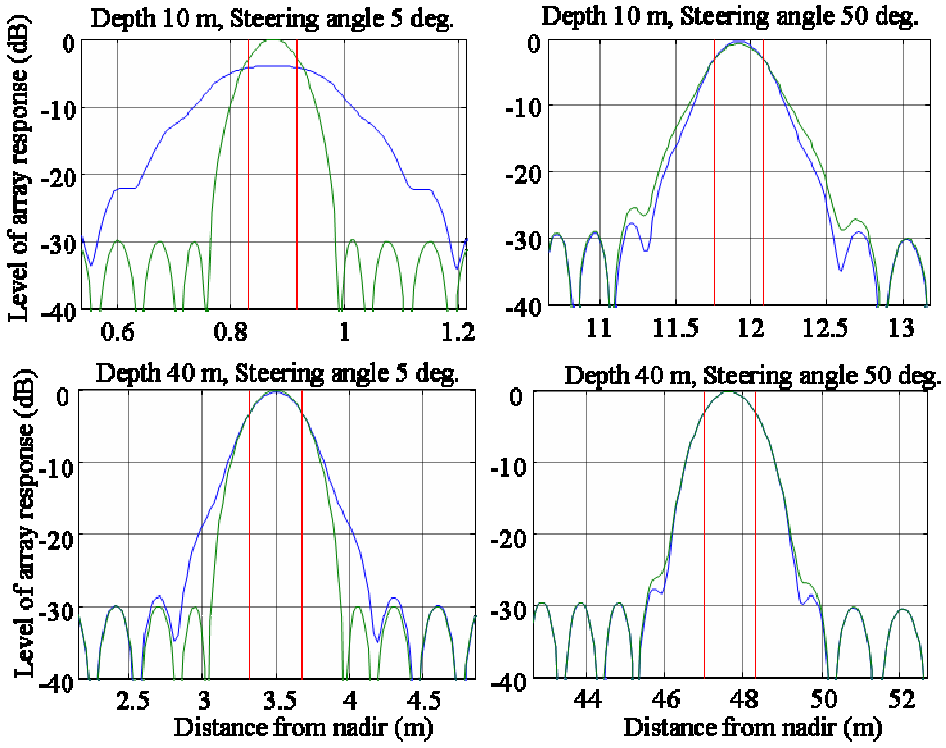

Figure 3.2: Beam patterns of the Reson 8125 receive array modelled with (green) and without (blue) dynamic focusing and shown projected onto the seafloor for different sea depths and steering angles. Red vertical lines show the footprint edges determined at the –3 dB level for the far field.

3.3 Logging multibeam sonar backscatter data

3.3.1 Introduction

At present, there are four main methods for logging backscatter data in the Reson 8125 and the majority of modern MBS systems:

- the complete backscatter waveform from each beam (referred to here as snapshots);
- a sidescan-like time series of amplitudes derived from snapshots by combining the backscatter signals from all beams (referred to here as sidescan);
- a fragment of the full backscatter envelope around the bottom return signal from each beam (referred to here as snippets);
- the maximum amplitude from within each snippet (i.e. one value per beam).

To demonstrate the relationships between the different backscatter logging methods, backscatter data were logged using simultaneously the snapshot, sidescan and snippet logging modes. The aim of this section is to assess the relative merits of each of the logging methods.

3.3.2 Data description

The data come from a survey over a coral reef system called Morinda Shoal located off Cape Bowling Green. Appendix A lists the sonar settings and shows the locations of track lines from the survey. The track line used for this analysis was BGB 57. At the time of this study, sidescan and snippets data could be simultaneously logged with the same software (Navisoft®), but snapshots required additional data acquisition software (SnapSaver®). Backscatter data are presented as outputted from the Reson 8125 with no additional processing (i.e. with system TVG applied to backscatter data).

3.3.3 Complete acoustic waveforms (snapshots)

In the Reson 8125 the snapshots mode logs the whole echo signal along each beam, including both the amplitude (Figure 3.3) and phase. This can be useful for water column investigations, such as fisheries acoustics (Parsons *et al.* 2006) and for investigation of the system operation in detail, such as in calibration exercises (see Section 3.4). However, for seafloor mapping it is not necessary to log the whole of the backscatter return. Moreover, the amount of data to be logged increases significantly when collecting the snapshot data, which may result in a considerable reduction of the ping rate. For instance, in this experiment the system was capable of logging snapshot data only from one of every five sonar pings. Although improvements in processing speed are starting to negate this problem (Parsons *et al.* 2007), it is advantageous to reduce the amount of data logged to maintain the highest possible ping rate and hence maximum along-track resolution. For seafloor investigations, there are two main methods for reducing the data logged from MBS systems. These are collecting a sidescan sonar-like output, or fragments of signals along individual beams (which Reson call snippets). MBS backscatter data collected by these two methods and their relation to the snapshot data are illustrated in Figure 3.4.

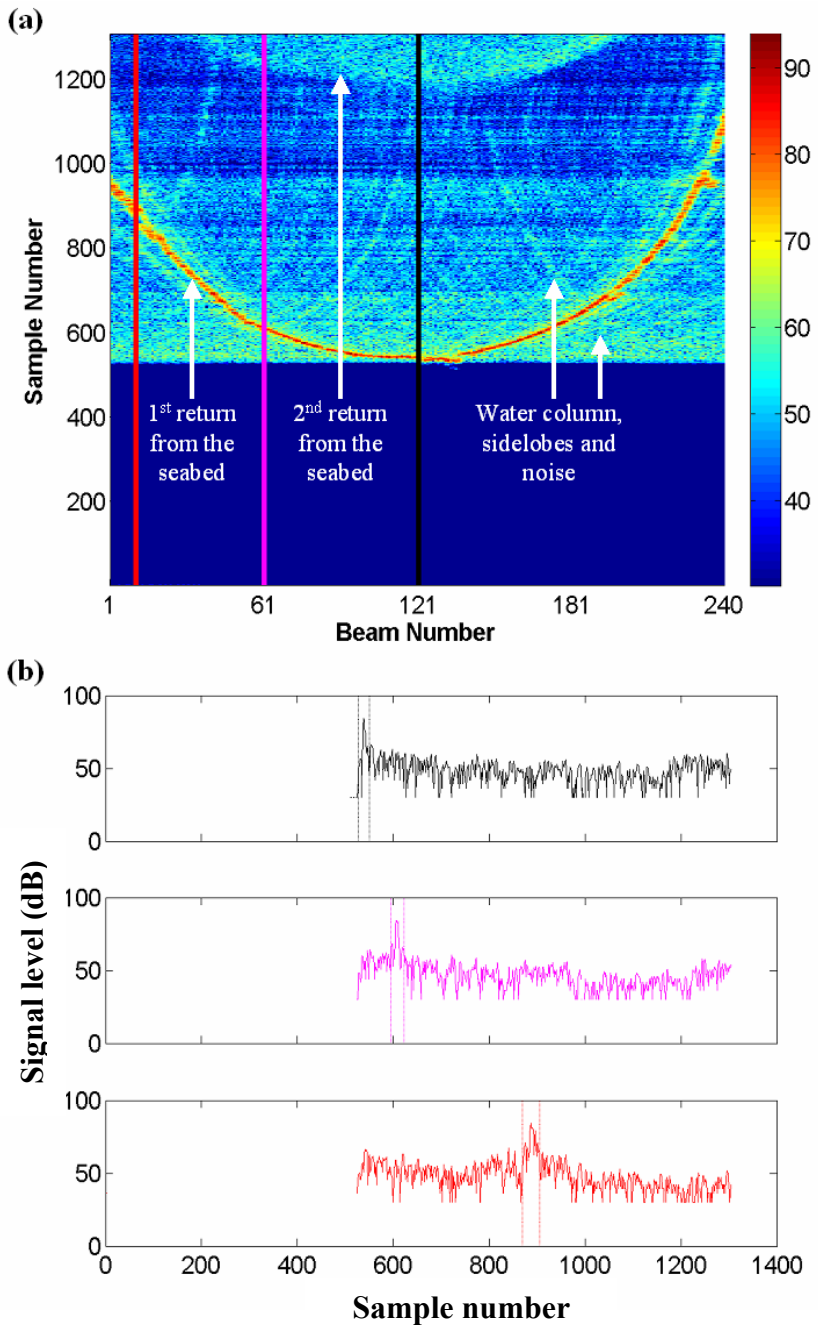

Figure 3.3: An example ping of snapshot signal level (relative dB) from BGB 57: (a) all beams and (b) some selected beams - 5 (red), 60 (pink) and 121 (black). Vertical dotted lines in plot (b) represent the snippet locations.

3.3.4 Sidescan logging mode

When recording in the "sidescan" mode, the system combines backscatter signals received along adjacent beams by stitching them together in the time domain with averaging within the overlapping sections, and as a result, it forms two sidescan beams (i.e. port and starboard). The combined beams produce a sidescan-like time-series of amplitudes (Figure 3.4(a)). The operator can choose whether to log all the data or to compress the data either with an "RMS" or "average" process (RESON Inc. 2002b). Here sidescan data were logged using the RMS compression mode, which resampled data to 1024 samples per side. The appearance of sidescan samples is rescaled so that the time scales of snapshot and sidescan signals are consistent with each other. The sidescan approach gives good across track resolution, as seen by the identification of the coral bommies[2] in the sidescan image from the first 275 pings of line BGB 57 (Figure 3.5(b)). However, combining all data from adjacent beams can add noise to the overall image, especially at nadir.

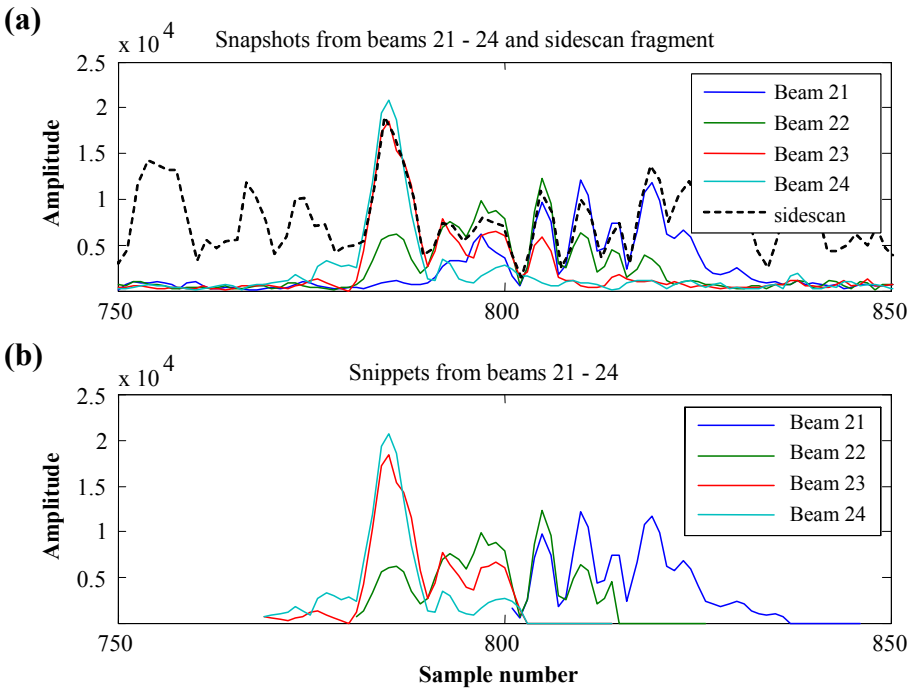

Figure 3.4: Comparison of snapshot, with (a) sidescan and (b) snippet data.

A2. [2] Coral bommies are relatively large reef structures.

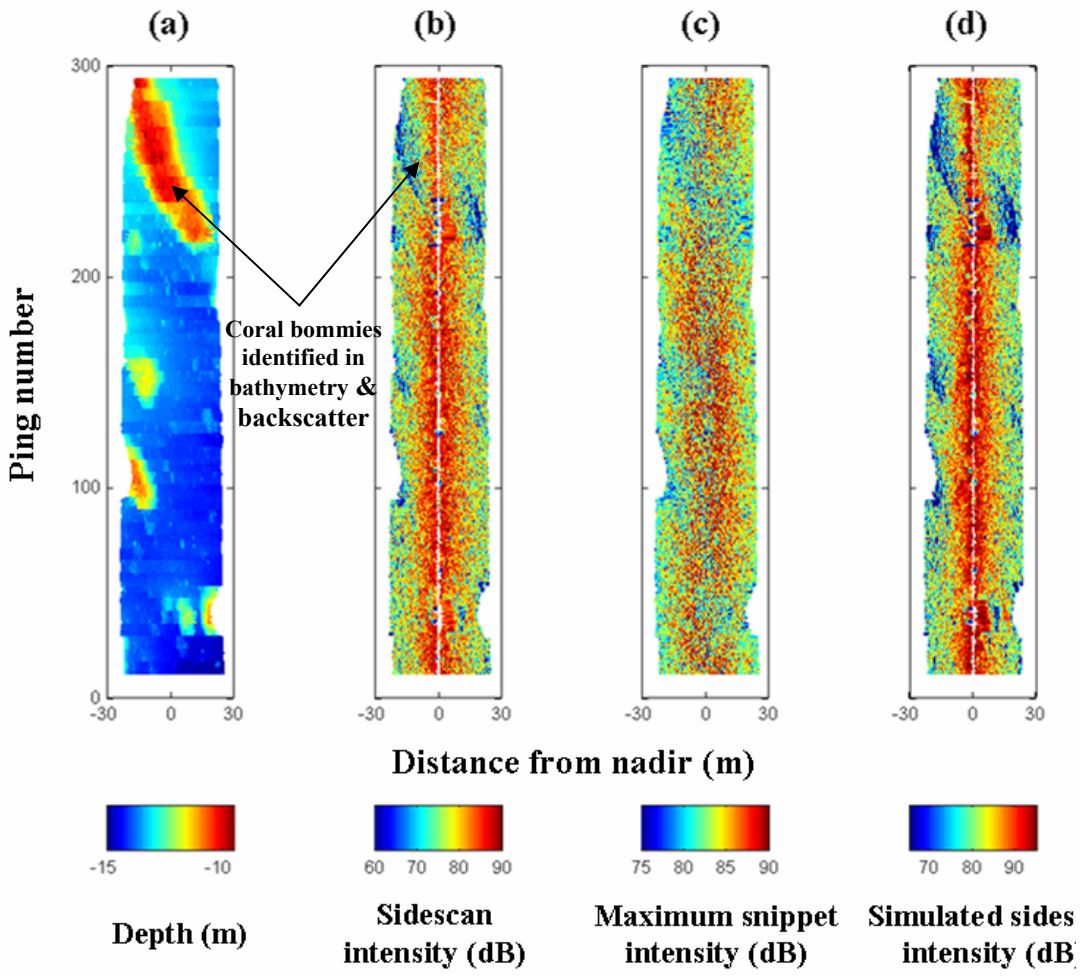

Figure 3.5: Multibeam sonar data collected from line BGB 57: (a) bathymetry (m), (b) sidescan simulated from full water column data, (c) snippets - peak beam intensity and (d) sidescan simulated from snippets.

3.3.5 Seafloor backscatter envelopes (snippets)

Snippets are fragments of the complete signal envelope that aim to contain the seafloor backscatter from each beam (Figure 3.4(b)). The start position of each snippet, known as the fragment offset, and the length (or number of samples) of each snippet is predetermined by the sonar processor based on the estimate of slant range to the edge of the beam footprint on the seafloor (Figure 3.6).

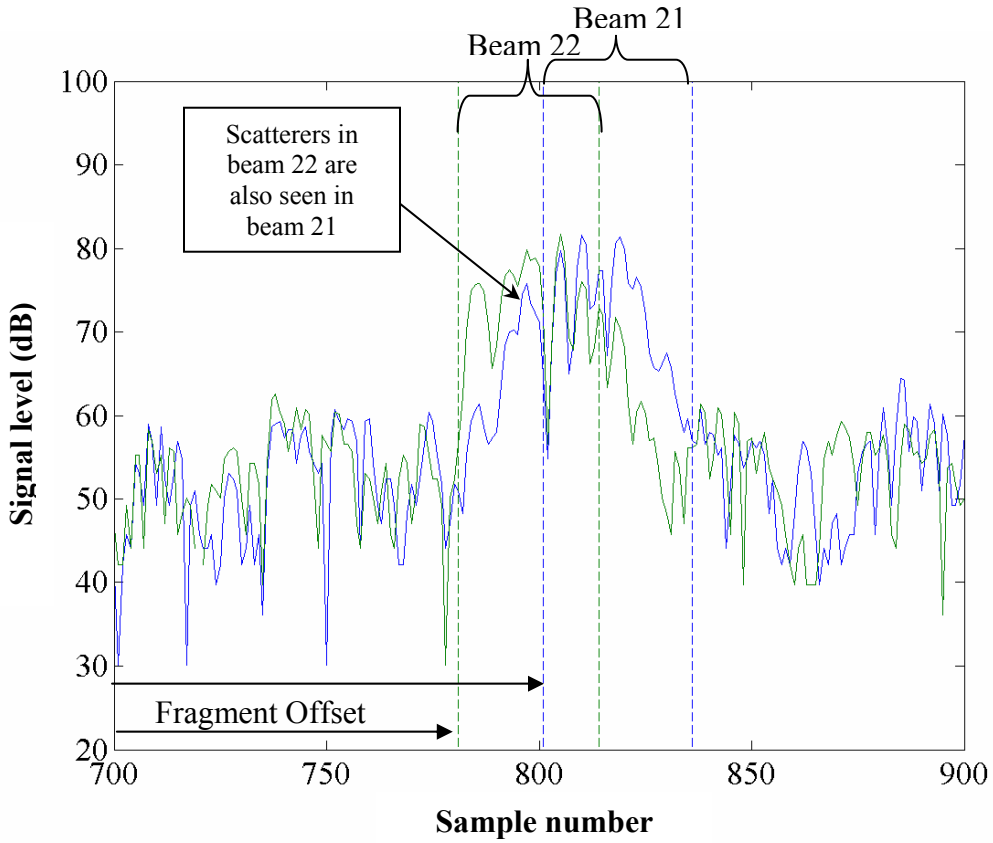

Figure 3.6: Location of the snippet fragments extracted from the signal envelope as recorded in snapshots for beams 21 and 22.

Collection of snippet data can be programmed in two different operational modes: uniform range and flat bottom. In the uniform range mode, the snippet window has a length of around 1/16 of the slant range to the bottom detect point and the centre coincides with that point. This mode is useful where the bottom slope significantly varies throughout the swath and it is impossible to accurately calculate the size of the footprint. However, in this mode there are more likely to be large gaps in the spatial coverage of the snippets, depending on the topography. In the flat bottom mode, the length and offset of each snippet are calculated from the seafloor depth and individual beam angle assuming a flat bottom model. The resulting backscatter information from the two modes was not significantly different; the flat bottom mode was chosen for collecting data in this study.

In the Reson 8125, the snippet fragment's start position and length are determined using stepwise functions. The automatic selection of the snippet location and length based on the flat bottom model is occasionally inadequate to include the full extent of the scatterers within the beam footprint. Figure 3.7 shows an example where the maximum amplitude of backscatter from the seafloor (as seen in the snapshot record) for beam 136 is not found within the snippet window. It could be argued that the seafloor surface patch of intense backscattering is located within the footprint of the adjacent beam (137); however, the adjacent beam does not return a higher value at this point.

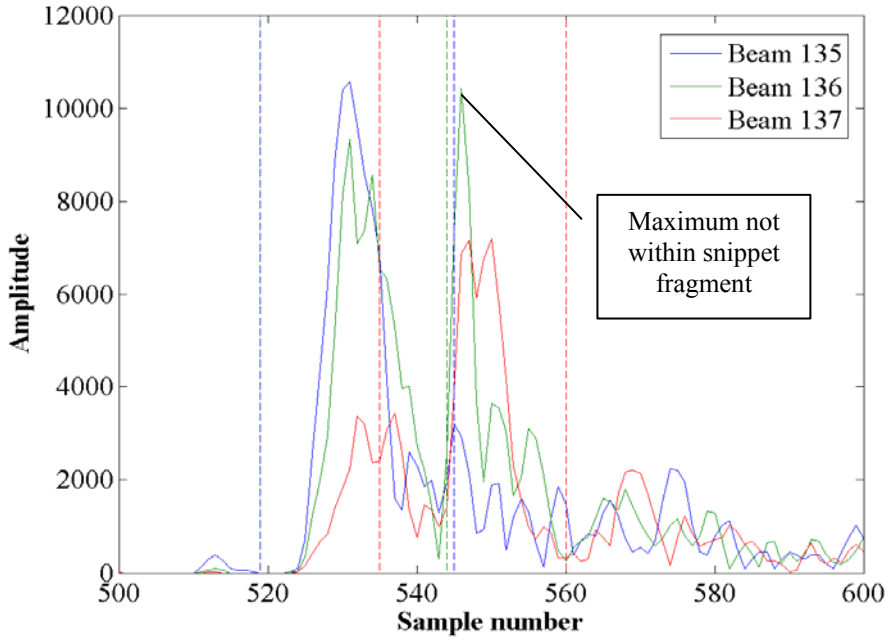

Figure 3.7: Example of inadequate snippet location, solid lines are the waveforms and dashed lines are the start and finish positions of the snippets. Beams 135 and 136 start at same position.

An approximate way to quantify the number of misaligned snippets is to examine if the maximum in the snippet corresponds to the maximum within the corresponding snapshot record. For this section, there was 99.3% match of snippet and snapshot peak amplitudes on average for all beams (Figure 3.8). The actual percentage of mismatches between snippets and snapshots cannot be an accurate measure of correct location of the snippets, as there could be backscatter sources other than the seafloor that produce higher

backscatter levels in the snapshot signals (e.g. fish schools). However, the trend of more inadequate snippet locations in the outer beams than the inner beams (seen in Figure 3.8) is plausible. Overall, though, the snippet data adequately reflect the seafloor backscatter signals received by MBS.

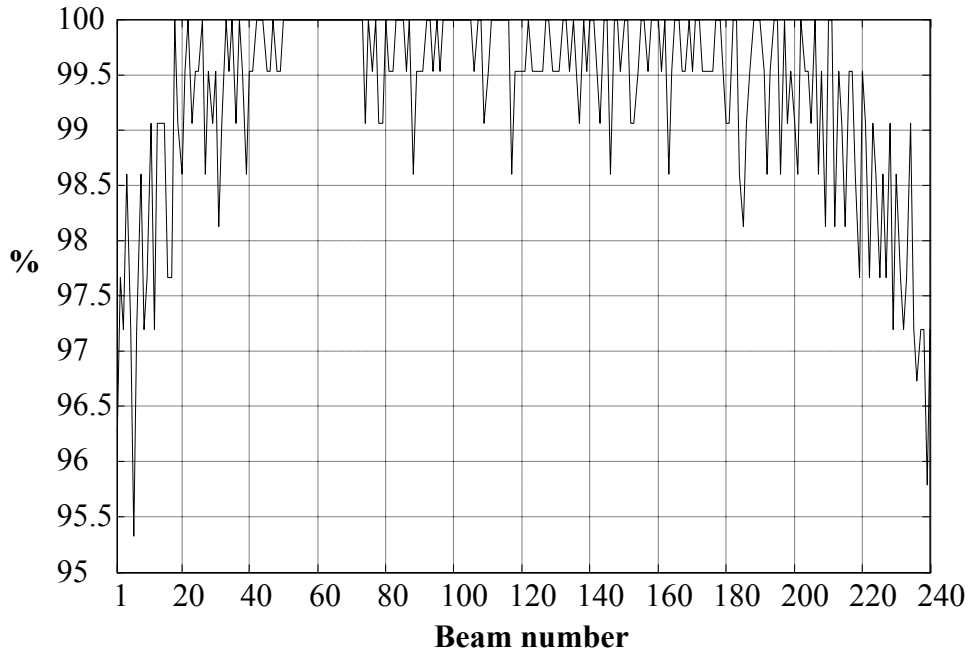

Figure 3.8: Percentage of matches in maximum amplitude between snippets and snapshots for each beam of the Reson SeaBat 8125 along line BGB 57.

There are two main approaches to processing snippets:

1. Determine one backscatter intensity value for each snippet;
2. Use a series of intensity values from each beam.

In the first approach usually either the maximum or average intensity values are calculated for each snippet. If the Reson 8125 system is set in the RI-Theta (range, intensity, beam angle) mode, the sonar processor finds the maximum value of each snippet and stores it in a separate backscatter intensity dataset. The backscatter image in Figure 3.5(c) is constructed using the maximum intensity values. However, it is advisable to log the snippets, as they have the advantage of allowing other values within the beam, such as the average intensity, to be measured. The average intensity is

calculated from the integral of the squared signal envelope, i.e. the sum of squared snippet samples, and is a robust estimate of backscatter intensity from within the beam. The seafloor backscatter strength can be found from the average backscatter intensity based on the energy conservation law and estimates of the transmission loss. Such an approach reduces noise due to stochastic variations of backscatter. However, using one backscatter value for each snippet does not allow resolution of useful backscatter features that may be present within the footprint of individual beams.

Using a series of amplitude values within the beam will offer finer spatial resolution. If all the values in the beam are used, then an image similar to sidescan can be created, which is shown in Figure 3.5(d), but with a reduction in noise from sidelobes and the water column compared to the actual sidescan recorded. However, synthesising adequate sidescan images or deriving a series of true backscatter intensity values from the snippet fragments collected along each beam of a MBS system requires proper correction for the individual beam patterns. Correcting for the beam pattern is not a trivial problem. Attempts have been made empirically (Beaudoin *et al.* 2002) and using models (Augustin & Lurton 2005), but beam pattern artefacts can persist. Whereas, analysis has shown (see Appendix B for details) the influence of beam pattern on the calculation of average backscatter per beam is almost insignificant with the total error about 0.3 dB for incident angles 5-60º.

3.3.6 Choice of backscatter logging method

Deciding which method to use to log backscatter data depends on the objectives of the study. For instance, if you are investigating objects in the water column then using the full backscatter signals (snapshots) is the most appropriate option. This was also the method chosen for the calibration experiment (Section 3.4). For benthic habitat mapping studies, reducing the backscatter data to either sidescan or snippets is a more practical option. The issues that were considered in this study when deciding which of these two logging method to use for this study, were:

- Spatial resolution
- Aim of study
- Processing of backscatter data

If high spatial resolution had been the main objective, e.g. for object detection, then sidescan data either as recorded by the system or synthesised from snippets might have been more applicable. However, it was decided that the relationship between backscatter strength and incidence angle was the main focus of this study. Therefore, the ability to produce backscatter strength that was solely dependent on only seafloor properties and incidence angle was one of the most important objectives. As discussed previously, using a series of amplitudes within each beam requires proper correction for the individual beam patterns. Although the beam pattern can be corrected through theoretical modelling or empirical methods, it often leaves imperfect results (Beaudoin *et al.* 2002). Alternatively, using physically meaningful parameters, such as the peak and integral value from each beam to derive the scattering coefficient, provides a more accurate solution. Furthermore, a one value per beam approach is much easier to implement than using a series of amplitudes from each beam. Therefore, for this study an algorithm to calculate the backscatter strength from the peak and integral of snippets was developed and is detailed in Section 3.5.

3.4 Calibration of the Reson SeaBat 8125 system

3.4.1 Introduction

To further understand the operation of a MBS system and produce backscatter characteristics that are system invariant, it is necessary to know the parameters of the system's transmit and receive beams. This involves calibrating the MBS system with a hydrophone for the transmit beam and recording backscatter from a target with known acoustic properties to calibrate the receive array. There has been little previous work on calibration of MBS. Foote *et al.* (2003) developed protocols for calibrating MBS systems, which is a good starting point for work of this kind. Also, a calibration of a Reson SeaBat 8125 performed by Trevorrow (2005) provided a useful comparison. The major difference between this study, and the work done by Foote *et al.* (2003) and Trevorrow (2005) is that they both used a volume scatterer, whereas, here a surface reflector is used. The important issue with using a surface reflector is that the target has to be bigger than the insonified area.

The objectives of this work were to:

1. Measure the transmit beam pattern both across and along track;
2. Estimate the system's processor gain G_p;
3. Evaluate the relative sensitivity across the swath (across beams);
4. Examine scattering strength from specular reflection and micro-scale roughness.

Measuring the transmit beam gave an opportunity to verify the quoted source level and the beam width at a –3 dB level, which is 1º along-track and 120º across-track. Estimating the system's processor gain G_p allowed us to determine absolute backscatter characteristics, such as the surface backscatter coefficient. It was also important to test the relative sensitivity of the system response across the swath. Finally, the controlled experiment allowed some preliminary examination of the scattering strength from specular reflection. Although this experiment was performed using the Reson 8125, the methods are thought to be applicable to other high-frequency multibeam systems.

3.4.2 Equipment and set-up

The experiment was performed in a swimming pool with the sonar head at one end of the pool orientated to transmit horizontally through the water column. At the other end of the pool at a distance of 6.44 m, a hydrophone was deployed to measure the transmit beam pattern and then a flat target was used to calibrate the receive beams (Figure 3.9). The set-up geometry and pulse duration used were such that the direct signal could be fully separated from the reflections from the pool walls. The transmit beam was measured using a Reson TC4034 hydrophone, which has a bandwidth from 1 Hz to 470 kHz and a sensitivity (re 1V/μPa) of –222 dB ±3 dB (at 450 kHz). The along-track beam width (at nadir) was estimated by vertically moving the hydrophone. The across-track beam geometry was measured by using the turntable to rotate the sonar head. The receive beams were characterised by recording in the snapshots mode the response from three surface targets: a flat aluminium sheet of about 10 mm thick, the same aluminium sheet with coarse sand paper on it, and a flat but rough concrete slab of about the same size and 20 mm thick.

3.4.3 Transmit beam

As the measurements were made at a relatively short distance from the sonar head, the transmit signal level was determined by comparing the amplitude of received signals to the numerical prediction made for the acoustic transmission loss in the near field of the transmit array. The acoustic field was calculated assuming that the transmit array is a semicylindrical piston of 210 mm long, which corresponds to the physical length of the projector. The transmission loss, as a function of range along the normal to the array, is shown in Figure 3.10. The transmit beam pattern as measured by the hydrophone and corrected for the actual transmission loss as a function of the along and across track angles is shown in Figures 3.11 and 3.12 respectively. The source level measured for the different power level settings was in agreement with the quoted levels. The along-track beam width measured at nadir (at the -3 dB level) is 1.2º, which is in good agreement with the 1º beam width quoted by Reson (2002b) and as measured by Trevorrow (2005). The across track beam was measured as 140º, which is in agreement with Trevorrow (2005) but slightly higher than the 130º width quoted by Reson (2002b).

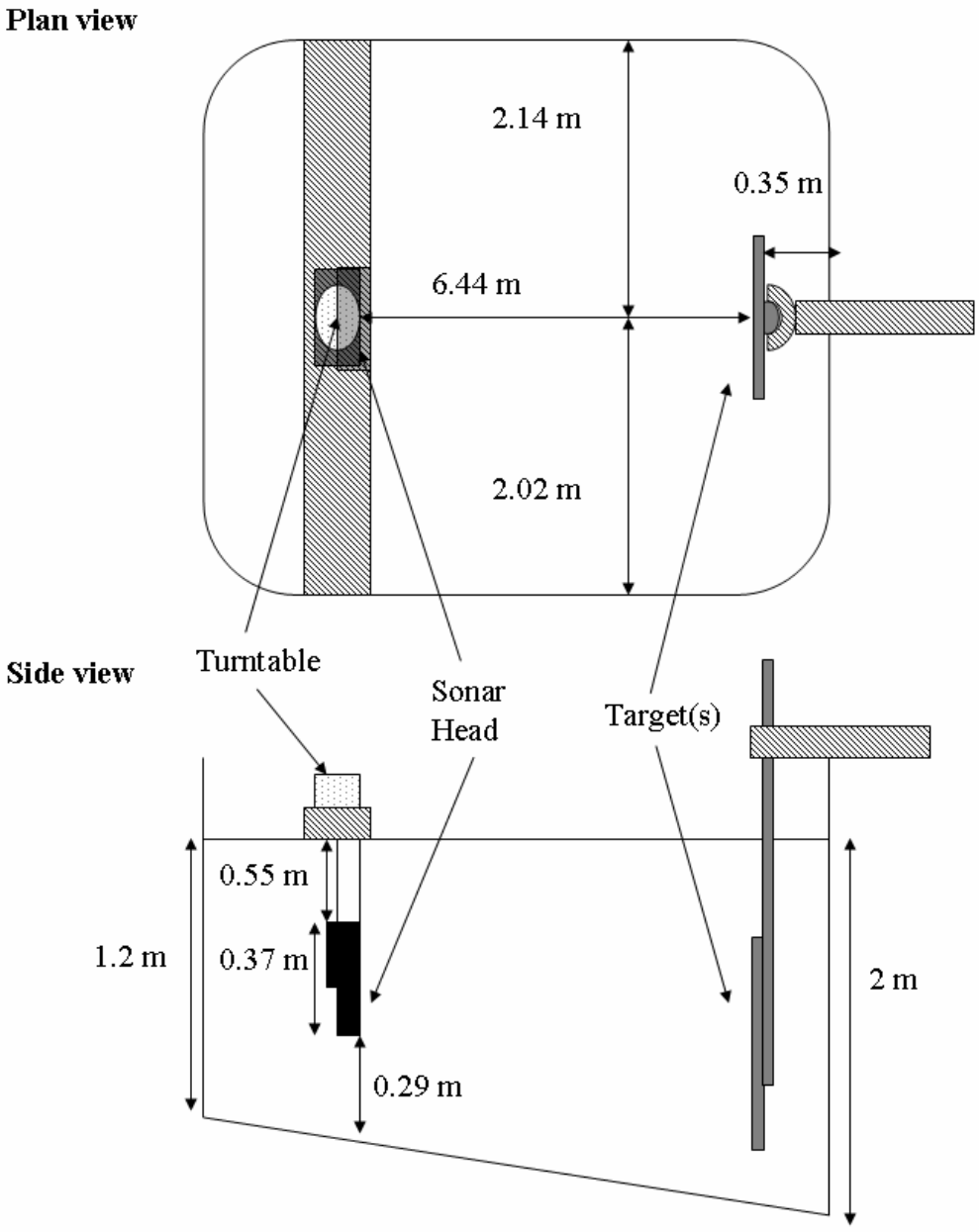

Figure 3.9: Experimental set-up for calibration experiment.

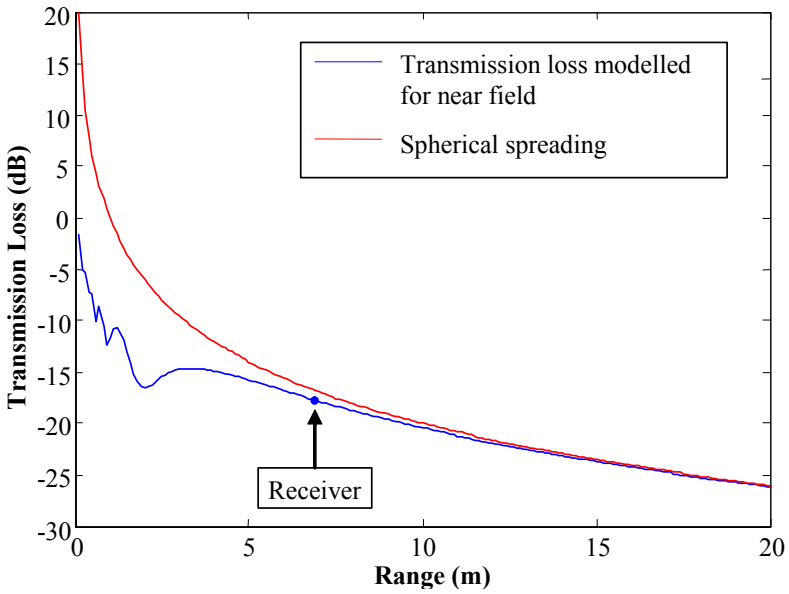

Figure 3.10: Transmission loss modelled along beam axis in the near field of the Reson SeaBat 8125 transmit array (blue) compared to spherical spreading loss (red).

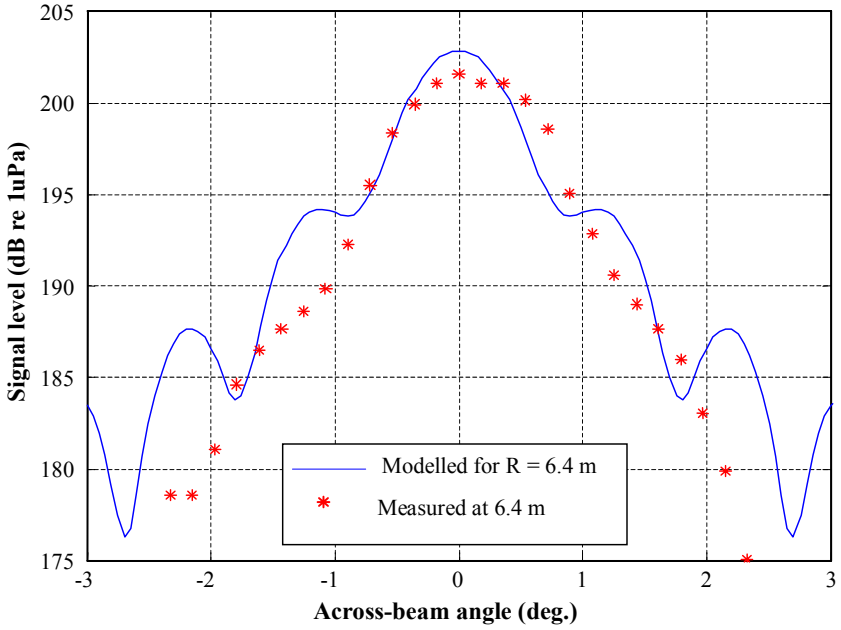

Figure 3.11: Along-track transmit beam pattern measured at 6.4 m from the transmit array (stars) and modelled for the same distance for a transmit power of 220 dB re 1 µPa at 1m.

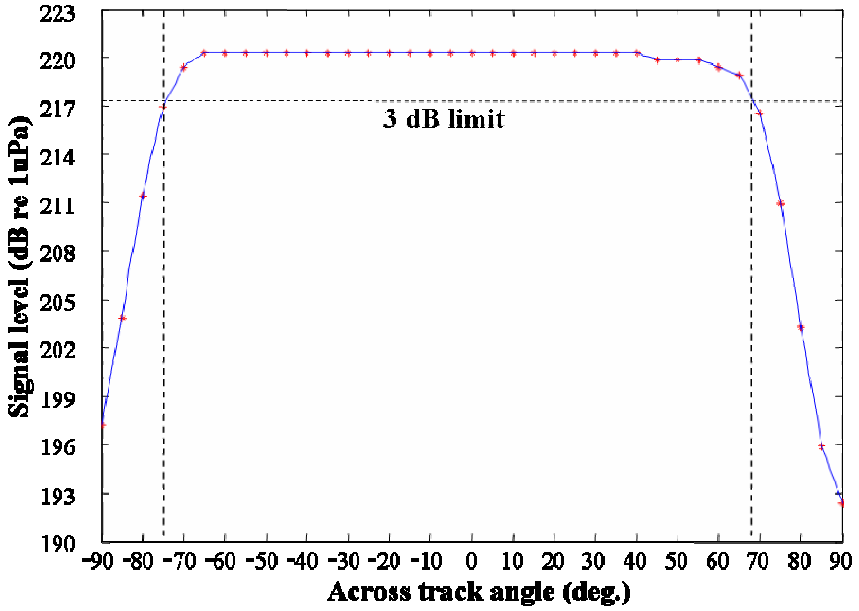

Figure 3.12: The across-track directivity pattern of the transmit beam (-) of the Reson SeaBat 8125. The -3 dB limit is indicated by the black dashed line.*

3.4.4 Receive Beams

3.4.4.1 Theoretical predictions

The main purposes of the receive system calibration were 1) to determine overall invariant system gain, G_p, which includes the sensitivity of the array's receive elements, the constant preamp gain, the ADC conversion rate, and gain of the beamforming processor; and 2) to examine the variation of system response with beam number. In order to determine the system gain and assess inter-beam variations, the flat aluminium plate was chosen as a target to measure the reflection coefficient at vertical incidence for different beams. The system gain was derived by comparing results of the measurement with modelling prediction for the target of known parameters. Reflection of the sonar signal from a flat target can be modelled using the Helmholtz-Kirchhoff method (Medwin & Clay 1998), according to which the sound field P of acoustic waves reflected from a finite surface S can be found from Equation 3.4:

$$P(\mathbf{R}) = \frac{1}{4\pi}\int_s \mathbf{K}\left\{P_S \frac{\partial}{\partial n}\left[\frac{\exp(-ikR')}{R'}\right] - \frac{\exp(-ikR')}{R'}\frac{\partial P_S}{\partial n}\right\}_S dS \qquad (3.4)$$

where: ***K*** is the local reflection coefficient depending in general on the incidence angle, P_S is the sound field of the incident wave on the surface *S* and *R'* is the slant range from a point on the surface *S* to a receiver at point **R**. The sound field P_S on the target surface can be modelled using known parameters of the sonar transmit array.

The reflection coefficient (for a plane wave) from a solid layer can be calculated using the exact analytical solution derived in Brekhovskikh and Lysanov (2001). Figure 3.13 shows the reflection and transmission coefficients calculated for an infinite aluminium plate of 10 mm thickness at 455 kHz. Notice that the reflection coefficient stays close to unity (about 0.98) for incidence angles less than 5º. In the measurement scheme realised for sonar calibration, the distance to the target was about 6 m and the target size was 0.4 m^2, hence the incidence angle did not exceed 2.5^o and the reflection coefficient could be assumed to be nearly constant.

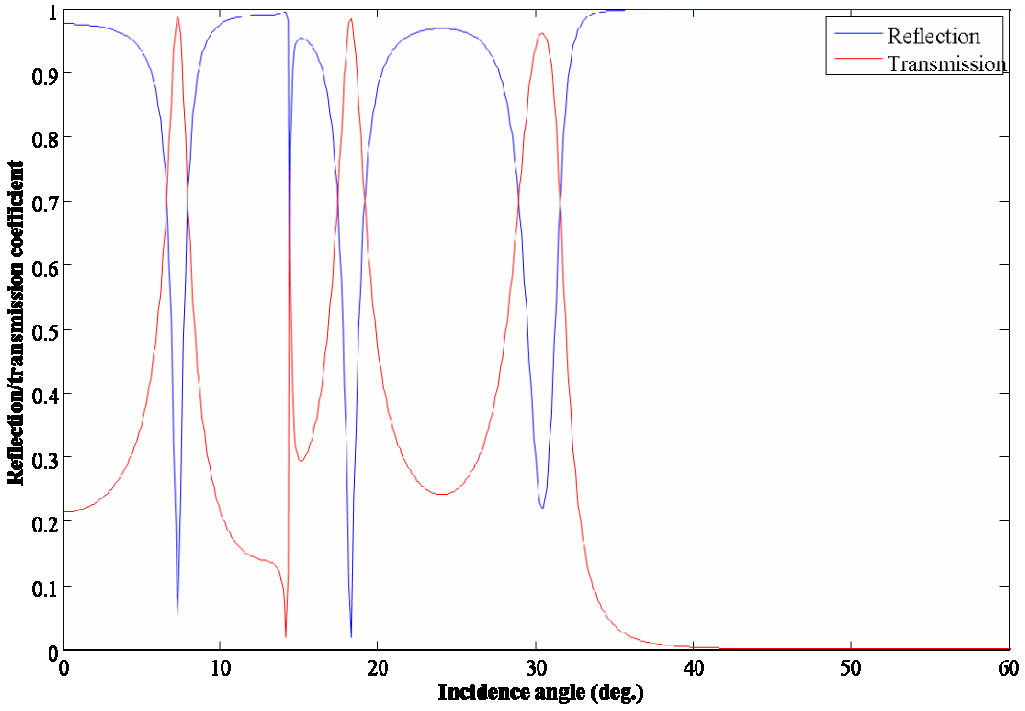

Figure 3.13: Modulus of the reflection and transmission coefficients from a 10 mm thick aluminium plate at 455 kHz (acoustic characteristics of aluminium: density 2700 kg m^{-3}; compressional wave speed 6320 m s^{-1}; shear wave speed 3130 m s^{-1}; compressional wave attenuation 0.01 dB $wavelength^{-1}$; shear wave attenuation 0.02 dB $wavelength^{-1}$).

The amplitude and phase of the reflected signal along the sonar receive array were calculated (using Equation 3.4) assuming the amplitude of the transmit signal to be unity at 1 m from the source (projected from the far field). The calculated results compared with spherical spreading are shown in Figure 3.14. For the acoustic waves radiated by the sonar, the size of the reflecting surface is limited to the target size in the horizontal direction and to the transmit beam footprint on the plate in the vertical direction, which is considerably smaller than the target width at 6 m from the sonar head. The limitation of the reflecting area causes a small reduction in the received amplitude, and amplitude and phase variations across the array due to edge effects. However, the amplitude variation is relatively small and the phase variation generally follows the spherical wavefront geometry (Figure 3.14). In the near field of receive arrays, such phase non-uniformity across the array is inevitable and can be compensated by dynamic focusing of the receive system realized in some sonar systems, including the Reson 8125. Thus, assuming that the Reson dynamic focusing compensates the spherical wavefront sufficiently, we can estimate the system response to the signal reflected from the aluminium plate, as follows:

$$A_{rec} = A_{tran} K G_{total} / 2R \qquad (3.5)$$

Where A_{rec} is the received signal amplitude (in ADC units), A_{tran} is the transmitted signal amplitude, R = 6.4 m is the distance to the target, K = 0.98 is the acoustic reflection coefficient of the target, and G_{total} is the total system gain. If A_{tran} is known and A_{rec} is measured, the system gain can be determined from Equation 3.5.

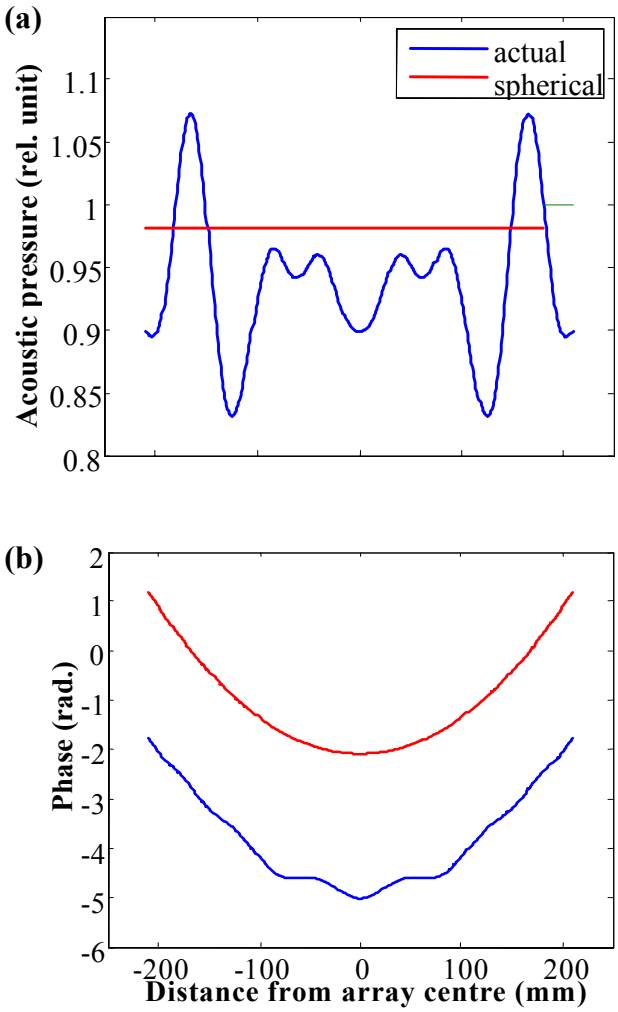

Figure 3.14: (a) Amplitude and (b) phase of the Reson transmit signal along the receive array, after reflection from an aluminium plate 40 by 40 cm wide and 10 mm thick. The amplitude is shown corrected for spherical spreading. The blue line is the result of numerical modelling using the Kirchhoff approximation. The red line shows a simple spherical spreading approximation for reflection from an infinite surface.

3.4.4.2 Measurements

For sonar calibration with the aluminium plate, the target was placed perpendicular to the direction of the sonar head, with the latter being slowly rotated in the horizontal plane with a small angular increment. Thus the target was always insonified by the transmit beam, but observed along different receive beams at different

times. The beam exhibiting the maximum signal amplitude among all other beams was assumed to receive the specular reflection from each sonar ping. The black line in Figure 3.15 shows the maximum signal level (in dB re system ADC unit) versus the corresponding beam number. The beam response is nearly uniform with a gradual decrease from the inner beams to the outer ones. The total decrease is approximately 3 dB. A possible reason for such change across beams maybe that the rotation axis of the sonar head was not exactly perpendicular, so that the transmit beam axis might deviate from vertical incidence on the target in the course of rotation. Bearing in mind that the transmit beam width is 1-1.2^{o} at –3 dB level, a misalignment of the sonar rotation axis of 0.5^{o} relative to the vertical might lead to such a decrease of the reflected signal amplitude. This differs with the findings of Trevorrow (2005), who found that at ranges less than 15 m there was a more significant decrease in received amplitude away from the centre beams than that measured in our calibration experiment.

The initial position of the sonar head, when the receive array was parallel to the target and the target was seen along the innermost beams, was accurately set up by aligning the sonar and target vertical orientation in order to get the maximum response. Therefore it is believed that the system response along the innermost beams corresponds to the specular reflection conditions, so that the system gain can be derived from the signal amplitude measured for those beams. The invariant system gain (G_p) was determined from the calibration results using Equation 3.5 to be 1.84 x 10^{-5} ± 0.08 x 10^{-5} ADC unit per μPa, i.e. -94.7 ± 0.4 dB re 1 ADC unit per μPa.

The measurement of the scattering strength from the sandpaper-covered aluminium plate and the concrete slab were performed by synchronous rotation of the sonar head and the target by the same angular increment in opposite directions, which was assumed to simulate backscattering from a flat bottom at different angles of incidence. Not all beams were measured in this experiment. The angular dependence of backscatter strength from the sandpaper-covered plate and concrete slab in Figure 3.15 exhibit a sharp peak at nadir, where the level of backscatter intensity from the sandpaper-covered plate is similar to the intensity of signals reflected from the bare aluminium plate. This

was expected because the thickness of sandpaper was smaller than the acoustic wavelength and hence the specular reflection strength was governed primarily by the acoustic impedance of the aluminium plate. At oblique angles, the estimates of backscatter strength vary from –30 to -40 dB relative to the peak value at nadir, which is comparable with the side-lobe level of the Reson 8125 receive array. This means that the roughness of sandpaper was too small to produce backscattered signals with the level detectable on the Reson array. Specular reflection from the concrete slab was about 5 dB weaker than that from the aluminium plate, which is likely due to a lower acoustic impedance of concrete (for a density of 2240 - 2400 kg m^{-3} and a sound speed of 3200 – 3600 m s^{-1}, the reflection coefficient from concrete in water varies from 0.6 to 0.7 at vertical incidence). The backscatter strength from the concrete slab measured at oblique angles was also weak and did not exceed the side-lobe level.

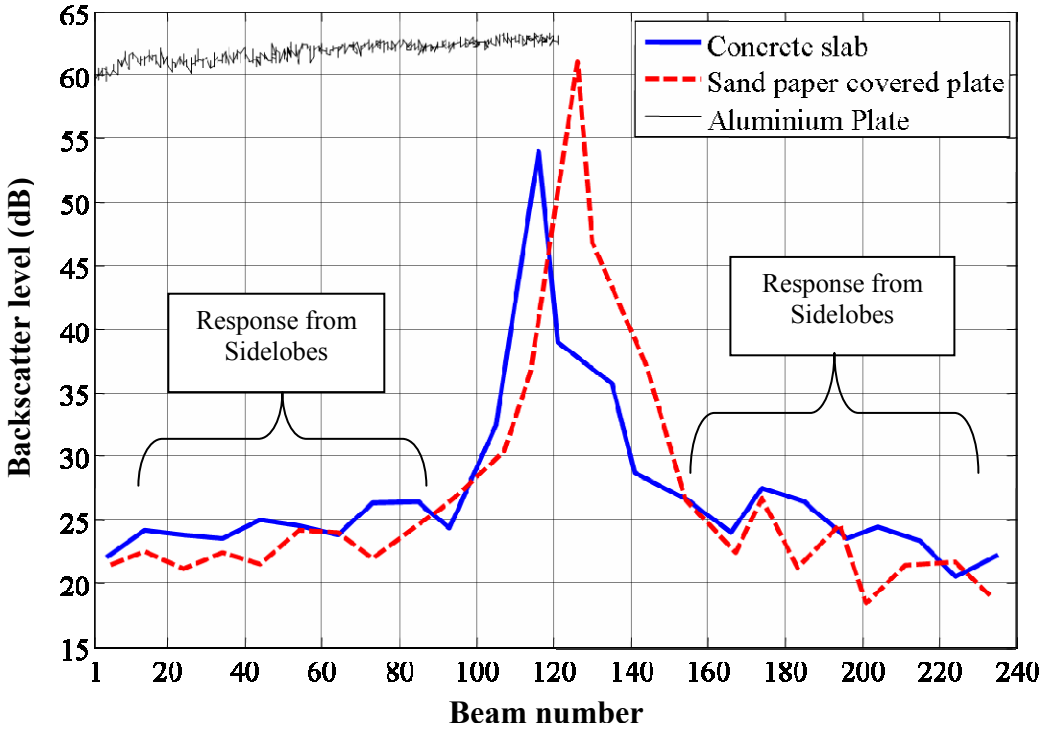

Figure 3.15: Average backscatter level (dB) of sonar signals reflected from the aluminium plate (-) and backscattered from the sand paper plate (--) and concrete slab (-) for each beam expressed in dB relative system ADC units.

3.5 Algorithm development for processing Reson SeaBat 8125 data

3.5.1 Introduction

An algorithm for processing MBS data was developed for the CWHM project by a team at the CMST (Gavrilov *et al.* 2005; Gavrilov, Siwabessy & Parnum 2005). The CMST team included the candidate, Prof. Gavrilov, Dr. Alec Duncan and Dr. Paulus Siwabessy. The algorithm calculates the backscatter coefficient from both the peak and integral values of the snippets corrected for system settings, transmission loss and insonification areas (see Equations 2.11 and 2.12 in Chapter 2), and is based on the equation given in Talukdar *et al.* (1995). With these measurements, the corresponding incidence angle and coordinates on the seafloor: X-Y and depth (z) are calculated. The full processing algorithm was developed into Matlab® code and is referred to as the MBS toolbox, it contains the following main steps:

1. Conversion from the XTF data format imported from Reson's NaviSoft® MBS processing software into the Matlab data format;
2. Calculation of X, Y, Z position and the incidence angle θ for each beam and each ping;
3. Calculation of the peak and average intensity of backscatter derived from the squared amplitude of the peak and integral of the snippets and correction for system settings, including the transmit power and receive gain for both values, and the transmitted pulse length for the integral value;
4. Removal of the system Time Varied Gain (TVG);
5. Calculation of the surface backscattering strength, which involves correction for transmission loss and area.

Although the methods were developed for the Reson 8125 system, they are applicable to other multibeam systems. For instance, data collected using the Reson SeaBat 8101 system were also processed with the developed algorithm and examples of this can be seen in the next section and in Chapter 5.

3.5.2 Conversion of data from the XTF format to Matlab

The Reson 8125, like most MBS systems, logs raw data in a proprietary binary format. However, this file format can be converted into an industry standard format known as eXtended Triton Format, or XTF (Clark 2002). A Matlab® library for converting binary files with MBS data in the XTF data format into Matlab® data files was developed. The data in the Matlab® format are saved in 5 data structures, which are listed in Table 3.1. As the MBS data files are usually large (of the order of 100MB), they are broken into approximately 20MB sections to speed up processing of bathymetry and backscatter data (these sections are recombined later).

Table 3.1: List of data structures created after conversion of XTF to Matlab data format.

Structure	Description
Attitude	Contains heave, roll, pitch and yaw data from motion sensor and gyro
Bathymetry	Two way travel time, GPS record and associated system settings and timing
Header	Contains information from the XTF header file
Sidescan	Sidescan and GPS record, and system settings and timing
Snippets	Snippet and GPS record, and system settings and timing

3.5.3 Calculation of X, Y, Z position and incidence angle (θ)

As part of the primary processing, the (X, Y, Z) position of the footprint centres relative to the sonar location and in absolute coordinates is calculated for each beam and each ping using the slant range, attitude and GPS data. This includes correcting for the measured static offsets of the sensors and the dynamic offsets calculated from the patch test (see Chapter 2). Figure 3.16 shows an example of bathymetry with and without correction for the ship motion. After a corrected (X, Y, Z) position is determined, the incidence angle θ is calculated for each beam and ping based on the relative footprint position.

Correction of swath data for the sound speed variation in the presence of 3-D motion of the surveying vessel has a well developed procedure (Lurton, Dugelay & Augustin 1994). However, the water in the areas surveyed as part of this work was shallow and well mixed so that changes in the sound speed with depth were small enough to be

neglected in the swath data processing for this study (Figure 3.17). Nevertheless, in other studies where there is a strong variation in sound speed through the water column, correcting footprint position and signal travel times along beams for sound refraction needs to be considered.

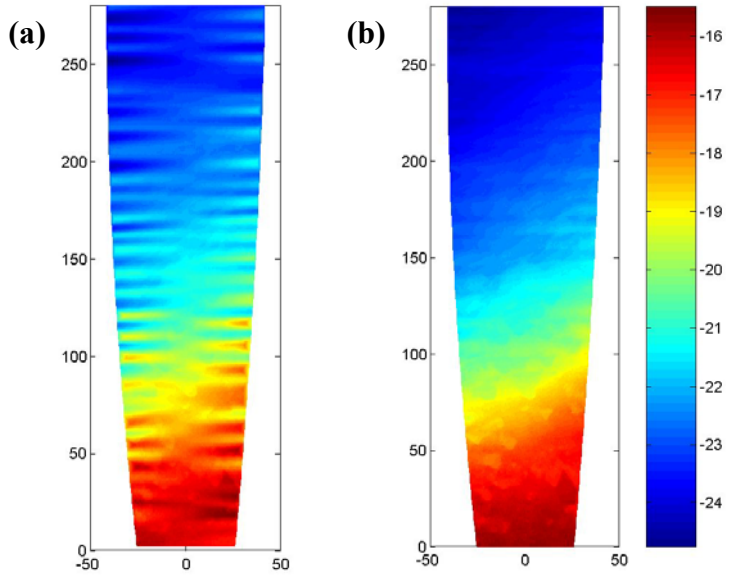

Figure 3.16: Bathymetry (m) images (a) before and (b) after compensation for ship's motion (data collected from Esperance Bay).

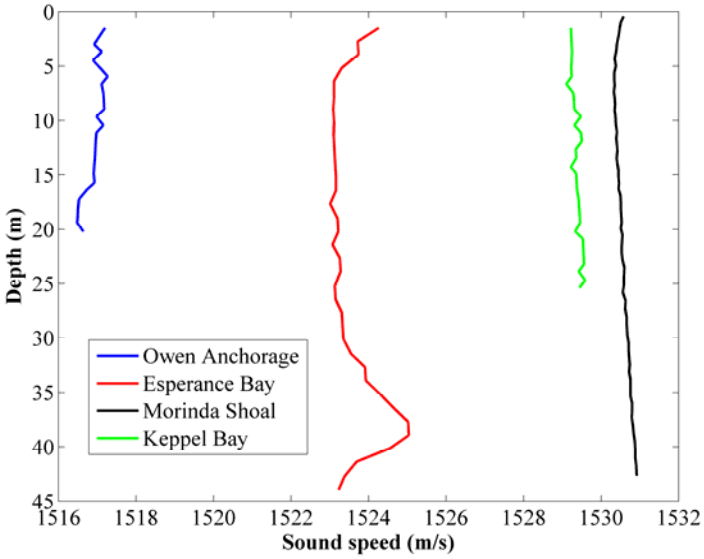

Figure 3.17: Typical sound velocity profiles from the different sites surveyed.

3.5.4 Calculation of peak and average intensity corrected for system settings

There are two physically meaningful characteristics of the backscatter intensity that are usually determined from the backscatter echo signal for each beam, i.e. for each snippet. They are the peak ($\hat{I}$) and integral ($\bar{I}$) intensity of the snippet. The peak intensity is proportional to the squared maximum amplitude in a snippet. The integral intensity is derived from the total snippet energy, i.e. the integral of the squared amplitude, which should then be normalized to the length of the transmitted pulse in order to comply with the energy conservation condition and make the measured parameter independent of system settings. The integral intensity can also be referred to as an average intensity, bearing in mind that the signal energy is divided by the transmitted pulse duration rather than the snippet length, which is generally larger. In order to estimate the seafloor backscatter coefficient, it is necessary to know the intensities of the transmitted and received signals. The latter is derived from the snippet amplitudes, corrected for the variable system gain selected by the operator and the constant system gain estimated from the calibration experiment (see Section 3.4) as 1.86 x 10^{-5} ADC unit per μPa for the Reson 8125 system. If TVG is applied, it also has to be compensated in order to obtain the actual intensity of the received signals, which is discussed in the next section (3.5.5). Before correction for TVG, the equation for calculating the received peak intensity normalized to the transmitted intensity and system receive gain can be expressed as follows:

$$\hat{\mathrm{I}}_{\mathrm{norm}} = \frac{\max(Amp^2)}{PG_o^2 G_p^2} \tag{3.6}$$

where *Amp* is the snippet amplitude and *P* is the source level in μPa^2. The equation for calculating the integral intensity, i.e. the received signal energy normalised to the transmitted energy and received gain, is:

$$\bar{\mathrm{I}}_{norm} = \frac{\sum_n (Amp_n^2)}{PG_o^2 G_p^2 T_w F_s} \tag{3.7}$$

where F_s is the sampling rate (s^{-1}) and T_w is the transmitted pulse duration (s).

The effectiveness of the normalisation procedure for changeable transmit power is demonstrated in Figure 3.18. During the transect shown in Figure 3.18, the power was increased in 3 dB steps and the operator gain was constant. After correction, the abrupt changes in the intensity of received signals due to changes in the system power disappeared in the backscatter image. However, there are certain situations where the changes in the systems settings are more difficult to effectively correct for, which is discussed in Section 3.6.

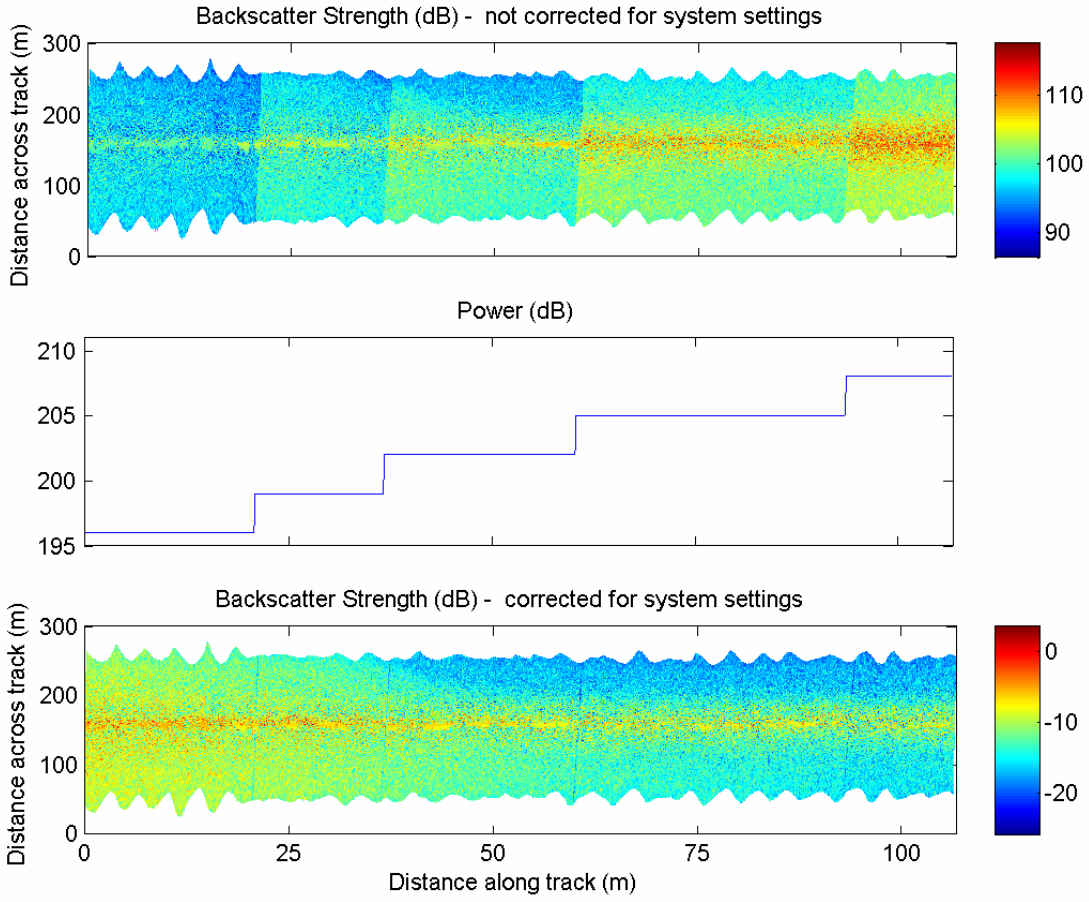

Figure 3.18: Backscatter images not corrected (top) and corrected (bottom) for changes in power (middle).

3.5.5 Removal of system Time Varied Gain

A TVG mode is available in the system to roughly correct the backscatter amplitude for the transmission loss which includes spreading and absorption losses. Equation 3.2, used by the system in the TVG mode, is a robust approximation to the transmission loss that aids in bottom detection in the real-time processing by equalizing, to some extent, the amplitude of signals received by the system at different angles and distances to the bottom. However, Equation 3.2 is not adequate for an accurate estimate of seafloor backscatter strength, even if the spreading and absorption loss coefficients are properly chosen. Hence the received intensity with system TVG applied ($I_{withTVG}$) is normalised by the TVG, using Equation 3.8, and then the resulting intensity values (I_{noTVG}) need to be corrected for the actual transmission loss, which is detailed in the next section.

$$I_{noTVG} = \frac{I_{withTVG}}{10^{TVG/10}} \tag{3.8}$$

3.5.6 Calculation of surface scattering strength

The surface scattering coefficient can be determined for both peak and integral intensity values by correcting the backscatter intensity for the actual transmission loss and normalizing the resulting values to the seafloor area from which the backscattered signal was received. The transmission loss is the energy lost due to spherical spreading of acoustic energy and acoustic absorption in the water column. Spherical spreading loss is a function of range R and for two-way travel is equal to $40\log_{10}R$ (dB). Absorption loss is also a function of range and the acoustic absorption coefficient α, so for two-way travel is $2\alpha R$ (dB). The areas that control the peak and integral intensity of backscatter are different and are outlined below.

The intensity of backscatter is governed by the seafloor area insonified instantaneously by the sonar transmit array and observed within each receive beam. All scattering elements of the surface within the insonified area contribute simultaneously to the backscattered signal and hence the peak intensity has to be normalized to the insonified

area in order to estimate the surface scattering coefficient (Medwin & Clay 1998). Equation (3.9) gives an expression for the surface backscattering coefficient SSC_{peak} derived from the peak intensity:

$$SSC_{peak} = \frac{\hat{I}_{norm\_noTVG} R^4 10^{2\alpha R/10}}{A_{receive} \cap A_{insonif}} \tag{3.9}$$

where: $A_{insonif}$ is the insonified area (Equation 2.11), $A_{receive}$ is the receive beam footprint area, and sign $\cap$ denotes intersection of sets. Hereinafter this intersection area will be simply referred to as the insonification area. R is the slant range from the sonar head to the centre of the insonification area.

The total energy of signals backscattered from the seafloor along each receive beam is made up of the contribution from all scattering elements within the beam footprint on the seafloor. Hence the estimate of the scattering coefficient derived from the integral intensity has to be normalized to the intersection area of the transmit and receive beam footprints, which for simplicity will be referred to as the footprint area (A_{fpa}) (Equation 2.12). An expression for the surface backscattering coefficient derived from the integral intensity (or signal average intensity) is given in Equation (3.10):

$$SSC_{integral} = \frac{\bar{I}_{norm\_noTVG} R^4 10^{2\alpha R/10}}{A_{fpa}} \tag{3.10}$$

The Backscatter Strength derived from the peak (BS_{peak}) and integral ($BS_{integral}$) values of each snippet are the scattering strength coefficients in dBs (Equations 3.11 and 3.12).

$$BS_{peak} = 10Log_{10}\, SSC_{peak} \tag{3.11}$$

$$BS_{integral} = 10Log_{10}\, SSC_{integral} \tag{3.12}$$

The seafloor backscatter strength should theoretically be only dependent on seafloor properties, acoustic frequency and the incidence angle. However, Appendix B shows

analysis on the effect of beam pattern on SSC_{peak} and $SSC_{integral}$ versus incident angle. The estimates of backscatter strength from the peak intensity contain noticeable errors due to beam pattern effects. These errors are angle-dependent and result from the finite width of insonification area limited also by the shape of the beam pattern. The estimates of backscatter strength, derived from the backscatter energy normalized by the transmit pulse width and the footprint area, do not suffer from such angle dependent errors. An error of about 0.3 dB, resulting from the approximation of the beam pattern by a rectangular shape, is nearly constant for all angles and at all values of the pulse width.

The effect of the corrections for the transmission loss and footprint area in comparison with the backscatter intensity measured with the system TVG and after TVG removal is demonstrated in Figure 3.19. Here the mean backscatter strength collected at an incidence angle of 30º from a single transect over a sloping sandy seafloor is plotted versus range to the bottom (Figure 3.19(a)) and footprint size (Figure 3.19 (b)). As range and footprint size increase, the mean backscatter strength with no corrections applied rapidly decreases. The TVG correction improves the range and area dependence, but is not adequate as the relative mean backscatter strength actually increases, whereas $BS_{integral}$ shows very little dependence on range and footprint size.

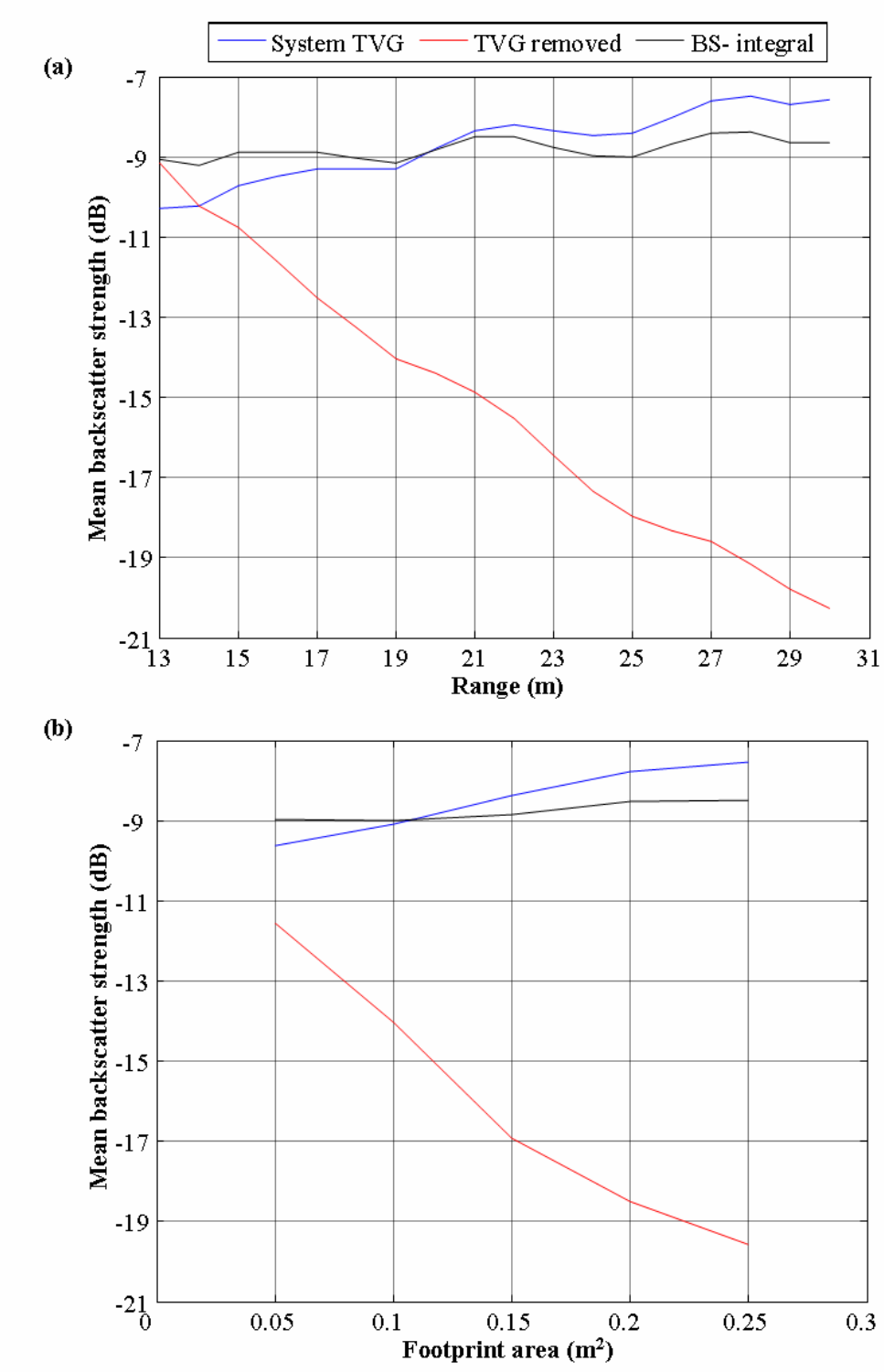

Figure 3.19: Backscatter intensity collected at an incidence angle of 30° with and without system TVG and the backscatter strength $BS_{integral}$ derived after all corrections versus (a) range and (b) footprint size.

3.6 Multibeam sonar system effects on backscatter data

3.6.1 Introduction

The previous section detailed the calculation of backscatter strength from the beam time series data stored in snippets. This showed backscatter beam time series data can be corrected for system settings, such as power, gain and pulse duration (for the integral value). However, there are some factors and situations that considerably complicate correcting backscatter data in full for system settings and experimental set-up. Specifically, this section shows the effects of the following:

- Beam pattern
- Saturation
- Pulse duration

The aim is to explain where system artefacts can appear in data and how best to avoid and overcome these situations. This advice is summarised at the end of this section as a quick reference guide for collecting backscatter data for benthic habitat mapping.

3.6.2 Effect of beam pattern on backscatter

The Reson 8125 used for this study was calibrated and found to have a relatively uniform beam pattern or sensitivity (see Section 3.4). However, some MBS systems do not have such a uniform beam pattern. One such system is the Reson SeaBat 8101, which is a 240-kHz MBS and insonifies a swath on the sea floor that is 150º across track by 1.5º along track and consists of 101 individual 1.5º by 1.5º beams (RESON Inc. 2002a). The relative across-track sensitivity of a Reson SeaBat 8101 from a known target as measured by Foote *et al.* (2003) is redrawn in Figure 3.20(a), where the reduction in sensitivity at nadir is about –5 dB relative to the maximum power at oblique angles. For comparison, Figure 3.20(b) shows the relative mean $BS_{integral}$ measured using a (different) Reson 8101 over a flat, homogeneous area of sand. Although the data were collect with different Reson 8101s, the artefacts due to the non-uniformity of the beam pattern identified in Figure 3.20(a) are clearly seen in the backscatter intensity measurements in Figure 3.20(b). If the actual beam pattern is not compensated for, then the angular dependence of backscatter is distorted, so that it

cannot be directly related to physical properties of the seafloor. However, if backscatter values are not corrected for beam pattern they could still be used by comparing backscatter levels from different habitats at the same angles of incidence.

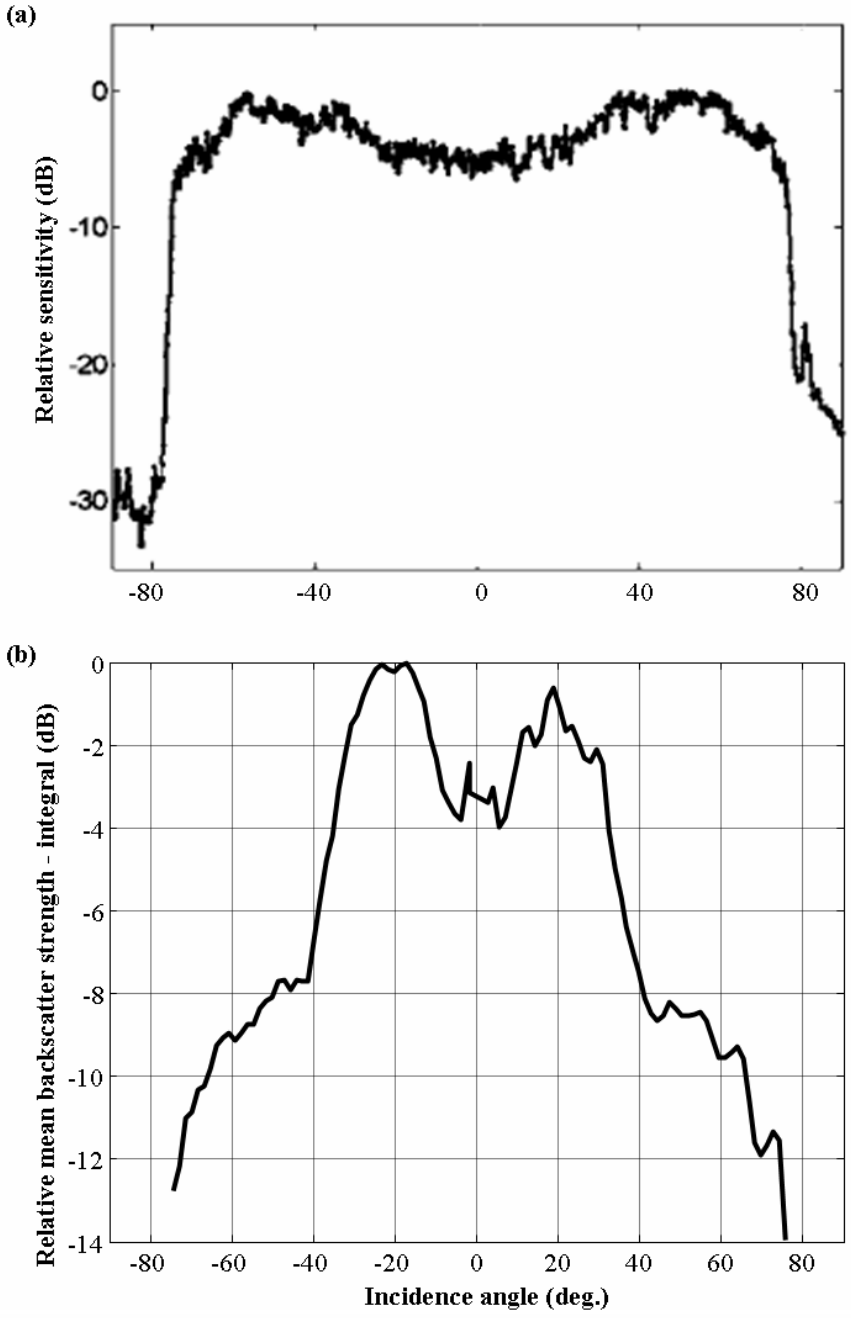

Figure 3.20: The Reson SeaBat 8101 (a) relative across-track sensitivity as measured by Foote et al. (2003), (b) the relative mean backscatter strength from a flat sandy seafloor (different 8101 system).

3.6.3 Effect of saturation on backscatter strength

The process of normalising data for changes in gain and power, as outlined in Equations 3.6 and 3.7, is relatively straightforward. However, backscatter data can only be normalised effectively if the received signals are not truncated by saturation of the receive system. If either the transmitted power or gain or both chosen by the operator are too high, saturation of the receive system will occur. This problem is demonstrated by Figure 3.21, where backscatter data was recorded over an area of flat sand and the gain was systematically increased along the transect, while all other settings were kept constant. At the start of the transect in Figure 3.21 the correction for gain works wells. From a gain setting of 20 (for this example) the signal starts to become truncated in the nadir beams and then, with the further gain increase to 30 dB gain, the system becomes completely saturated in the inner beams (90-150). The deformation of the signal is first seen at nadir, as this is the incidence angle of the highest return. Backscatter data distorted by saturation are problematic to use for benthic habitat mapping.

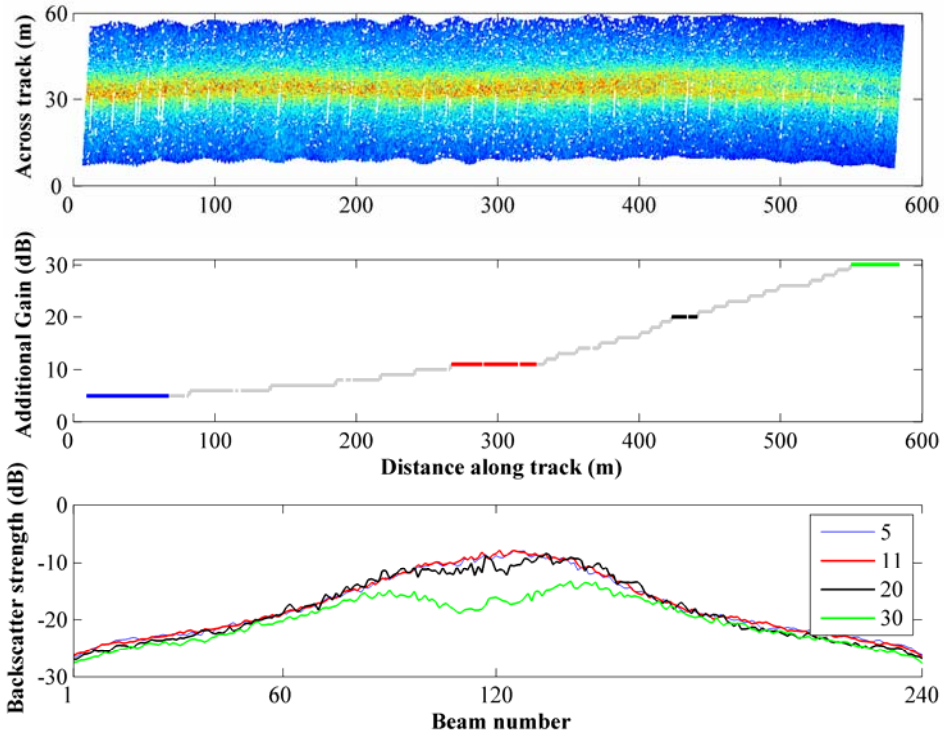

Figure 3.21: Backscatter image (top) corrected for changes in gain (middle) and the mean beam response (bottom) for fixed operator gain (dB) of 5 (blue), 11 (red), 20 (black) and 30 (green).

3.6.4 Effect of pulse duration on backscatter

The duration of the transmitted pulse theoretically influences only the insonification area, but not the estimates of the backscatter strength corrected either for the insonification area for the peak value, as outlined in Equation 3.9, or for the footprint area for the integral intensity, as in Equations 3.7 and 3.10. However, in a series of experiments with Reson SeaBat 8111 and 8160 MBS systems by Fonseca *et al.* (2006), it was found that for short pulses the correction was not adequate, and the backscatter strength corrected for the transmitted pulse width increased monotonically with the pulse duration.

To examine the effect of pulse duration on backscatter collected with the Reson 8125, a series of transects over the same area of flat sand were performed with different pulse durations. The mean $BS_{integral}$ and BS_{peak} values versus incidence angle are shown in Figure 3.22 for the different pulse widths. When the pulse duration was longer than 73 μs, the $BS_{integral}$ was adequately corrected for the pulse length, but when shorter than this the mean $BS_{integral}$ was underestimated. A similar trend was apparent in BS_{peak}, but the shortest pulse duration to adequately correct was 101 μs. Even above 101 μs there was some dependence on the pulse length seen in the mean BS_{peak} at smaller angles of incidence.

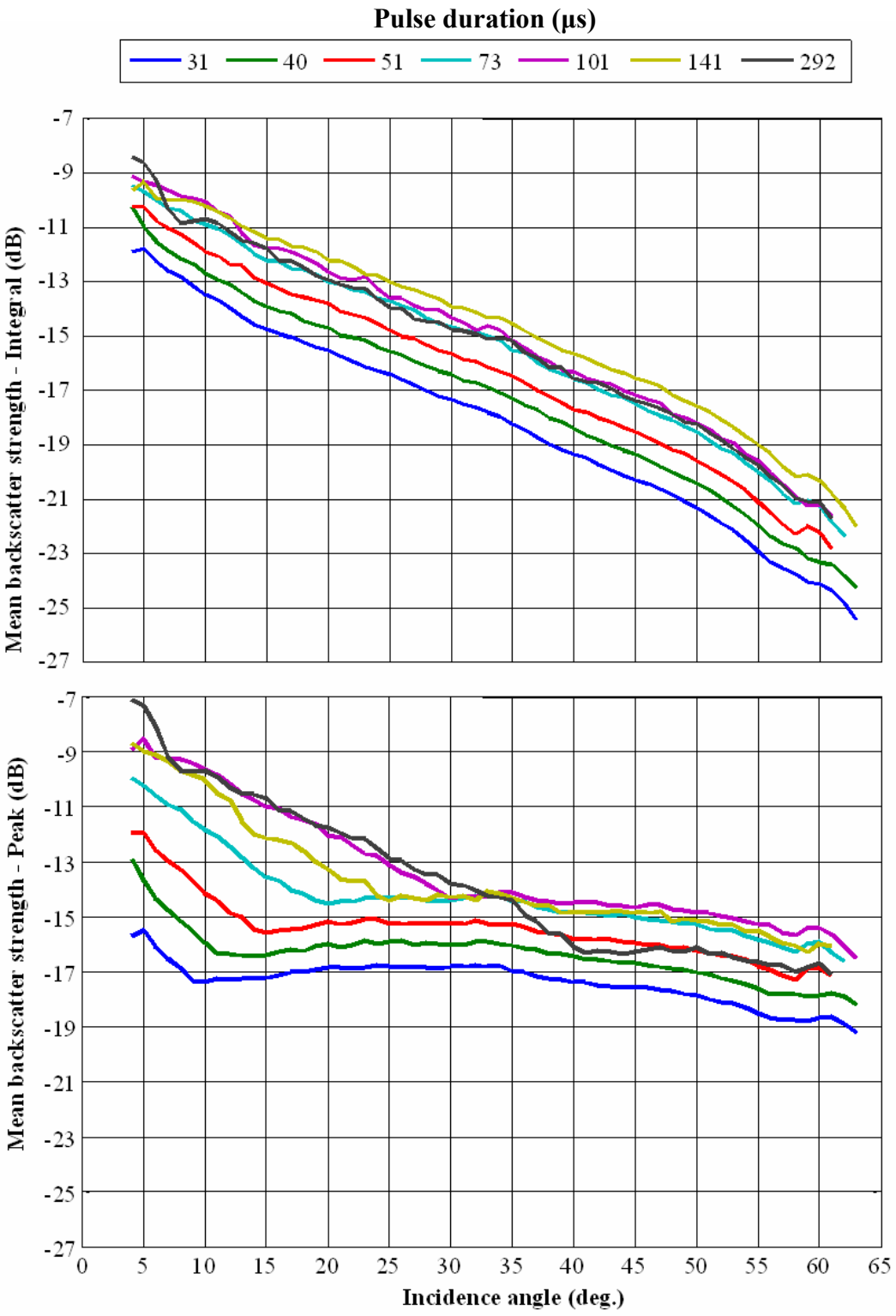

Figure 3.22: Mean (a) $BS_{integral}$ and (b) BS_{peak} versus incidence angle from an area of flat sand for a range of pulse durations 31-292µs.

To understand the reason for this observed pulse duration dependence, the pulse form of the signals reflected from the aluminium plate (as part of the calibration experiment (Section 3.4)) at different transmit pulse durations were examined (Figure 3.23). The peak amplitude for the pulse durations of 151 and 292 μs were nearly the same and were generally consistent with the signal level expected for the power and gain settings and experimental setup. At 101 μs, the peak is slightly lower and at 51 μs the peak has dropped almost by half. This is the result of a limited frequency bandwidth of the MBS system, which causes the front slope of received pulses to be finite. For a rectangular pulse generated by the transmit system, the front slope of received pulses governed by the system bandwidth remains approximately the same for different pulse widths. However, if the width of transmitted pulses is shorter than the front transition time, then the amplitude does not reach its maximum. This is evident in Figure 3.23, where the peak amplitude of the snippet (and hence its energy) decreases with the decrease of the pulse width starting from approximately 100 μs. Furthermore, the Reson 8125's sampling interval is about 35 μs and thus the estimates of peak and integral intensity would be very inaccurate if the pulse width is shorter than 70 μs.

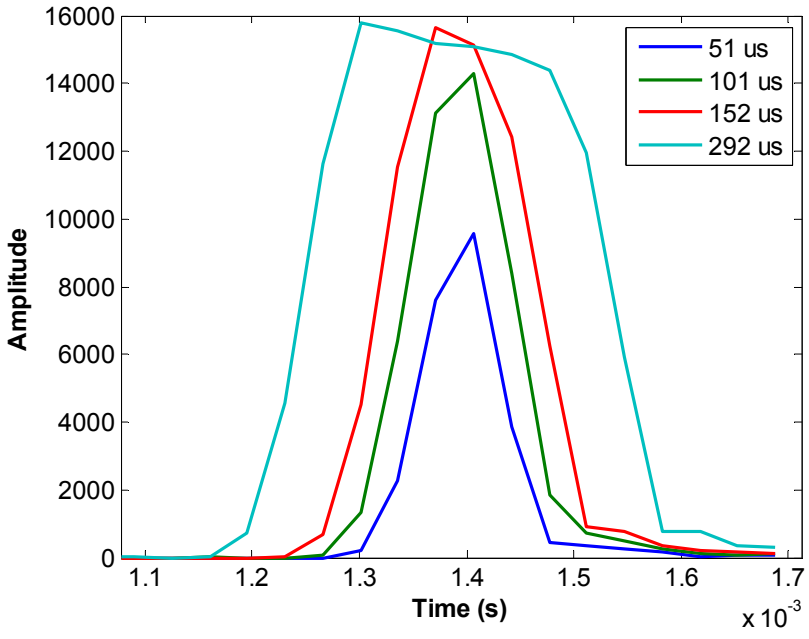

Figure 3.23: Pulses reflected from an aluminum plate for different pulse durations of the Reson SeaBat 8125.

The effect of pulse duration on backscatter measurements is an important finding, as shorter pulse durations are usually preferred for bathymetric surveys to increase the resolution. For instance, the Reson 8125 manual recommends a pulse width of 51 μs. However, based on Figures 3.22 and 3.23, a pulse duration greater than 100 μs is recommended when recording backscatter with the Reson 8125. Similarly, a pulse duration greater than 150μs is recommended for collecting backscatter data with the Reson 8101. An alternative is to correct the transmit power level for pulse distortion due to the limited frequency band of the sonar system. However, this will require knowing in detail the frequency characteristics of both transmit and receive arrays. Using a shorter pulse duration than recommended without proper correction for the system's frequency characteristics will lead to:

- Underestimation of the peak and average backscatter intensity;
- Lower Signal to Noise Ratio (SNR) of backscatter recordings; and
- Inconsistency of backscatter measurements made at different pulse durations.

In the next chapters, quantitative analysis is only performed on the data collected within this study with a pulse duration equal to or longer than that recommended.

3.6.5 Guidelines for collecting backscatter data for benthic habitat mapping

It has been shown that although backscatter data collected with MBS systems under different experimental conditions can be corrected for most system settings, there can still be residual artefacts persisting due to either inappropriate selection of system settings or inadequate understanding of the system's technical characteristics, such as the frequency band and dynamic range. Therefore, it is important to consider possible effects of system settings on the measurements of backscatter strength, especially when collecting data. In particular, the following should be considered:

1. Calibration of the MBS system is desirable, especially to determine the overall system's gain and frequency band and the shape of transmit and receive beam patterns. Ideally calibration is to be performed in a controlled environment with known targets and an accurate and well-controlled alignment of the sonar head and targets.
2. Power and gain should be set to provide a strong, but not saturated signal.
3. Consideration should be given to selecting an appropriate pulse duration when collecting backscatter. A pulse duration greater than 100 μs is recommended when recording backscatter with the Reson SeaBat 8125. Similarly, a pulse duration greater than 150 μs is recommended for collecting backscatter data with the Reson SeaBat 8101.

If these recommendations are followed, measurements of backscatter strength should only be dependent on the seafloor properties and the incidence angle.

CHAPTER 4

THE EFFECTS OF INCIDENCE ANGLE ON THE INTENSITY AND STATISTICS OF SEAFLOOR BACKSCATTER DATA COLLECTED WITH HIGH-FREQUENCY MULTIBEAM SONAR

4.1 Overview

It is well known from various theoretical models and experimental observations that acoustic backscatter from the seafloor is dependent on incidence angle (APL 1994; de Moustier & Alexandrou 1991; Hughes Clarke 1994; Jackson *et al.* 1996; Jackson, Winebrenner & Ishimaru 1986; Lyons, Anderson & Dwan 1994; Novarini & Caruthers 1998; Talukdar, Tyce & Clay 1995; Williams *et al.* 2002). In addition, the backscatter intensity and its statistical properties measured with multibeam sonar systems depend on the insonification area and footprint size of the receive beams (Hellequin, Boucher & Lurton 2003). The aim of this chapter is to examine the relationship between the seafloor backscatter strength measured with high frequency MBS and:

- Incidence angle;
- The insonification area and the footprint size; and
- Different seafloor properties (or different habitats)

As the overall aim of the study was to develop MBS for benthic habitat mapping, the analysis of this chapter was more focused on the implications for processing backscatter data rather than developing theoretical models. The chapter starts with an examination of the effect of incidence angle, insonification area, footprint size and seafloor properties on the individual beam backscatter envelopes (snippets). Section 4.2 highlights that the key parameters derived from snippets are the seafloor backscatter strength values determined from the peak and integral (also referred to as the average) intensities. However, Section 4.3 shows that the mean value of the backscattering strength derived from the peak intensity is expected to be overestimated relative to the actual backscatter strength, especially at oblique angles. Hence, backscatter strength derived from the integral intensity values was primarily used for this study. Section 4.4 compares the angular dependence of backscatter strength derived from a theoretical model with field measurements from a wide variety of the benthic habitats from around the Australian

coast. This is followed by a more comprehensive analysis of statistical properties of the average backscatter intensity. Examination of various statistical characteristics, including higher order moments and distribution function shapes is done with respect to their effectiveness in seafloor classification. Some initial results from this work have been published in several conference papers (Parnum, Gavrilov & Siwabessy 2007; Parnum *et al.* 2005; Parnum *et al.* 2006; Siwabessy *et al.* 2006).

4.2 Dependence of backscatter envelopes on incidence angle and seafloor type

The aim of this section is to demonstrate the effect of incidence angle, insonification area and seafloor type on the shape and properties of backscatter envelopes collected by high-frequency MBS. Figure 4.1 shows representative snippets (with system TVG) collected using a Reson Seabat 8125 from nadir (beam 120), moderate (beam 60) and oblique (beam 5) beams from areas of flat sand (black) and sand covered in dense rhodolith (grey). Both sets of data are from the same transect (Esperance 361) performed in between Thomas and Woody Islands in Esperance Bay in 2005. The location of the line and system settings is given in Appendix A. These backscatter envelopes serve a useful comparison because they represent different kinds of scattering surface, but are found at the same water depth. Rhodolith (sometimes in the literature referred to as maerl) is a hard, unattached, red coralline algae encrustation that can range in size from a few millimetres to a few centimetres, and can form a dense cover over sand. This means that rhodolith form a much rougher scattering surface than flat sand, which results in the higher backscatter amplitudes recorded across all the beams, especially for the outer beams at oblique angles.

While sand and rhodolith are characterized by different levels of backscatter amplitude, these and other seafloor types surveyed by the author exhibit similar changes in the snippet shape with change in incidence angle. At nadir (Figure 4.1(a)), the backscatter envelopes have a sharp well-defined, single-peak pulse form. As the incidence angle increases, additional peaks appear in the backscatter envelope (Figure 4.1(b)). At oblique angles, the backscatter envelope comprises a series of peaks of comparable amplitudes (Figure 4.1(c)). The changes observed are related to the relationship between

the insonification and footprint areas and scattering mechanisms within different angular domains.

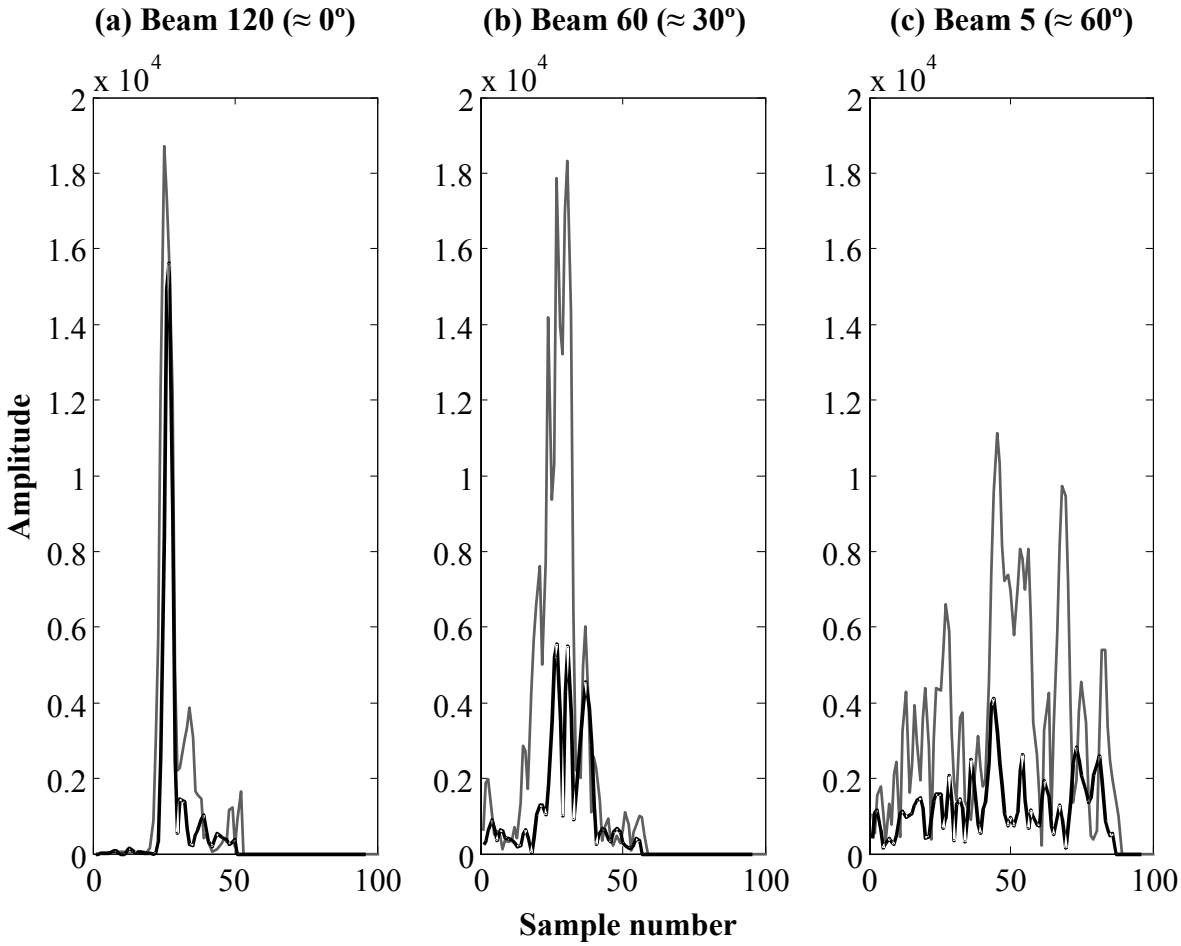

Figure 4.1: Backscatter envelopes from sand (black) and rhodolith (grey) for beams (a) 120, (b) 60 and (c) 5 of the Reson 8125.

As the incidence angle increases so does the footprint size, while the insonification area decreases. For the inner beams (beam 120), the footprint is smaller than the insonification area, so that the backscatter signal consists of a single prominent peak. As the footprint increases and the size of the insonification area decreases with the increase of the incidence angle, the footprint of the receive beams contains more and more different areas of the seafloor insonified at different times, which results in a series of peaks observed in the backscatter envelope. In addition, there are different scattering

mechanisms dominating in different angular domains. At nadir, scattering is dominated by specular reflection affected by random variations of the local slope of large-scale roughness, whereas at oblique angles high-frequency scattering is predominately governed by small-scale roughness. Therefore, backscatter characteristics and their statistics derived from the backscatter envelopes collected with MBS should be dependent on the incidence angle.

As discussed in Chapter 3, the seafloor backscatter strengths derived from the peak and integral backscatter intensities for each snippet were chosen as the principal parameters for seafloor discrimination. However, in the multi-peak backscatter signal at oblique angles, the maximum backscatter amplitude, and hence the peak intensity, does not always adequately characterise the average backscatter strength across the beam footprint on the seafloor. This is because it is affected by interference of waves scattered from different parts of the insonification area. The integral intensity, however, provides an estimate of the seafloor backscatter strength based on the energy conservation principle, which are less noisy. Moreover, it is shown in the next section (4.3) that the mean value of the backscatter strength derived from the peak intensity is dependent on the envelope length.

4.3 Dependence of the peak backscatter intensity on incidence angle

The peak backscatter intensity data is commonly used for producing backscatter imagery of the seafloor and for mapping benthic habitats. As discussed in Chapter 3, the Reson 8125 and 8101 along with the majority of MBS systems have an option to collect backscatter intensity data, as one value per beam and ping, instead of, or in addition to, the snippet data. This value is the maximum amplitude of the backscatter return, from which the peak intensity $\hat{I}$ (Equation 3.6) can be calculated. However, it will be shown in this section that the mean values of the backscattering strength derived from the peak intensity are expected to be overestimated relative to the actual backscatter strength, especially at oblique angles.

The backscatter return along oblique beams is usually created from the signals backscattered from different insonification areas or scattering cells, which can be referred to as elementary backscatter returns, clearly seen in Figure 4.1(c). Variations of each elementary return from a single insonification area within the footprint of any particular beam with time (or with the ping number) can be considered as a stochastic process with a certain distribution function. Let the number of elementary returns from the footprint of an individual beam be *M*, so that the full backscatter signal comprises a series of *M* stochastic process. If these processes are independent and identically distributed, then, according to the extreme value theorem by Fisher-Tippett (Embrechts *et al.*, 1997), the distribution of extreme values in each series tends to one of the three known families of distributions: type I (Gumbel), type II (Frechet) or type III (Weilbull), as *M* tends to infinity. The type of extreme value distribution depends on the fall off rate in the tail of the PDF of individual processes. If the fall off rate is exponential or nearly exponential, such as that of the exponential, Gamma, Rayleigh and *K* distributions, the maximum value distribution is of type I (Johnson, Kotz & Balakrishnan 1995), which can be approximated by a generalized Gumbel (Fisher-Tippett) distribution for finite *M*. Its PDF is:

$$P(x) = \frac{1}{\alpha}\exp\left[\frac{x-\beta}{\alpha} - \exp\left(\frac{x-\beta}{\alpha}\right)\right], \tag{4.1}$$

where α is the scale parameter and β is the location parameter.

The mean μ and standard deviation σ of the Fisher-Tippett distribution are:

$$\mu = \beta + \zeta\alpha \tag{4.2}$$

$$\sigma = 6^{-1/2}\pi\alpha\ , \tag{4.3}$$

where $\zeta \approx 0.57721$ is the Euler-Mascheroni constant.

If backscatter from different insonification areas is statistically independent and has a Gaussian distribution, then the instantaneous intensity has the exponential distribution

and hence the peak value distribution is of type I. A type I distribution is also expected for the peak values, if the instantaneous backscatter amplitude is *K*-distributed.

The scale parameter in 4.1 depends on the mean value of individual processes, i.e. on the average value of instantaneous backscatter intensity, while the location parameter and, consequently, the mean of the maximum value distribution depends on the number *M* and the PDF of individual processes. This means that the average value of peak intensity depends on the number of statistically independent scattering cells within the beam footprint. No exact analytical expression is known for the location parameter as a function of the number of statistically independent samples. However, this relationship can be modelled numerically for stochastic processes of certain PDFs with exponential tails. Figure 4.2 shows the variation of the mean value of peak intensity with the number of statistically independent samples used to determine the maximum, which was modelled assuming that complex backscatter amplitudes have a Gaussian distribution and the mean value of their absolute amplitude is unity.

It is evident from Figure.4.2 that the mean value of the peak intensity increases with the number of scattering cells contained in the beam footprint. The mean of the peak intensity equals the mean intensity only when the footprint contains one scattering cell. For five cells in the footprint, the mean of peak intensity is about double the mean intensity, and the ratio of these quantities grows further with the number of scattering cells. Consequently the measurements of the seafloor backscatter coefficient based on the peak intensity give overestimated values, especially for oblique beams. The degree of overestimation depends on a number of parameters, including: the incidence angle, transmit pulse length and sea depth; and is a complicated non-linear function of the incidence angle.

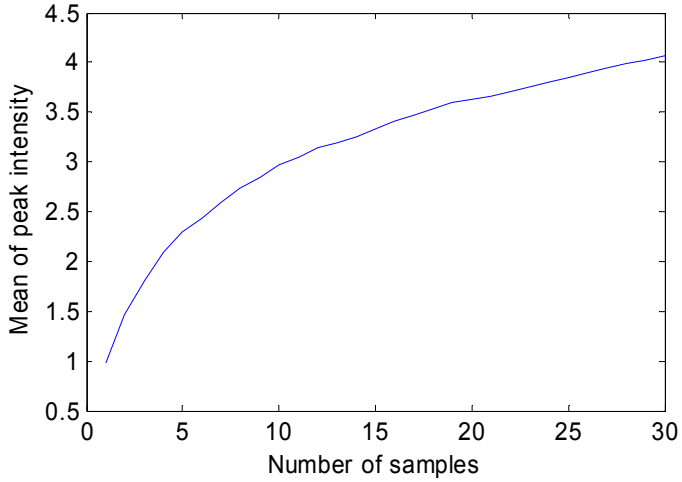

Figure 4.2: Numerically modelled mean value of the peak intensity versus the number of samples (scattering cells) for a mean intensity assumed to be unity.

Figure 4.3 demonstrates the effect of the number of scattering cells in the footprint on the estimates of the seafloor backscattering strength using the peak intensity values. In the given example, the insonification area is limited to the beam footprint up to an incidence angle of 35°. Within this angular domain, the backscattering strength estimates from the peak and integral intensity values are consistent with each other. At oblique angles beyond 35°, the insonification area becomes smaller than the footprint, which results in rapid divergence of the peak intensity estimates from those based on the integral intensity. At 60°, the footprint contains about six non-overlapping insonification areas and the peak intensity estimates are about 4 dB, i.e. almost 2.5 times higher than those based on the integral intensity. This is consistent with the prediction shown in Figure 4.2. Such an inconsistency of backscatter strength estimates determined through the peak intensity values was one of the key reasons for choosing the integral intensity as the principal parameter for further analysis of MBS backscatter data.

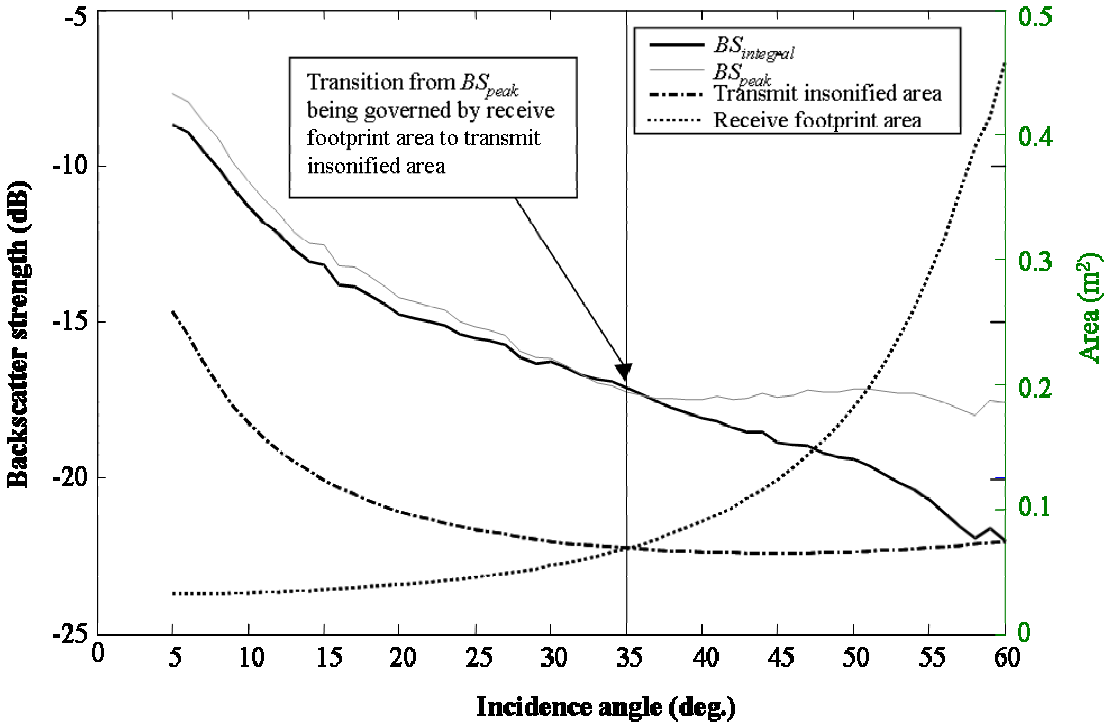

Figure 4.3: Mean backscatter strength (determined from the peak and integral intensity), sonar receive footprint and transmit insonification areas versus incidence angle.

4.4 Dependence of the mean backscatter strength on incidence angle and seafloor habitat

4.4.1 Model predictions

Comprehensive seafloor backscatter models valid at high frequencies, such as 455 kHz, when the Rayleigh number (Equation 2.2) is much larger than unity, have not been well developed to date. This means that a comparison of the experimental results obtained within this study and theoretical predictions, even based on the most advanced models, is not fully adequate. This is unfortunately a problem for many researchers working with modern high-frequency MBS systems. Faced with the same problem, Anstee (2001) decided to use the Applied Physics Laboratory (APL) model (APL 1994) to derive the backscatter strength versus incidence angle for some generic seafloor types at different frequencies including 455 kHz. Details of the APL model, developed at the University of Washington (USA), were given in Chapter 2. Although the APL model is primarily intended for much lower Rayleigh numbers, Anstee (2001) chose to use the APL model and recommended input parameters as it was physically based and expected to give reasonable predictions even if the absolute values of backscatter strength were incorrect.

Anstee's (2001) results are redrawn in Figure 4.4. Backscatter strength from rock was predicted to be at least 10 dB greater than that from medium sand over incidence angles of 0 to 60º. For oblique angles, backscatter from medium sand was predicted to be 10-12 dB stronger than that from clay. The angular dependence of backscatter strength becomes flatter as the surface becomes rougher, especially at oblique angles. More recent models based on a high order small-slope approximation predict the angular dependence of backscatter to be nearly uniform when the Rayleigh number is much larger than unity (Broschat & Thorsos 1997). Although these models for surface scattering are suitable for large Rayleigh numbers (Equation 2.2) of an order of ten, these Rayleigh numbers are still smaller than those expected for real seafloor surfaces at 455 kHz. In addition to the lack of models valid for seafloor backscatter at very high frequencies, there is also inadequate information regarding the theoretical prediction of acoustic scattering from marine vegetation and corals.

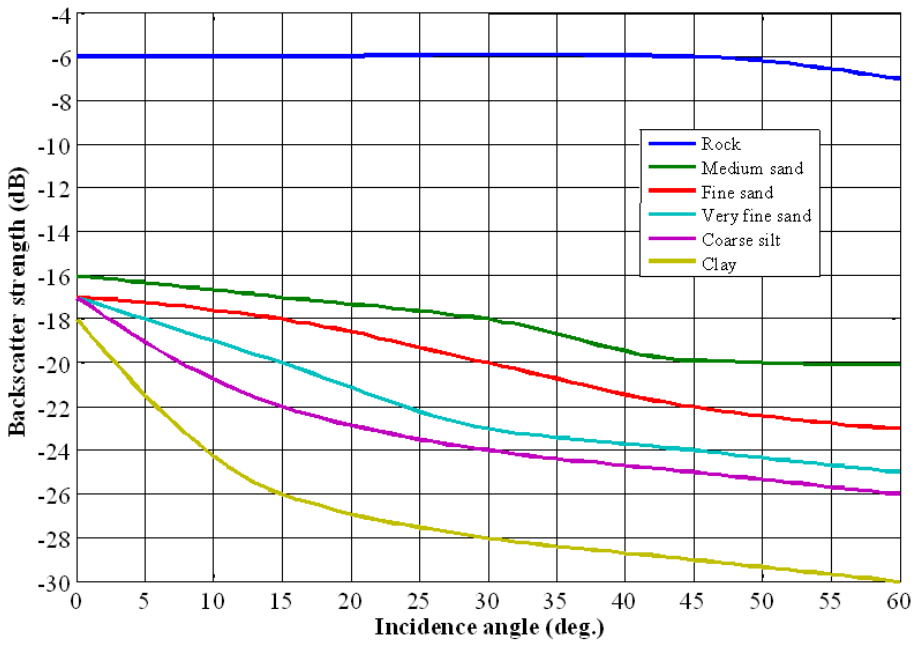

Figure 4.4: APL model (APL 1994) predictions as determined for generic sediment types at 455kHz by Anstee (2001).

4.4.2 Field measurements

Mean backscatter strength ($BS_{integral}$) versus incidence angle measurements collected with the Reson 8125 for a variety of seafloor habitats are shown in Figure 4.5[1]. The data represent a wide variety of seafloor types typical for the shallow coastal waters of Australia. The mean backscatter strength was lowest for the fine sediments (e.g. mud and flat sand) and, in general, as the sediment grain size and surface roughness increased so did the backscatter strength. The highest backscatter strength values were recorded not only from hard and rough substrates such as rock, coral reef and gravel, but also from marine vegetation, such as rhodolith and some seagrasses. The reasons for higher backscatter strength from hard substrates are apparent, and are large roughness and high acoustic impedance. These are also the most likely reasons for stronger backscatter from rhodolith. The reasons for the stronger scattering recorded from seagrass, however, are less obvious.

[1] Data comes from a variety of multibeam surveys performed 2004-2006. Seafloor habitat was confirmed with grab sample and/or underwater video recordings.

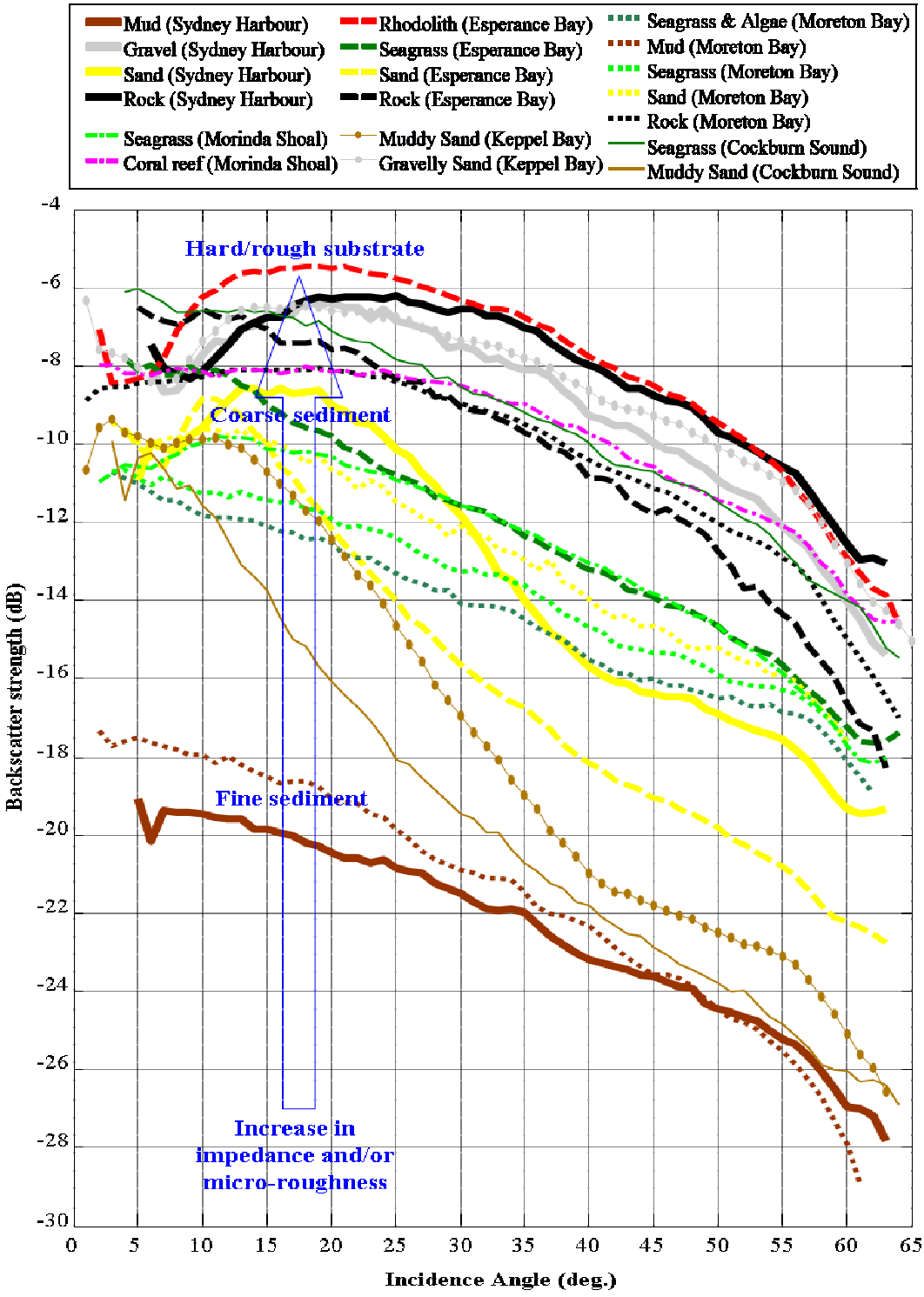

Figure 4.5: Mean backscatter strength ($BS_{integral}$) (dB) versus incidence angle (deg.) for a variety of benthic habitats from around the Australian coast measured using a Reson SeaBat 8125 MBS system.

The mean values of backscatter strength measured from seagrass were found to be generally much higher than those from areas of bare sand observed in the same survey area (Figure 4.5). Also, the backscatter strength from temperate seagrasses (e.g. *Posidonia sinuuosa* in Cockburn Sound) was found to be, in general, higher than that from the shorter and less dense tropical seagrasses (e.g. *Halophila ovalis* in Moreton Bay). This could imply that the size and density of canopy influences the amount of acoustic energy scattered back to the sonar, which is supported by laboratory experiments (Wilson & Dunton 2007). It is unknown to what degree gas filled channels within the seagrass and gas bubbles generated by the plants during photosynthesis dominate the acoustic behaviour (Wilson & Dunton 2007). Gas content and production in rhodolith should also be considered as a possible reason for stronger scattering. Further study of the relative contribution of acoustic energy that is scattered from gas micro-bubbles produced by both seagrass and rhodolith would be useful, especially to determine temporal changes in backscatter level due to changes in gas production, as well as the effect of epiphytes.

The field measurements compare well with the theoretical predictions, but also show some discrepancies. For instance, at nadir where backscatter is dominated by contributions from specular reflection, the APL model predicts quite accurately the values measured for rock and fine sediment. However, the values of backscatter measured at nadir for some sandy beds were noticeably higher than predicted. For the majority of seafloor types surveyed, the mean slope of the angular dependence at angles from 20 to 60˚ was not significantly different, revealing a decrease of the order of 6-8 dB over this angular sector. This is small compared to that measured with low-frequency systems which is typically 2-3 times larger (de Moustier & Alexandrou 1991; Talukdar, Tyce & Clay 1995). This is consistent with the theoretical models that predict levelling of the angular dependence of backscatter as the Rayleigh number increases (Broschat & Thorsos 1997). However, some areas of sand and mixed sand did show noticeably different slopes of the angular dependence, which could be due to variations in geomorphological features of the seafloor surface (e.g. presence of sand ripples) and actual sediment content (e.g. presence of seashell debris, gas content, etc). Also, for

some areas of rock, gravel and rhodolith, the backscatter strength exhibited a small decrease towards nadir. Such dips in backscatter strength at nadir have been observed previously for some other highly rough gravely /pebble-like surfaces (Beaudoin *et al.* 2002), They could be either real or due to measurement artefacts, such as the beam pattern effect in combination with a low sampling rate (as discussed in Appendix B). Further work is required to determine the reasons behind these features in the angular dependence curves.

It is evident from Figure 4.5, that the key property of backscatter with respect to discriminating different habitats is the mean backscatter strength, especially at the oblique angles. However, there are also some changes in slope, which might be exploited. Statistical distributions and higher order moments of the average backscatter intensity will be examined in more detail in the next section.

4.5 Statistical distribution of the average backscatter intensity

4.5.1 Introduction

The statistical distribution of backscatter values has been previously identified as a potential characteristic for classifying the seafloor. Exploiting the variation in backscatter measurements for seafloor classification has been achieved mainly through texture analysis (Blondel, Parson & Robigou 1998; Milvang *et al.* 1993), probability density distributions (PDF) (Stewart *et al.* 1994) or high order moments (Le Chenadec *et al.* 2005). The aim of this section is to examine the effect of incidence angle, insonfication area and seafloor habitat on the statistical characteristics of backscatter values. First, the theoretical model for the distribution of the average backscatter intensity (derived from the integral of the snippet) is detailed, namely the gamma model. The gamma model is then compared with field measurements from different seafloor habitats. The potential of the gamma model parameters for seafloor classification is discussed.

4.5.2 Theoretical predictions

Middleton (1999) demonstrated theoretically that the statistical distribution of the average backscatter intensity for a Gaussian scattering process should follow a gamma distribution. The gamma distribution (Γ-pdf) is a 2-parameter model characterized by the scale λ and shape β parameters. For β = 1, the Γ-pdf reduces to an exponential distribution with the rate parameter 1/β, which describes statistical variations of the instantaneous intensity of a complex Gaussian process. When λ = 2, the Γ-pdf simplifies to the chi-squared distribution with the degrees of freedom 2β. If the backscattering process is Gaussian (or nearly Gaussian), i.e. the number of statistically independent scatterers (or scattering facets) that contribute instantaneously to the backscatter signal is large enough to satisfy the central limit theorem (CLT), then according to Middleton (1999), the shape parameter represents the number of statistically independent scattering cells observed at different times and the Γ-pdf tends to the Gaussian distribution when the number of scattering cells becomes large (β >> 1).

If the instantaneous complex backscatter amplitude p is Gaussian distributed. Then the average backscatter intensity $\bar{I}$:

$$\bar{I} = \frac{1}{c\rho T}\int_0^T |p(t)|^2 dt \tag{4.4}$$

where: c is the sound speed (m s^{-1}), ρ is density (kg m^{-3}), is gamma distributed, i.e. its PDF is:

$$f\left(\bar{I}\right)_\Gamma = \left(\bar{I}/\lambda\right)^{\beta-1} \frac{\exp\left(-\bar{I}/\lambda\right)}{\lambda\,\Gamma(\beta)} \tag{4.5}$$

The mean value $\mu \equiv \langle I \rangle$ of a gamma-distributed process is a product of the shape and scale parameters: $\mu = \beta\,\lambda = \langle p\,p' \rangle$, where $\langle\ \rangle$ denotes ensemble average. Thus the mean value of I is a consistent estimate of the mean backscatter intensity. In the algorithm for calculating the seafloor backscatter coefficient through the integral intensity, the measured backscatter energy is divided by the footprint size, which is equivalent to calculating the time-average intensity. As a result, the estimate of the mean backscatter

coefficients is also consistent. On the other hand, the variance (σ^2), Equation 4.6, of a gamma-distributed process depends on the shape factor β and, hence, the footprint size and incidence angle.

$$\sigma^2=\beta\lambda^2 = \mu^2/\beta \qquad (4.6)$$

The variance can therefore vary with incidence angle, even if the mean backscatter coefficient is independent of incidence angle. When the insonification area is not large enough for the number of statistically independent scatterers within that area to satisfy the CLT, the *K*-distribution has been shown to fit instantaneous backscatter intensity collected with MBS (Hellequin, Boucher & Lurton 2003). If the instantaneous intensity values are to be averaged, e.g. when calculating the integral intensity or gridding backscatter images, then according to Hellequin *et al.* (2003), the distribution of the average backscatter values can be approximated by a "generalized *K*-distribution", which represents a product of two independent gamma-distributed processes. The shape parameter of the *K*-distribution related to the number of elementary scatterers has been used in addition to the mean backscatter to discriminate between different seafloor habitats (Hellequin, Boucher & Lurton 2003; Le Chenadec *et al.* 2005). However, the shape parameter of the K-distribution is dependent on the incidence angle due to the change in the insonification area with the incidence angle.

In the next sections, statistical moments and distributions of backscatter data from different habitats in different angular domains are examined. The suitability of the gamma model as an approximation for the statistics of seafloor backscatter strength derived from the integral intensity data is considered. It will be demonstrated that the gamma distribution model based on an assumption of CLT validity is a simple but quite accurate approximation for statistical features of the seafloor backscatter strength derived from the integral intensity collected from incidence angles 5-60º. This observation is used to assess the usefulness of the Γ-pdf shape parameter and higher moments as a means to discriminate between different habitats.

4.5.3 Data description

This study uses two transects (swath lines) from different areas, each of which cover three different habitats. The first transect (Esperance 309) was made during the survey of Esperance Bay and was recorded over rhodolith, sand and temperate seagrass. The second transect (BGB 11) comes from the survey of Morinda Shoal and was recorded over a coral material (rubble/debris), sand and tropical seagrass. These transects were chosen because changes in insonfication and footprint areas for the different incidence angles were very similar for all data (Figure 4.6). The bathymetry and backscatter strength for the two transects were calculated using the methods described in Section 3.5 and are shown in Figure 4.7. The location of the lines and the system settings are given in the Appendix A. The gamma shape parameter β shown in Table 4.1 was estimated using the maximum likelihood method in Matlab®.

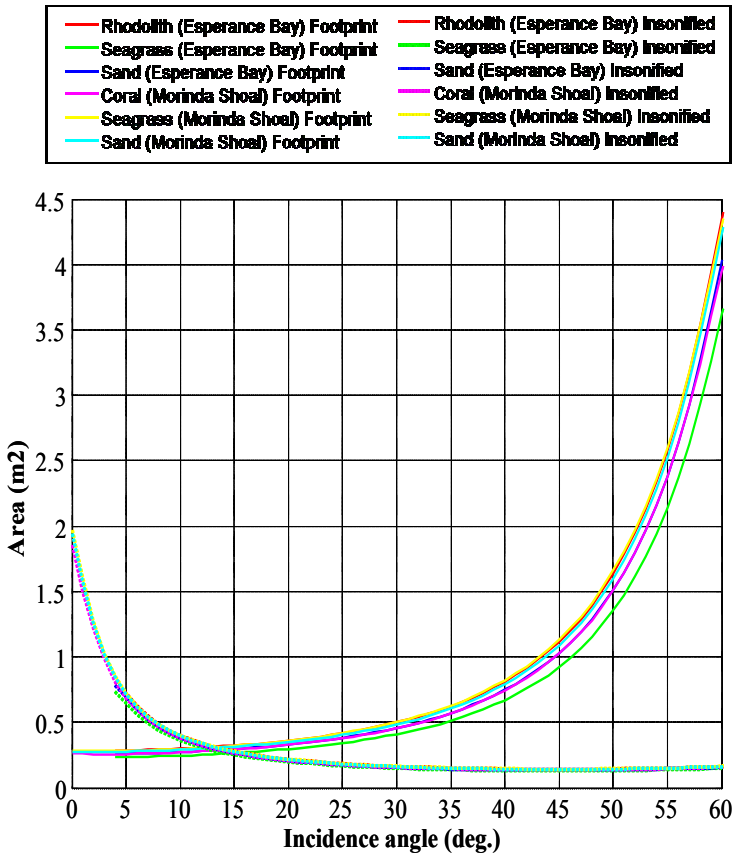

Figure 4.6: The mean footprint and insonification areas versus incidence angle for the different seafloor habitats analysed in this section.

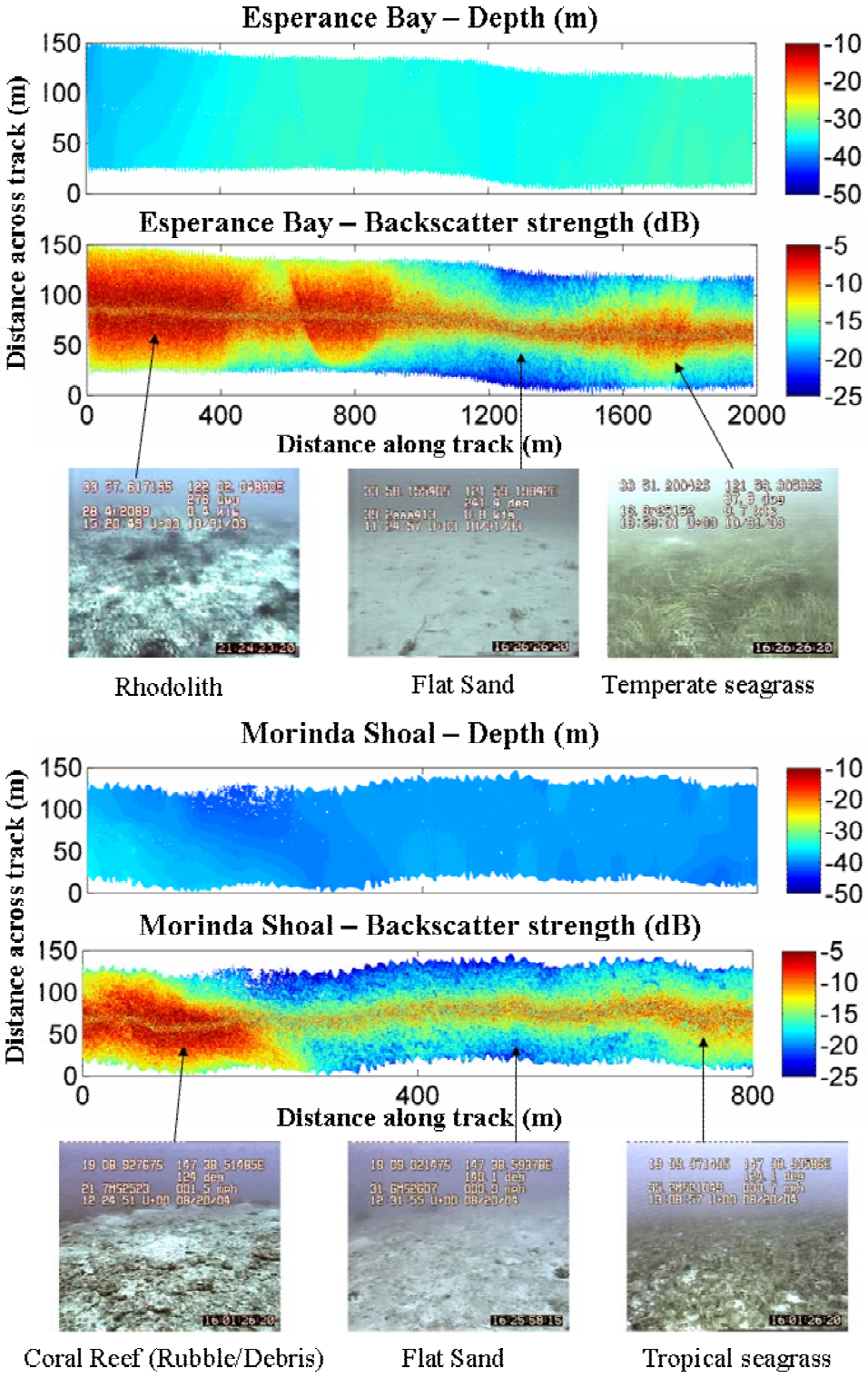

Figure 4.7: Transects used for statistical analysis (Backscatter images are not corrected for angular dependence).

4.5.4 Results

The angular dependence of the seafloor backscatter strength averaged over areas of homogeneous habitats, and the coefficient of variation of backscatter intensity for the main habitats observed along the transects in Esperance Bay and Morinda Shoal are shown in Figure 4.8. The highest mean backscatter strength for these sets of habitats was obtained from coral rubble and rhodolith, which had similar angular responses of backscatter strength. After the areas of coral and rhodolith, the seagrass regions yielded the next highest mean backscatter strength. Although the temperate and tropical seagrasses are different species, they exhibited similar angular response of backscatter. The lowest mean backscatter strength came from the two areas of sand, but they had different angular dependences. Sediment grab data are available only for the Esperance Bay sand area, which reveals the sediment composition to be 93% sand, 5% gravel and 1% mud. It is likely that sand content, including grain size, different intrusions (e.g. coral material), etc., at Morinda Shoal differs from that in Esperance Bay resulting in the different angular response.

The trend in the coefficient of variation (CV) of the average backscatter intensity with incidence angle is the same for all of the six habitats examined here (Figure 4.8(b)). The CV at normal incidence for all habitats is just below unity, as the incidence angle increases the CV of all data decreases almost linearly. At angles greater than 45-50º, the trend in CV with incidence angle starts to become more uniform. Overall, the backscatter variations about the mean value appear to relate to the incidence angle either directly or through changes in the insonfication area and footprint size rather than seafloor properties.

$$CV=\sigma/\mu \qquad (4.7)$$

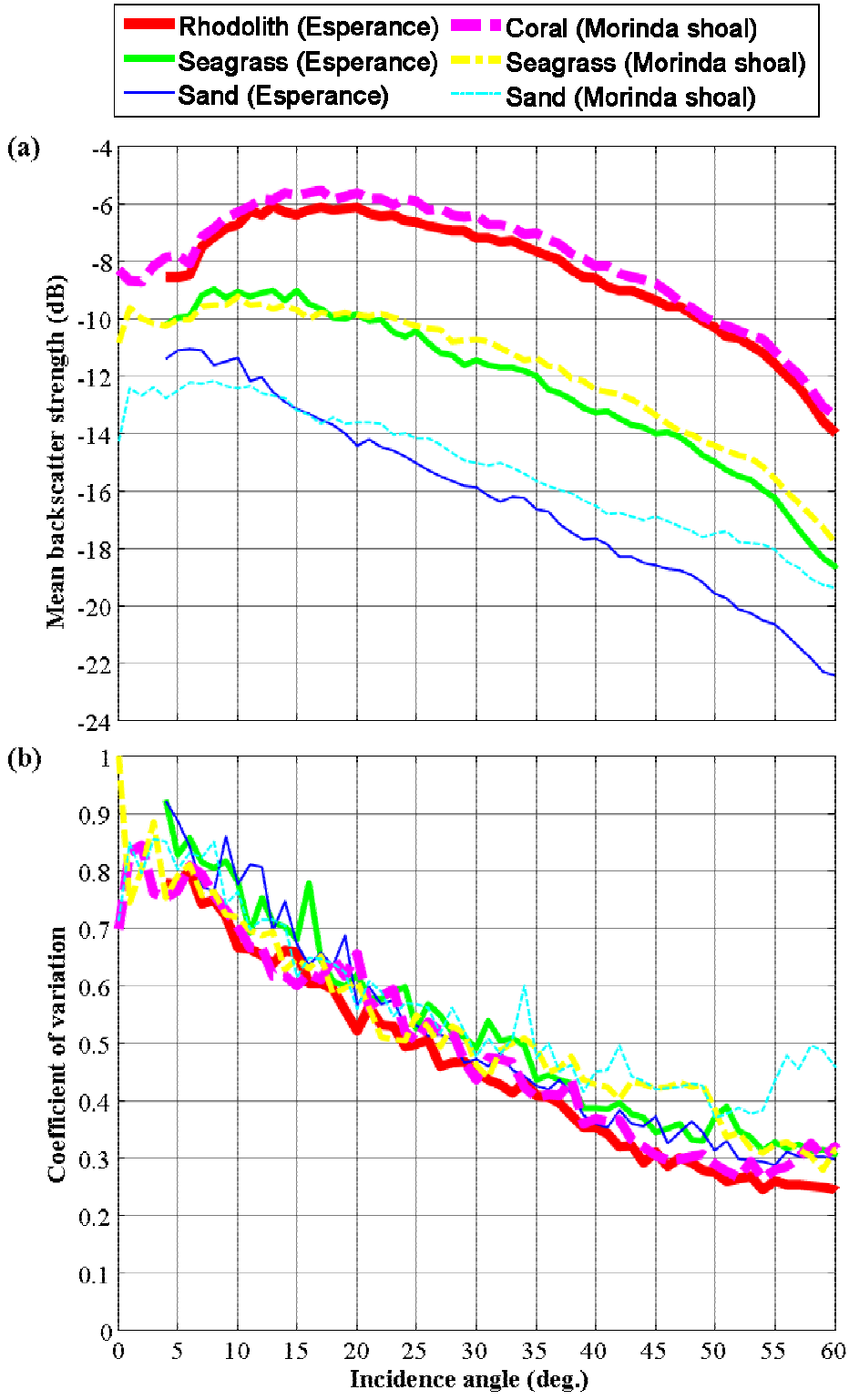

Figure 4.8: (a) Mean backscatter strength and (b) coefficient of variation versus incidence angle for the different habitats.

One of the ways to examine the suitability of the gamma distribution to model the actual backscatter intensity data is to analyse the relationship between the skewness squared and kurtosis of measured PDFs (Figure 4.9). For the gamma model, this relationship is a function of the shape parameter β and is shown as a black line in Figure 4.9. The backscatter intensity data from all habitats are well approximated by the gamma model. When β=1, the gamma distribution simplifies to an exponential distribution and as β tends to infinity the distribution tends to a Gaussian distribution. The majority of the data fits well with the gamma model, although the relationship between incidence angle and the model parameters is not clear from Figure 4.9. There are, however, some outliers that correspond to a kurtosis greater than 9 and are below the gamma model prediction. This implies that for these outliers β is less than 1, a reason for this is not evident.

The probability density distributions of the backscatter intensity (normalised by the standard deviation) for all habitats at 5º, 30º and 55º incidence angles are shown in Figure 4.10 and 4.11. The gamma distribution model provided a very good visual fit for all habitats over all angles of incidence (Figure 4.10). Estimates of the shape parameter β for all the distributions shown in Figure 4.10 are given in Table 4.1. As the incidence angle increases so does the shape factor. Moreover, the shape factor and distributions are very similar for all habitats at incidence angles 5º and 30º (Table 4.1 and Figure 4.11. However, at 55º there are some significant differences in the shape parameter between habitats, notably Rhodolith from Esperance Bay and Sand from Morinda Shoal.

Table 4.1: Gamma scale (λ) and shape (β) parameters for the distributions shown in Figure4.10.

Habitat	**Angle domain**					
	5º		30º		55º	
	β	λ	β	λ	β	λ
Rhodolith (Esperance Bay)	1.9	0.7	5.3	0.4	16.8	0.2
Seagrass (Esperance Bay)	1.6	0.7	4.4	0.5	10.1	0.3
Sand (Esperance Bay)	1.5	0.8	4.7	0.5	12.1	0.3
Coral Reef (Morinda Shoal)	1.8	0.7	5.6	0.4	13.8	0.3
Seagrass (Morinda Shoal)	1.9	0.7	5.1	0.4	10.3	0.3
Sand (Morinda Shoal)	1.8	0.7	4.8	0.4	7.1	0.4

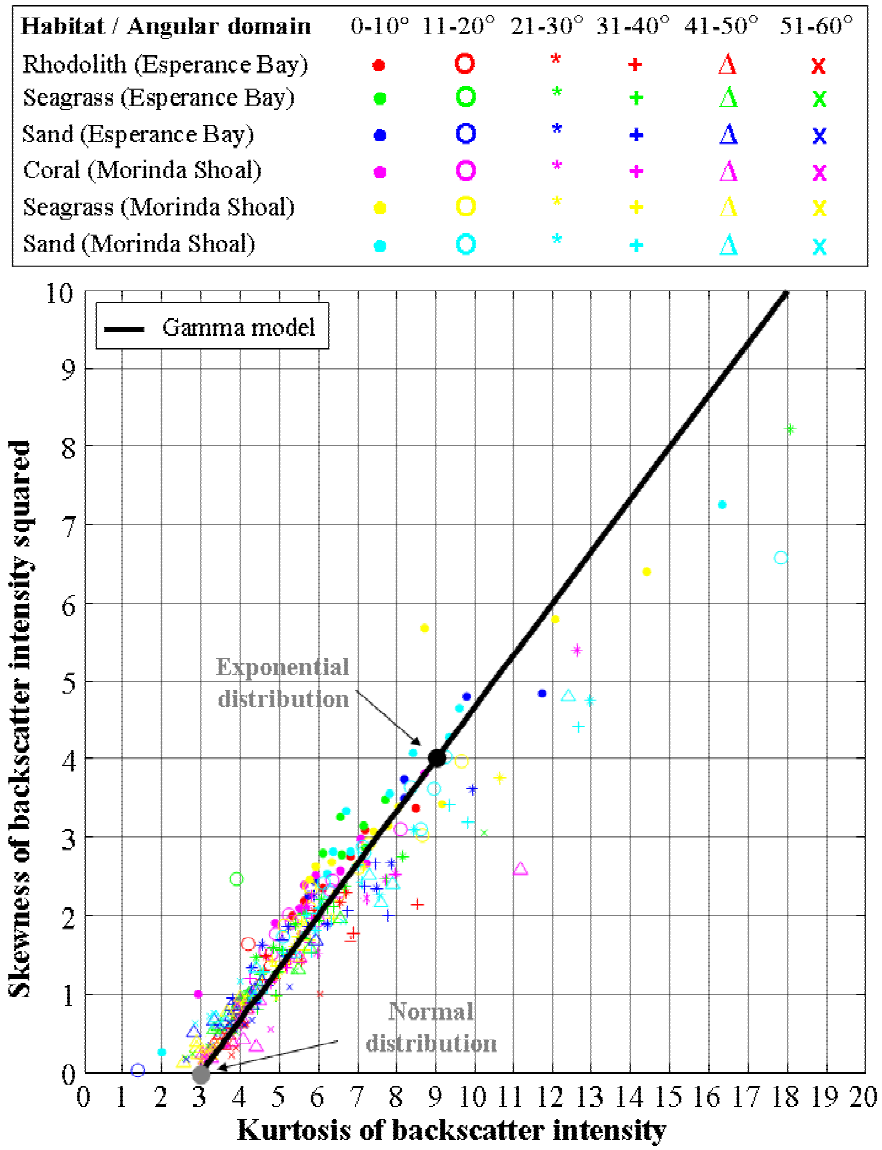

Figure 4.9: Skewness squared versus kurtosis of backscatter intensity in different angular domains for the different habitats. The dependence predicted from the gamma model is shown as a black line along with the positions of a Gaussian (●) and exponential (●) distribution.

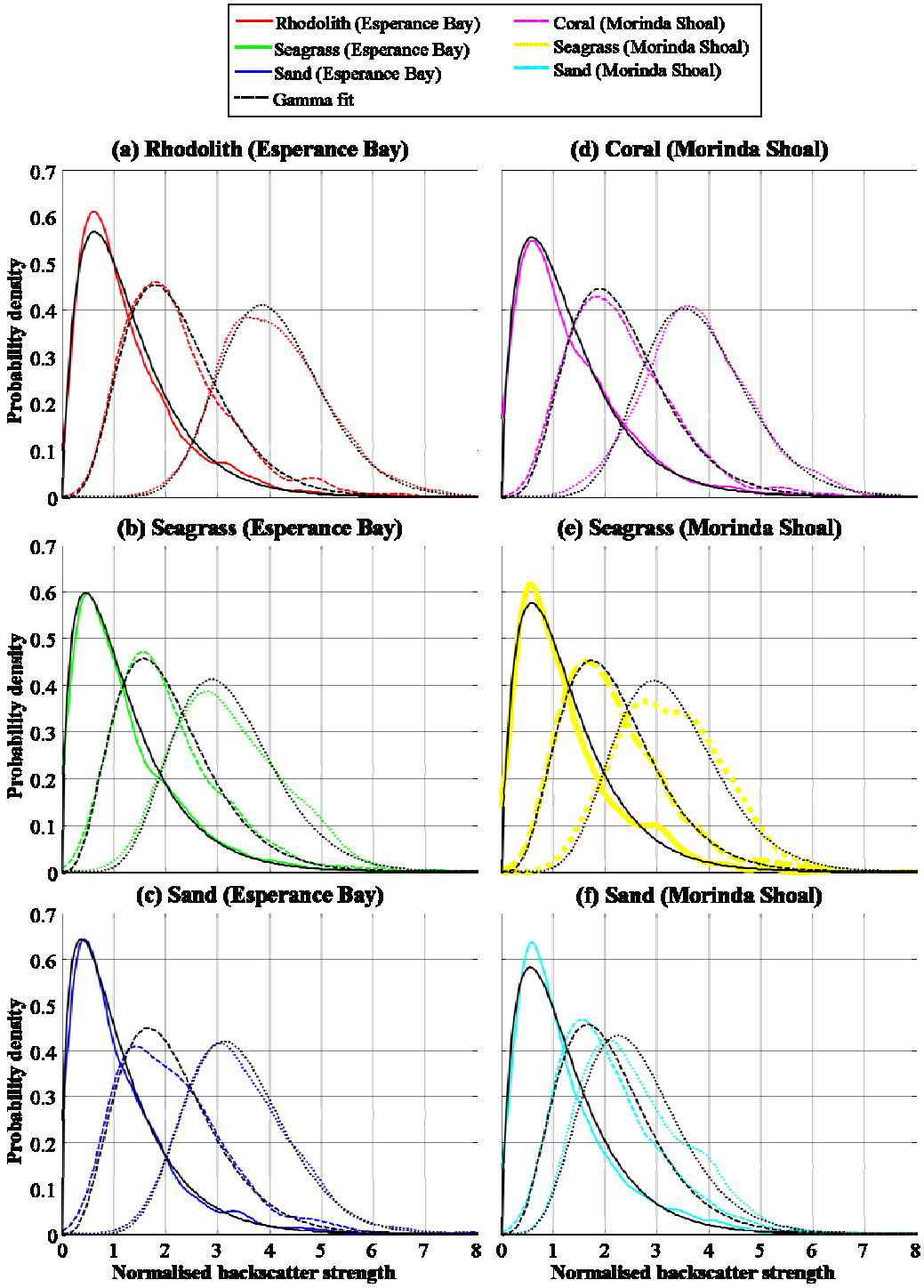

Figure 4.10: Probability density for normalised backscatter intensity for a variety of habitats for incidence angles 5 ° (- solid lines), 30 ° (-- lines) and 55° (¨lines). Black line shows the gamma model fit.

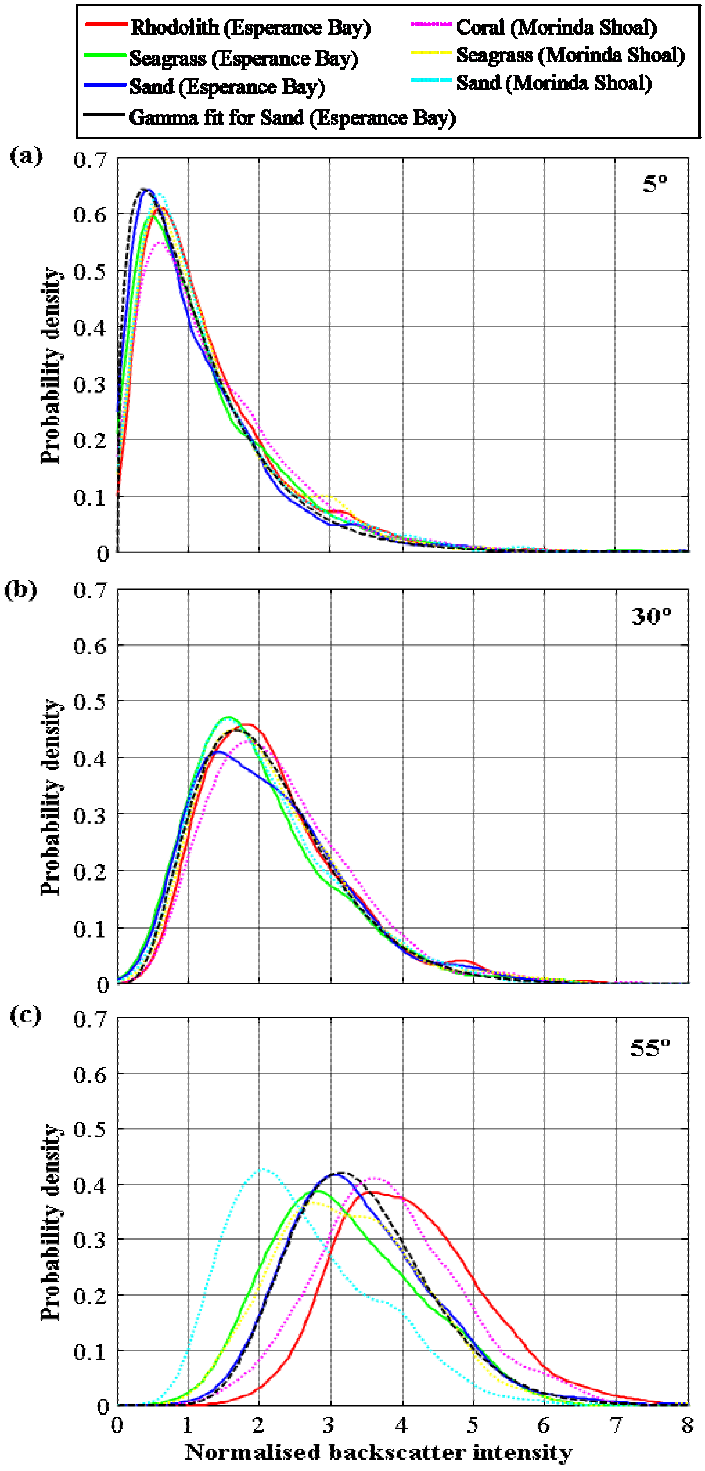

Figure 4.11: Probability density for normalised backscatter intensity for a variety of habitats for incidence angles (a) 5 °, (b) 30 ° and (c) 55°. Black dashed line shows the gamma model fit for sand (Esperance Bay).

The value of β (as estimated from Equation 4.6) for the different habitats as a function of incidence angle is shown in Figure 4.12(a). As indicated by Table 4.1, as the incidence angle increases so does β. Following arguments put forward by Middleton (1999), if backscattering from the adjacent insonification areas can be regarded as statistically independent processes, then it is most likely that the change in β relates more to the number of insonfication areas contained within the footprint of receive beams rather than to the incidence angle itself. The shape parameter β versus the ratio of insonfication area to the footprint size (for each incidence angle) is shown in Figure 4.12(b), which reveals two scattering regimes.

The first scattering regime occurs when the ratio of insonification area to footprint size is less than 5, which corresponds to incidence angles below approximately 40°. In this regime the shape factor is linearly proportional to the ratio of insonification area to footprint size. This regime corresponds to a nearly Gaussian scattering process and the shape factor is not significantly different between different habitats. However, it is necessary to note that the experimental estimates of the shape parameter β are about one unit higher than those expected for the estimated number of statistically independent scattering cells. This is likely a result of the real backscatter process not being purely Gaussian but rather a superposition of two or more processes of different spatial scale.

The second scattering regime is for an insonification area to footprint size ratio greater than 5, which, for this dataset, equates to an incidence angle greater than 45°. In the second scattering regime the dependence of shape factor β on the ratio of insonfication area to footprint size almost vanishes and some degree of separation appears between habitats. At large area ratios, the hard and rough substrates of coral and rhodolith have the highest values of β, followed by the seagrasses and the sand in the Esperance data and the lowest values of β come from the sand from the Morinda Shoal data.

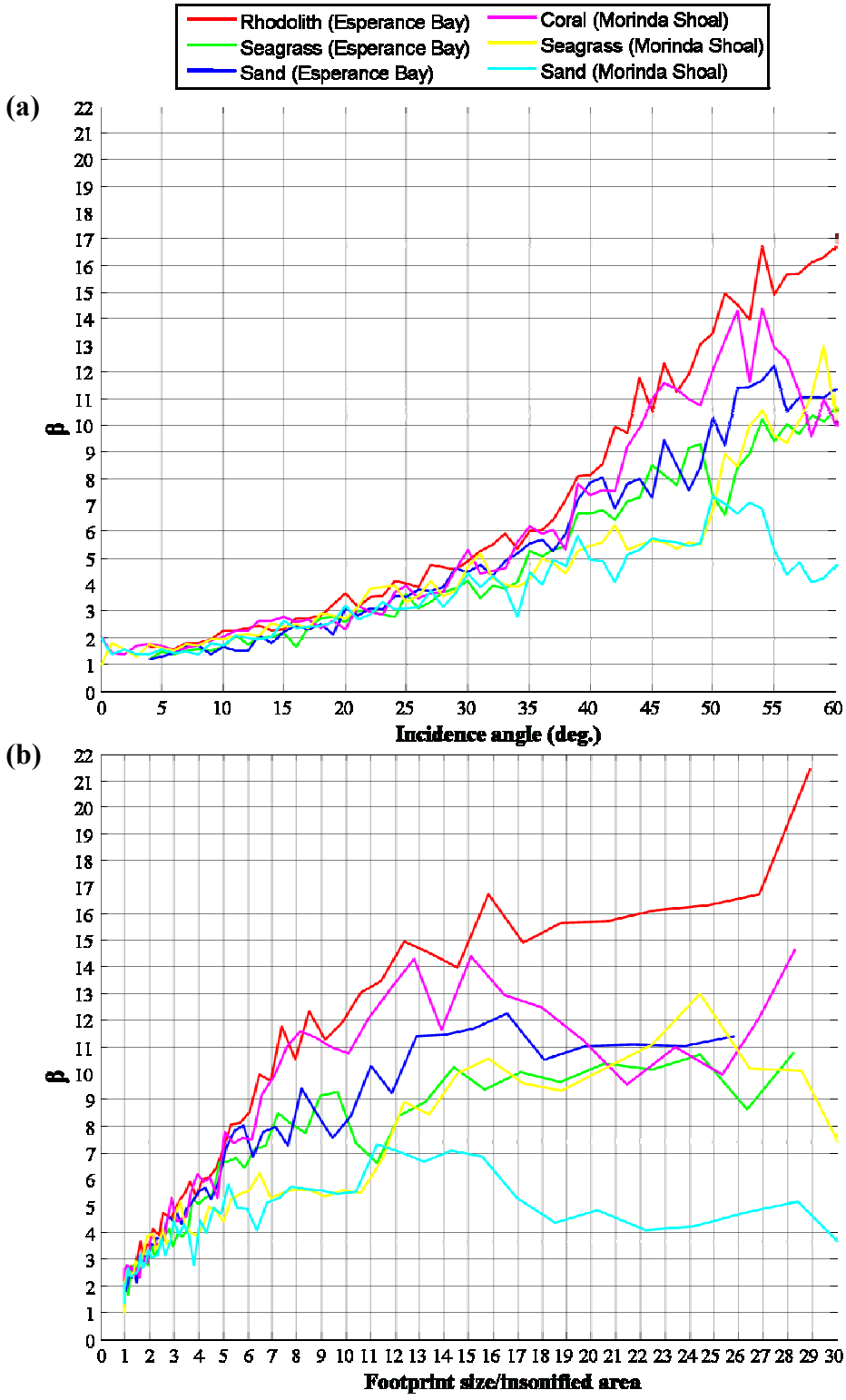

Figure 4.12: The gamma shape parameter β versus (a) incidence angle (deg.) and (b) the ratio of the insonfication area to footprint size.

At present, the statistical principles and physics controlling this second regime are not apparent. One possibility is that the decrease in insonfication area may have reached a threshold after which the roughness scale becomes comparable or larger than one of the area dimensions. In that case, the CLT is invalid and the shape parameter does not depend on the ratio. If the differences between values of β for different seafloor habitats can be attributed to different properties of the seafloor, then β might be a useful parameter in seafloor classification. However, until this scattering regime is better understood, it is problematic to implement any classification procedure based on the shape parameter. Also, this second regime represents a small percentage of the data across the swath for the Reson 8125, e.g. for this dataset the second regime represents about 10% of the beams. Therefore, for this study, the mean backscatter strength was used as a the major parameter to characterize the acoustic properties of the seafloor, but with the recommendation for further research into the use of some other statistical characteristics of backscatter, such as the gamma shape parameter, as additional features to help distinguish different habitats.

4.6 Implications for benthic habitat mapping

This chapter has examined some of the effects of incidence angle, insonificaiton area and seafloor habitat on seafloor backscatter strength measured with high-frequency MBS. The implications of these findings for benthic habitat mapping are as follows:

1. The peak and the integral intensity derived from the backscatter waveform are useful parameters in discriminating between different seafloor habitats. Changes in waveform shape relate more to changes in the footprint size and insonification area with the beam angle rather than to changes in seafloor properties.
2. Mean backscatter strength derived from the peak intensity will be overestimated, especially at oblique angles. Therefore, backscatter strength derived from the integral intensity was primarily used for this study.
3. Mean backscatter strength derived from the intergral intensity is a good descriptor of changes in benthic habitats and distinct angular responses are observed for hard rough substrate, seagrass, coarse sediment and fine sediment.

4. Acoustic backscatter models are generally in agreement with the mean backscatter angular responses measured in this study, but at present are not significantly accurate for high frequencies, such as that of the Reson 8125, to aid in benthic habitat mapping.
5. The gamma distribution adequately describes the variation of the average backscatter intensity at 455 kHz for a range of seafloor habitats for incidence angles 5-60º.
6. The scale parameter of a gamma-distributed backscatter intensity is dependent on the incidence angle and the seafloor properties.
7. The shape parameter β of a gamma-distributed backscatter intensity reveals two regimes of backscattering. The first regime corresponds to a Gaussian scattering process where the shape parameter is approximately proportional to the ratio of the insonification area to the footprint size. Hence, the shape parameter increases with incidence angle in this regime, but there is no significant difference in its value between different habitats. Therefore, this regime is not useful for seafloor classification. The second regime corresponds to small grazing angles and here the shape parameter can be different for different seafloors, and can potentially be used for discriminating different benthic habitats. However, this observation requires further research to provide a practical means for seafloor classification.
8. The key property of the backscatter angular dependence appears to be the mean level, although additional information can be obtained from the slope. Exploiting the mean backscatter angular response is explored more in the next Chapter (5).

CHAPTER 5

PROCESSING TECHNIQUES FOR VISUALISATION AND CLASSIFICATION OF BACKSCATTER STRENGTH DATA COLLECTED WITH MULTIBEAM SONAR

5.1 Overview

Two principal objectives of this part of the study were to improve methods for spatial visualisation of backscatter properties and to develop seafloor classification techniques using MBS data. The previous chapter (4) showed that the mean backscatter strength could discriminate between different seafloor habitats, such as sand, seagrass and rock. However, because the backscatter strength is also dependent on incidence angle, backscatter images can be difficult to interpret. Moreover, combining several overlapping MBS swath lines to produce a backscatter mosaic is not a trivial problem because of the angular (i.e. beam) dependence of the measured backscatter strength. The traditional approach has been to correct backscatter images for the angular dependence through removing either an empirical (Beaudoin *et al.* 2002; Preston & Christney 2003) or model-based (Augustin & Lurton 2005) prediction of the underlying angular variation. It will be shown in this chapter, however, that even after an angular correction has been applied, backscatter images can still be dependent on incidence angle. The aim of this chapter is to present a new method developed by the candidate to visualise backscatter properties, and to demonstrate how it can be utilised for seafloor classification.

This chapter starts by presenting the algorithms examined and developed by the candidate for removing the angular trend from backscatter images to enable mosaicing of multi-swath backscatter data (Section 5.2). It was through this investigation that a new approach for visualising backscatter properties was developed. This new method puts all backscatter data collected from the survey into a 3-dimensional sparse matrix. Two dimensions of the matrix are geographic coordinates (x, y) and the third dimension is the incidence angle. Through interpolation in the spatial domain, an estimation of the backscatter strength collected at each grid node at each incidence angle is obtained. The resulting solid matrix is referred to as an angle cube. The method and considerations for

constructing angle cubes are discussed in more detail in Section 5.3. Section 5.4 then demonstrates the use of angle cubes in seafloor classification. The design of new pattern recognition tools was beyond the scope of this study, and therefore established classification methods were applied to the various backscatter properties derived from the angle cubes. However, it is likely that new techniques based on more sophisticated methods of classification will provide a more accurate classification and mapping of the seafloor. The implications of the results of this chapter to benthic habitat mapping are summarised at the end of the chapter in Section 5.5. Initial results related to this chapter have been presented by the author at various conferences (Gavrilov *et al.* 2005; Parnum, Gavrilov & Siwabessy 2007; Parnum *et al.* 2005; Parnum *et al.* 2006; Parnum, Siwabessy & Gavrilov 2004).

5.2 Correcting backscatter images for angular dependence

5.2.1 Methodology

There is a desire to produce MBS backscatter intensity images similar to other remotely sensed images, such as from satellite and aerial photography. This has lead to the development of various methods to correct multibeam backscatter for its dependence on incidence angle. Hence, during this study different methods were examined and developed to correct backscatter images for angular dependence. The aim of this section is to show the advantages and shortcomings of the different methods examined by the author.

The first approach used in the course of this study (Parnum, Siwabessy & Gavrilov 2004) was to correct backscatter images by predicting the angular backscatter trend using a Lambertian-based model similar to the one proposed by Hellequin *et al.* (2003). It was concluded that this model was not adequate for all habitat types, hence, it was not effective at correcting backscatter images derived from high-frequency MBS data (Parnum, Siwabessy & Gavrilov 2004). Moreover, as discussed in the previous chapter, there are as yet no adequate theoretical models of the backscatter angular dependence that are fully suitable for high frequencies of hundreds of kHz. Therefore, it was

concluded that an empirical correction (i.e. deriving the angular trend from the data) would be a more appropriate way to proceed.

The effectiveness of the different incidence angle correction approaches examined is demonstrated using the backscatter strength data from Esperance line 309, which was used in the previous chapter. The backscatter strength data before correction is compared to the results of different corrections for angular dependence in Figure 5.1. An area of sand, which is indicated by a rectangular window in Figure 5.1, is used to examine the mean and standard deviation of backscatter data across track before and after the different corrections have been applied.

5.2.2 Results of different angular corrections

Four empirical corrections for angular dependence of backscatter strength were examined, which applied correction for (removal of) the following values:

(a) global or track-mean angular trend, similar to Beaudoin *et al.* (2002);

(b) global track-mean and standard deviation angular trends, similar to Preston and Christney (2003);

(c) local mean angular trend, which was described in Gavrilov *et al.* (2005);

(d) local mean and standard deviation angular trends, which was described in Parnum *et al.* (2006).

Correction (a) is similar to that proposed by Beaudoin *et al.* (2002), which obtains the mean backscatter strength angular trend over the whole data set, or in the example shown in Figure 5.1(b) - the track mean. The mean values at each angle are then removed from the data collected with each sonar ping. The algorithm can be expressed as follows:

$$BScor(\theta) = BS(\theta) - \overline{BS}(\theta) + \overline{BS}(30°) \qquad (5.1)$$

where $BScor(\theta)$ is the corrected backscatter strength, $BS(\theta)$ are backscatter data before correction collected at angle θ, $\overline{BS}(\theta)$ is the mean backscatter strength for all data collected at angle θ . $\overline{BS}(30°)$ is the mean backscatter at 30º for the whole data set

which is added to the whole dataset to make the result more comparable with the other methods of correction. Any moderate angle of incidence between approximately 20-50º can be used as a reference point for backscatter level to characterize seafloor properties. In this study, a reference angle of 30º was chosen because 1) it is also half way across the Reson 8125's swath and 2) backscatter level around this incidence angle is a robust characteristic for detecting change in seafloor properties, as demonstrated in Chapter 4.. The results of applying correction (a) are shown in Figure 5.1(b). Although there is a visible improvement in the data appearance in the outer beams (Figure 5.1(b)), it is evident that the mean backscatter strength at nadir is still dependent on incidence angle (Figure 5.2(a)). Moreover, the standard deviation of backscatter strength after correction (a) is identical to that of the original data (Figure 5.2(b)).

Correction (b) is similar to that proposed by Preston and Christney (2003), which in addition to correcting for the global mean, as implemented in correction (a), also normalises the residual data by the global standard deviation measured for each angle. The algorithm can be expressed in the following form:

$$BScor(\theta) = \frac{BS(\theta) - \overline{BS}(\theta)}{BS_{std}(\theta)} + \overline{BS}(30°) \qquad (5.2)$$

where $BS_{std}(\theta)$ is the standard deviation of backscatter strength data for all data collected at angle θ. Similarly to correction (a), the mean backscatter strength for all data at 30º is added to the whole dataset to provide comparable absolute values derived after all corrections. The results of correction (b) are shown in Figure 5.1(c). Correction (b) provides better results than correction (a), both in terms of the quality of the image (i.e. reduction of angular dependence artefacts) and the dependence of the track-mean and standard deviation of backscatter strength on incidence angle. However, there is still a noticeable local dependence on incidence angle in the backscatter images. The reason for this is that corrections (a) and (b) assume all habitat types found within the surveyed area to have the same angular dependence, which is usually not the case, as seen in Figure 4.5 from the previous chapter.

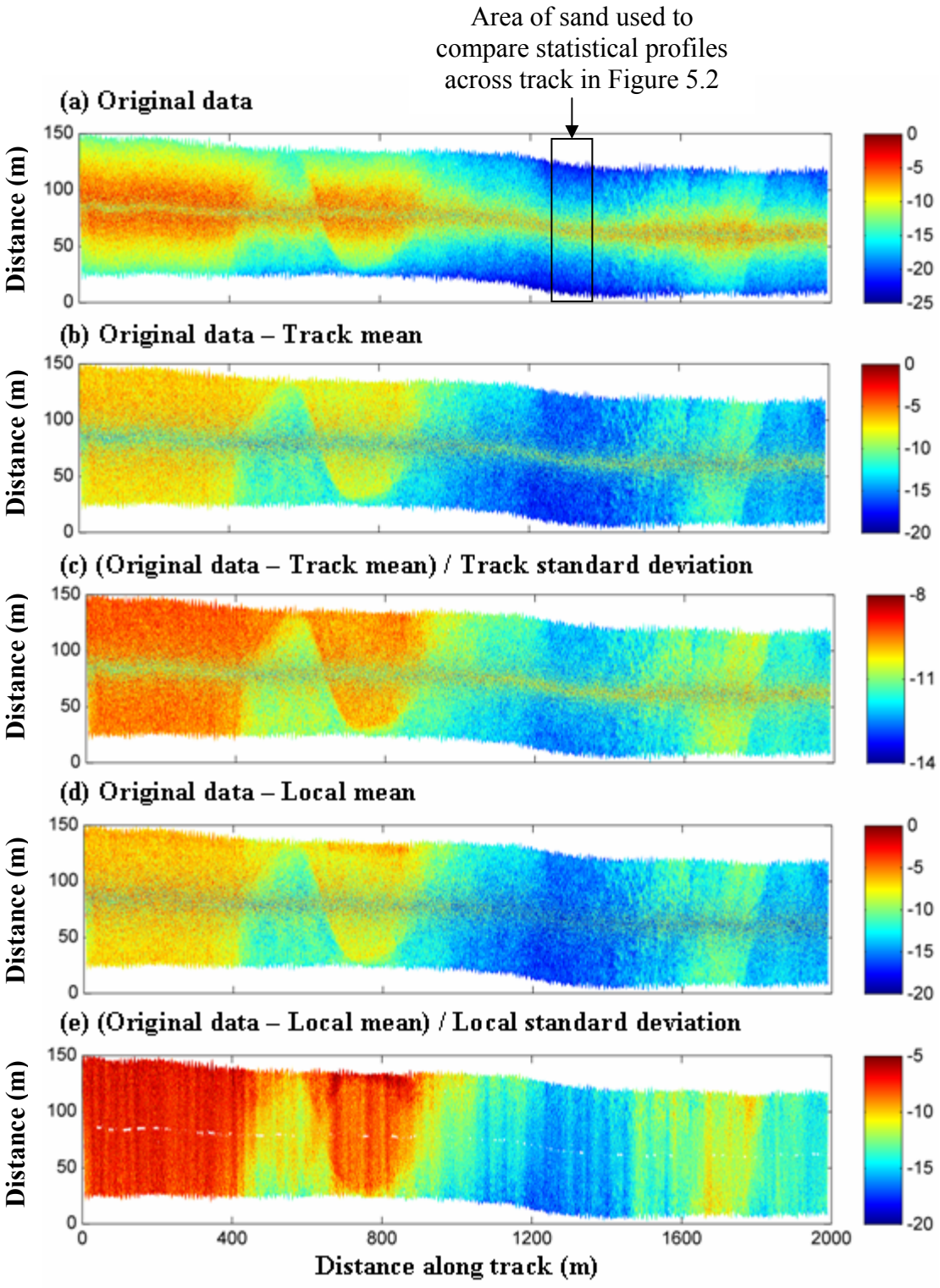

Figure 5.1: Backscatter strength (dB) from line Esperance 309 with the results of various corrections for angular dependence.

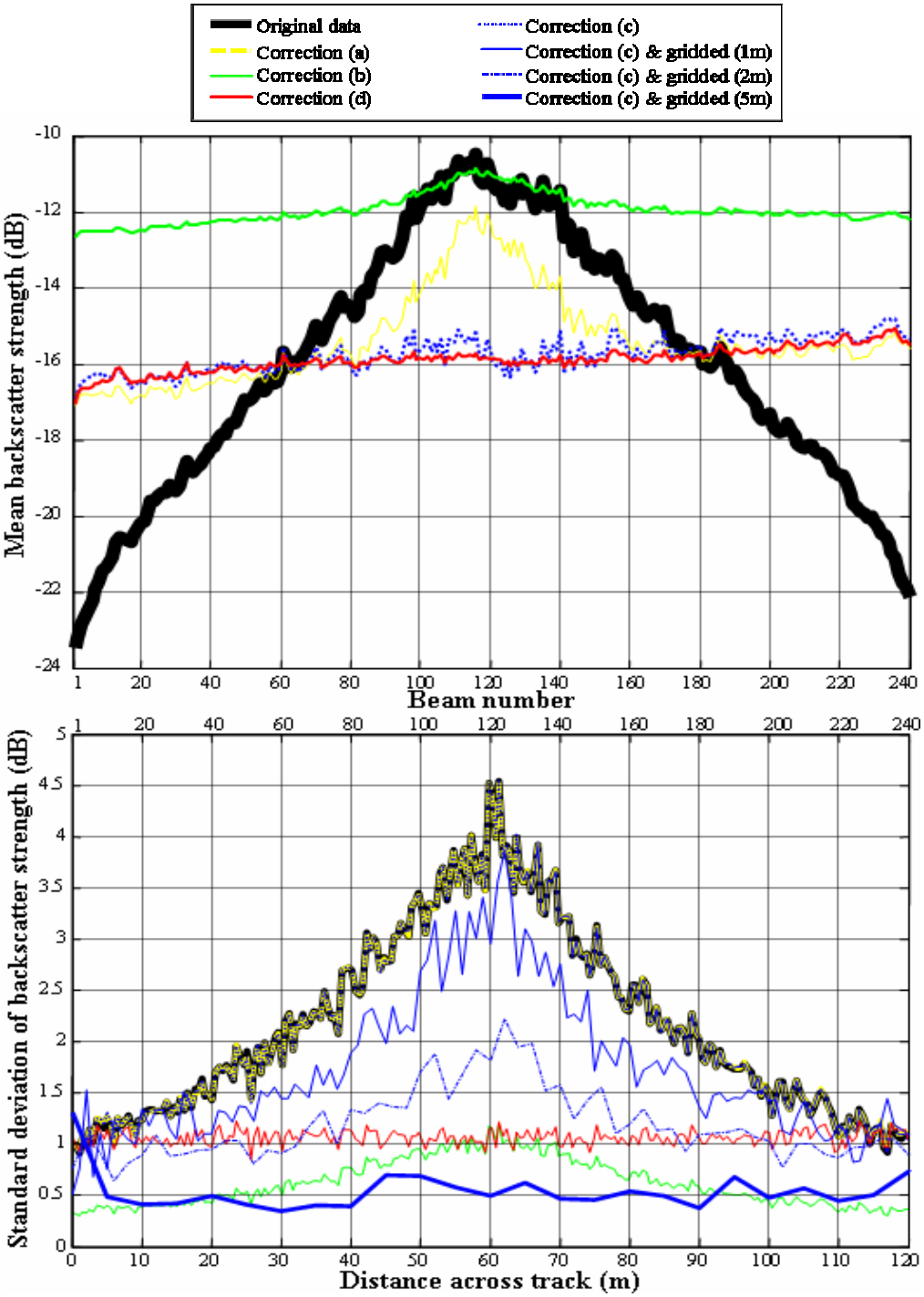

Figure 5.2: (a) Mean and (b) standard deviation of backscatter strength versus beam number for sand before and after various angular corrections. Plot (b) also shows the effects of gridding (blue lines) on the results of correction (c) as a function of across track distance.

To try to overcome the problem of corrections (a) and (b), the angular trend of a local mean value of backscatter strength was derived using a sliding spatial window of an appropriate length which could be adjusted to the scale of spatial changes in habitat types. This algorithm of correction (c) was described in detail in Gavrilov *et al.* (2005). Removing the local mean angular trend also filters out large-scale variations due to change, either sharp or gradual, in the habitats along the swath line. To recover this useful information and obtain absolute values of backscatter strength, the angularly equalized backscatter strength within each spatial window is to be increased by adding the window-mean level at a reference angle (a moderate angle of 30º was used for these examples). The algorithm is formulated by equation 5.3:

$$BScor(X,Y,\theta) = BS(X,Y,\theta) - \overline{BS}(X,Y,\theta) + \overline{BS}(X,Y,30^{\circ}) \qquad (5.3)$$

where $BS(X,Y,\theta)$ is all the backscatter data within the sampling window (X, Y) at angle θ, $\overline{BS}(X,Y,\theta)$ is the mean backscatter strength within the sampling window (X, Y) at angle θ, and $\overline{BS}(X,Y,30^{\circ})$ is the mean backscatter strength measured within the sampling window at the reference angle of 30º. The results of this method are seen in Figure 5.1(d).

Correction (c) removes the mean angular trend from homogenous areas quite well as seen in the mean backscatter strength over the sand area (Figure 5.2(a)). However, the variation of the corrected backscatter strength around the mean value is still dependent on the incidence angle, especially around the nadir. As discussed in the previous chapter, this is due to the relationship between the variance, parameters of the gamma distribution and the ratio of the insonification and footprint areas. This remaining angular dependence can be suppressed after gridding the resulting backscatter strength data, which is similar to low-pass spatial filtration and demonstrated in Figure 5.2(b). Data after correction (c) had been applied were gridded to 1, 2 and 5m and the median value in each cell was used. The standard deviation of the gridded backscatter strength across track for the area of sand is shown in Figure 5.2(b). The increase in grid size

suppresses the angular dependence. A grid size of 5m is large enough to completely suppress all remaining trends in data. However, gridding data at large cell size smooths backscatter images and hence fine features of the seafloor can disappear from backscatter images.

The final approach considered, correction (d), was developed by the candiadate and was first presented in Parnum *et al.* (2006). It is similar to correction (c) as it uses a moving window to derive the mean angular trend and remove it from the data. In addition, correction (d) normalises the residuals by the standard deviation of backscatter strength within the sampling window measured at the same angle as the data being corrected. Then, like correction (c), the mean backscatter strength measured within the sampling window at 30º is added to the angularly equalized backscatter strength. This is shown by Equation (5.4):

$$BScor(X,Y,\theta) = \left(\frac{BS(X,Y,\theta) - \overline{BS}(X,Y,\theta)}{BSstd(X,Y,\theta)} \right) + \overline{BS}(X,Y,30^{\circ}) \qquad (5.4)$$

where: $BSstd(X,Y,\theta)$ is the standard deviation of backscatter collected at angle θ in the sampling window. Correction (d) removes all angular dependence of backscatter strength in the image (Figure 5.1(e) and 5.2). However, this algorithm has problems at boundaries between habitats.

5.3 Visualising backscatter properties: Angle cubes

5.3.1 Methodology

The aim of producing backscatter strength mosaics and maps is to represent the changes in backscatter properties in the spatial domain. When surveying the seafloor with a MBS system, data is collected from parallel overlapping tracks from different incidence angles. Ideally data from each point in the grid would have been sampled within a range of incidence angles, but this is logistically uneconomical. However, using spatial interpolation, the angular dependence of backscatter can be approximately reconstructed at each point of the grid, which can then be visualized as an angular cube and used for seafloor segmentation. This is the principle behind the method presented in this section, the result of which is referred to as an angle cube. An angle cube can be thought of as analogous to a hyperspectral cube (Richards & Jia 1999).

The overall process of creating an angle cube is shown in Figure 5.3, using 4 MBS lines from north of Thomas Island in Esperance Bay, Western Australia. In the first step, all the MBS backscatter strength data from the survey area are represented as a function of 3 dimensions: spatial coordinates X and Y, and the incidence angle, which produces a 3-dimensional sparse array of data. The amount of overlap between survey lines and grid cell size will determine how sparse the array will be. A larger overlap between lines will produce a less sparse array and hence more accurate interpolation. Then data in each angle layer are interpolated into each node of the X-Y spatial grid, producing a 3-dimensional matrix, or angle cube. Of the commonly used interpolation techniques, kriging (Burroughs & McDonnell 1998) was found to give satisfactory results; as the predicted values did not reveal any unrealistic values.

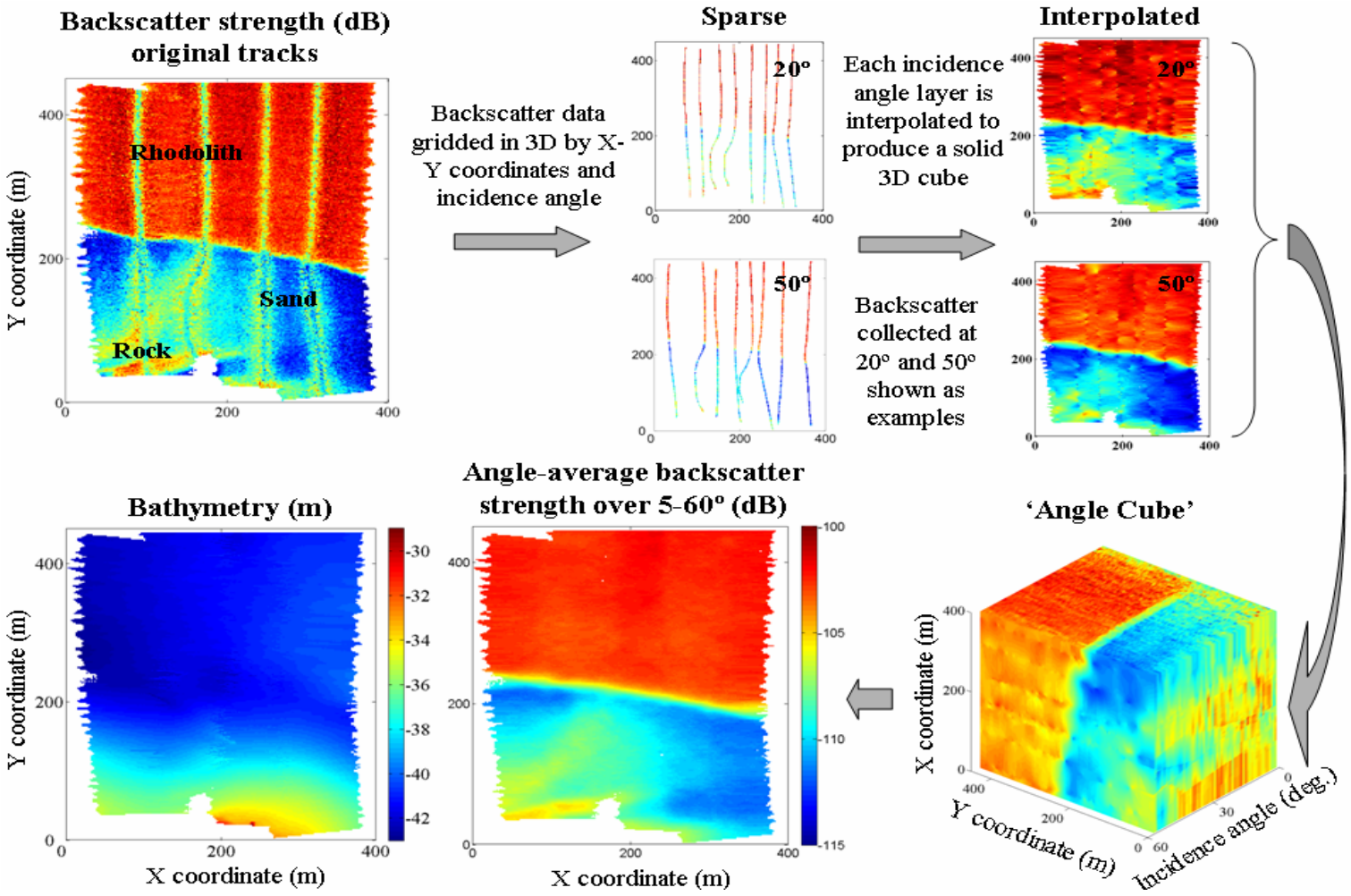

Figure 5.3: The production of an angle cube (2m x 2m x 1˚), and the resulting angle-average backscatter strength over 5-60° (dB) compared to the bathymetry (m). Data from a MBS survey north of Thomas Island in Esperance Bay, Western Australia.

The angle cubes can be used to extract and visualise spatial trends in the angular dependence properties for either the entire angular range or for different angular regions. The example in Figure 5.3 shows the angle-average backscatter strength over 5-60˚. The resulting backscatter image shows the spatial distribution of the seafloor habitats (sand, rhodolith and rock) not observed in the bathymetry alone. The mean backscatter image shown in Figure 5.3 can be compared with the results of using the methods described in the previous section. Corrections (a)-(d) were applied to the same dataset used in Figure 5.3, then data were gridded to 2m (Figure 5.4). Using the angle cube method, the resulting backscatter image (Figure 5.3) is free of the angular artefacts present in the original tracks. Whereas, the imperfections of the angular dependence corrections are noticeable, especially in corrections (a) and (b).

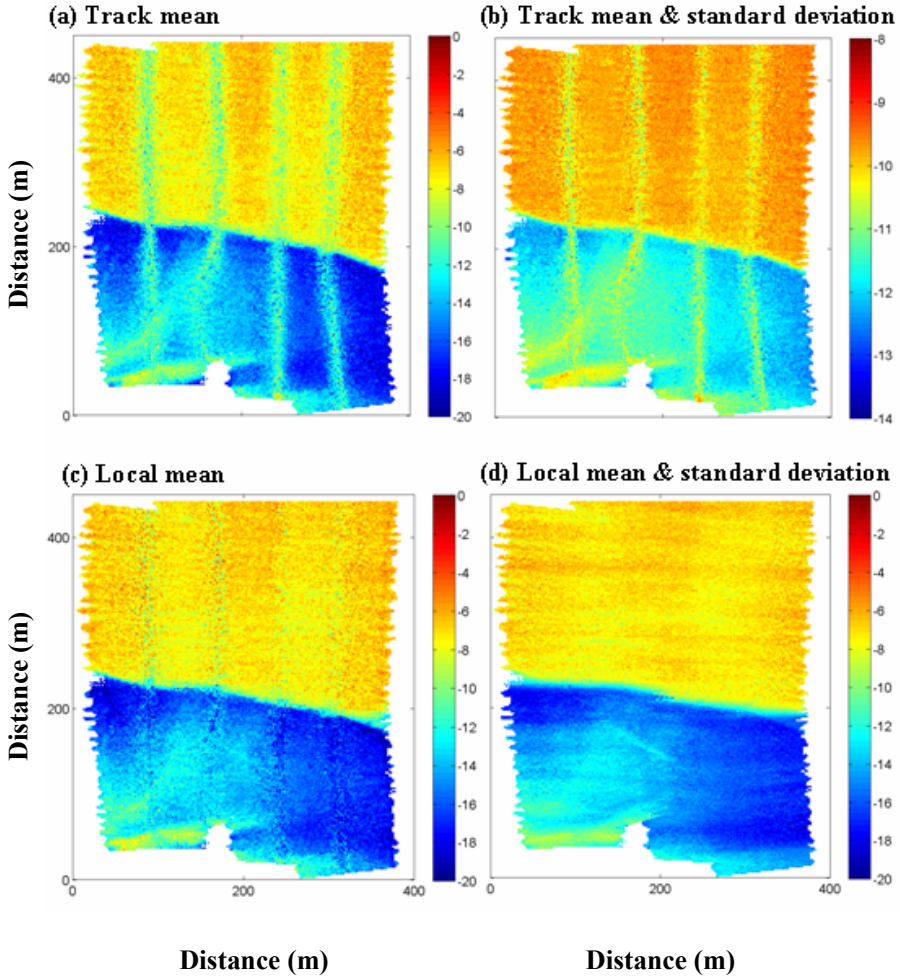

Figure 5.4: The results of applying four methods of angular correction to 4 lines of backscatter strength data (dB) with subsequent gridding to 2m. Data were collected north of Thomas Island in Esperance Bay, Western Australia.

Any properties derived from the angle cube will represent general trends and could possibly miss or smooth some small features due to spatial interpolation. However, benthic habitat mapping is usually concerned with changes in the seascape on a relatively large scale (~km^2). Small features are better examined by direct observations, such as underwater video. To examine the appropriateness (or accuracy) of backscatter strength data represented by the angle cube, it is worth examining the effect of track spacing, grid size and interpolation algorithm on the results. This is the subject of the next section (5.3.2).

5.3.2 Track spacing, grid size, and interpolation algorithm

Increasing the overlap between track lines will improve results. This can be examined by removing tracks from a dataset and reprocessing as shown in Figure 5.5. Figure 5.5 also highlights the performance of triangular interpolation compared with the kriging algorithm. The triangular-based linear interpolation used here suffered problems at the edges of this dataset; some of the predicted values were unreasonable or in some cases values could not be predicted. As the edges usually make up a small percentage of a survey area, triangulation could be used with the edges trimmed appropriately. For the datasets analysed in this study, the kriging algorithm provided more accurate interpolation and better representation of seafloor backscatter properties, although some other methods of spatial interpolation would also be worth examining for different datasets.

The spacing of the spatial X-Y grid used to build the angle cube should reflect the resolution or density of the dataset. The minimum grid size is determined by various factors, including: the track spacing, vessel speed, depth, resolution of the system, etc. The distribution of the footprints over the survey areas is a useful starting point for estimating the minimum grid size. For instance, in the dataset shown in Figures 5.3-5.5 the footprint size ranged from about 0.4 m to 1.3 m with a median of about 0.7 m and the maximum separation between footprints was smaller than the maximum footprint size. Figure 5.6 shows the same dataset reprocessed for grid sizes 1, 5 and 10 m all with an angle bin size of 1°. The histograms of the number of samples for the angle layer at 30° are shown to give an indication of the number of samples used to estimate the mean value. Cells with no samples present are excluded from the graphs. Although the image of 1 m resolution looks reasonable, in the

majority of the cells the mean value was calculated from only 1 sample. While increasing the grid size allows statistics to be calculated from a greater sample number, large grid sizes can blur boundaries and smooth features, as seen for the grid size of 10 m (Figure 5.6).

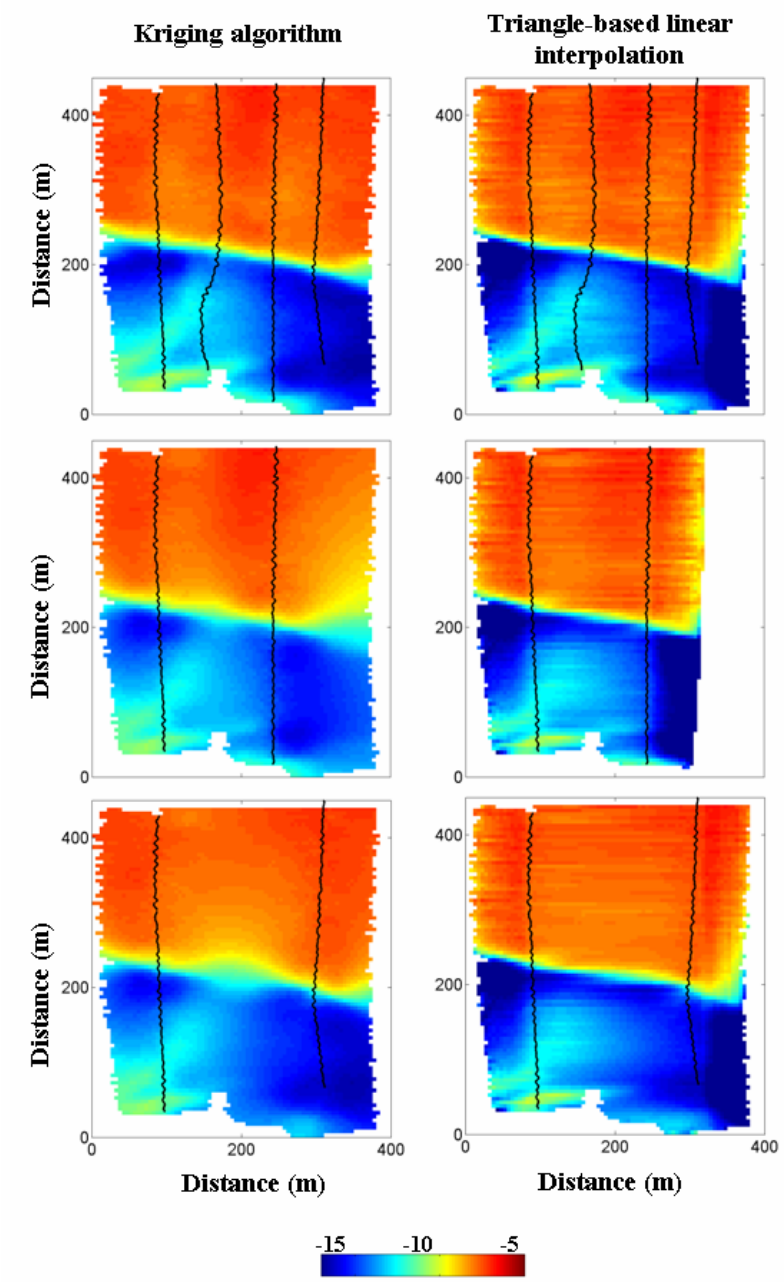

Figure 5.5: The effect of track spacing (ship's tracks shown in black) and interpolation algorithm on the angle-average backscatter strength over 5-60° (dB) for a 5 m grid size.

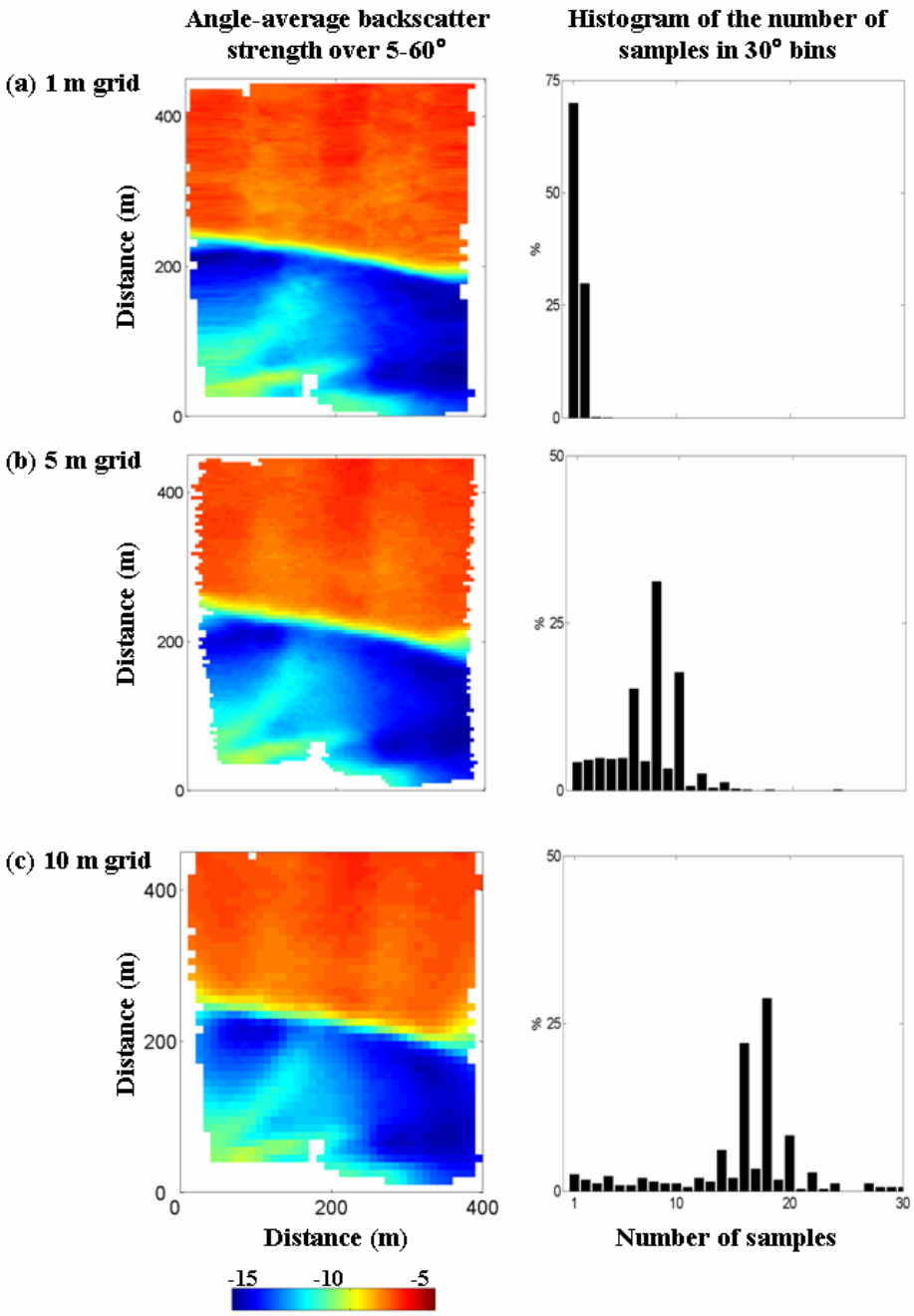

Figure 5.6: The effect of spatial grid size on the angle-average backscatter strength over 5-60° (dB) and the distribution of the number of samples in the 30° grid cells for (a) 1 m, (b) 5 m and (c) 10 m grid sizes (all for 1° angle bins). Cells with no values are omitted from the histograms.

In addition to the spatial grid size, selection of the angle bin size is also important. The resolution of the system will normally determine the minimum angle bin size, as it is irrational to choose an angle bin size less than the across-track beam width. So, a useful starting point is the maximum across-track beam width, e.g. for the Reson 8125 this is 1˚. Increasing the angle bin size will eventually add more angular artefacts to the image (Figure 5.7). For most of the examples used in this study, either 1˚ or 2˚ angle bin sizes were used.

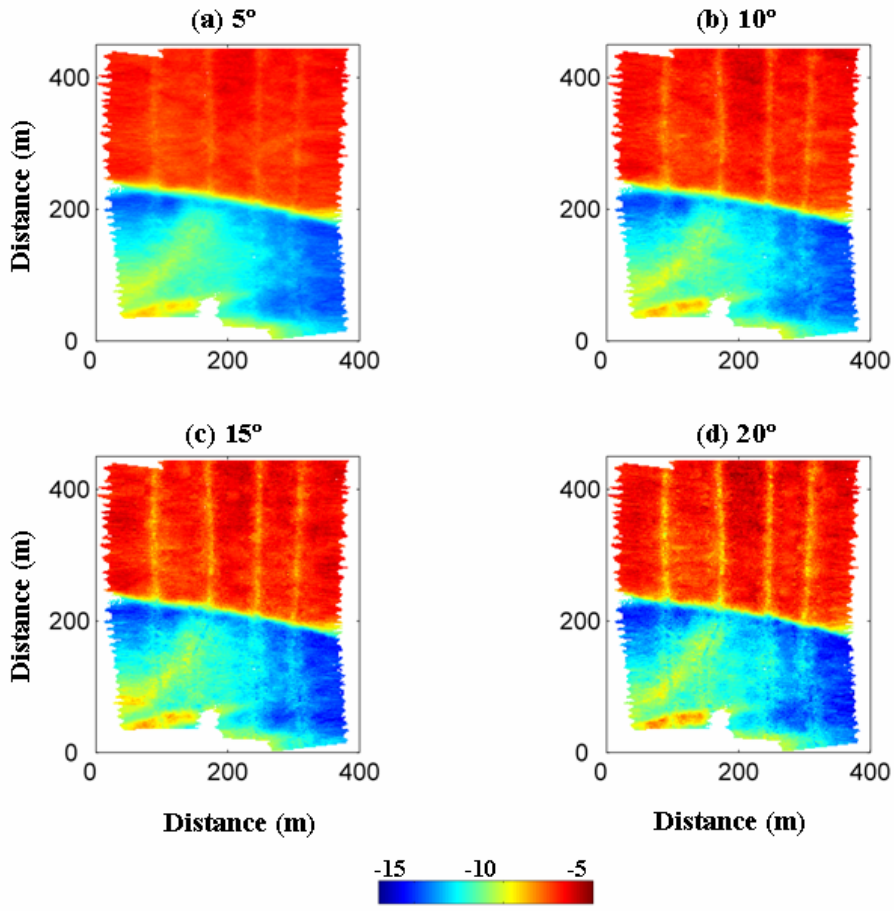

Figure 5.7: The effect of angle bin size used to create an image of angle-average backscatter strength over 5-60° (dB): data gridded to a 2 m grid and angle bin size of (a) 5, (b) 10, (c) 15 and (d) 20 degrees.

To demonstrate the usefulness and adaptability of the angle cubes, two case studies are presented. The first demonstrates the different useful acoustic properties that can be visualised. In the second case study, the angle cube method is applied to a dataset obtained with a different MBS system.

5.3.3 Case Study 1: Keppel Bay, Queensland

The usefulness of the angle cube method is further demonstrated on backscatter data collected from part of a survey of the Centre Banks region in Keppel Bay, Queensland. The MBS settings used and the map of track lines are shown in Appendix A. Using the methods described in Section 3.5, depth, seafloor coordinates X and Y, incidence angle and backscatter strength were derived for each beam and an angle cube was generated using a cell size of 2m x 2m x 1˚. The bathymetry of the study area is shown in Figure 5.8(a), which reveals the presence of large dunes. From the grab sample data there are three dominant sediment types: coarse sand that contains shell debris, muddy sand, and mud.

From the bathymetry alone it is not evident how the different sediment types are spatially distributed. This can be done by examining the backscatter properties. Firstly by plotting a two-dimensional histogram of mean backscatter strength versus incidence angle (i.e. a density plot) for the angle cube data, three distinct backscatter curves are revealed (Figure 5.8(d)) corresponding to the three sediment types. To visualise backscatter properties of these areas, either the average backscatter strength (Figure 5.8(b)) or the (linear) slope of its angular dependence (Figure 5.8(c)) at the oblique incidence angles can be used. The addition of these backscatter images allows further understanding of the sediment transport occurring in this area. For instance, the low average and steep slope of the mean backscatter strength show the deposition of mud to the left of the image, mainly on the shallow bank, and the accumulation of coarser sediment to the right side of the sand waves. The average and slope of the mean backscatter strength are strongly correlated, which agrees with the physical model for backscatter from sediments of different grain size.

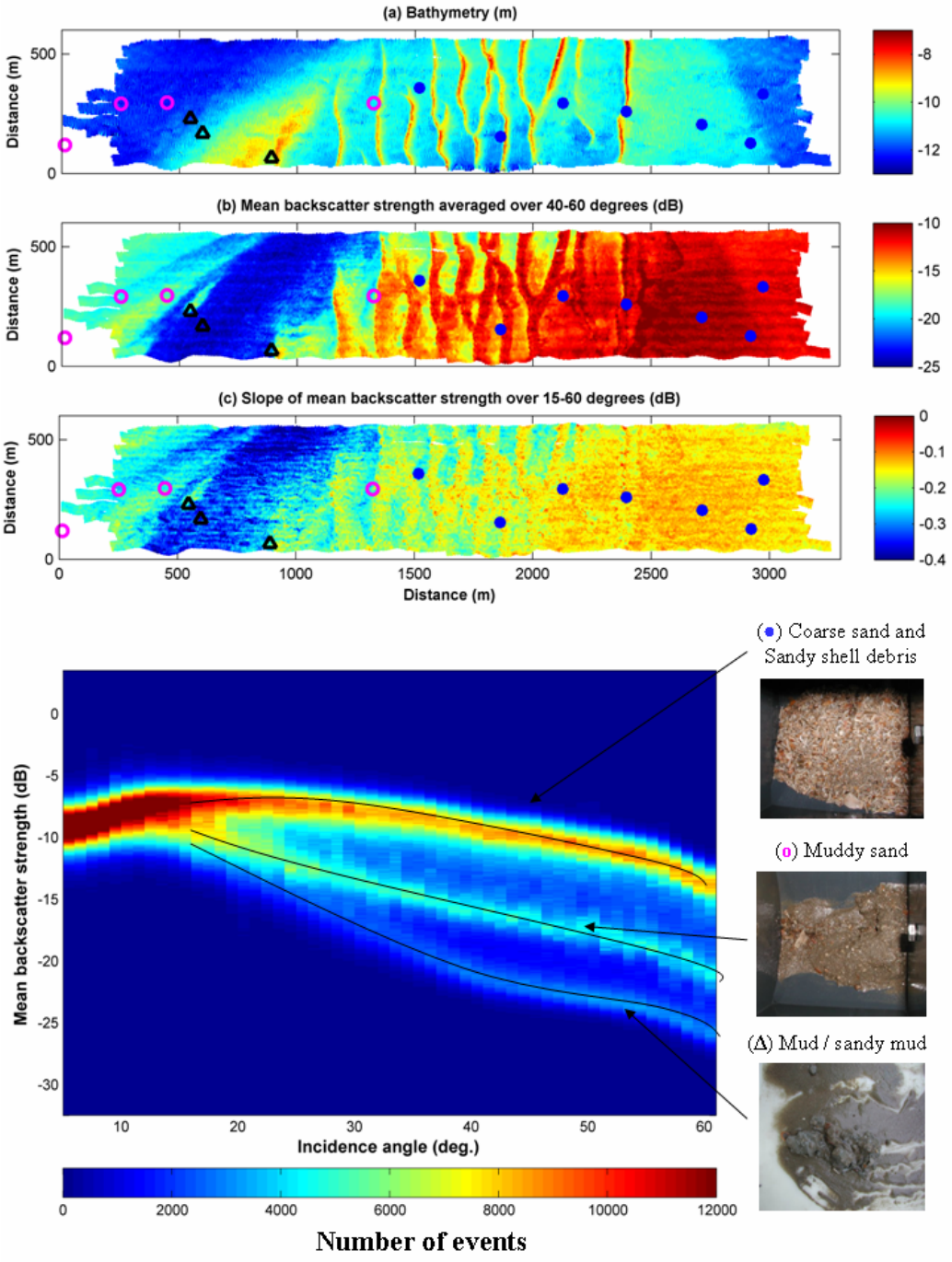

Figure 5.8: (a) Bathymetry, (b) average backscatter strength and (c) slope of its angular dependence with corresponding grab samples of sediment and (d) density plot of mean backscatter strength versus incidence angle using data collected in the Centre Banks area of Keppel Bay, Queensland.

5.3.4 Case Study 2: Marmion Marine Park, Western Australia

To test the robustness of the angle cube method as a means for backscatter analysis, a dataset obtained with a different MBS system was used. During 2004 and 2005, part of Marmion Marine Park (Western Australia) was surveyed by Fugro Survey Pty. Ltd. using a variety of MBS systems including a Reson Seabat 8101 (Kennedy 2005). The Reson 8101 system was not calibrated, so neither the system fixed gain was determined nor the relative sensitivity of the beams across track. Figure 5.9(a) shows an aerial photograph of the study area with the location of the track lines. Using the methods described in Chapter 3, seafloor coordinates X and Y, incidence angle and backscatter strength were derived for each beam and a angle cube was generated using a cell size of 2m x 2m x 2˚. The mean backscatter strength averaged over 5-80˚ is shown in Figure 5.9(b). Comparing the mean backscatter strength with the aerial photograph shows a good agreement with respect to the location of the rocky outcrops and bare sand as areas which are characterized by high and low backscatter strength respectively.

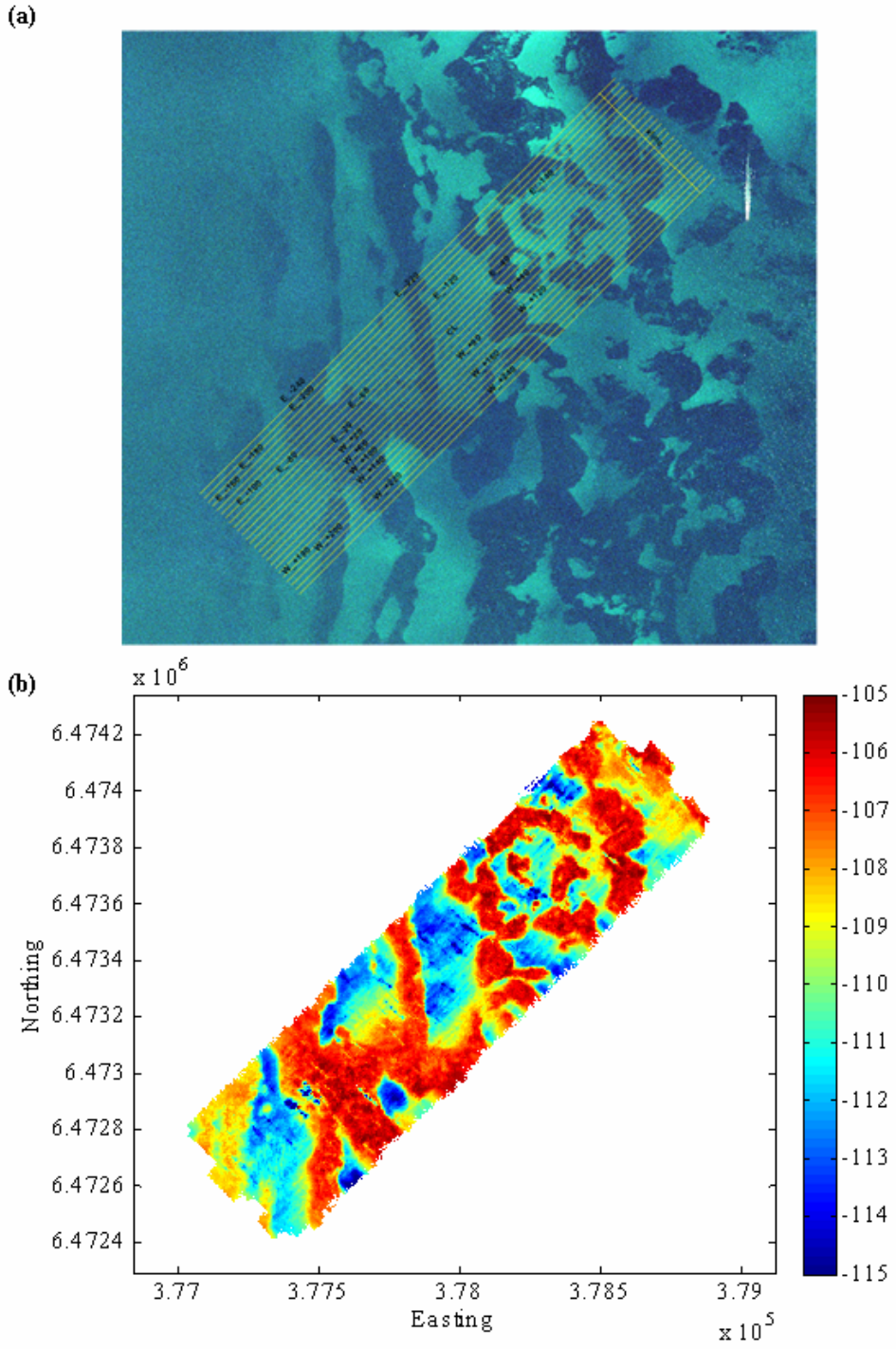

Figure 5.9: Marmion Marine Park, Western Australia survey: (a) aerial photo with MBS survey lines, (b) angle-average backscatter strength from 5 to 80˚ collected with Reson SeaBat 8101 (relative dB). UTM zone 50 south.

5.4 Seafloor classification using multibeam sonar data

5.4.1 Methodology

The overall classification methodology that was used in this study is shown in Figure 5.10. There are two main data products from a MBS survey: depth and backscatter strength. This study has focused on the development of utilising backscatter for seafloor classification. In this section, the angle cube method presented in the previous section will be used to classify the seafloor. Extracting key features from the angle cube can be done through either feature selection or feature reduction and is considered in the first part of this section. These key backscatter features combined with terrain feature(s) derived from the bathymetry data (where appropriate) can then be segmented through either unsupervised or supervised classification. In this section, these methods are described and applied to a case study from Esperance Bay, Western Australia.

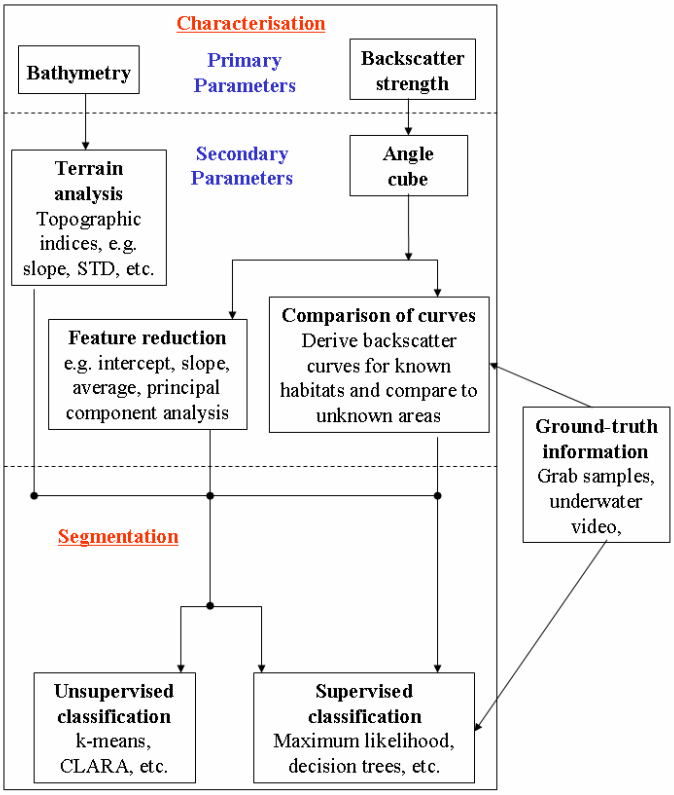

Figure 5.10: The process used in this study for seafloor classification using multibeam sonar data.

5.4.1.1 Extracting useful features of the backscatter strength versus incidence angle

Using the angle cube method gives an estimation of the mean backscatter strength at different angles of incidence for each X-Y location. Each of the angle layers in the angle cube can be considered as a feature. The majority of the datasets used for this study were collected with the Reson Seabat 8125 and were gridded within an angle range of 5-60º with 1º spacing, giving a total of 55 features. These 55 features could be directly segmented into statistically similar groups or used to determine the best fit to those features derived for known homogeneous seafloor areas (i.e. curve fitting). However, classification of data in high-dimension space has various problems (Duda, Hart & Stork. 2001). Hence, it was decided to reduce the number of features to the key properties, which can be done through feature selection or feature reduction.

Feature selection is the selection of individual features that characterise the backscatter properties of specific seafloor types in the most unambiguous way, e.g. the backscatter strength at 30º. Feature reduction is using a combination of features, e.g. the average value over 5-60º has already been shown in this chapter to be a useful property. Due to high correlation between the mean backscatter strength at different angles, feature reduction methods are recommended.

Feature reduction can either be based on physical parameters, such as the average value, intercept (at normal incidence) and slope of the angular dependence determined from linear regression, etc. or performed through multivariate statistics. Specifically, using linear orthogonal transformations can remove the redundancy in the dataset. Here two linear orthogonal transformations are examined (Duda, Hart & Stork. 2001):

- Principal component analysis (PCA)
- Linear discriminate analysis (LDA)

PCA transforms the data into a new coordinate system such that the greatest variance of the data is represented by the first coordinate (called the first principal component), the second greatest variance is along the second coordinate (called the second principal component), and so on. LDA finds the linear combinations of features that maximises the Fisher criterion (FC) (Equation 5.5) for each pair of

classes. Hence, the number of linear combinations will be equal to the number of classes minus 1. The resulting combinations may be used as a linear classifier or, more commonly, for dimensionality reduction before later used in classification. The main difference between the two methods is that PCA is an unsupervised method as it requires no knowledge about the dataset, whereas LDA requires data to be assigned classes to determine the linear combination that best separates pairs of classes. After reducing multiple features of the backscatter response at different angles to one or two feature combinations, those combinations can be used to segment the seafloor. Additionally, plotting the loading coefficients of each combination against the incidence angle can help determine the key acoustic properties.

$$FC = \frac{\mu_1 - \mu_2}{\sigma_1 + \sigma_2} \tag{5.5}$$

where μ_1 and σ_1 are the mean and standard deviation of the feature for class 1, and μ_2 and σ_2 are the mean and standard deviation of the feature for class 2. The FC was used to assess the discrimination ability of the different features or feature combinations in classification. A FC less than 2 means that values of this feature are not significantly different between the two classes being compared, whereas FC values greater than two indicate that the feature can be used to discriminate between the two classes. In this study, only backscatter feature combinations or derivatives were used, and are referred to simply as features. Ideally, the features being used for classification should not be correlated with each other. So the correlation coefficient was calculated for the set of features considered for classification.

5.4.1.2 Unsupervised and supervised classification

In supervised classification data from areas of known seafloor classes are used to derive statistics that represent those particular classes, and then either a probability or statistical distance to each class is calculated for all unknown seafloor areas. Unsupervised classification does not use any prior knowledge except the number of classes and segments data into statistically similar groups. The *classify* and *k-means* functions in the Matlab® Statistics Toolbox were used for supervised

and unsupervised classification respectively. The function *classify* fits a multivariate normal distribution function to the training data for each habitat class and then posterior probabilities of each class for each data point are calculated. The posterior probability is defined as the probability that the training group of habitat class *j* was the source of the *i*th sample observation, i.e. *Pr(training group j|obs i)*. The highest posterior probability is used to assign the *i*th observation to a habitat class. The *k*-means algorithm partitions the data into *k* clusters (i.e. number of classes determined by the user). The clusters are derived through an iterative partitioning that minimises the sum, over all clusters, of the within-cluster sums of point-to-cluster-centroid distances. The Mahalanobis distance measure (Duda, Hart & Stork. 2001) would have been preferred, but it was computationally too expensive, so the squared Euclidean distance (Duda, Hart & Stork. 2001) was used instead with feature data normalised by its standard deviation.

After data has been classified, contextual editing is usually beneficial to improve the overall classification accuracy (Mumby *et al.* 1998). Contextual editing is where areas that are obviously misclassified are reclassified into what class they are more likely to be based on knowledge of the area or habitat type. As contextual editing can be subjective, it is often better to follow a general rule that is based on certain prior assumptions and applied to the whole dataset. For example, depth thresholds can be established for seagrass and other types of marine vegetation.

Assessing the accuracy of classification of remotely sensed classes of objects is commonly done through a confusion matrix (Tso & Mather 2001). A confusion matrix is a table *n* x *n*, where *n* is the number of classes. The columns in a confusion matrix represent the test data and the rows represent the labels assigned by the classifier. The main diagonal entries of the confusion matrix represent the number of data given the same habitat class as the test and classifier, and these are considered to be correctly classified. The overall classification accuracy is calculated as the sum of the entries in the diagonal divided by the total number of samples (multiplied by 100). Other indices that can be obtained from the confusion matrix include the producer and user accuracy. For each habitat class *j*, the producer's accuracy is calculated by dividing the entry (*j*,*j*) by the sum of column *j* (multiplied by 100). The producer's accuracy is the proportion of the pixels in the test data that are correctly

recognised by the classifier. The user's accuracy is calculated by dividing the entry (*j*,*j*) by the sum of row *j* (multiplied by 100). The user's accuracy is the proportion of pixels identified by the classifier as belonging to class *j* that agree with the test data.

5.4.2 Case Study: Esperance Bay, Western Australia

5.4.2.1 Study area and methods

The methods discussed above are demonstrated on part of the dataset collected from the survey in Esperance Bay. The data comprise 12 transects between Woody and Thomas Islands. The details of the MBS settings and location of the track lines are given in Appendix A. Bathymetry and backscatter strength were calculated using the methods described in Chapter 3. An angle cube (as described in section 5.3) was produced using a grid size of 5m x 5m x 1º for the angle range 5 to 60º as there was insufficient data less than 5º and greater than 60º. Grab samples reveal two habitats, *sand* and *rhodolith*. Bedrock, referred to as *rock*, off both Thomas Island (lower left) and Woody Island (right) can be clearly identified from the bathymetry (Figure 5.11).

5.4.2.2 Analysis of backscatter features

The mean backscatter strength versus incidence angle is shown in two different ways in Figure 5.12. Figure 5.12(a) is a two-dimensional histogram, which identifies three distinct curves in the angular domain. The mean backscatter angular response for the three habitat classes, *sand*, *rhodolith* and *rock*, were extracted from the angle cube based on the locations of the grab samples (for *sand* and *rhodolith*) and terrain analysis of the bathymetry data for *rock* (Figure 5.11). It is evident from Figure 5.12 that these habitats constitute the three main acoustic classes in the dataset. Examination of the angular dependence curves shows they are well discriminated by their slope at angles from 5-40º and the mean value within 40-60 º. These backscatter features are shown with the bathymetry and terrain slope in Figure 5.11.

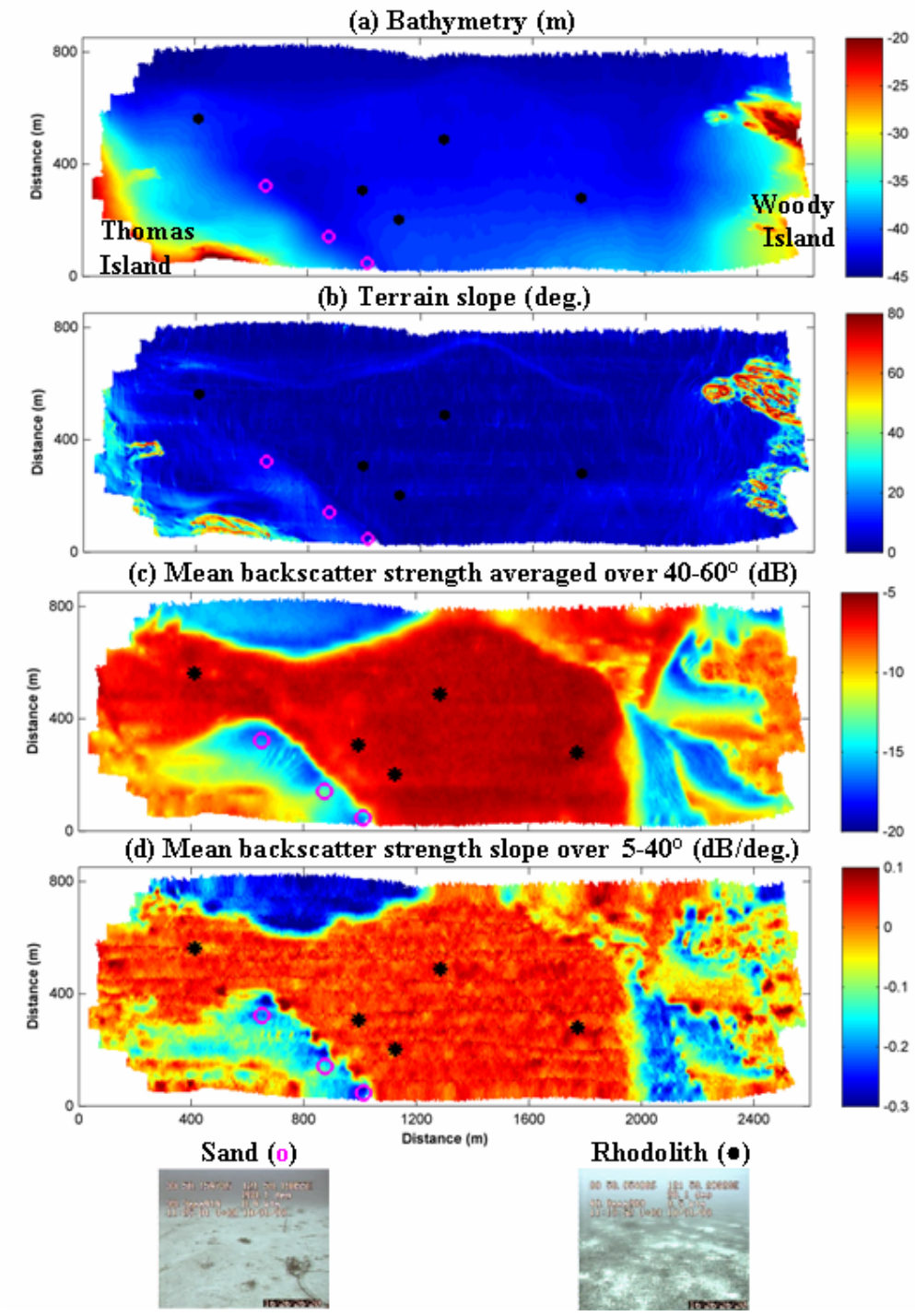

Figure 5.11: (a) Bathymetry, (b) terrain slope (deg.), (c) angle-average backscatter strength over 40-60° (dB) and (d) slope of the backscatter angular dependence over 5-40° (dB/deg.). Data comes from a MBS survey between Thomas and Woody Island in Esperance Bay, Western Australia.

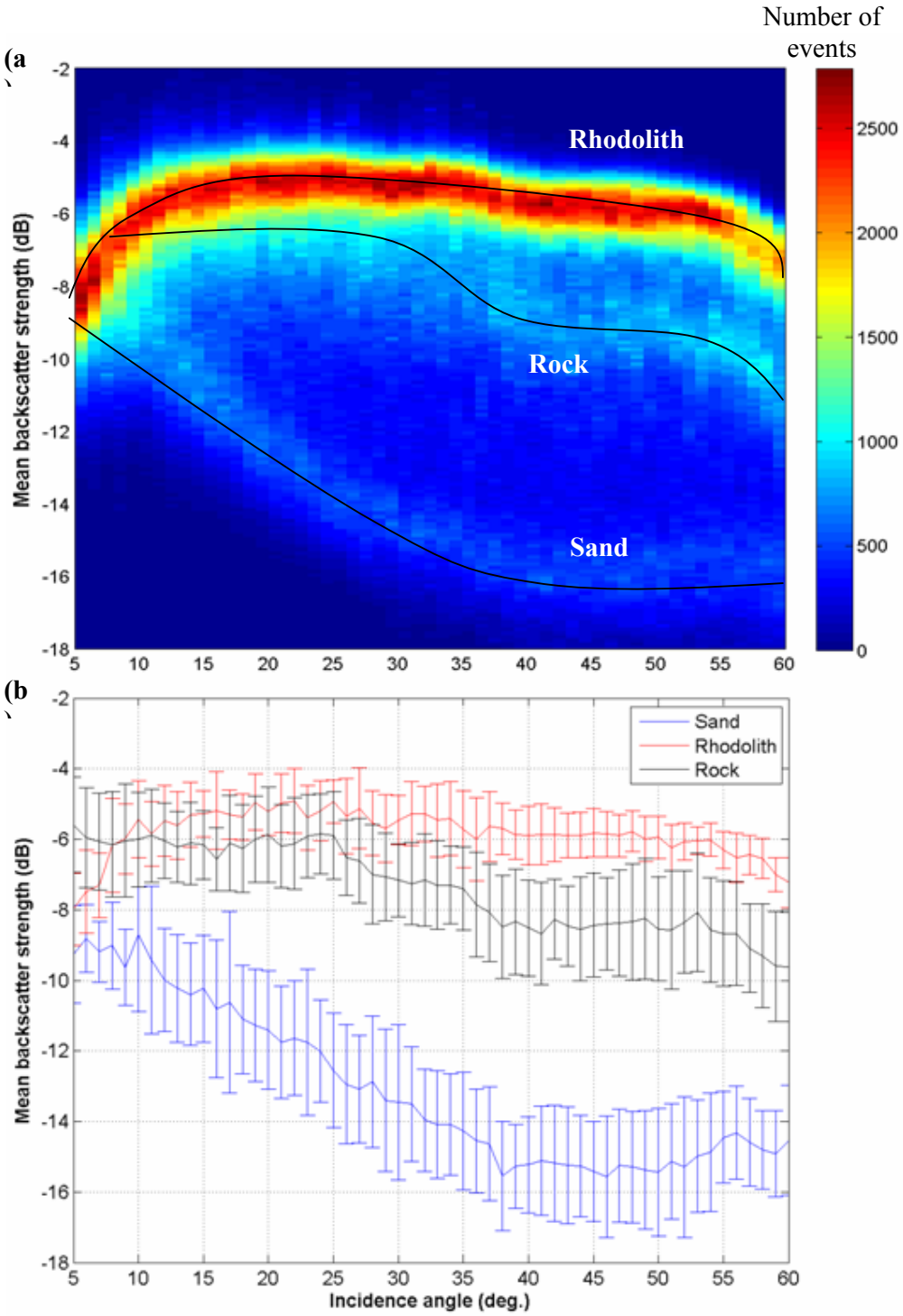

Figure 5.12: Mean backscatter strength (dB) versus incidence angle (deg.) for: (a) all data in the angle cube shown as a density plot (colour represents number of data points), and (b) areas of sand, rhodolith and rock habitats (error bars represent +/- one standard deviation). Data were gathered from part of a MBS survey between Thomas and Woody Islands in Esperance Bay, Western Australia.

.

Although the bathymetry (Figure 5.11(a)) and its slope (Figure 5.11(b)) can be used to identify areas of *rock* from the islands, neither parameter reflects the relative distributions of *sand* and *rhodolith*, whereas both the average backscatter strength (Figure 5.11 (c)) and slope of its angular dependence (Figure 5.11 (d)) clearly identify areas of *sand*, *rhodolith* and *rock*. As can be seen from the angular response curves (Figure 5.12), *sand* has the lowest average and steepest angular slope of mean backscatter strength and is readily distinguished from *rhodolith* and *rock*. The difference between *rhodolith* and *rock* is less clear, with *rhodolith* generally giving a higher average and flatter slope than *rock*. The mean value of the backscatter strength and slope of its angular dependence are correlated with each other. However, the mean backscatter strength provides a slightly better image, because the slope-based images are slightly noisier. This is an artefact of the interpolation process. It should be noted that the average and slope over all angles in the angle cube (5-60º) are just as useful as the selected angle ranges (Figure 5.13(a) and (b)).

PCA and LDA were applied to the angular dependence curves obtained through interpolation in the angle cube. The first and second principal components (PCs) derived from PCA of the interpolated angular dependences are shown on the area maps in Figure 5.13(c) and (d) respectively. In LDA, a training dataset was used to determine the linear combinations of parameters that best separates the three classes. The two combinations (LDA1 and LDA2) were applied to the whole angle cube and the sum of these combinations is shown in Figure 5.13(e) and (f). The loading coefficients for each incidence angle of the angle cube from LDA and for the first two PCs from PCA are shown in Figure 5.14.

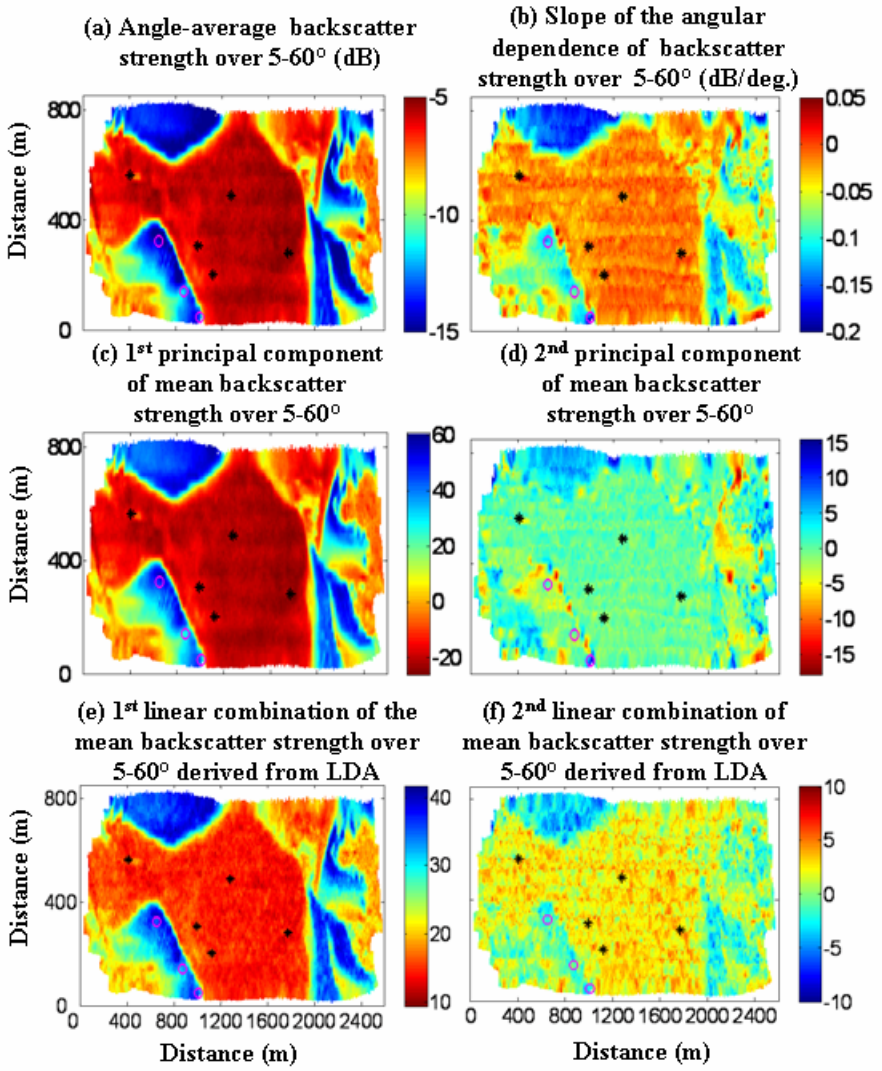

Figure 5.13: Results of analysis of the angle cube produced from backscatter data obtained from a MBS survey between Thomas and Woody Islands in Esperance Bay, Western Australia.

The 1st PC of PCA (Figure 5.13(c)) correlates strongly with the angle-average backscatter level (Table 5.1). The loading coefficients shown in Figure 5.14, indicate the 1st PC is equivalent to the angle-average backscatter level but with a slight weighting to the more oblique angles. The 1st PC represents about 90% of the variation. The loading coefficients versus incidence angle of the 2nd PC show it is the difference between the nadir and oblique angles (Figure 5.14). This would suggest the 2nd PC is similar to the slope of the mean angular response. This is supported by

examination of the images (Figure 5.13(e) and the correlation coefficient of 0.44 (Table 5.1). The 2nd PC represents about 3% of the variance in the data.

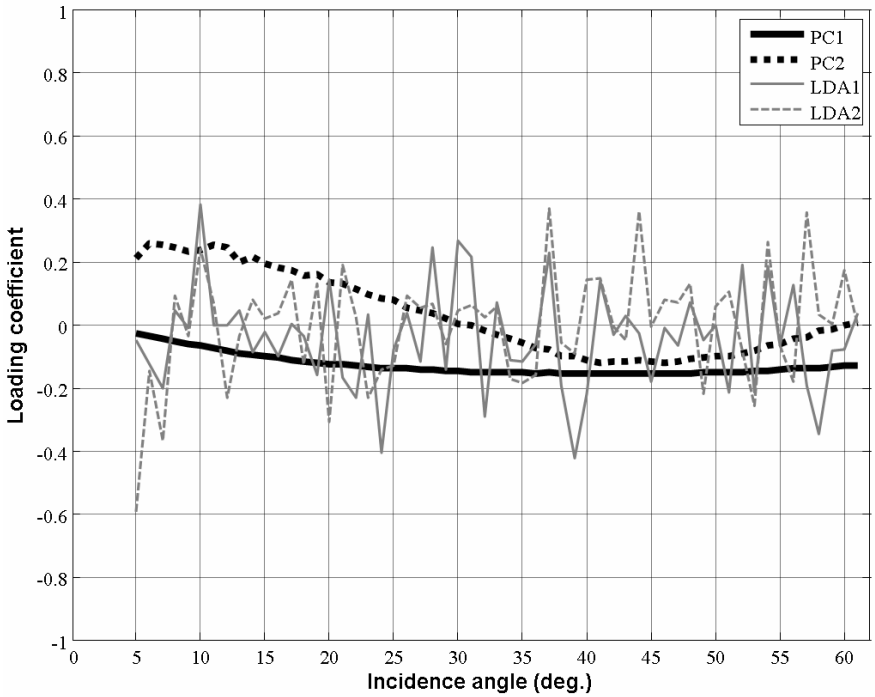

Figure 5.14: Loading coefficients from PCA and LDA of mean backscatter strength from MBS data collected between Thomas and Woody Islands in Esperance Bay, Western Australia.

As there were three classes identified, LDA gives two combinations (Figure 5.14). For the mean backscatter strength, the first LDA combination (LDA1) correlates with the angle-average value (Table 5.1). However, the variation in the loading coefficient (Figure 5.14(a)) results in the image being a little noisier than that of the average value or the 1st PC (Figure 5.13(e)). The second combination derived from LDA seems to correlate mainly with the slope (Table 5.1). However, like the 1st combination, the variation in the 2nd combination of coefficients with incidence angle (Figure 5.14) makes the image appear noisier than that derived directly from the slope (Figure 5.13(f)).

5.4.2.3 Classification of features

Table 5.2 shows the FC calculated using the training data for all the features shown in Figures 5.11 and 5.13. In terms of separating the seafloor classes for the whole survey area, the most robust feature for this dataset is the angle-average backscatter strength (BS_{mean}). This can be either as the average over all angles (Figure 5.13(a)), a selected angle range (Figure 5.11(c)), or with specific loadings to certain angles (1st PC and LDA1). As *sand* was found to be relatively easily separated from *rhodolith* and *rock*, more consideration was given to maximising the separation between *rock* and *rhodolith*. Unsurprisingly the FC was greatest for the LDA linear combinations. However, the loading coefficients derived by LDA do not necessarily produce the most effective combination. This is because LDA is trying to optimise the separation of classes in the training data and can produce a combination that can be optimum for a specific dataset, but may not always be applicable to the whole survey area. This is apparent from the images resulting from LDA shown in Figure 5.13(e)-(f). Therefore, the mean backscatter strength averaged over 40-60° was chosen as the primary feature for classification.

The correlation coefficient calculated for different pairs of backscatter and terrain features (Table 5.1) was also examined in order to determine additional features that could be used. There were only two features that were not highly correlated with the angle-average backscatter strength over 40-60°, the 2nd PC of PCA and the terrain slope. The 2nd PC provides very little discrimination ability between the different habitat classes (Table 5.2), whereas, the terrain slope provided some reasonable discrimination of the *rock* from the *sand* and *rhodolith* classes (Table 5.2). Therefore, the angle-average backscatter strength over 40-60° and the terrain slope were finally used to classify and map the seafloor assuming these three classes to comprise the main habitats in the surveyed area. These two parameters are shown in feature space by a two dimensional histogram shown as a density plot in Figure 5.15. The different clusters of the *sand*, *rhodolith* and *rock* classes can be clearly identified.

Table 5.1: Matrix of correlation coefficients for different features derived from data collected from a MBS survey between Thomas and Woody Islands collected from of Esperance Bay, Western Australia. Where: Average is angle-average backscatter strength (dB); Slope is the angular dependence of backscatter strength (dB/deg.); PC1 and PC2 are the first and second principal components; LDA1 and LDA2 are first a second features derived from LDA; and, terrain slope (deg.).

Feature	*Average 5-60°*	*Average 40-60°*	*Slope 5-60°*	*Slope 5-40°*	*PC1*	*PC2*	*LDA1*	*LDA2*	*Terrain slope*
Average 5-60°	1.00	0.99	0.85	0.89	-1.00	0.04	-0.99	0.73	-0.06
Average 40-60°	0.99	1.00	0.90	0.90	-1.00	-0.05	-0.99	0.77	-0.08
Slope 5-60°	0.85	0.90	1.00	0.91	-0.86	-0.44	-0.86	0.85	-0.14
Slope 5-40°	0.89	0.90	0.91	1.00	-0.90	-0.35	-0.90	0.81	-0.08
PC1	-1.00	-1.00	-0.86	-0.90	1.00	-0.01	0.99	-0.74	0.06
PC2	0.04	-0.05	-0.44	-0.35	-0.01	1.00	-0.01	-0.38	0.11
LDA1	-0.99	-0.99	-0.86	-0.90	0.99	-0.01	1.00	-0.72	0.06
LDA2	0.73	0.77	0.85	0.81	-0.74	-0.38	-0.72	1.00	-0.19
Terrain slope	-0.06	-0.08	-0.14	-0.08	0.06	0.11	0.06	-0.19	1.00

Table 5.2: Fisher criterion for a variety of features derived from the angle cubes and the seafloor (terrain) slope from MBS data collected between Thomas and Woody Islands in Esperance Bay, Western Australia. See Table 5.1 for abbreviations. Highest values for each combination of habitat are shown in bold.

Feature	Fisher criterion		
	Rhodolith-Sand	*Rock-Sand*	*Rhodolith-Rock*
Average 5-60°	33.0	20.9	8.0
Average 40-60°	41.8	19.6	11.6
Slope 5-60°	11.9	1.9	5.5
Slope 5-40°	21.3	4.3	3.4
PC1	36.1	22.0	10.1
PC2	0.4	0.1	2.3
LDA1	**102.7**	**65.1**	12.2
LDA2	17.4	0.0	**13.8**
Terrain slope	3.1	3.8	4.7

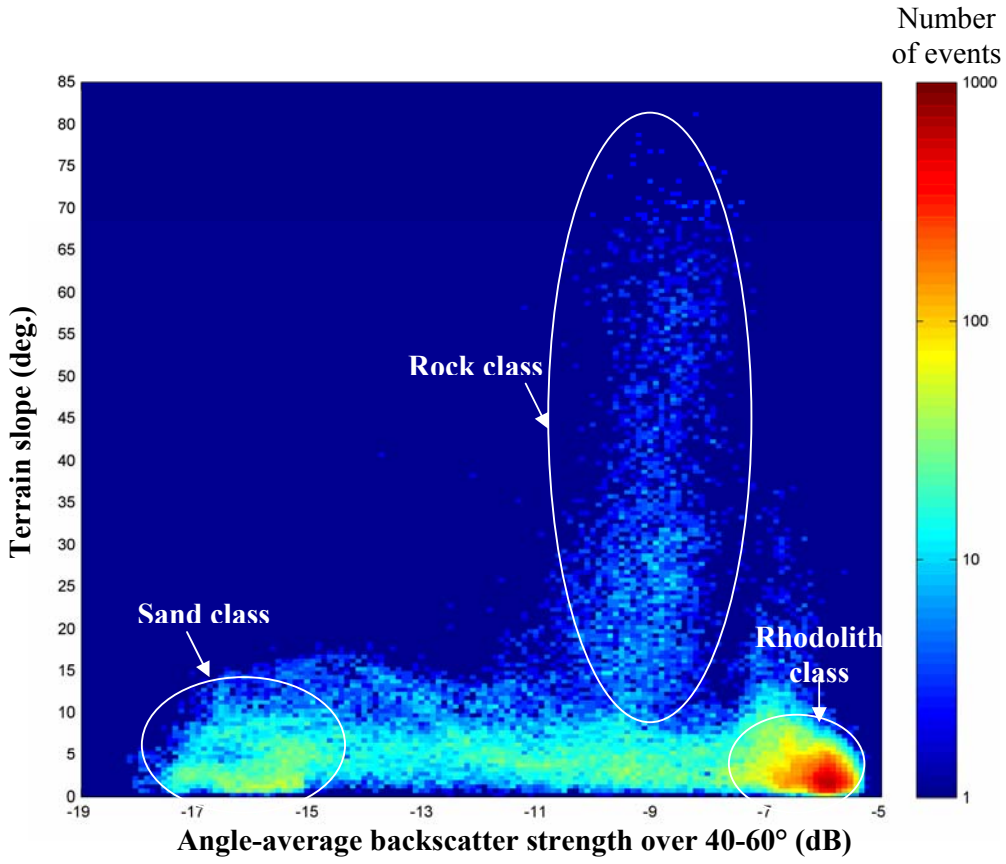

Figure 5.15: Two-dimensional histogram (colour displays number of samples) of the terrain slope (deg.) versus the angle-average backscatter strength over 40-60° (dB). Features derived from data collected from a MBS survey between Thomas and Woody Islands, Esperance Bay, Western Australia.

The results of supervised classification are shown in Figures 5.16-18. Figure 5.16 shows the scatter plot of data in feature space, highlighting the different classes and location of training data. Figure 5.17 shows the posterior probabilities of the *sand*, *rhodolith* and *rock* classes derived from the supervised classification. Figure 5.18 shows the hard classification maps resulting from supervised and unsupervised classification with and without contextual editing applied.

Overall the MBS data collected in this area have been well segmented by both classification methods, but there is still some misclassification between the *rhodolith* and *rock* classes. Unfortunately, there was insufficient ground-truth information for a comprehensive accuracy assessment. In the absence of ground-truth information for the whole area, confusion matrices of classification have been derived using the training data (shown in Tables 5.3 and 5.4). Supervised and unsupervised classification for the training data had an overall accuracy of 100% and 90% respectively. For the supervised classification (Figure 5.18 (a)), there appeared to be some misclassification along the boundaries between *sand* and *rhodolith* which were being classed as *rock*. However, this occurs to a lesser extent in the results of the *k*-means clustering. In contrast to supervised classification, the shallow water areas classified by the k-means clustering as *rhodolith* are more likely to be *rock* (Figure 5.18(c)). These results can be improved through contextual editing, using the rules that 1) the areas classified as *rock* and being deeper than 30m are to be identified as *rhodolith* and 2) the areas shallower than 30m and classified as *rhodolith* are to be identified as *rock* (Figures 5.18(b) and (d)). However, this is not a universal approach because contextual editing is somewhat subjective and should be applied with caution. Nevertheless, results of both the supervised and unsupervised methods demonstrate reasonable capability of classification.

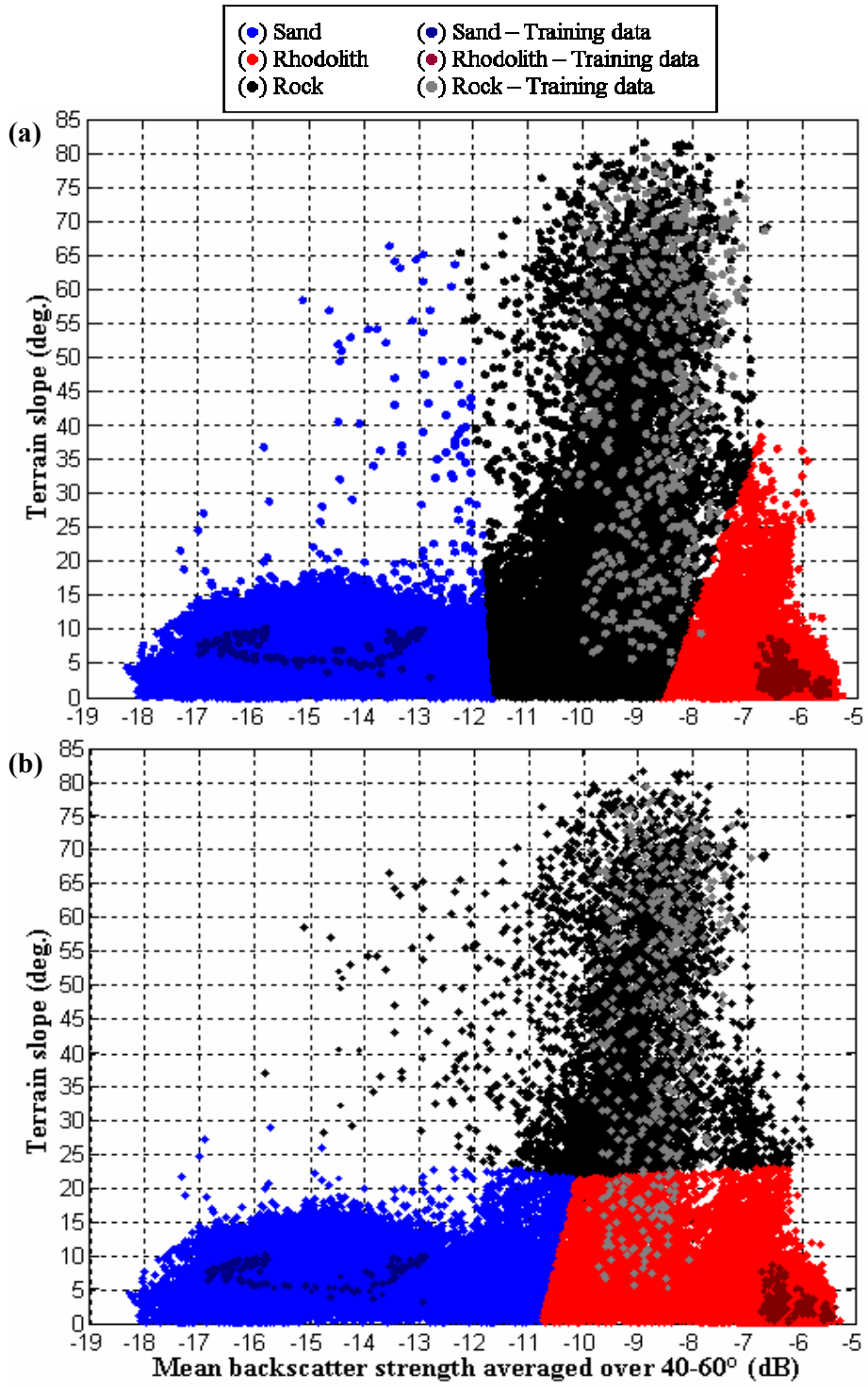

Figure 5.16: The terrain slope (deg.) versus the mean backscatter strength averaged over 40-60° (dB) for all data, segmented through (a) supervised and (b) unsupervised classification. Features derived from data collected from a MBS survey between Thomas and Woody Islands, Esperance Bay, Western Australia.

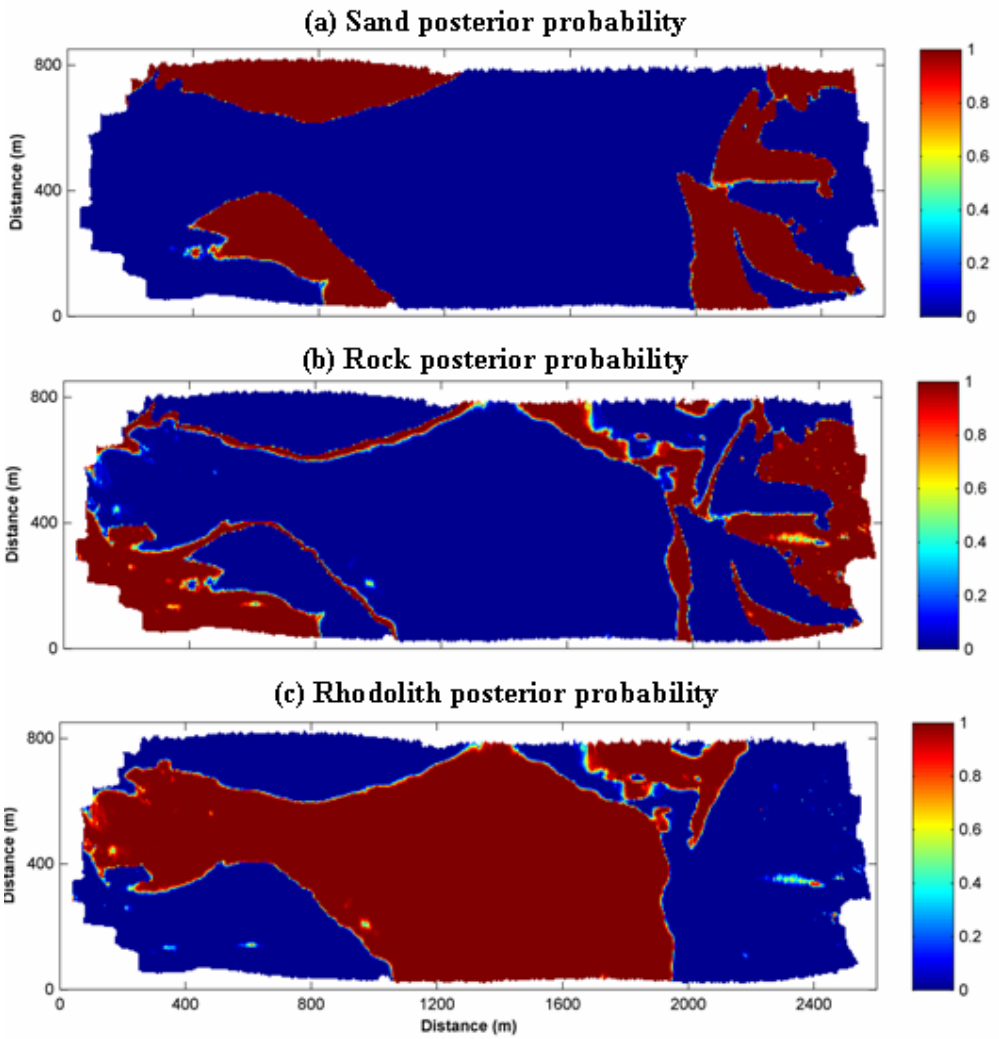

Figure 5.17: Posterior probabilities for (a) sand, (b) rock and (c) rhodolith classes determined through the multivariate probability density model derived from the training data. Based on features derived from data collected from a MBS survey between Thomas and Woody Islands, Esperance Bay, Western Australia.

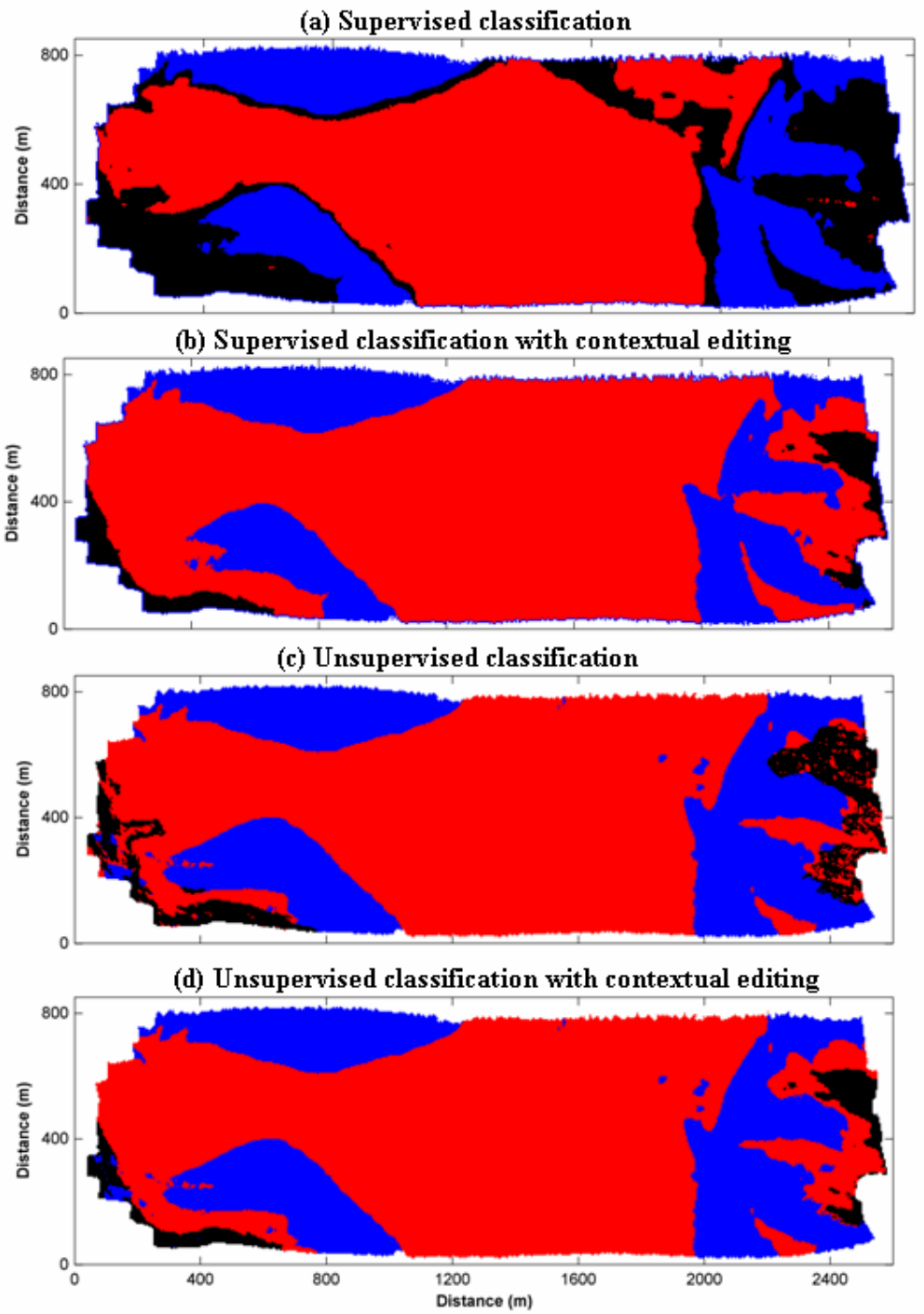

*Figure 5.18: Results of seafloor classification based on features derived from data collected from a MBS survey between Thomas and Woody Islands, Esperance Bay, Western Australia. Sand (**blue**), rhodolith (**red**) and rock (**black**) classes. Data segmented with (a) supervised classification; (b) same as (a) but after contextual editing, (c) k-means clustering and (d) same as (c) but after contextual editing.*

Table 5.3: Confusion matrix for the training dataset from results of supervised classification. Based on data collected from a MBS survey between Thomas and Woody Islands, Esperance Bay, Western Australia.

		Training data				
		Sand	Rhodolith	Rock	*Total*	*User Accuracy (%)*
Classifier	Sand	103	0	0	103	100
	Rhodolith	0	441	0	441	100
	Rock	0	0	180	180	100
	Total	103	441	180	724	
	Producer accuracy (%)	100	100	100		

Table 5.4: Confusion matrix for training data from results of unsupervised classification. Based on data collected from a MBS survey between Thomas and Woody Islands, Esperance Bay, Western Australia.

		Training data				
		Sand	Rhodolith	Rock	*Total*	*User Accuracy (%)*
Classifier	Sand	103	0	0	103	100
	Rhodolith	0	180	0	180	100
	Rock	0	75	366	441	83
	Total	103	255	366	724	
	Producer accuracy (%)	100	71	100		

5.5 Implications for benthic habitat mapping

This chapter has demonstrated new methods developed to analyse and visualise seafloor backscatter strength data collected by MBS systems and to use the backscatter data for seafloor classification. The process of benthic habitat assessment and mapping based on these methods of backscatter analysis involves the following steps:

1. Constructing an angle cube for the mean backscatter strength;
2. Using the angle cube to produce angular dependence curves for any known habitats and a two-dimensional histogram of all the data in the study area. This helps establish the likely number of acoustic classes and the key properties of the angular dependence curve.
3. Visualisation of useful backscatter properties in the spatial domain using the interpolated data (i.e. the angle cube), e.g. the mean backscatter strength.
4. Determination of useful classification features through Fisher's criterion and correlation analysis.
5. Segmentation of data through either supervised or unsupervised classification methods, with the application of contextual editing where appropriate.
6. Visualisation of results in the feature space and as classification maps.
7. Assessment of misclassification through a confusion matrix for survey areas where ground-truth data are available.

In the next chapter, these methods will be applied to the MBS data collected from different seafloor environments in four case studies conducted around the Australian coast.

CHAPTER 6

ANALYSIS OF MULTIBEAM SONAR DATA FROM DIFFERENT SEAFLOOR HABITATS

6.1 Overview

This chapter applies the methods developed in the previous chapters to four case studies from sites within the CWHM project. In addition to the analysis of backscatter data collected from different habitats, each site had specific questions to be addressed. For each case study, maps of acoustic backscatter properties are produced, which are independent of MBS system settings, environmental parameters and incidence angle. These maps are used to classify the seafloor into distinct habitat classes determined from ground-truth information. The overall aim of this chapter is to examine the ability and limitations of MBS in benthic habitat mapping studies, which is discussed at the end of the chapter. Some of the preliminary results have been presented by the author at conferences (Parnum, Gavrilov & Siwabessy 2007; Parnum *et al.* 2006).

6.2 Data description

The case studies include two temperate (Owen Anchorage and Esperance Bay) and two tropical (Moreton Bay and Morinda Shoal) sites, and cover a range of different benthic habitats (Table 6.1). The habitat classes were identified through either grab samples or towed video. This chapter starts with the simplest case of two classes (Owen Anchorage) before progressing to more complex examples, such as the environments found at Esperance Bay and Morinda Shoal.

Table 6.1: The case studies, their benthic habitats and angle cube cell size used in Chapter 6.

Site Name	Classes	Angle cube dimensions
Owen Anchorage	*Seagrass (Temperate), Muddy sand*	2m x 2m x 1º
Moreton Bay	*Seagrass (Tropical), Sand, Muddy sand*	4m x 4m x 1º
Morinda Shoal	*Coral Reef, Seagrass (Tropical), Sand,*	4m x 4m x 1º
Esperance Bay	*Rhodolith, Rock, Seagrass (Temperate), Sand*	5m x 5m x 1º

All MBS data was obtained using the Reson SeaBat 8125. Location of track lines and system settings can be found in Appendix A. The X-Y coordinates, incidence angle (deg.), depth (m) and backscatter strength (dB) were calculated using the methods outlined in Chapter 3. Angle cubes were generated for each site using the method outlined in Chapter 5. The cell sizes used to build the angle cubes were based on the density of MBS data collected and are listed in Table 6.1.

Analysis and classification of MBS data follows the process outlined in Sections 5.4 and 5.5. The slope of the angular dependence derived from linear regression, and angle-average backscatter strength were examined for their effectiveness in classification. The terrain slope was used to aid in discriminating high relief, such as *rock*. The Fisher criterion (FC) (Equation 5.5) was used to evaluate the discrimination ability of features. The FC values greater than 2 were considered to be large enough to discriminate between habitats. The chosen features were classified using supervised classification based on linear discriminate analysis and implemented in the Matlab *classify* routine. The algorithm produces posterior probabilities of each class and a hard classification. For the data collected in Owen Anchorage, unsupervised classification using the *k*-means clustering algorithm was also used for classification. Classification accuracy was assessed with the training areas using a confusion matrix. Contextual editing was employed to improve the accuracy of classification, where necessary. See Chapter 5 for more details on classification procedures.

6.3 Owen Anchorage, Western Australia

6.3.1 Site description

Owen Anchorage is a shallow coastal region located between the Perth mainland and Garden Island. Quantifying the change in distribution of *seagrass* is an important environmental management issue. From aerial photography, Kendrick *et al.* (2002) determined that *seagrass* coverage in the Perth region had declined by 77% since 1967, citing algal blooms related to nutrient loading from industries as the main possible reason. The study found that benthic features were difficult to resolve from aerial photographs at sea depths greater than 10m. Therefore, this case study was used to test

the ability of MBS to distinguish *seagrass* meadows from the surrounding bare sediment, *muddy sand,* in water deeper than 10m. The bare sediment was concluded to be *muddy sand* from nearby sediment samples (Skene *et al.* 2005).

6.3.2 Results

The plots of mean backscatter strength versus incidence angle in Figure 6.1 reveal three acoustically distinct classes of which the most abundant was identified as *muddy sand*. This class was characterised by significantly lower mean backscatter strength than the other, much sparser class identified as *seagrass*. The difference in the mean backscatter strength between *muddy sand* and *seagrass* was around 5 dB at 10º and 7 dB at 60º. The angle-average value and slope of the angular dependence are shown along with the bathymetry of the area in Figure 6.2. The angle-average backscatter strength over 5-60º (Figure 6.2(b)) clearly identifies *seagrass* patches on the bare sediment. This is also indicated by the FC values of 125 determined from the training data. The slope of the angular dependence of backscatter strength (Figure 6.2(c)) does not identify the *seagrass* patches as distinctively as the angle-average backscatter strength. For this parameter, the Fisher criterion for the training data was only 3. However, the slope of backscatter angular dependence adds some additional information regarding the presence of another acoustic class. This third acoustic class has a lower average and a steeper slope than both the *muddy sand* and *seagrass* classes. This can be seen more clearly in the density plot of the angle-average backscatter strength versus the slope of angular dependence (Figure 6.3). However, without further ground-truth information it is not possible to determine what type of seafloor this class represents.

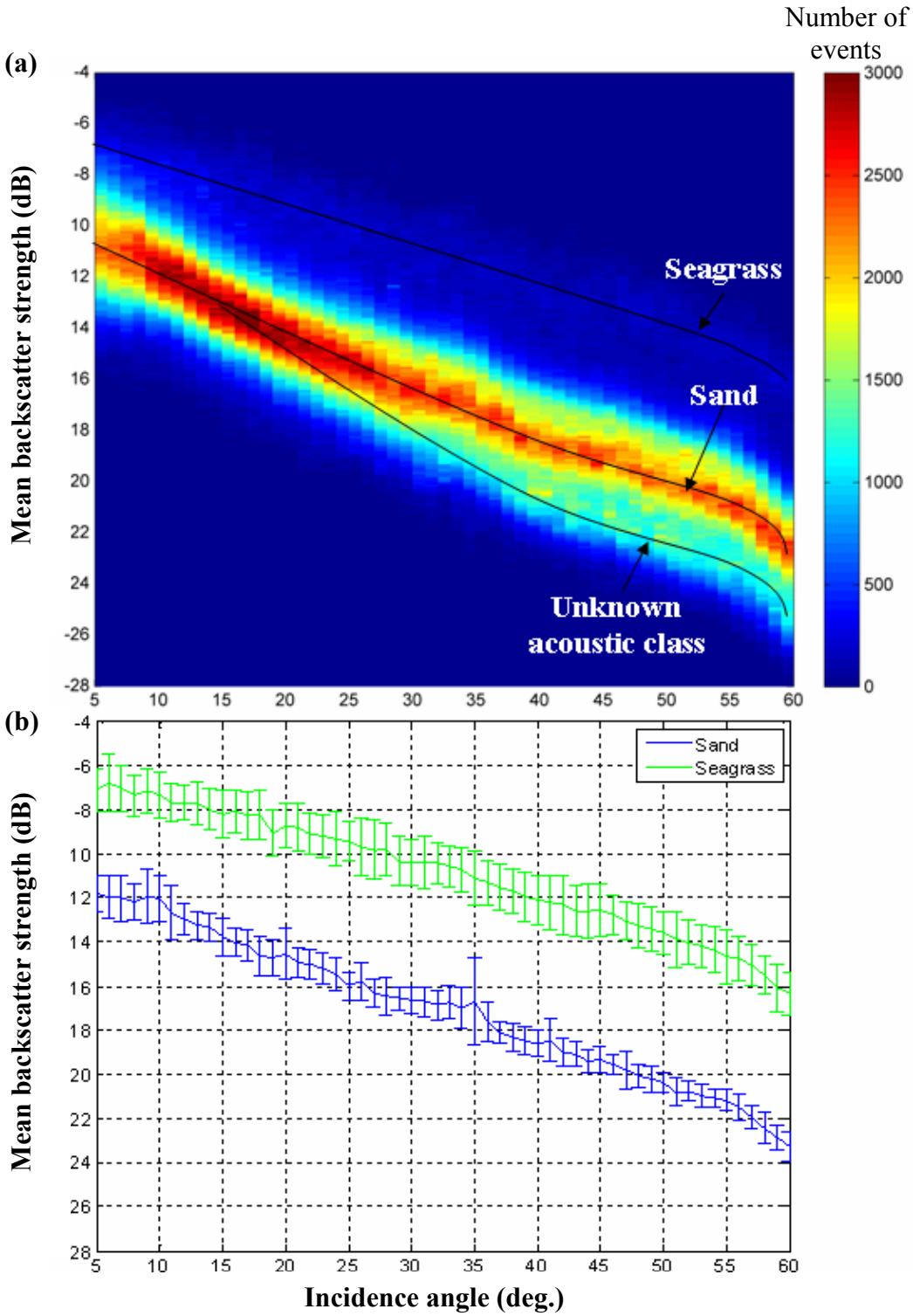

Figure 6.1: Mean backscatter strength (dB) versus incidence angle (deg.): (a) two-dimensional histogram for all of the data; and (b) the mean value for sand and seagrass found in Owen Anchorage (error bars show the standard deviation measured at different angles).

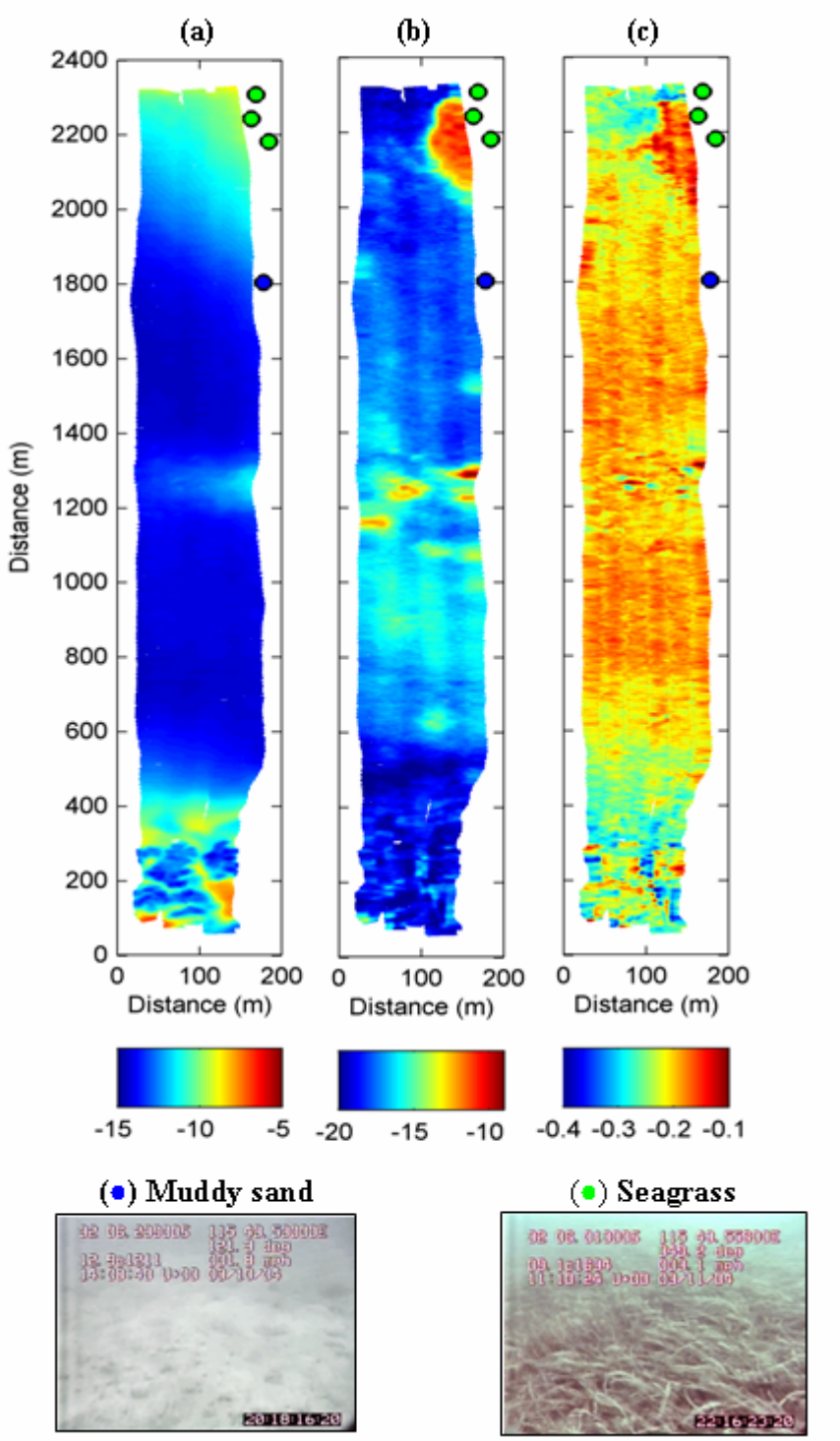

Figure 6.2: (a) Bathymetry (m), (b) angle-average (dB) and (c) slope of angular dependence (dB/deg.) of backscatter strength for incidence angles from 5 to 60°. Data from a MBS survey in Owen Anchorage, Western Australia. Representative still images from the towed video transects are also shown.

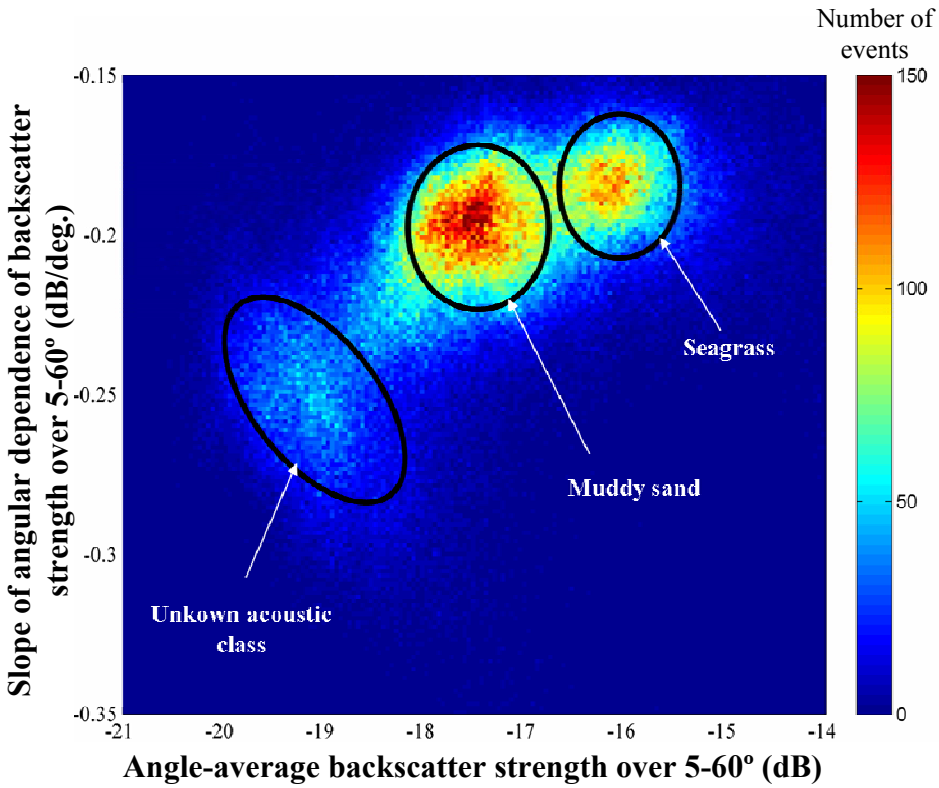

Figure 6.3: Two-dimension histogram of slope of the angular dependence (dB/deg.) versus angle-average backscatter strength (dB) over 5-60º incidence angles. Data from a MBS survey in Owen Anchorage, Western Australia.

Classification of the survey area in Owen Anchorage was done in two ways. Firstly, supervised classification using the linear multivariate model was used to produce a map of the distribution of *muddy sand* and *seagrass*. Secondly, an unsupervised classification was performed using the *k*-means clustering routine to segment the seafloor into three regions that aimed to represent the *muddy sand*, *seagrass* and the unknown acoustic class. For comparison, both classification routines were performed using the angle-average and slope of the backscatter strength. The results of classification are shown in feature space in Figure 6.4 and as maps in Figure 6.5. It is evident from Figure 6.4 that based on the training data the classification accuracy was 100%. Both the supervised and unsupervised classification maps clearly identify the *seagrass* patches (Figure 6.5). The unknown acoustic class is likely to be sediment of finer grain size or smoother surface than the *muddy sand* class, as it has a lower angle-average backscatter strength and steeper angular dependence.

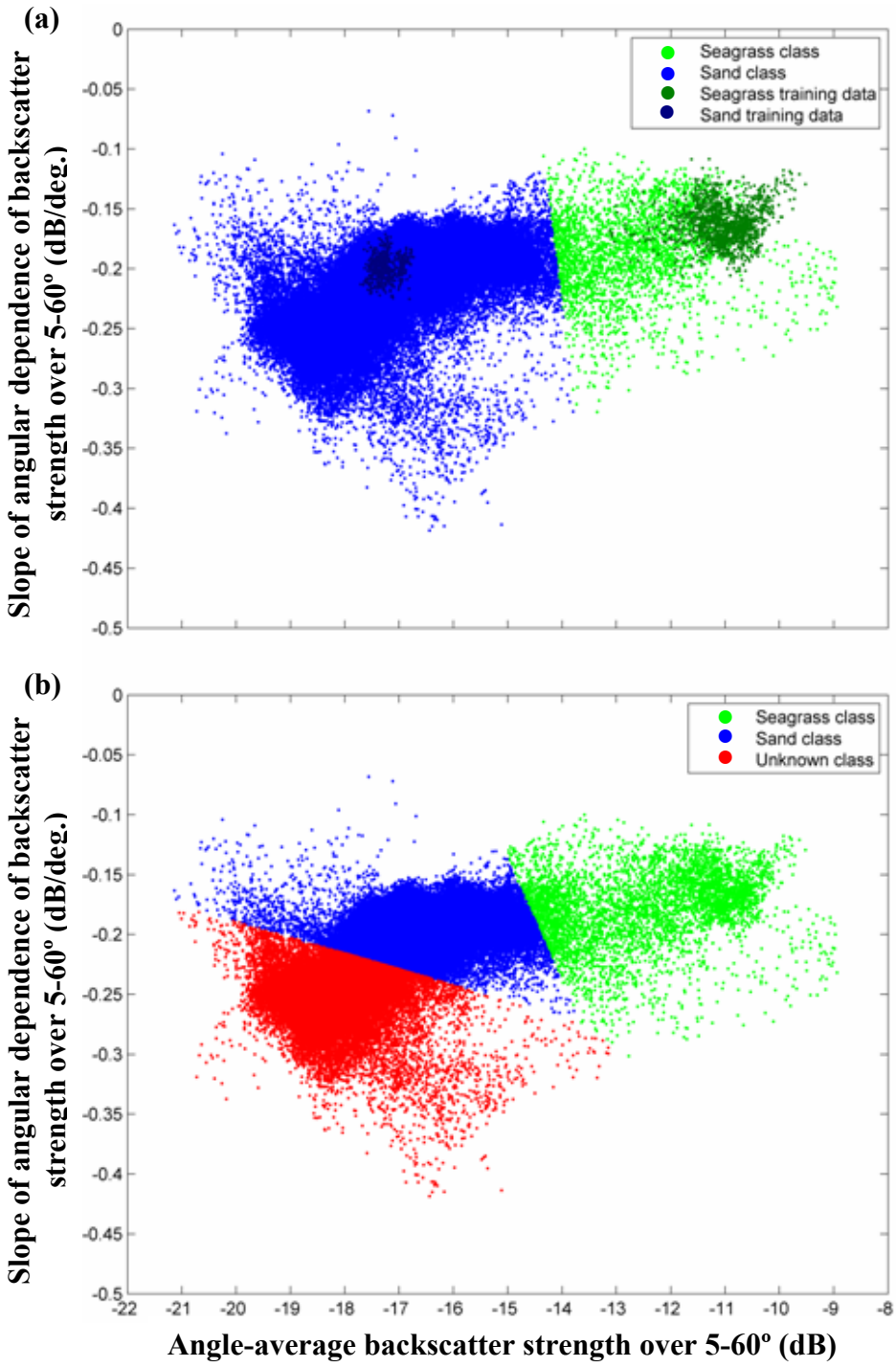

Figure 6.4: Slope of angular dependence (dB/deg.) versus angle-average (dB) of the mean backscatter strength over 5-60° incidence angles: (a) sand (●) and seagrass (●) classes determined by supervised classification (sand (●) and seagrass (●) training data also shown); (b) sand, seagrass and an unknown acoustic class (●) determined by k-means clustering. Data from a MBS survey in Owen Anchorage, Western Australia.

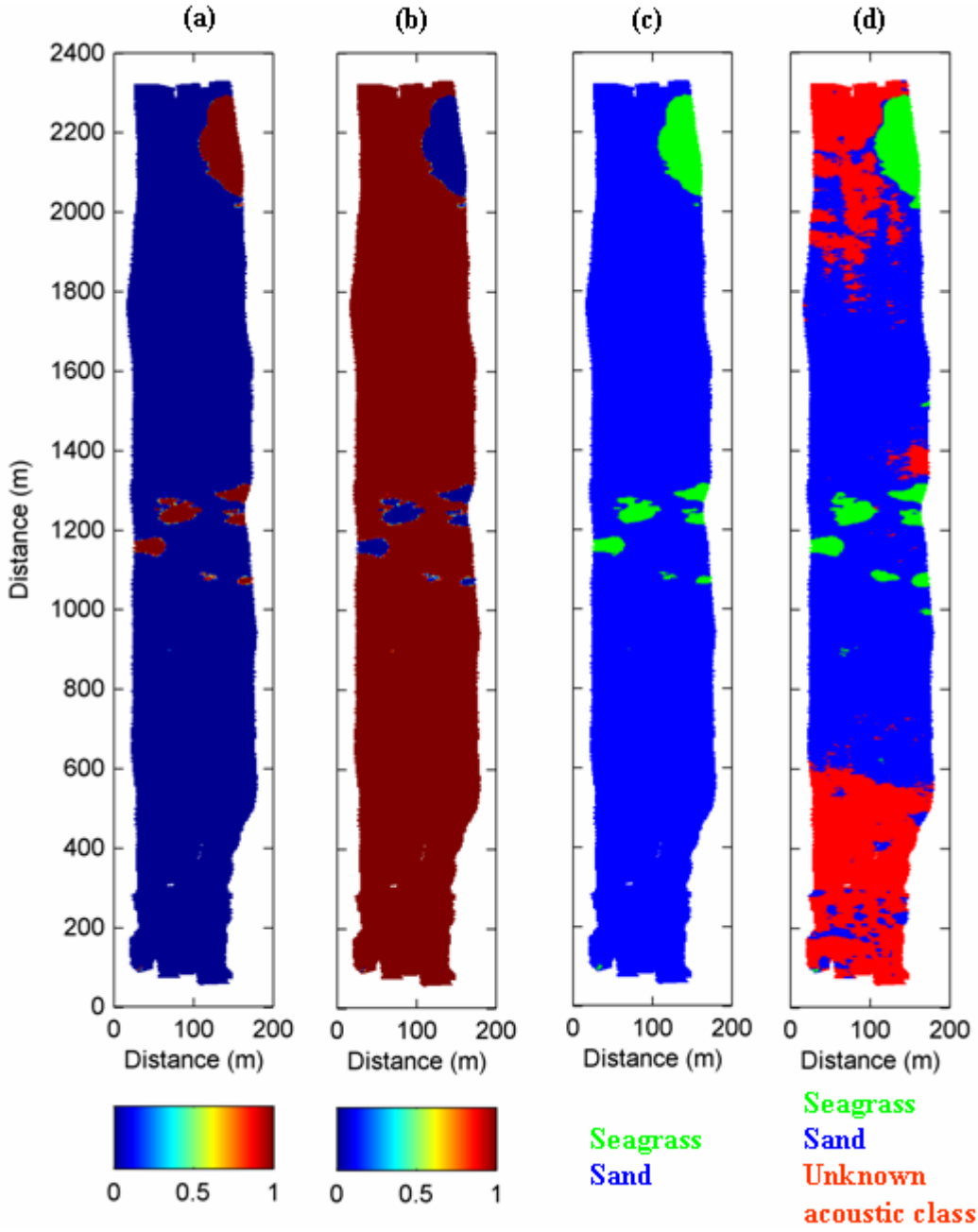

Figure 6.5: Results of seafloor classification from the MBS survey in Owen Anchorage, Western Australia: (a) seagrass and (b) sand class posterior probabilities; (c) class map derived from supervised classification using a linear multivariate normal density model; and (d) classification assigned by the k-means algorithm assuming the presence of an additional unknown class.

6.4 Moreton Bay, Queensland

6.4.1 Site description

Moreton Bay is one of the largest estuarine bays in Australia and was designated a Marine Park in 1993. Part of the conservation interest includes the large populations of turtles and dugongs. These populations feed on the *seagrass* meadows found in the bay, particularly on the pastures located in the Moreton Banks region on the east of the bay (Turner *et al.* 2004). Previous studies have shown that these meadows do not usually grow in areas where the water depth is greater than 12m (Udy & Levy 2002). Monitoring the extent of the *seagrass* meadows is an important aspect of the management of the Marine Park. Similar to Owen Anchorage, the objective of the survey in Moreton Bay was to examine whether *seagrass* could be distinguished from the surrounding bare sediment. It should be noted, that the tropical *seagrass* found in the Moreton Bay is much shorter and sparser than the temperate *seagrass* seen in Owen Anchorage. Also, in Owen Anchorage the bare sediment surrounding the *seagrass* was predominantly *muddy sand*, whereas around the Moreton Banks site there are two distinctive types of sediment present: *muddy sand* and a coarser medium *sand* (Harris *et al.* 1992). In this study, these two sediment classes were distinguished by their appearance on the video and by the ability of sediments to adhere to the towed video camera when it was dug into the seafloor. Sediment was classified as (cohesive) *muddy sand*, if it adhered to the video camera, and as (uncohesive) *sand*, if it did not adhere. The *sand* class also contained some intrusions of large particle size. The effect of an additional class of a coarser sediment (i.e. *sand*) on the effectiveness of distinguishing *seagrass* was also a focus of this case study.

6.4.2 Results

The backscatter strength versus incidence angle for the whole dataset (as a two-dimensional histogram represented by a density plot) and the angular dependence of the mean values for the different habitat classes are shown on the top and bottom panels of Figure 6.6 respectively. The *sand* class exhibits the strongest backscatter response, but it is only slightly higher than that from *seagrass*, which in turn is slightly higher than backscatter from the *muddy sand* sediment. The angle-average and slope of backscatter

strength within incidence angles from 5 to 60º were considered to be the most informative parameters. These parameters are shown alongside the bathymetry and towed video classification in Figure 6.7. Representative fragments of the along track video recordings with the respective values of depth and the angle-average and slope of the mean backscatter strength are shown in Figure 6.8. The transitions in the video classification between *muddy sand* and *sand* and *seagrass* correlate well with changes in the angle-average backscatter strength. The correlation is less strong with the slope of backscatter strength versus incidence angle. *Muddy sand* has the steepest slope among those classes. There are notable fluctuations in the value of the slope of backscatter angular dependence at transitions between habitats. This was likely a result of the interpolation process when creating the angle cube.

The FC values for the angle-average and angular slope of mean backscatter strength are shown in Table 6.2. The angle-average backscatter strength is the most robust parameter to discriminate between the different habitats. Although not as effective as the angle-average backscatter strength, the slope of the backscatter strength does discriminate the *seagrass* from the *muddy sand* (Figure 6.9(a)). As these two parameters were not correlated (correlation coefficient = 0.6), they were both used in supervised classification. The results of supervised classification are shown as separate clusters in feature space in Figure 6.9(b), as posterior probabilities maps for the *sand*, *seagrass* and *muddy sand* classes in Figure 6.10, and as class maps in Figure 6.11.

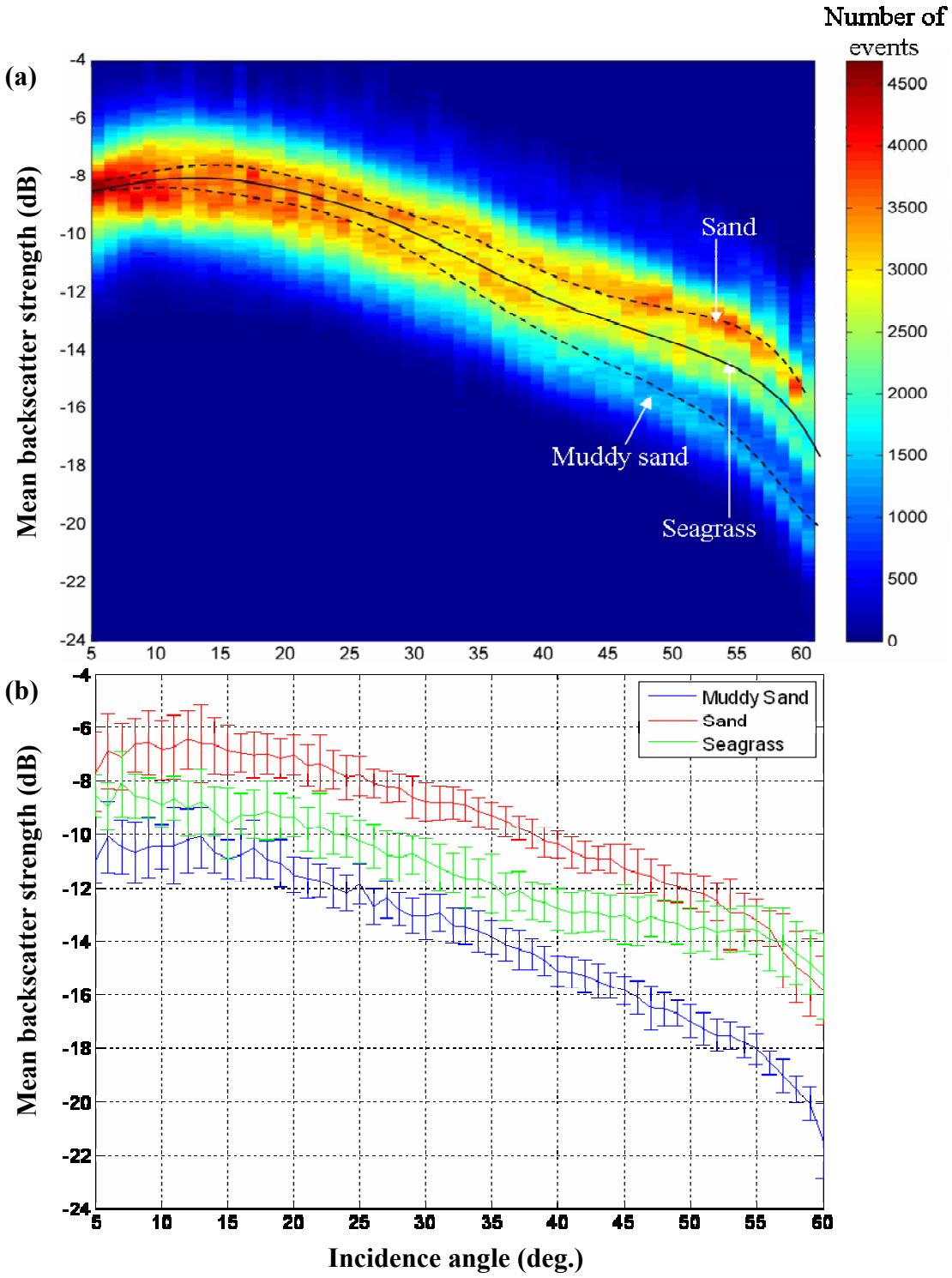

Figure 6.6: Mean backscatter strength (dB) versus incidence angle (deg.): (a) a two-dimensional histogram for all of the data and (b) for muddy sand, sand and seagrass found in Moreton Bay, Queensland (error bars show the standard deviation measured at different angles).

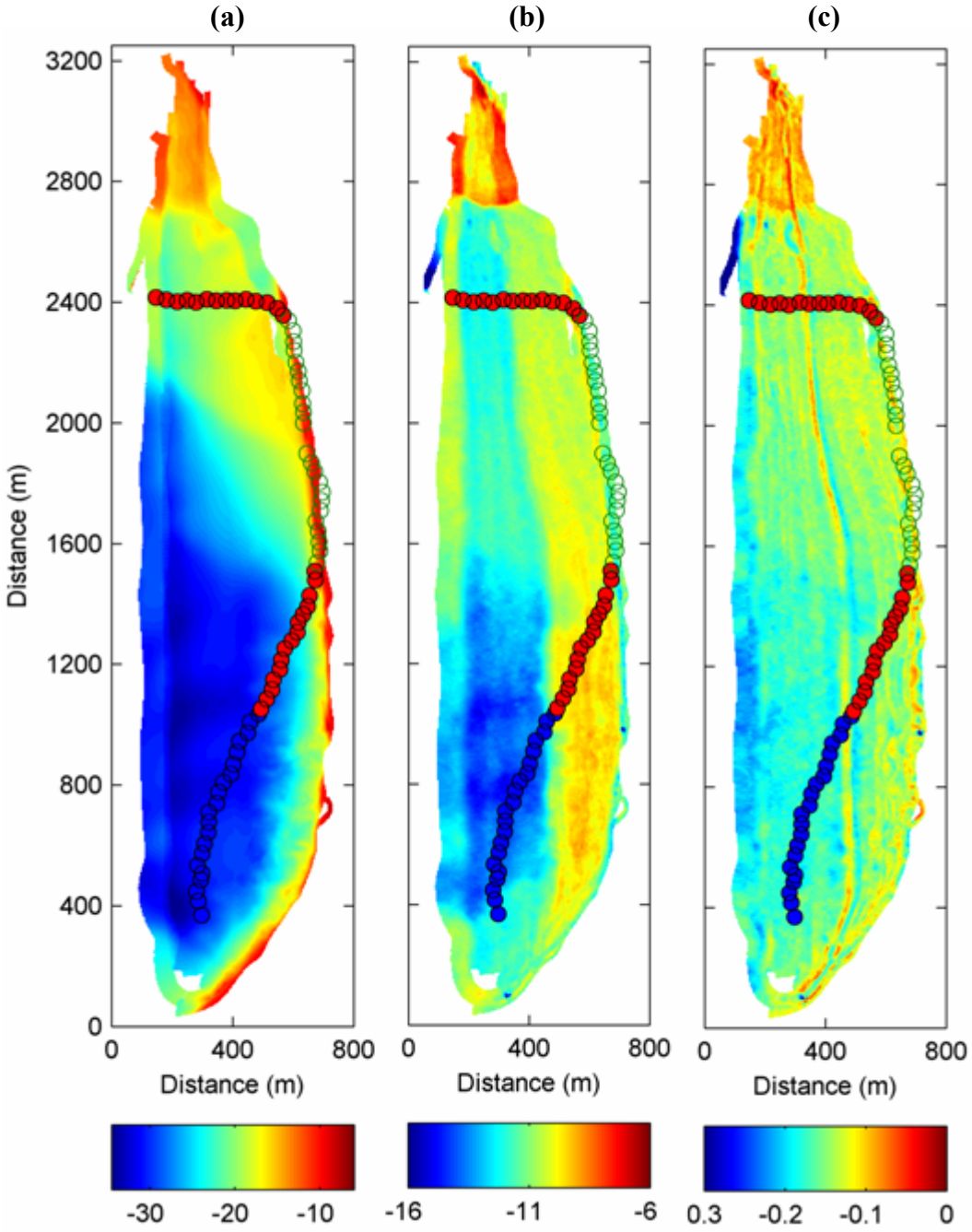

Figure 6.7: (a) Bathymetry (m), (b) angle-average (dB) and (c) slope of the angular dependence (dB/deg.) of backscatter strength over 5-60° from the MBS survey in Moreton Bay, Queensland. Circles represent seafloor classification based on towed video: muddy sand (●), sand (●) and seagrass (o).

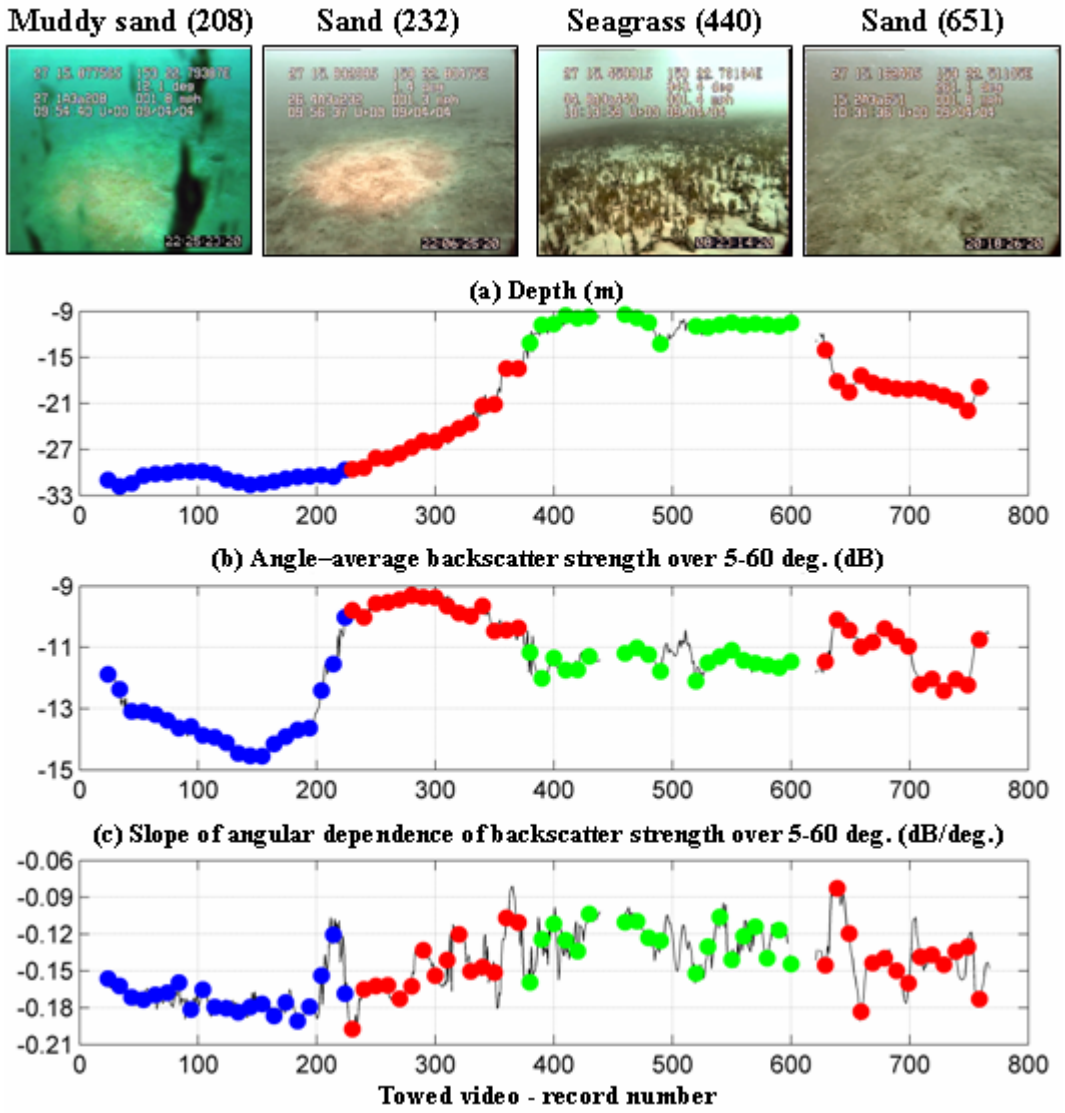

Figure 6.8: Seafloor acoustic features from MBS data along towed video tracks: (a) Depth (m); (b) angle-average (dB) and the (c) slope of angular dependence (dB/deg.) of backscatter strength (dB) over 5-60° from the MBS survey in Moreton Bay, Queensland. Video classification shown: muddy sand (●), sand (●) and seagrass (●). Still images from the underwater video labelled with record number and class assigned.

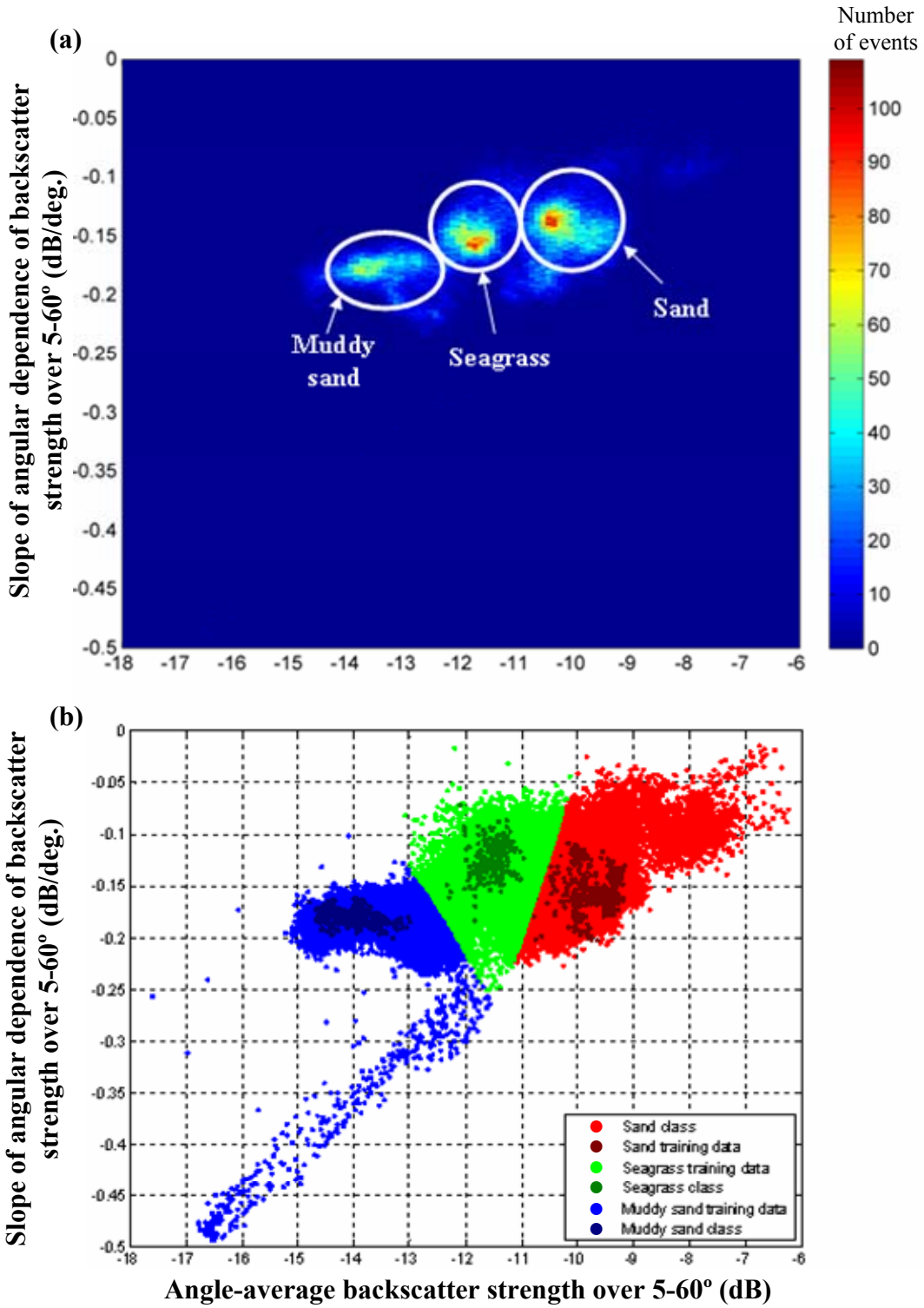

Figure 6.9: Feature space of the slope of angular dependence (dB/deg.) versus angle-average backscatter strength (dB): (a) two dimensional histogram and (b) scatter plot segmented by supervised classification into sand, seagrass and muddy sand classes with the training areas shown by darker dots. Data from a MBS survey in Moreton Bay, Queensland.

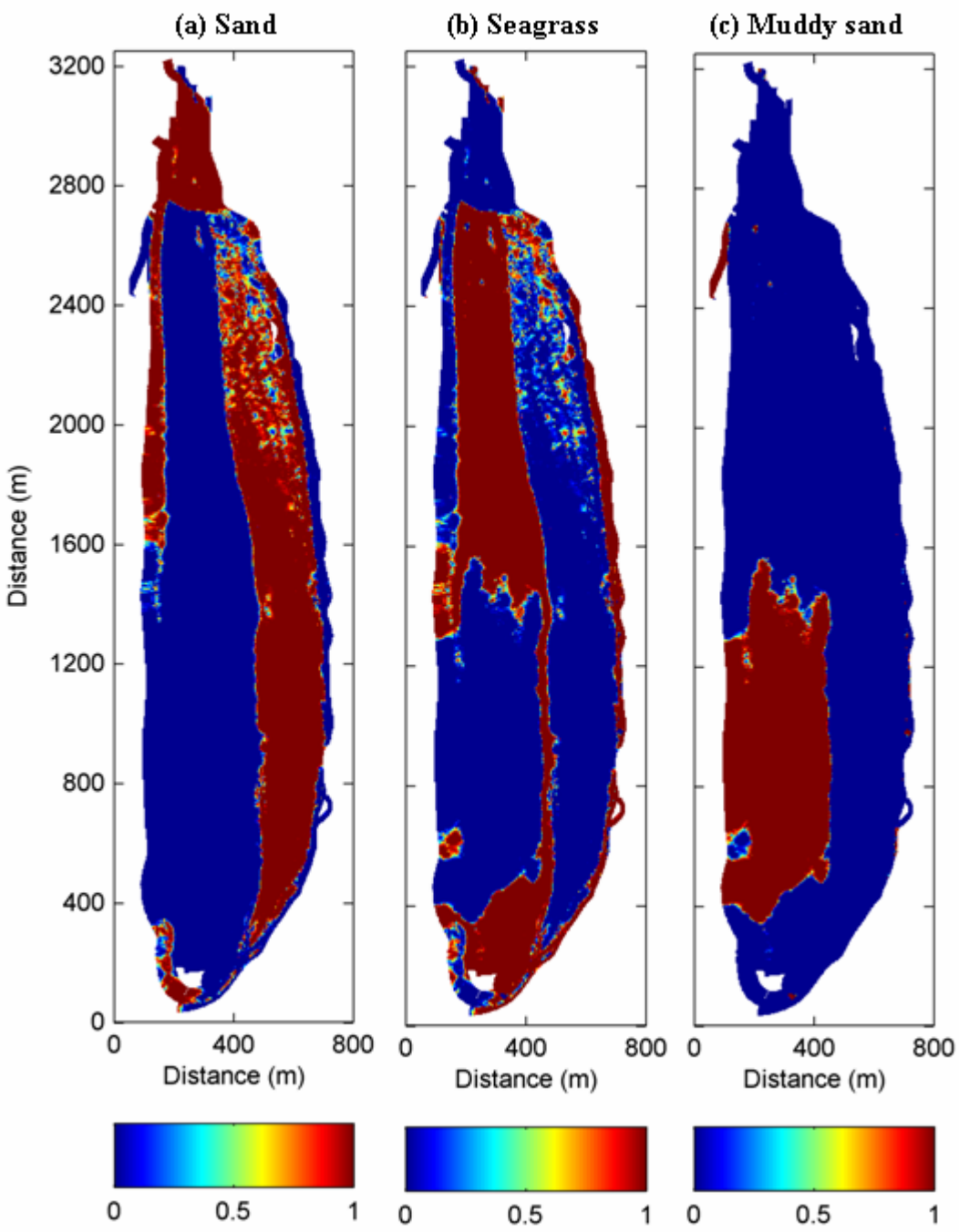

Figure 6.10: The posterior probabilities of the (a) sand, (b) seagrass and (c) muddy sand classes. Data from a MBS survey in Moreton Bay, Queensland.

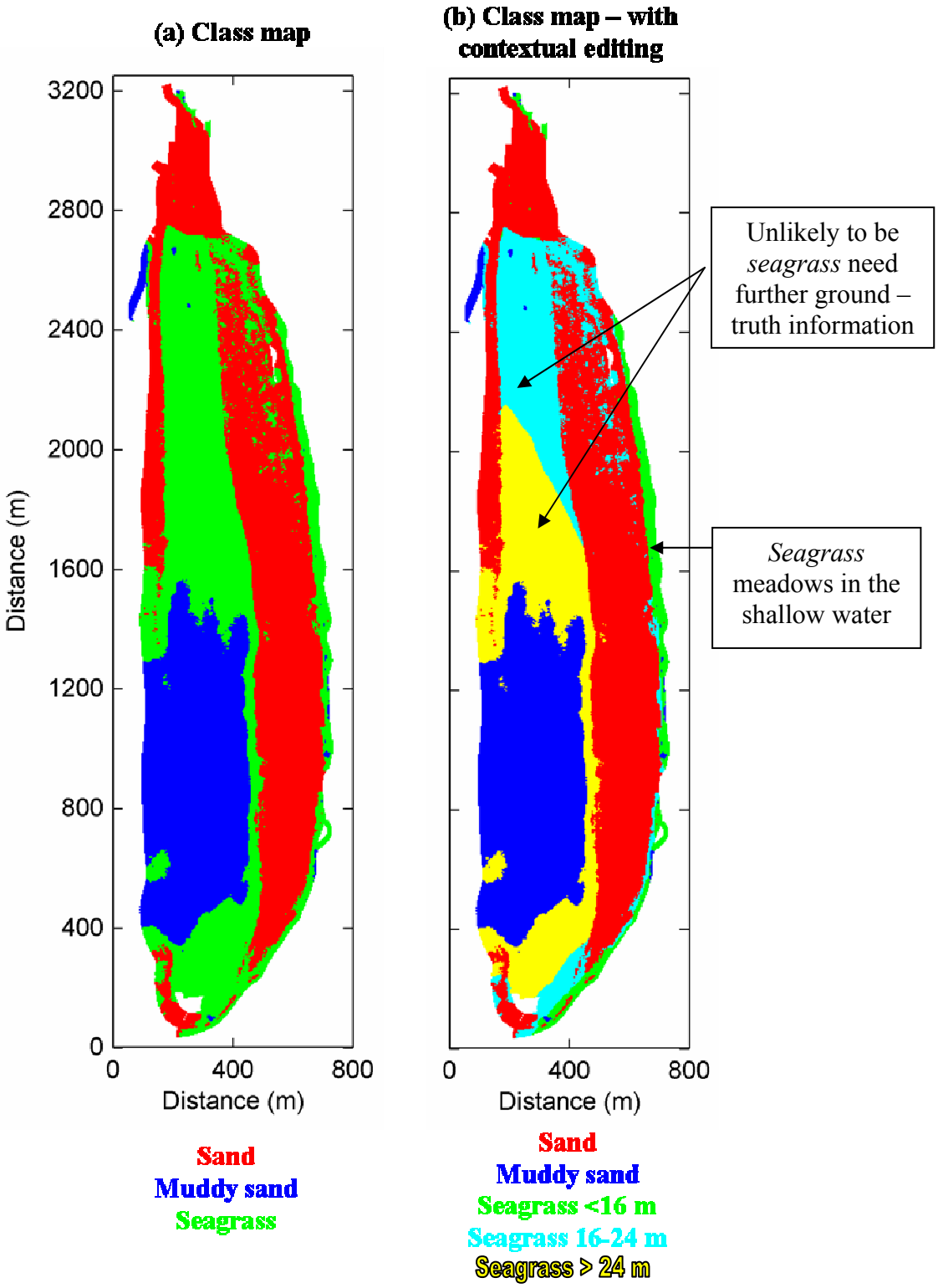

Figure 6.11: The results of supervised classification without (a) and with (b) contextual editing. Data from a MBS survey in Moreton Bay, Queensland.

Table 6.2: FC values for different backscatter parameters of the seagrass, muddy sand and sand classes. Data from the MBS survey in Moreton Bay, Queensland.

Feature	Fisher Criterion		
	Seagrass Muddy sand	*Coarse sand Seagrass*	*Muddy sand Coarse sand*
Average 5-60°	26.0	16.7	75.4
Slope 5-60°	5.9	0.9	1.6

The confusion matrix for the training data is given in Table 6.3. The overall classification accuracy was 99.4%. However, this high accuracy obtained for the training dataset could be misleading when classification is applied to the whole area. This is because some areas classified as *seagrass* were located in water deeper than expected for significant *seagrass* coverage in Moreton Bay, from observations in this survey and other studies (Udy & Levy 2002) (i.e. >15 m). This misclassification could have been caused by the similarity in the mean backscatter strength of the sand and seagrass classes. The distribution of depth values within the area classified as the *seagrass* class reveals three somewhat distinct depth ranges for this class (Figure 6.12). The *k*-means algorithm was used to subjectively segment the *seagrass* class into these three subclasses based on depth. The three subclasses discriminated by the different colours on the histogram in Figure 6.12 are indicated in the same colours in a modified class map in Figure 6.11(b). The first subclass of *seagrass* (green) corresponds to depths less than 16 m. From the video classification this class appears to represent the dense *seagrass* meadows that were found all along the edge of the survey area. The second subclass represents depths from 16m to 24 m (cyan) which, according to the towed video, are most likely areas of *sand* as no seagrass was observed. The third subclass classified as *seagrass* lies below 24 m (yellow). There is no video coverage of this area, however *seagrass* is not considered likely to be present, as previous studies have shown that seagrasses at a depth of 12 m in Moreton Bay are close to their minimum light requirements (Udy & Levy 2002). As the subclasses represent different depth bands of the *seagrass* class, further ground-truthing is required to establish if these subclasses correspond to distinctive habitats and why such subclasses had a backscatter response similar to seagrass.

Table 6.3: Confusion matrix for the coarse sand, seagrass and muddy sand classes. Data from a MBS survey in Moreton Bay, Queensland.

		Training data				
		Coarse sand	*Seagrass*	*Muddy sand*	*Total*	*User Accuracy (%)*
Classifier	*Coarse sand*	462	0	0	462	100
	Seagrass	6	206	0	212	97
	Muddy sand	0	0	389	389	100
	Total	468	206	389	1063	
	Producer accuracy (%)	99	100	100		

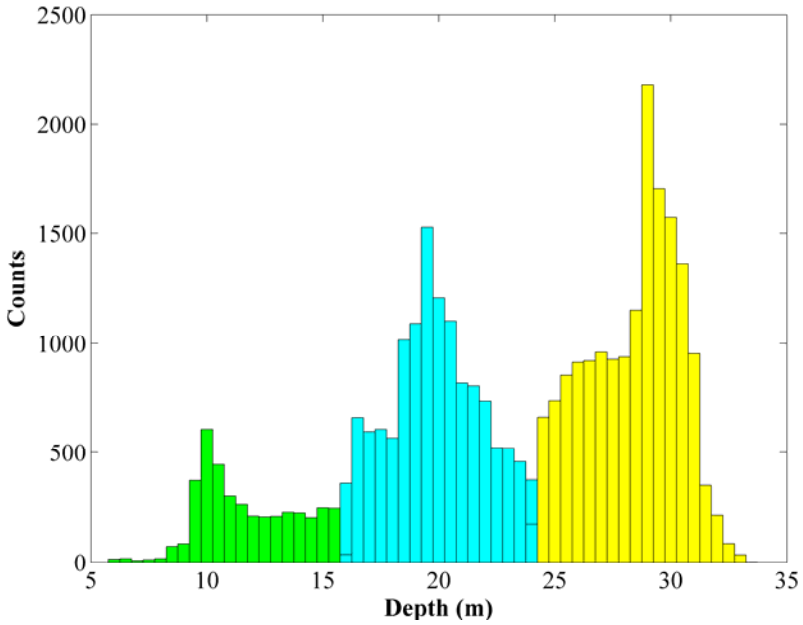

Figure 6.12: Distribution of depth values for the seagrass class segmented into 3 subclasses as shown in Figure 6.11(b). Data from a MBS survey in Moreton Bay, Queensland.

6.5 Esperance Bay, Western Australia

6.5.1 Site description

Esperance Bay is located off the south-east coastal town of Esperance in Western Australia. Esperance Bay is a temperate, high wave energy environment. The area used for this case study is a section of the MBS survey east of Woody Island (see Appendix A for details). Grab samples and towed video used to ground-truth acoustic measurements, identified four main seafloor types in this area: *sand*, *seagrass*, *rhodolith* and *rock*.

Seagrass in Esperance Bay is of typical temperate morphology forming dense covers with long shoots. *Rhodolith* is a calcareous red algae that range from a few mm to a few cm in diameter as described in Section 4.2. The high profile *rock* bed was found predominately in the area of the shoal called 'Time Rock'. The focus of this case study was to assess the ability of MBS measurements to discriminate two different types of marine vegetation: *rhodolith* and *seagrass*.

6.5.2 Results

The backscatter strength versus incidence angle for the dataset (two-dimensional histogram) and the angular dependence curves for *sand*, *seagrass*, *rock* and *rhodolith* from the training areas identified by grab samples and underwater video are shown in Figure 6.13. The mean level of backscatter strength was lowest for *sand*. The backscatter strength from *seagrass* was 3-4dB higher than from *sand* at the oblique angles of 20-60°. The highest backscatter strength came from *rock* and *rhodolith*, with the latter being on average slightly higher. The angle-average and slope of the angular dependence of the backscatter strength over 5-60º are shown alongside the bathymetry and terrain slope in Figure 6.14. The terrain slope clearly identifies areas of *rock*, but it does not characterise other habitats, whereas the backscatter parameters identify the spatial distributions of all habitats in the survey area.

The FC values for the different parameters for different pairs of habitats are shown in Table 6.4. The angle-average backscatter strength has the highest FC values for each compared habitat pair (Table 6.4). As the two backscatter parameters were highly correlated (Table 6.5), only the angle-average backscatter strength was used for classification with the addition of terrain slope to aid the separation of *rock* from the other habitats. The different acoustic classes are seen in a two-dimensional histogram of the angle-average backscatter strength versus terrain slope (Figure 6.15(a)).

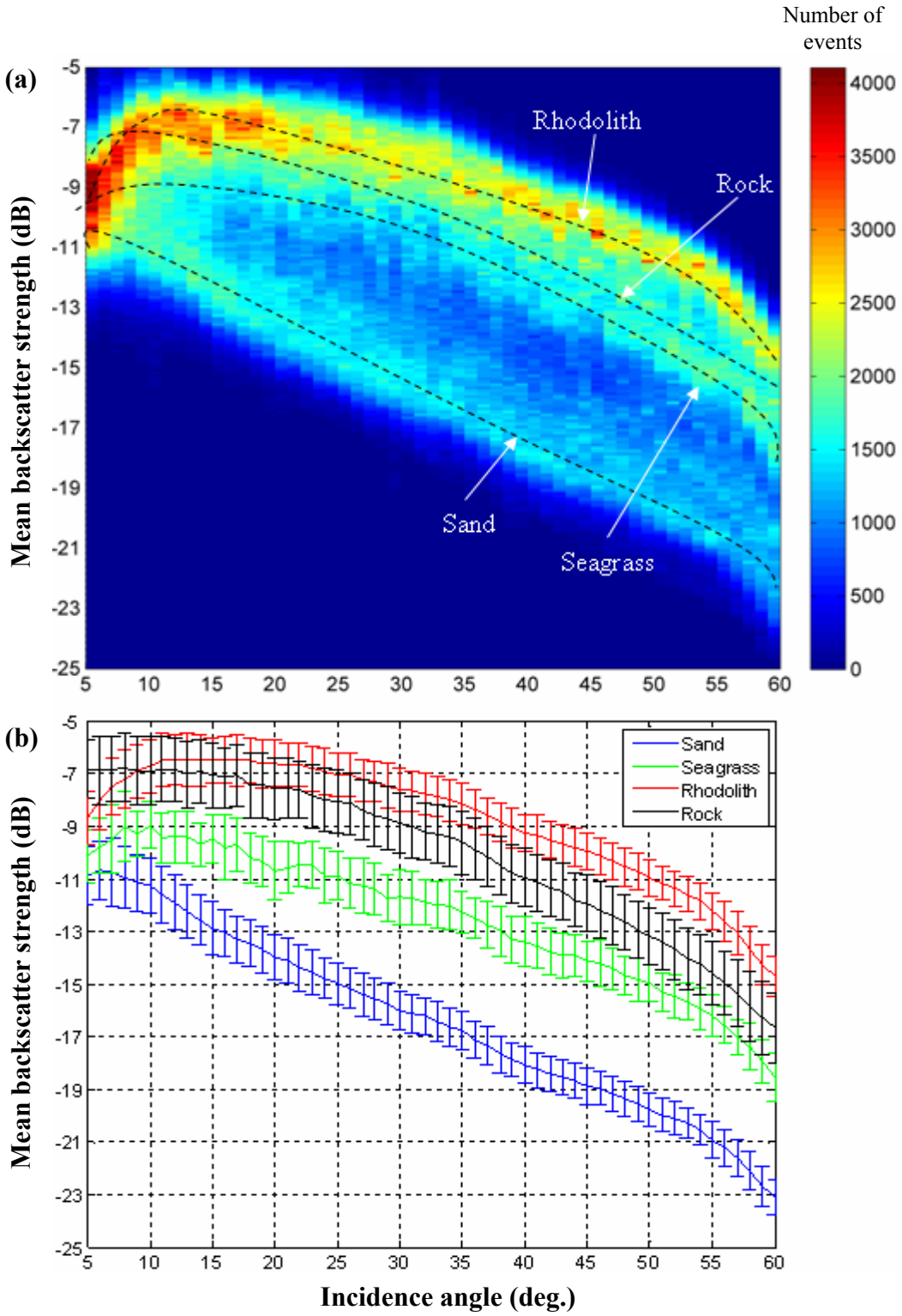

Figure 6.13: Mean backscatter strength (dB) versus incidence angle (deg.): (a) a two dimensional histogram for all of the data and (b) mean value from sand, seagrass, rhodolith and rock from east of Woody Island in Esperance Bay, Western Australia (error bars show the standard deviation measured at different angles).

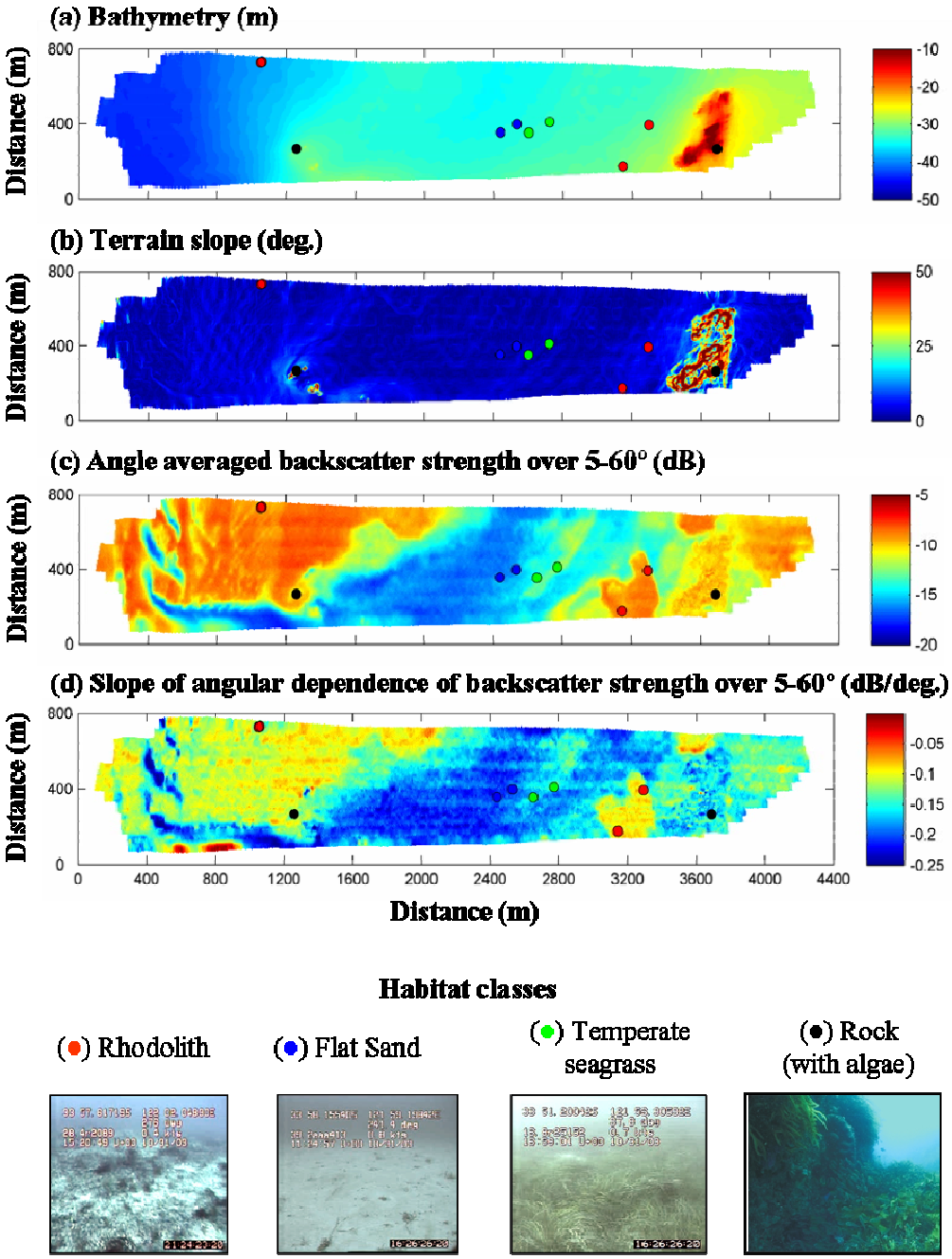

Figure 6.14: (a) Bathymetry (m), (b) terrain slope (deg.), (c) angle-average (dB) and (d) slope of the angular dependence (dB/deg.) of backscatter strength over 5-60° for MBS data collected east of Woody Island in Esperance Bay, Western Australia. Grab sample data and underwater video images of: rhodolith (●), sand (●), seagrass (●) and rock (●) are also shown.

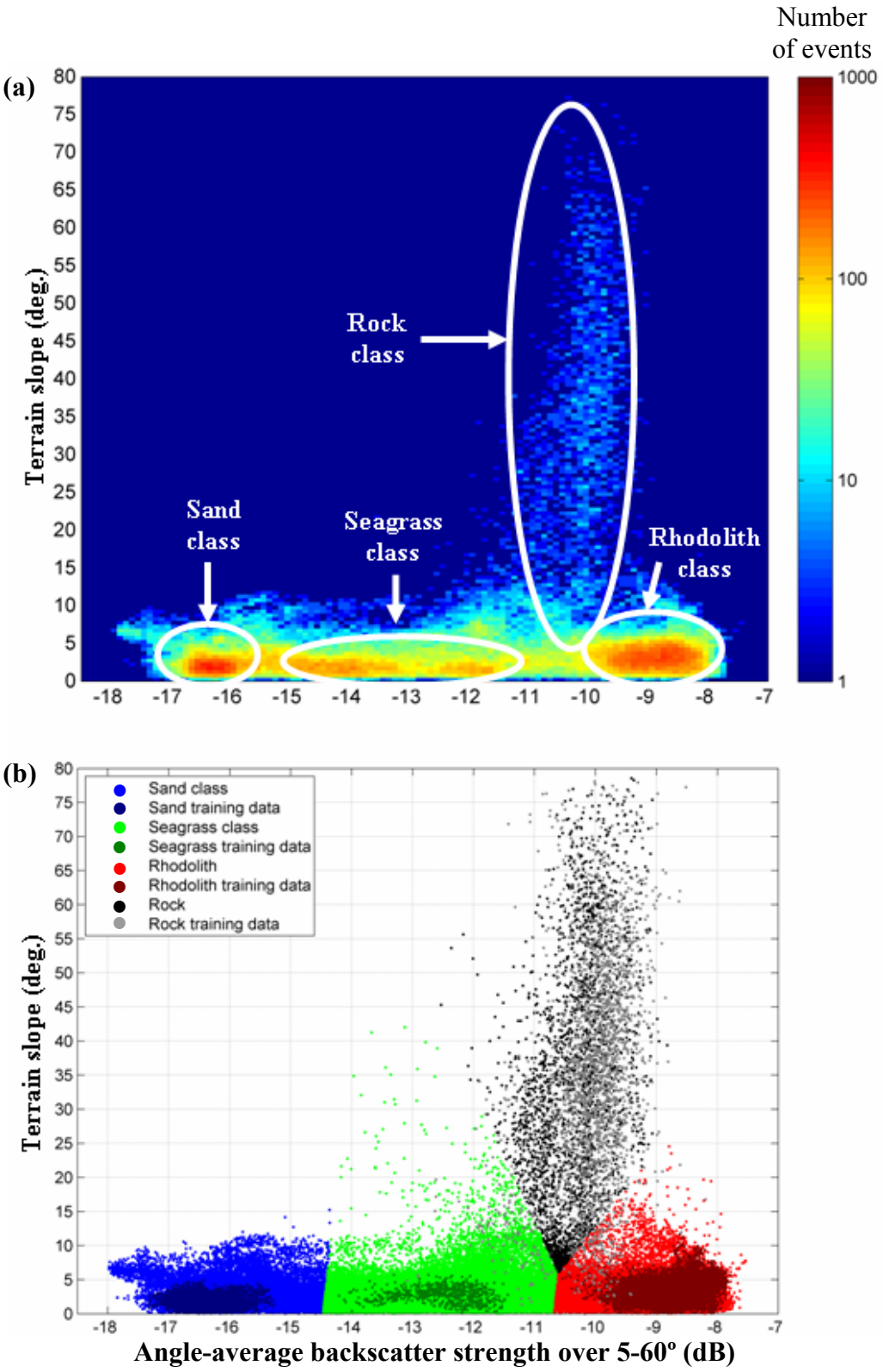

Figure 6.15: Terrain slope (deg.) versus the angle-average backscatter scatter (dB): (a) two dimensional histogram and (b) scatter plot segmented by supervised classification into sand, seagrass, rhodolith and rock classes. Data from a MBS survey east of Woody Island in Esperance Bay, Western Australia.

The results of supervised classification are shown in feature space in Figures 6.15(b), and as posterior probabilities and class maps in Figure 6.16. The training dataset was used to calculate a confusion matrix shown in Table 6.6. An overall accuracy of supervised classification for the training set was 99%. Misclassification of the training data occurred with some areas of *rock* being classified as either *rhodolith* or *seagrass*. Moreover, almost all the areas around the boundary between *rhodolith* and *sand* were classified as *seagrass*. Although it is possible for there to be *seagrass* in some of the transition areas, it is more likely to be a sparse cover of *rhodolith*.

Table 6.4: The FC calculated for different pairs of habitat classes and compared for different backscatter properties and terrain slope. The highest value for each habitat pair is shown in bold. Data from a MBS survey east of Woody Island in Esperance Bay, Western Australia.

Feature	**Fisher criterion**					
	Seagrass Rhodolith	*Seagrass Sand*	*Rhodolith Sand*	*Seagrass Rock*	*Rock Sand*	*Rhodolith Rock*
Average	**27.1**	**35.8**	**197.8**	**9.5**	**99.6**	3.4
Slope	4.9	11.9	32.1	0.6	2.8	**5.0**
Terrain slope	0.1	0.4	0.6	3.8	4.0	3.6

Table 6.5: The correlation coefficient for the backscatter parameters and terrain slope. Data from a MBS survey east of Woody Island in Esperance Bay, Western Australia.

	Average	**Slope**	**Terrain slope**
Average	1	0.85	0.17
Slope	0.85	1	-0.03
Terrain slope	0.17	-0.03	1

Table 6.6: Confusion matrix for the training data from a MBS survey east of Woody Island in Esperance Bay, Western Australia.

		Training data					
		Sand	*Seagrass*	*Rock*	*Rhodoltih*	*Total*	*User Accuracy (%)*
Classifier	*Sand*	4941	0	0	0	4941	100
	Seagrass	0	651	121	0	772	84.3
	Rock	0	0	2314	0	2314	100.0
	Rhodoltih	0	0	66	9174	9240	99.3
	Total	4941	651	2501	9174	17267	
	Producer Accuracy (%)	100	100	92.5	100		

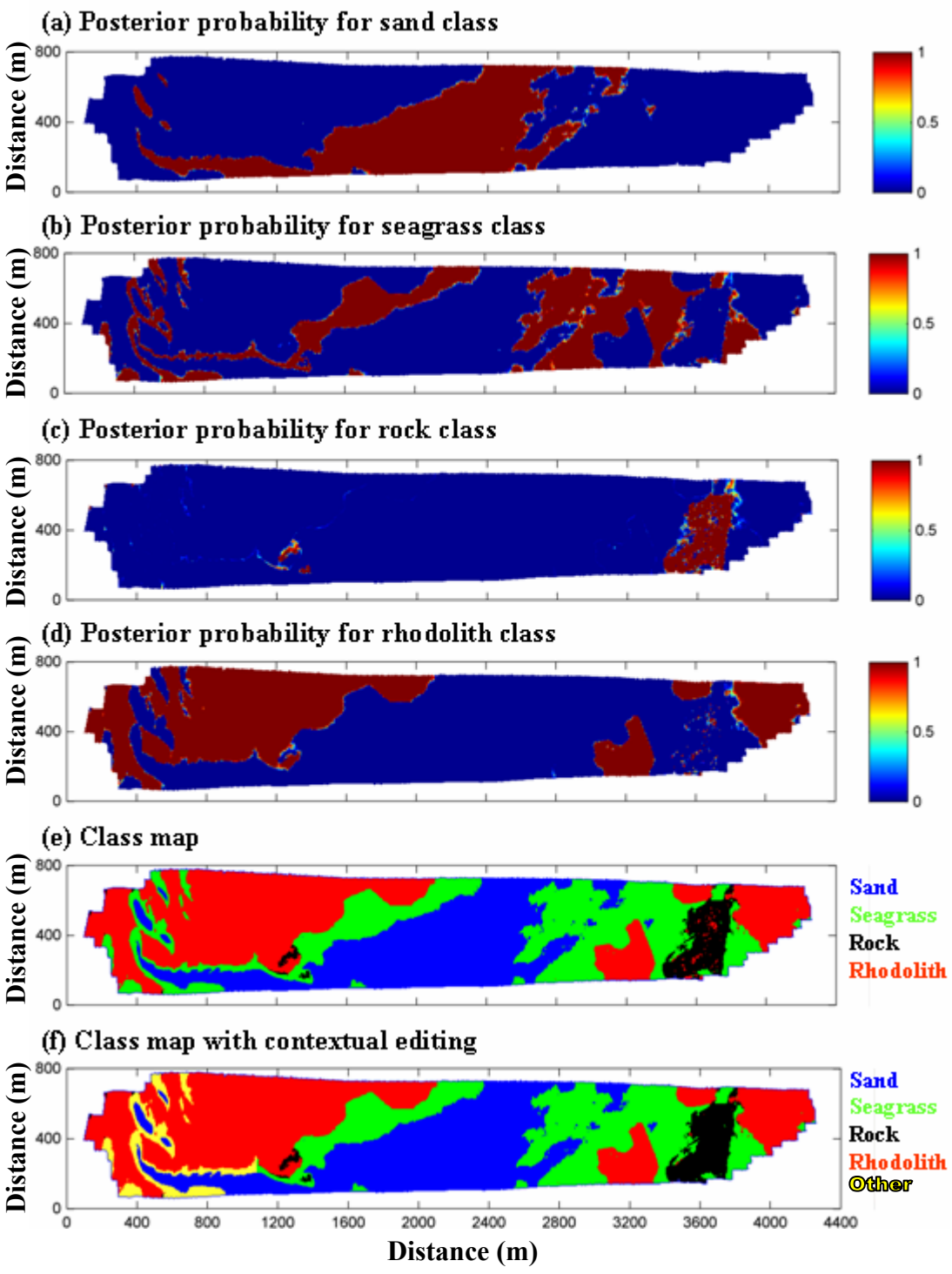

Figure 6.16: Results of supervised classification of MBS data collected east of Woody Island in Esperance Bay, Western Australia: posterior probabilities of (a) sand, (b) seagrass, (c) rock and (d) rhodolith classes, and resulting class map without (e) and with (f) contextual editing of the seagrass class using the k-means algorithm.

Contextual editing can be employed to amend these two problems of misclassification. As *rhodolith* usually forms on *sand* and not *rock* (Perry 2005), areas classified as *rhodolith* when surrounded by *rock* were reclassified as *rock*. As depth is an important determinant to the distribution of *seagrass*, this was used to apply contextual editing to the classification and the result is shown in Figure 6.16(f). Figure 6.17 shows the depth distribution of the *seagrass* class, which reveals two distinct subclasses. Similarly to the previous section (6.4), the *k*-means method was used to segment the *seagrass* class into two subclasses based on the difference in depth. The subclass of lower depth distribution (<37m) was assigned to the actual *seagrass* class as it was identified by the grab samples, while the subclass of larger depth (>37m) was assigned as ”other”. This ”other” class is likely to be a low-cover of *rhodolith*, but without ground-truthing by either video observation or grab samples this cannot be verified.

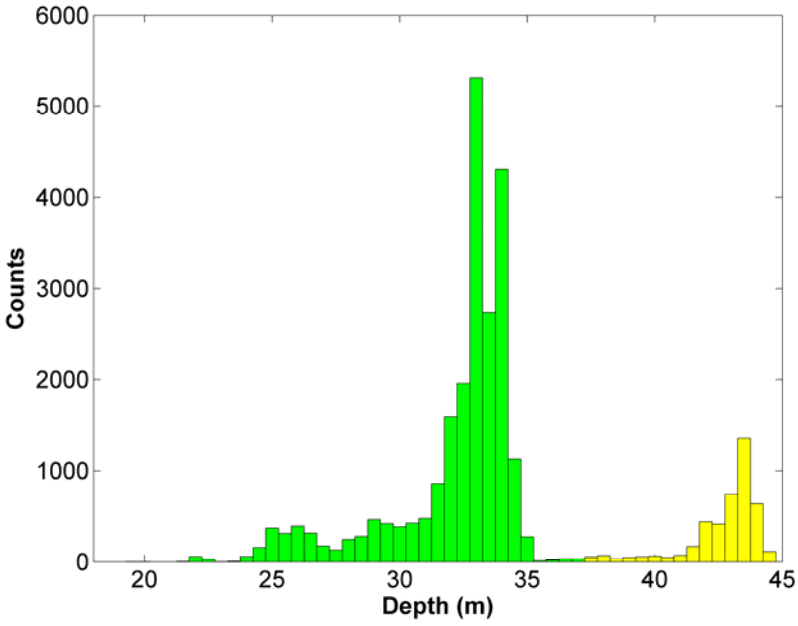

Figure 6.17: Distribution of depth values of the seagrass class east of Woody Island in Esperance Bay. The two colours represent subclasses segmented by depth using k-means clustering. The spatial distribution of these subclasses can be seen in Figure 6.16(f).

6.6 Morinda Shoal, Queensland

6.6.1 Site description

The reef-capped Morinda Shoal is located north-east of Cape Bowling Green (Queensland) and is situated in the central section of the Great Barrier Reef Marine Park. A video survey of the area found hard standing *coral* reef and *coral* rubble, tropical *seagrass* and bare sediment. Although there were distinct homogeneous areas, there were also complex heterogeneous areas. In addition to mapping the distribution of *seagrass*, distinguishing hard standing *coral* reef from *coral* rubble was also an objective of this case study, which would be useful in monitoring the health of reef ecosystems as well as understanding the physical processes occurring.

6.6.2 Results

An analysis of the towed video recordings in the survey area identified six distinct benthic classes:

1. *Coral reef* – a mixture of hard standing *coral* features of morphologically different structure with some *coral* rubble;
2. *Coral rubble* - *coral* rubble and debris typically covered in algae growth*;*
3. *Dense seagrass* – greater than 50% *seagrass* cover from the video analysis;
4. *Sparse seagrass* – less than 50% *seagrass* cover from the video analysis;
5. *Mixed sparse coral and seagrass* – a complex and heterogeneous area which is a mixture of sparse *seagrass* and sparse *coral* cover;
6. *Bare sediment – Sand,* predominately flat, occasionally containing *coral* material or patches of *seagrass* or algae;

The backscatter strength versus incidence angle is shown in Figure 6.18 for the entire dataset as a two-dimensional histogram (Figure 6.18(a)) and as the mean angular dependence curves for each particular habitat identified by the video (Figure 6.18(b)). The histogram shows classes containing *coral* to be the most abundant. The mean angular dependence curves indicated that the angle-average backscatter strength was the most effective backscatter property to discriminate between the different habitats.

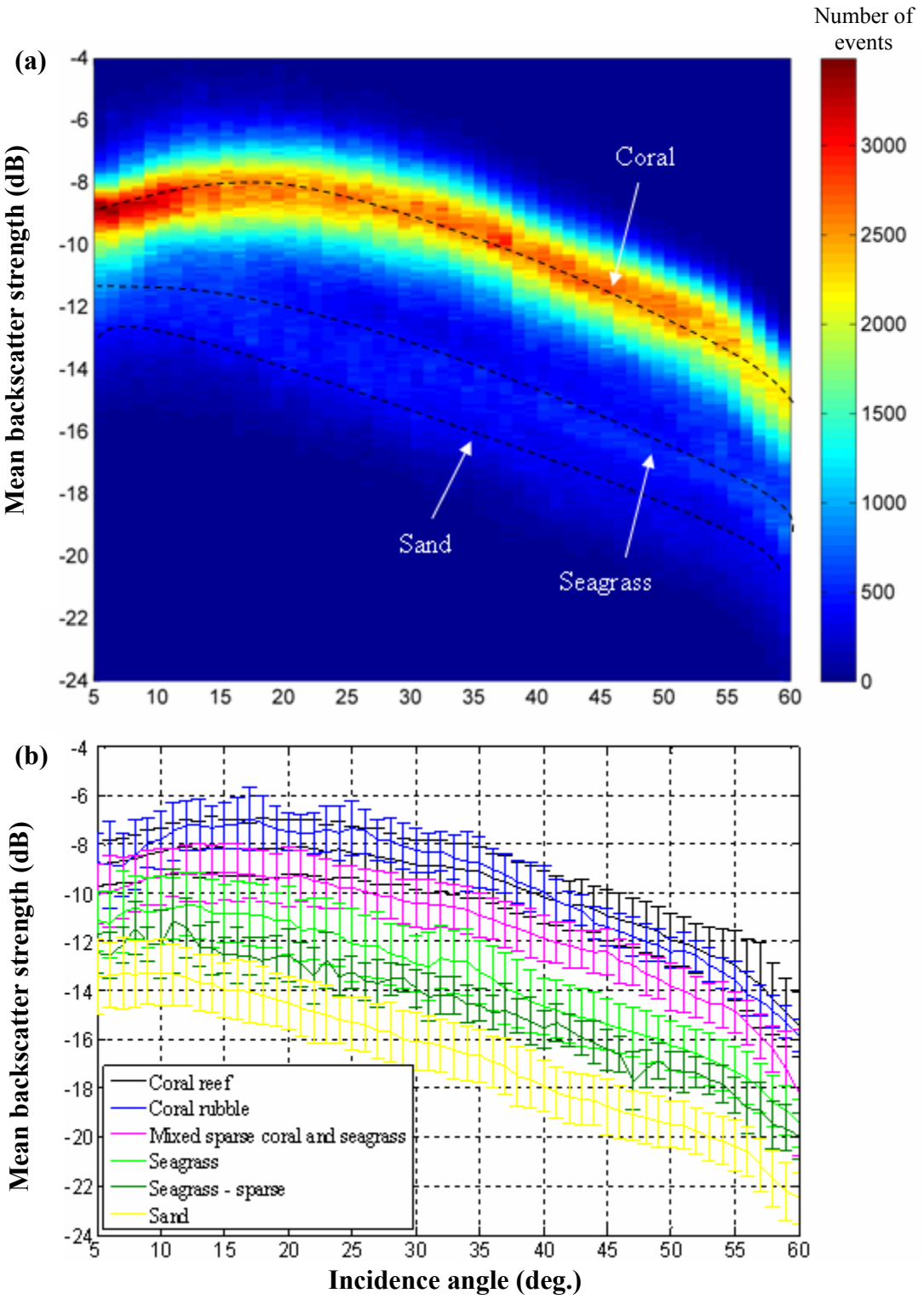

Figure 6.18: Mean backscatter strength (dB) versus incidence angle (deg.): (a) a two-dimensional histogram for all of the data and (b) the mean angular dependence with standard deviation (error bars) for different habitats. Data from a MBS survey of Morinda Shoal, Queensland.

The depth, terrain slope, angle-average backscatter strength and slope of its angular dependence were mapped for the whole survey area, and are shown with the classified video transects in Figure 6.19. Values of these features are also shown along the two video transects with classified habitats in Figure 6.20 and 6.21. Although areas of high relief are clearly seen in the bathymetry and terrain slope, the transitions between areas of *coral* (reef and rubble), *seagrass* and bare *sand* are more distinct in the angle-average backscatter strength. However, subclasses within those groups were difficult to distinguish by using any single feature shown in Figures 6.20 and 6.21. For instance, there was little difference in the backscatter parameters between *coral reef* and *coral rubble*. This is also indicated by the FC values as no feature was shown to discriminate between *coral reef* and *coral rubble* and between *dense seagrass* and *sparse seagrass* (Table 6.7). Therefore, it was decided to combine those classes for the purposes of acoustic classification. This gives 4 acoustic classes: *coral*, *seagrass*, *mixed coral and seagrass*, and *sand*. As relief is an important physical attribute of a *coral* reef system, it was decided to subdivide the *coral* class into high and low relief classes using the terrain slope. Based on the data shown in Figures 6.20 and 6.21, a terrain slope of 20º was selected as the boundary between high and low relief classes. This gave 5 acoustic classes:

1. *High relief coral* –this is *coral* material with a slope higher than 20º, which represents high relief *coral* features, such as bommies, reef slope, etc;
2. *Low relief coral* – this is *coral* material with a slope lower than 20º, which likely represents dense *coral* cover, but may include rubble;
3. *Seagrass* – areas of *seagrass* dense enough to acoustically contrast from bare sediment;
4. *Mixed coral and seagrass;*
5. *Sand* – bare sediment.

These acoustic classes can be identified as clusters in a density plot of the terrain slope versus the angle-average backscatter strength (Figure 6.22).

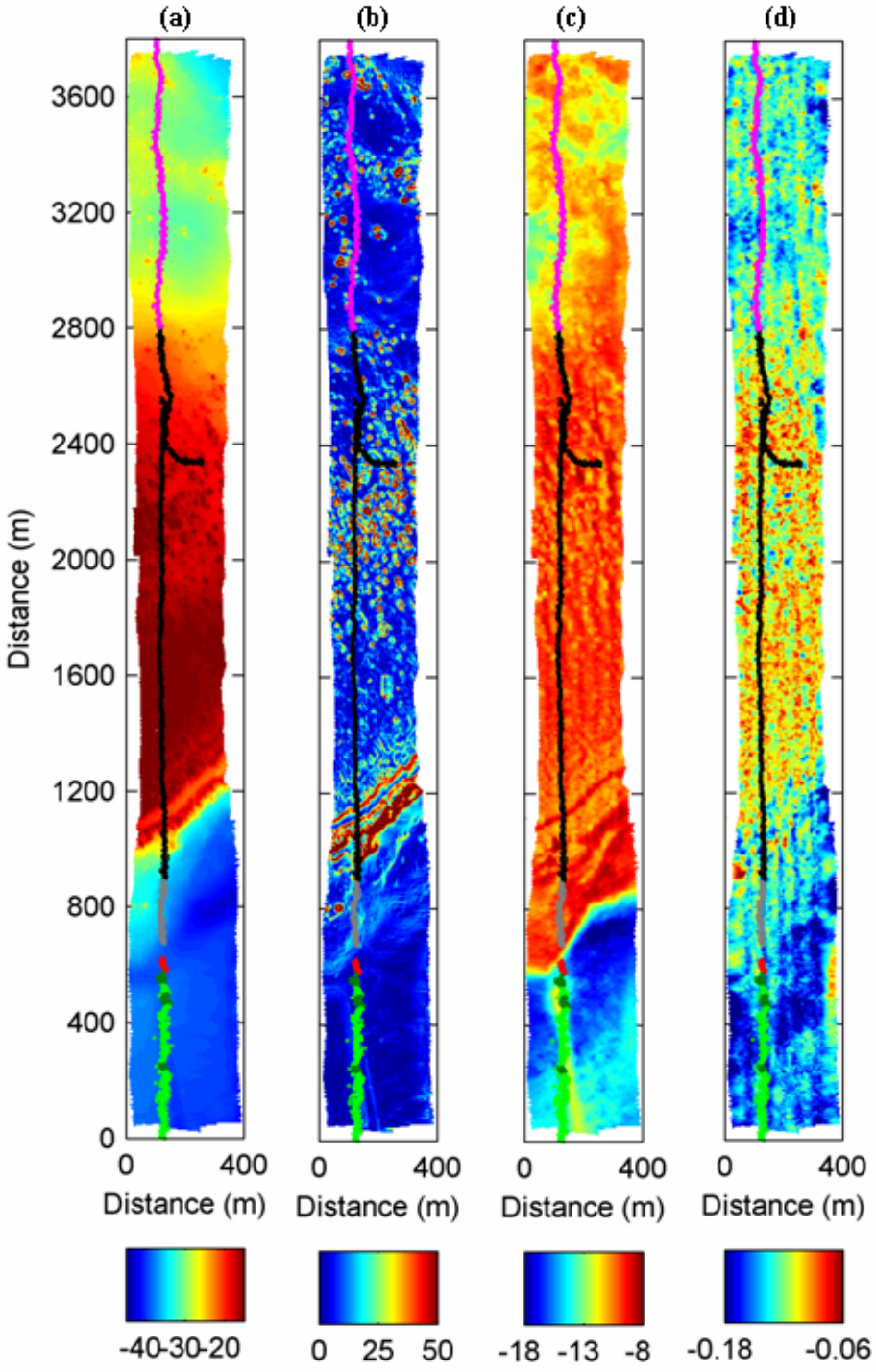

Figure 6.19: (a) Bathymetry (m), (b) terrain slope (deg.), (c) angle-average (dB) and (d) slope of the angular dependence (dB/deg.) of backscatter strength with video tracks colour-coded according to the following classification: Coral Reef (●), Coral Rubble (●), Seagrass – dense (●), Seagrass – sparse (●), Sand (●) and Mixed coral and seagrass (●). Data from a MBS survey of Morinda Shoal, Queensland.

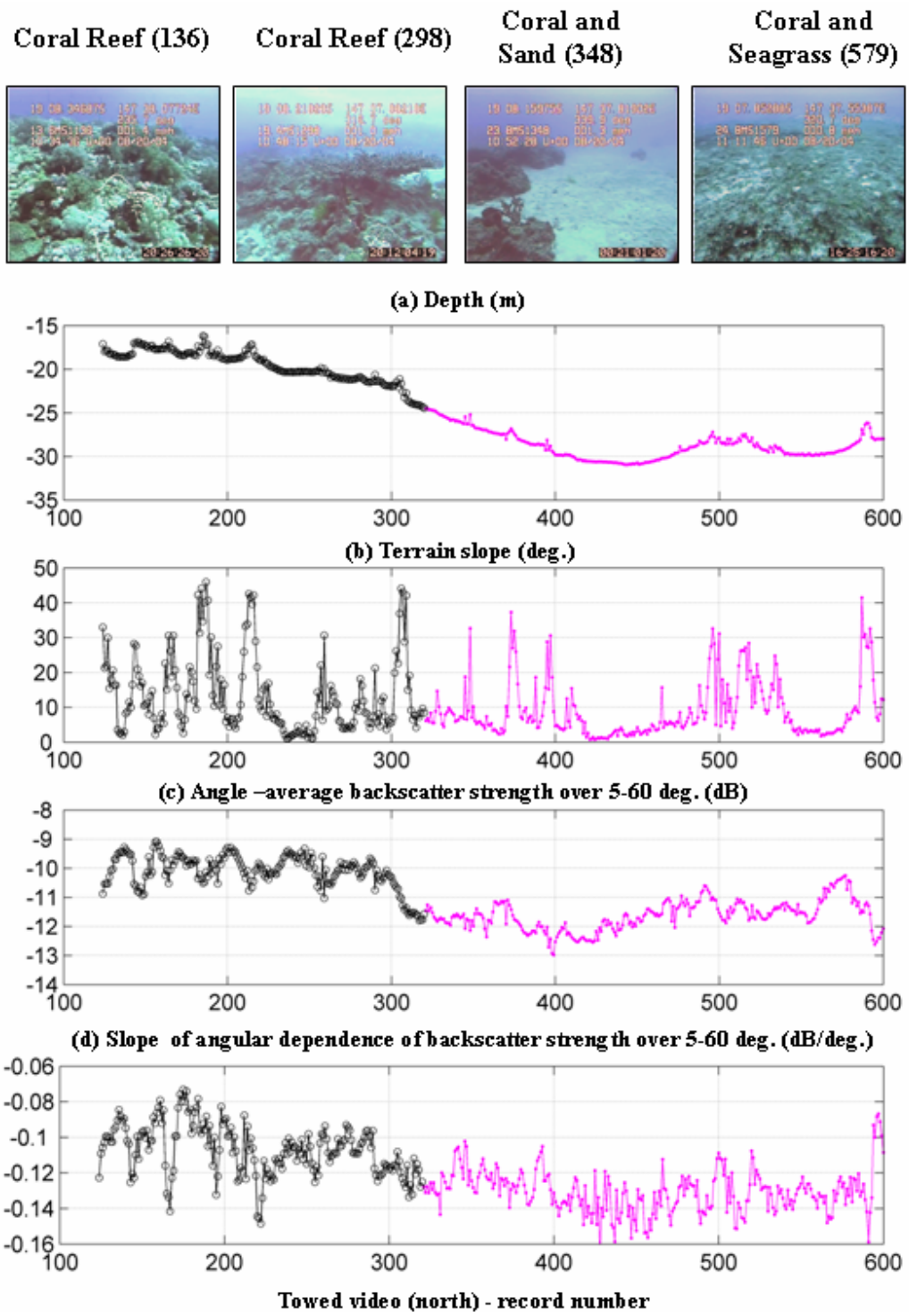

Figure 6.20: Seafloor acoustic features from MBS data along the northern Morinda Shoal towed underwater video: (a) Depth (m), (b) terrain slope (deg.), (c) angle-average (dB) and (d) slope of angular dependence (dB/deg.) of backscatter strength. Video classification: Coral Reef (●) and Mixed coral and seagrass (●).

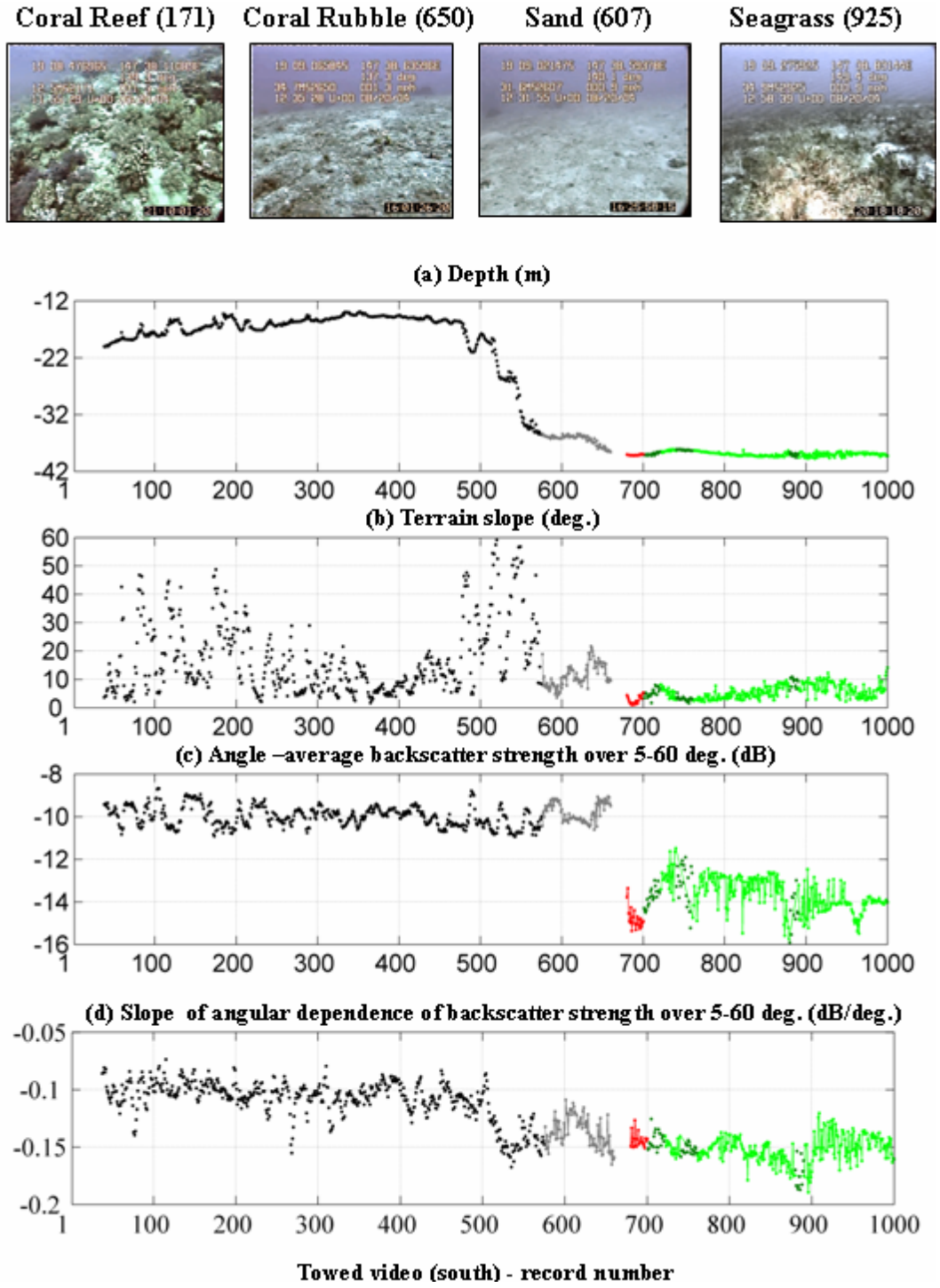

Figure 6.21: Seafloor acoustic features from MBS data along the southern Morinda Shoal towed underwater video: (a) Depth (m), (b) terrain slope (deg.), (c) angle-average (dB) and (d) slope of angular dependence (dB/deg.) of backscatter strength. Video classification: Coral Reef (●), Coral Rubble (●), Seagrass – dense (●), Seagrass – sparse (●), Sand (●).

Table 6.7: Fisher criterion values for the different acoustic properties of the habitat classes identified by analysis of video recordings. Data collected from a MBS survey of Morinda Shoal, Queensland.

Habitat comparison		*Average 5-60°*	*Slope 5-60°*	*Terrain slope*
Dense Seagrass	*Coral Reef*	10.7	3.0	0.7
Dense Seagrass	*Coral Rubble*	14.4	0.7	1.2
Dense Seagrass	*Sand*	8.1	0.3	0.6
Dense Seagrass	*Coral & seagrass*	3.9	1.1	0.1
Dense Seagrass	*Sparse seagrass*	1.4	0.4	0.8
Coral Reef	*Coral Rubble*	0.1	1.0	0.2
Coral Reef	*Sand*	54.2	4.7	1.1
Coral Reef	*Coral & seagrass*	3.5	0.7	0.3
Coral Reef	*Sparse seagrass*	73.7	1.7	3.1
Coral Rubble	*Sand*	6.4	0.0	0.0
Coral Rubble	*Coral & seagrass*	60.4	0.1	3.5
Coral Rubble	*Sparse seagrass*	37.9	2.5	0.5
Sand	*Coral & seagrass*	6.2	1.5	0.0
Coral & seagrass	*Sparse seagrass*	22.3	0.4	0.5

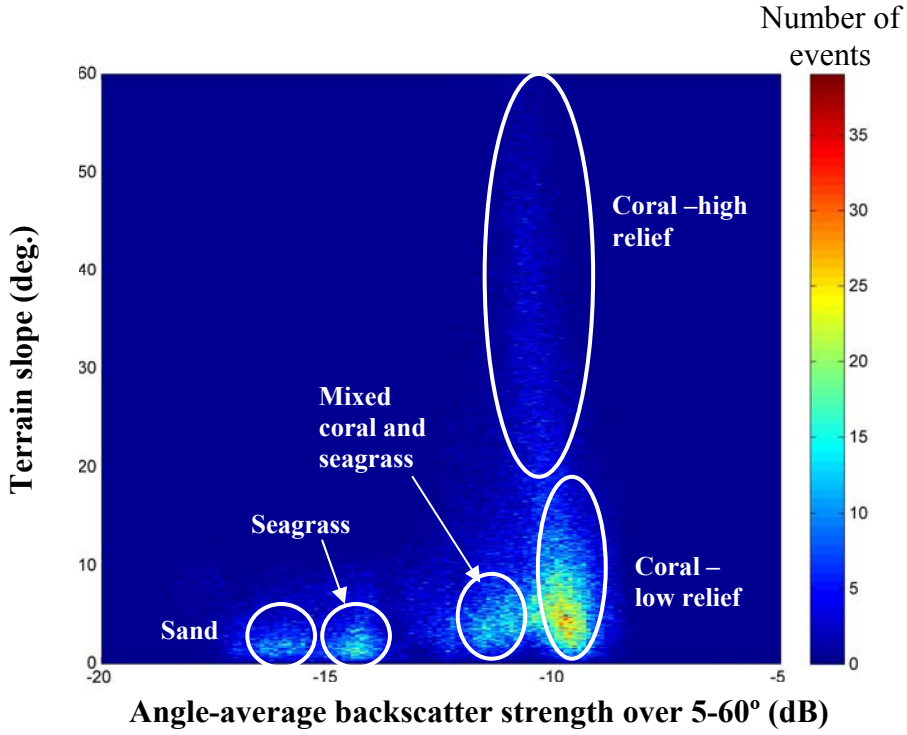

Figure 6.22: (a) Two- dimensional histogram of terrain slope (deg.) versus angle-average backscatter strength over 5-60º (dB). Data collected from a MBS survey of Morinda Shoal, Queensland.

For classification purposes the terrain slope, angle-average backscatter strength and slope of backscatter angular dependence were used to segment the survey area into areas of: *coral*, *seagrass*, *mixed coral and seagrass*, and *sand*. The features used for classification were not significantly correlated (Table 6.8). The classification results obtained for the training areas are plotted in feature space in Figure 6.23. The posterior probability maps for the different classes are shown in Figure 6.24. These probability maps were used to produce the four class map shown in Figure 6.25(a). Using the terrain slope feature to subdivide the *coral* class resulted in the 5-class map shown in Figure 6.25(b). The classification accuracy was assessed using the training dataset for the four main classes: *coral*, *seagrass*, *mixed coral and seagrass* and *sand*. The confusion matrix of classification is shown in Table 6.9. The overall classification accuracy was 93%. This is a good result considering the level of complexity of the survey area. The main misclassification rate occurred with the mixture class, which was unsurprising as this class represented a heterogeneous area combining features of both the *coral* and *seagrass* classes.

Table 6.8: Correlation matrix of the different properties derived from the MBS data collected over Morinda Shoal, Queensland.

	Average 5-60°	*Slope 5-60°*	*Terrain slope*
Average 5-60°	1.00	0.63	0.24
Slope 5-60°	0.63	1.00	0.17
Terrain slope	0.24	0.17	1.00

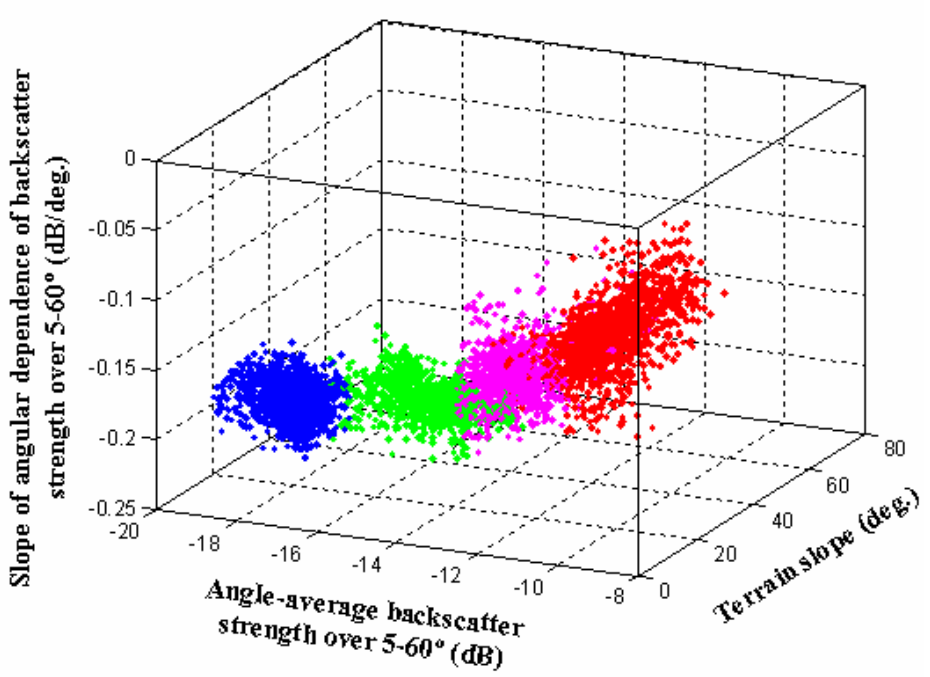

Figure 6.23: Plot of slope of angular dependence of backscatter strength (dB/deg.) versus angle-average backscatter strength (dB) (both over 5-60°) versus terrain slope (deg.) for training data used for supervised classification of Morinda Shoal, Queensland. Coral (●), coral and seagrass (●), seagrass (●) and sand (●).

Table 6.9: Confusion matrix for the training datasets from the classification of acoustic data collected from a MBS survey of Morinda Shoal, Queensland.

		Training						
		Sand	*Seagrass*	*Coral*	*Mixture*	Total	*User (%)*	*Accuracy*
Classifier	*Sand*	128	4	0	0	132		97
	Seagrass	0	808	0	37	845		96
	Coral	0	0	1577	79	1656		95
	Mixture	0	57	83	956	1096		87
	Total	128	869	1660	1072	3729		
Producer accuracy (%)		100	93	95	89			

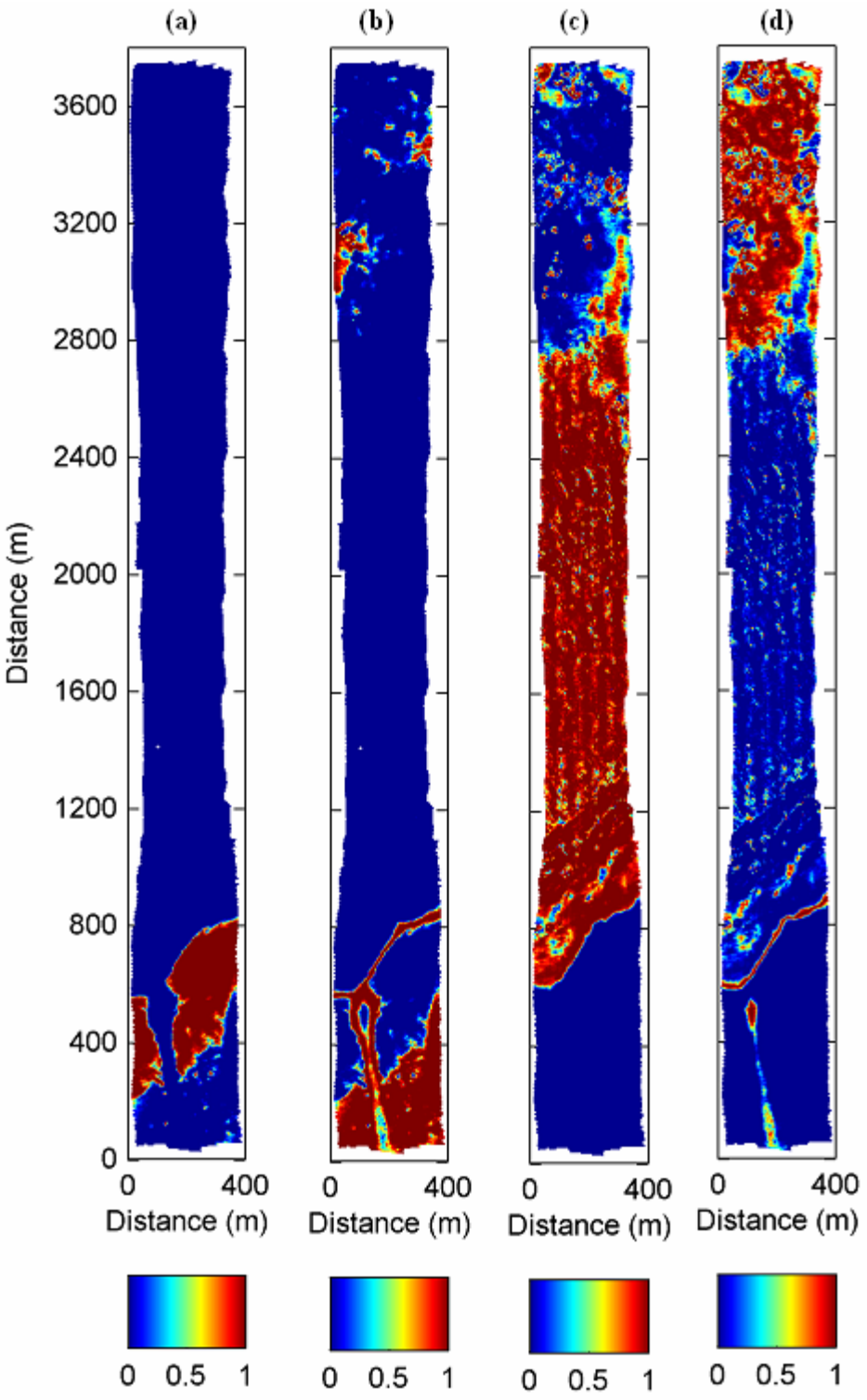

Figure 6.24: Posterior probabilities for the four acoustic classes Morinda Shoal: (a) Sand, (b) Seagrass (c) Coral and (d) Mixed coral and seagrass.

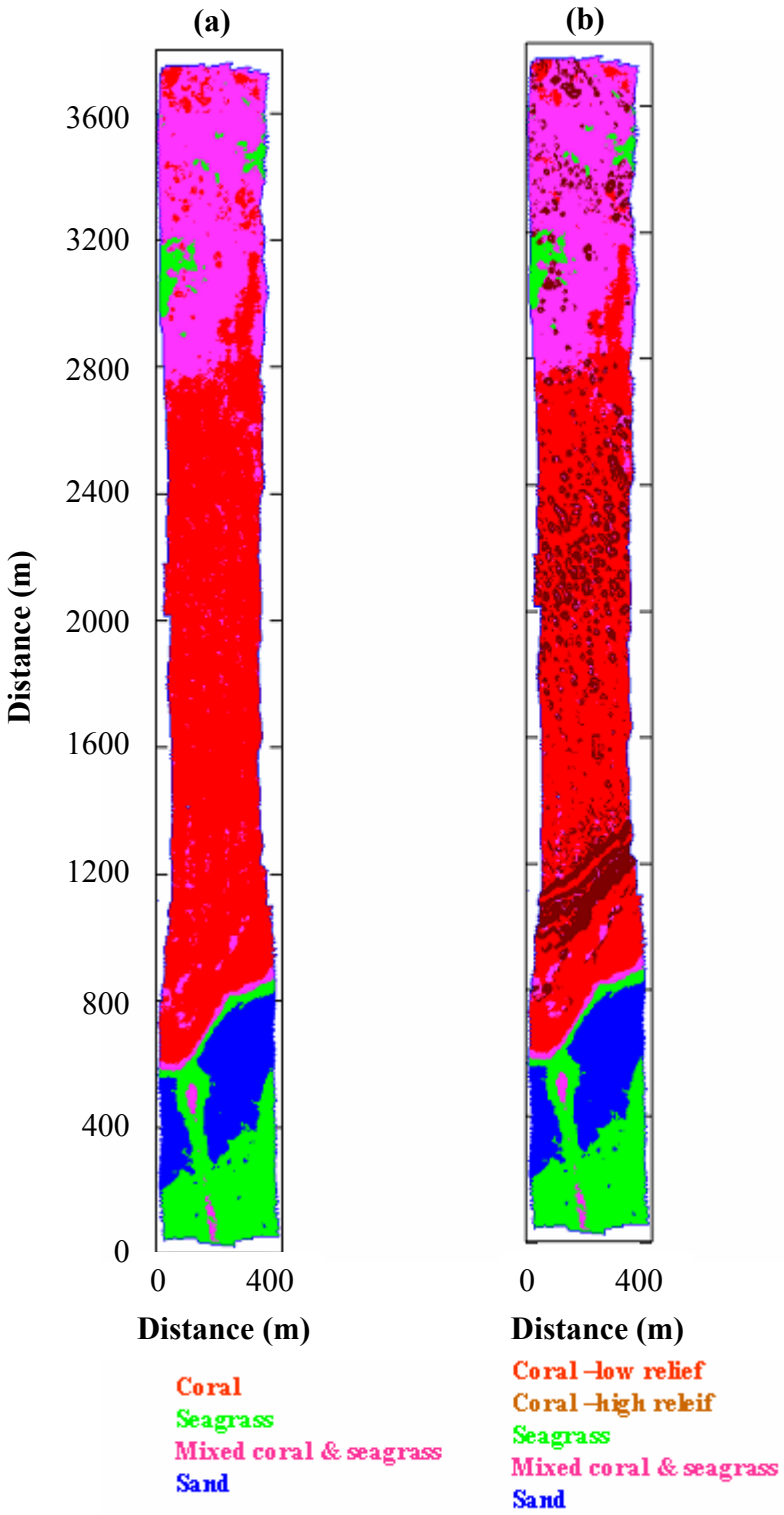

Figure 6.25: Class maps of Morinda Shoal using (a) supervised classification and (b) the addition of two subclasses determined by terrain slope.

6.7 Implications for benthic habitat mapping

The case studies shown in this chapter have highlighted both the potential and limitations of using MBS in benthic habitat mapping. Also, these case studies have tested the algorithms and methods developed in the previous chapters. It is evident from all these examples that the angle cube method developed in this study is capable of producing backscatter images of the seafloor which distinguish different habitats, mirror their spatial distribution on the seafloor and are free of artefacts due to the specificity of MBS measurements. From the case studies the following can be concluded:

- Angle-average backscatter strength derived from the angle cube is a robust discriminator between different benthic habitats.
- Slope of the angular dependence of backscatter strength provides additional information that may be useful for distinguishing certain habitats which are characterised by similar values of the angle-average backscatter strength. However, the slope of angular dependence is a much noisier parameter than the angle-average backscatter strength
- Features generated from the angle cubes can suffer from boundary effects, especially over highly heterogeneous areas. For the angle-average feature this generally results in a smoothing of transition areas, whereas, for the slope of backscatter angular dependence this can result in extreme values. Future work could use this information to discriminate habitat boundaries.
- Further understanding of the correlation of these acoustic properties with the physical and morphological properties of the seafloor is needed.
- Increasing the number of classes and complexity of the seafloor environment decreases the accuracy of classification of certain, less distinct classes.

Figure 6.26 shows the relationship between the slope of angular dependence and the angle-average backscatter strength measured within some of the selected training areas representing different habitats from the different case studies. An analysis of such relationships between different backscatter characteristics is useful for identifying the similarity and difference of habitats acoustically observed in different regions. For instance, in Moreton Bay the class labelled *sand* has a much higher angle-average

backscatter strength than other soft sediment classes and is similar to the values obtained from *rock* (in Esperance Bay) and *coral* (in Morinda Shoal). This could be due to a number of reasons, such as hard intrusions of larger particle size or gas content present in the sediment. These hard intrusions could be of different origin, including shell debris, eroded bedrock or exposed bedrock underlying a thin layer of sand. Further investigation of habitats in such areas by means of direct probes would be necessary to establish the actual reasons for anomalous backscatter.

From the results of this chapter and those illustrated by Figure 6.26 in particular, it appears that there are principally four acoustic classes that can be distinguished through an analysis of MBS data: classes of high (e.g. rough and hard substrate), medium (e.g. *seagrass*) and low (e.g. bare sediment) backscatter levels and a high-relief class (usually high backscatter strength), which can be additionally separated using terrain analysis.

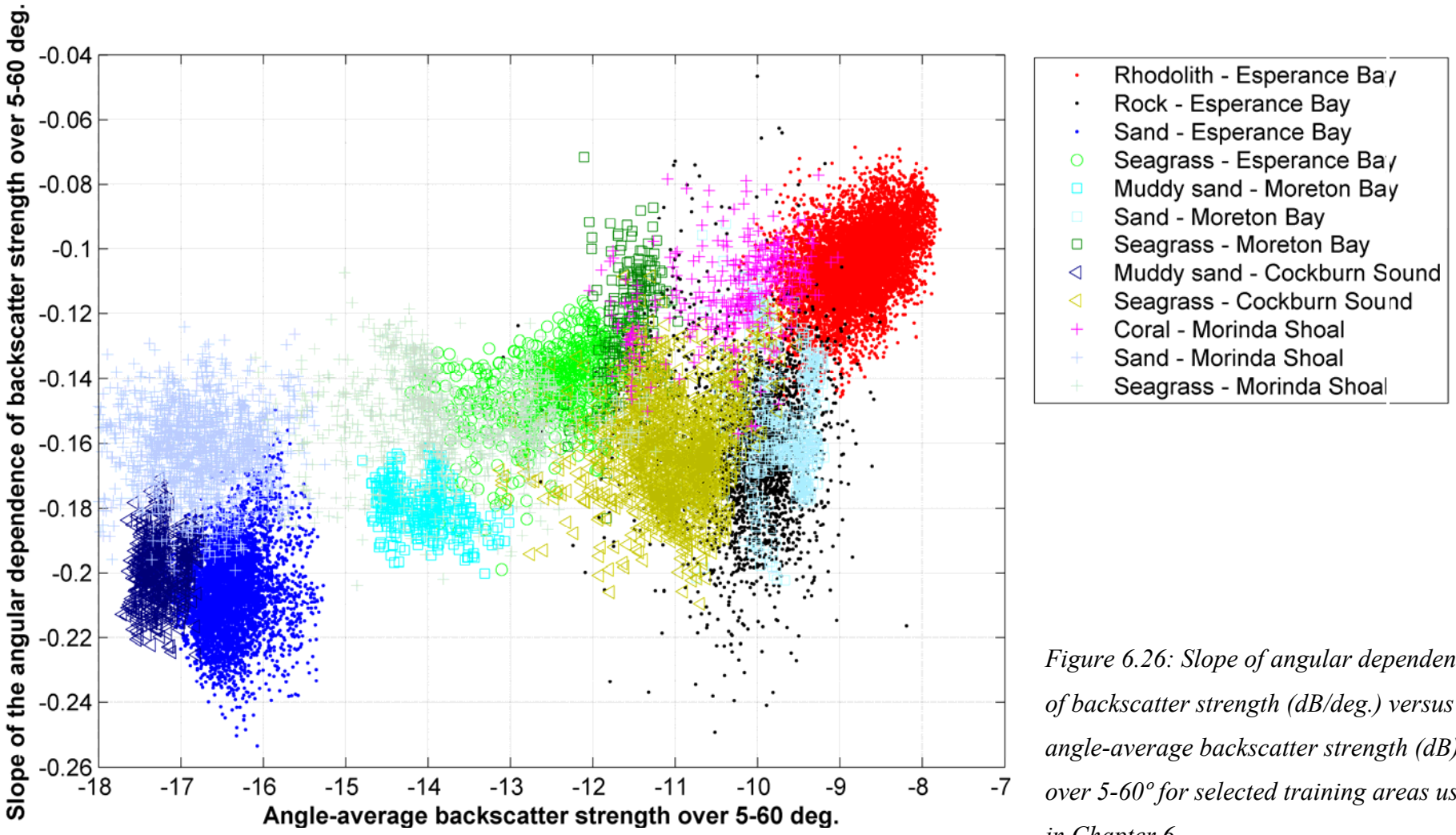

Figure 6.26: Slope of angular dependence of backscatter strength (dB/deg.) versus angle-average backscatter strength (dB) over 5-60° for selected training areas used in Chapter 6.

CHAPTER 7

DISCUSSION

7.1 Overview

The aim of this chapter is to discuss the results and findings of this study in relation to the original objectives. It ends with a summary of recommendations for future work and conclusions related to benthic habitat mapping using MBS systems.

7.2 Achievements of the study

The primary aim of this study was to examine and develop new methodologies for using MBS backscatter data for benthic habitat mapping. This aim was broken down into seven objectives, which were outlined in Chapter 1. The results achieved towards fulfilling these objectives are discussed below.

1. Collection of MBS backscatter data from a variety of shallow water habitats around the Australian coast.

This objective was achieved through the fieldwork program set out by the Coastal CRC (Penrose 2007). Data from six sites from around the Australian coastal zone were primarily used in this study. The results are summarised in Figure 4.5 in the form of the measured backscatter strength of the seafloor versus incidence angle for a wide variety of benthic habitats found around the Australian coast. Benthic habitats surveyed in this study included: seagrass meadows, rhodolith beds, coral reef, rock, gravel, sand, muddy sand, and mixtures of those habitats. Habitats that were not included in this study that might be of interest for future work are sponge gardens, fine sediments, such as clay and silt, and bedrock with kelp compared to bare bedrock. Also, comparing backscatter characteristics collected from the same set of habitats but with different MBS systems would be of interest.

2. Development of methods for processing backscatter data collected with high-frequency MBS systems.

Methods for processing MBS backscatter data developed for the CWHM project by the CMST are detailed in Section 3.5 of Chapter 3. The CMST algorithm calculates

the seafloor backscatter strength derived from the peak and integral intensity of backscattered signals for each beam. The algorithm was shown to adequately correct for changes in transmit power, pulse length and receive gain, and provide seafloor backscatter strength measurements independent of range and footprint and insonification areas. The CMST algorithm has been implemented into a standalone PC program available from the CMST (Gavrilov, Siwabessy & Parnum 2005). Other studies, such as those by Beaudoin *et al.* (2002) and Augustin *et al.* (2005), have used a sidescan like approach to maximise the resolution of backscatter imagery produced by MBS system. This can provide a better spatial resolution and more information about seafloor properties when the insonification area is significantly smaller than the footprint. However, implementation of such an approach is not trivial because it requires adequate correction for the beam pattern. The angle cube method developed by the candidate for producing images of backscatter properties free from angular dependence artefacts is discussed under Objective 6.

3. Examination of system settings effects on collection of MBS backscatter data.

Although the CMST algorithm used to measure seafloor backscatter strength was shown to adequately correct for power, gain and, to some extent, the transmit pulse length, there were still some system effects found to persist. Three such system effects were considered in Section 3.6: signal saturation (truncation), non-uniformity of across-track beam patterns and the effect of pulse duration. Signal saturation can be easily prevented through selecting the appropriate power and gain settings. The across-track relative beam sensitivity was assessed for the Reson 8125 through a calibration exercise (Section 3.4). It was concluded that the Reson 8125 system has a small difference in the sensitivity between beams, which could be ignored, unlike the Reson 8101 system (Foote *et al.* 2003) which has a transmit beam with a significantly non-uniform beam pattern. When using a MBS system for backscatter strength measurements, it is recommended that the transmit beam pattern and sensitivity of receive beams are measured in order to make adequate corrections of the angular response.

For the Reson 8125, when the pulse is shorter than 100μs, the backscatter strength derived from both the peak and integral intensity is dependent on the pulse duration. Based on the results of the calibration experiment discussed in Section 3.4, it was concluded that this was a result of the limited frequency bandwidth of the MBS system. Consequently, an appropriate pulse duration should be selected when collecting backscatter data. A pulse duration of greater than 100 μs is recommended when recording backscatter with the Reson 8125. Similarly, a pulse duration greater than 150μs is recommended for collecting backscatter data with the Reson 8101. Otherwise, the backscatter strength measurements should also be corrected for the transfer function of the transmit and receive systems of the MBS, which is not trivial to implement without thorough calibration. This is an important finding as a pulse duration shorter than these recommendations is often used to achieve the maximum range resolution for bathymetry measurements (RESON Inc. 2002). Consideration should, therefore, be given to the MBS system bandwidth before selecting the transmit pulse length for backscatter measurements.

4. Investigation of the relationship between seafloor backscatter characteristics and the angle of incidence in high-frequency MBS systems.

This objective was the focus of Chapter 4, which examined the effects of incidence angle on backscatter waveforms, mean backscatter strength and the distribution of backscatter intensity. The backscatter waveforms were shown to be different in shape and amplitude in different beams. Changes in waveform shape relate more to changes in the footprint size and insonification area with the beam angle rather than to changes in seafloor properties. The peak and the integral intensity derived from the backscatter waveform are dependent on incidence angle. The mean value of backscatter strength estimated from the integral backscatter intensity was shown to correspond to the actual backscatter strength of the seafloor and its angular dependence. However, the mean backscatter strength derived from the peak intensity was found to be overestimated at oblique angles where the insonification area is much smaller than the footprint size. This is a property of the extreme value distribution for multiple samples. Some systems, such as the Reson 8125 and 8101, offer an option to store only the peak

values in each beam. If this option is selected, the effect of extreme value statistics must be taken into account. Hence, collection and processing of backscatter waveform (snippet) data is recommended where it is possible.

The mean backscatter angular dependence collected with the Reson 8125 at 455 kHz showed distinct differences between hard rough substrates, seagrass, coarse sediments and fine sediments (Figure 4.5). The highest backscatter strength was observed not only for the hard and rough substrate, but also for marine vegetation, such as rhodolith and seagrass. The main difference in acoustic backscatter from the different habitats was the mean level, or angle-average backscatter strength. However, additional information can also be obtained from the rate of change of backscatter strength with incidence angle.

The measured backscatter angular responses were compared with predictions from the APL model. Although the observed and predicted results were generally in agreement, they were not considered accurate enough to aid in benthic habitat mapping. There are three particular issues that need to be considered when implementing the existing backscatter models in order to carry out model based classification of the seafloor:

- Inadequacy of existing models for surface roughness of high Rayleigh numbers
- Complex effects of beam geometry (e.g. small insonification area, near-field effects, etc.)
- Lack of models of backscatter from epi-benthic structure

Some previous studies suggested using statistical features of backscatter variations as a useful discriminator of different habitats (Le Chenadec *et al.* 2005; Milvang *et al.* 1993; Preston *et al.* 2001). The simplest statistical models based on a Gaussian mechanism of backscatter were examined in this study. It was shown that the gamma distribution model for variation of the signal average backscatter intensity is a sufficiently accurate approximation, which is in agreement with the theoretical prediction by Middleton (1999) for Gaussian-like backscatter processes. The gamma model is a two parameter model characterized by scale (λ) and shape (β) parameters. Both λ and β were found to

be dependent on incidence angle. The scale parameter changes with the angle of incidence in accordance with the angular dependence of backscatter. The shape parameter, β, was shown to relate to the ratio of the insonification area (which can be interpreted as a scattering cell) to the footprint size rather than to the backscatter strength. The parameter β is nearly linearly proportional to the ratio of the insonification area to footprint size, when this ratio is less than 5. Although the variation of the average backscatter strength in this regime corresponds to a Gaussian scattering process, the experimental estimates of the shape parameter are about one unit higher than those expected from the number of independent scattering cells estimated from the insonification area and the footprint size. This is likely to be a result of the backscatter process not being purely Gaussian. Above a ratio of 5, the gamma shape parameter β is not significantly dependent on the ratio and there is a noticeable difference in β between different seafloor types. Further research and theoretical consideration are needed to better understand statistical characteristics of backscatter measured in this regime.

5. Evaluation of the ability of various backscatter characteristics to discriminate between different seafloor types and identification of key backscatter parameters that characterize the seafloor at high frequencies of hundreds of kHz.

In this study, backscatter strength derived from the average intensity has been shown to be a robust parameter to discriminate between different seafloor habitats. Due to the stochastic nature of backscatter, the seafloor backscatter properties cannot be adequately estimated using individual samples of backscatter strength. Statistics of the average backscatter intensity were examined in Chapter 4, where it was found that the most useful statistical descriptor for seafloor discrimination is the average value and its angular dependence. As discussed in Chapter 4, higher order moments of the backscatter data collected at 455 kHz for the majority of data measured at incidence angles between 5º and 60º were similar for different habitats. It was only data from far oblique angles where a noticeable difference in the gamma shape factor was observed for different habitats. This angular domain (angles greater than about 45º) contained a very small proportion of the data collected for this study. It would be valuable to carry out a further

investigation of backscatter statistics using datasets with a higher proportion of the data collected in this regime.

Different properties of the angular dependence of mean backscatter strength were investigated in Chapters 4, 5 and 6 and it was evident that the key backscatter parameter to discriminate between different seafloor habitats was the angle-average backscatter strength. This was primarily because at such high frequencies the slope of the angular dependence was similar for the majority of different seafloor habitats surveyed in this study. However, the slope of angular dependence was useful when the angle-average backscatter strength was similar between habitats. Further understanding of the correlation of these acoustic properties with the actual physical and morphological properties of the seafloor would improve seafloor classification accuracy, when ground-truthing observations are not possible or limited.

6. Development of methods to visualise the spatial distribution of seafloor backscatter properties (i.e. backscatter intensity images).

The angle cube method presented in Chapter 5 provided a new approach to producing images of backscatter properties. Previous approaches corrected backscatter data for angular dependence before mosaicing them together, but were found to have certain problems. One of the main issues is that it is not just the mean backscatter strength that is dependent on incidence angle, but as discussed previously, the variance of backscatter strength is also dependent on incidence angle. Thus, when the mean angular trend is removed, the remaining residuals are still dependent on incidence angle. This is usually seen most prominently as persistent speckle noise around nadir. Another issue is that some corrections assume that the slope of angular dependence of backscatter is nearly the same for all habitats, whereas this is not the case for some seafloor types and, moreover, the angular response depends on sonar frequency.

A method was developed in this study that overcame these problems by applying a correction for the angular dependence of both the mean value and standard deviation within relatively small areas along the survey tracks (Parnum *et al.* 2006). This method,

however, suffered from artefacts in backscatter images due to effects of the averaging window crossing boundaries between different habitats. Moreover, it was apparent from the statistical analysis in Section 4.5, that the variations observed about the mean values were similar for different habitats. Therefore, in most cases there was no benefit to preserving those variations, which were considered as noise. Since the distribution of variation can be modelled by the gamma distribution and these variations can be regarded as noise, it is worth examining maximum a posteriori (MAP) noise filtration based on the gamma distribution, such as that used in the radar community (Isar *et al.* 2005; Tso & Mather 2001), for MBS backscatter data.

The angle cube method uses interpolation to predict the mean backscatter strength for each angle at each grid node of the survey area. This allows the spatial visualisation of backscatter properties to be free from artefacts of the angular dependence and provides accurate estimates of the backscatter strength, when the overlap of swath tracks is sufficiently large. However, as data are interpolated, some boundaries in the angle-average backscatter images become smoother and estimates of the angular dependence slope may be unrealistic. These problems are not unique and are also faced by previous methods discussed. Ultimately, the angle-average backscatter strength provides a useful way to visualise the physical nature of the seafloor. This notion is further demonstrated in Figure 7.1, where the backscatter strength is draped over the bathymetry measured in the Morinda Shoal survey.

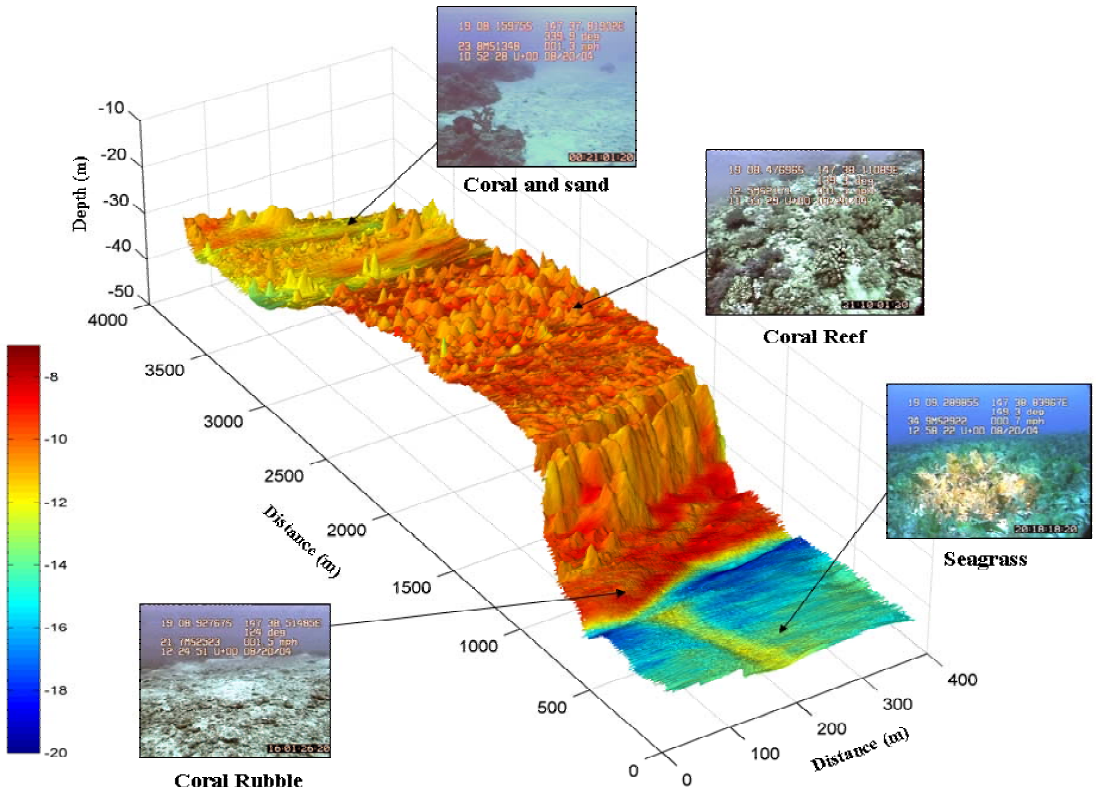

Figure 7.1: Backscatter strength (dB) draped over bathymetry (m) from a MBS survey of Morinda Shoal, Queensland. Representative still images from the underwater video show major habitats found.

7. Demonstration of the use of MBS data in seafloor classification.

In Chapters 5 and 6, habitat probability and classification maps based on MBS data showed distributions of sand, marine vegetation (e.g. seagrass and rhodolith) and hard substrate (e.g. coral and bedrock) in different survey areas. There was not enough ground-truth information to comprehensively assess the classification accuracy for every seafloor type at all sites. However the distance between major habitat classes in feature space showed that discrimination of classes was generally adequate enough for the purposes of broad scale mapping. Moreover, compared to the results of seafloor classification from MBS backscatter images that have been obtained in many previous studies (Dartnell & Gardner 2004; Diaz 1999; Houziaux *et al.* 2007; Whitmore 2003),

the angle cube approach to deriving the backscatter characteristics substantially reduces artefacts due to angular dependence. Therefore, the angle cube method provides backscatter datasets more suitable for automatic (either supervised or unsupervised) segmentation, which are likely to have a noticeably lower rate of misclassification and require less contextual editing. Nonetheless, there are a number of issues that could be investigated to further improve work in this area, which are discussed below.

Collection of additional ground-truth data after the initial processing of acoustic data would have improved the classification results and the confidence of the accuracy assessment. For instance, sampling areas of habitats that were discriminated by backscatter analysis but not identified through ground-truthing may help determine if the acoustic class correspond to a different habitat class. Also, sampling with a vibrocore would allow preservation of the top layer of the seafloor to help correlate seafloor properties with the acoustic parameters. In planning future benthic habitat mapping projects, it is recommended that collection of ground-truth information should be scheduled after initial classification maps are produced from MBS data to optimise ground-truthing sampling arrangement, as considered by Holmes *et al.* (2006). However, it is recognised that the financial and time limitations of projects do not always allow this to happen, as was the case with the CWHM project.

More sophisticated pattern recognition tools, such as neural networks, decision trees, etc., could be investigated to see if they improve the results shown in this study. Although the use of non-linear approaches might improve the classification accuracy, they must be used with caution as they can be over specific to training data. Another way to use MBS data for seafloor mapping and classification is to utilise physical and ecological models, where available, for the surveyed area. For example, the AVO model developed by Fonseca *et al.* (2005) shows potential to predict seafloor properties based on correlation between various characteristics of the sediment and MBS backscatter measurements. Applying physical models to backscatter strength data obtained using the angle cube approach might not only improve seafloor classification results, but also help with the validation of the model. Ecological models have previously used bathymetry

and derivatives of it (e.g. slope, aspect) to predict presence of benthic species (K.W. Holmes *et al.* 2005). Incorporating seafloor segmentation based on backscatter characteristics such as the angle-average backscatter strength, may help improve the results of these models.

Despite the improvements that can be made to seafloor classification work, there are some inherent issues that will always be present. For instance, increasing the number of classes and complexity of the seafloor environment decreases the accuracy of classification, which was evident from the results discussed in Chapter 6. As the number of classes increases, the probability of overlap between different classes in feature space increases. Increasing the dimensions of feature space by adding new effective and statistically independent backscatter parameters is expected to improve classification results to a greater extent than using different pattern recognition algorithms. Ultimately, seafloor habitat maps provide predictive distribution of habitats based on the maximum probability. Furthermore, marine environments are dynamic, thus, the distribution of different habitats may change over time. There is, therefore, a need for further research into optimising monitoring strategies using MBS surveys, which would need to assess the minimum change in the habitat distribution that can be detected in the presence of the habitat map errors.

7.3 Summary of recommendations for further work

Considering the results and findings of this study, the following recommendations for future work can be made to further develop the methods of benthic habitat mapping using MBS systems.

Modelling seafloor backscatter and statistical analysis

- Studies aimed at further understanding of acoustic scattering from epi-benthic covers of the seafloor, such as marine vegetation, including examination of temporal and species variations.
- Further examination of the appropriateness and limitations of Gaussian statistics to describe variations of backscatter characteristics derived from MBS data.

Specifically, further investigation is needed to understand the relationship between the system parameters and measurement geometry resulting in the insonification area and footprint size, the seafloor roughness scale (height and correlation length) and the distribution of backscatter variations. In particular, it is worthwhile to investigate using other MBS systems in different environmental conditions (different sea depth and habitat types), whether the gamma distribution is a good approximation for variations of the average backscatter intensity, and what situations more complex distribution models, such as the "generalized *K*-distribution", are needed.

Processing multibeam sonar backscatter

- Develop a method to utilise more backscatter intensity values within the beams, where the insonification area is significantly smaller than the footprint, which will adequately correct the instantaneous amplitude of backscatter signals for the beam pattern.
- Examination of the potential of gamma noise filtration in order to reduce noise in seafloor backscatter images derived from the average backscatter intensity.

Seafloor classification using multibeam sonar data

- Application of more sophisticated pattern recognition and classification algorithms, such as neural networks and decision trees to the backscatter data represented in the form of the angle cubes
- Introduction of seafloor segmentation by backscatter parameters, such as the angle-average backscatter strength, to ecological modelling to predict the presence of benthic species.
- Carry out repetitive MBS surveys over the same area to examine errors of habitat mapping for efficient planning of future monitoring of seafloor habitat distributions and their changes over time.

Of these recommendations, the areas that are likely to yield the most in terms of cost-benefit are the further statistical analysis of backscatter data, implementation of

ecological models and optimized ground-truthing. Further investigation of the statistical distributions of the average and instantaneous intensity could help determine if there are other parameters that could be derived for seafloor classification and could aid processing of backscatter through noise filtration. Overall, a multidiscipline approach to habitat mapping would help realise the full potential of MBS systems in mapping and monitoring the seafloor.

7.4 Conclusions

This study into benthic habitat mapping using MBS systems has fulfilled its aim and objectives. It has developed techniques to process MBS backscatter, improved methods for spatial visualisation of seafloor backscatter characteristics and examined the effectiveness of MBS backscatter data in seafloor classification. The study has demonstrated that the combination of high-resolution bathymetry and backscatter strength data, as collected by MBS, is an effective tool for benthic habitat mapping in coastal zones.

REFERENCES

Abraham, DA & Lyons, AP 2002, 'Novel Physical Interpretations of K-Distributed Reverberation', *IEEE Journal of Oceanic Engineering,* vol. 27, no. 4, pp. 800-13.

Anstee, S 2001, *Removal of range-dependent artifacts from sidescan sonar imagery*, DSTO-TN-0354, Maritime Operations Division, Aeronautical and Maritime Research Laboratory.

APL 1994, *APL-UW High-Frequency Ocean Environment Acoustic Models Handbook*, APL_UW TR9407.

Atallah, L, Smith, PJP & Bates, CR 2002, 'Wavelet analysis of bathymetric sidescan sonar data for the classification of seafloor sediments in Hopvagen Bay - Norway', *Marine Geophysical Researches,* vol. 23, no. 5-6, pp. 431-42.

Augustin, J-M, Le Suave, R, Lurton, X, Voisset, M, Dugelay, S & Satra, C 1996, 'Contribution of multibeam acoustic imagery to the exploration of the sea bottom', *Marine Geophysical Researches,* vol. 18, pp. 459-86.

Augustin, J-M & Lurton, X 2005, 'Image amplitude calibration and processing for seafloor mapping sonars', *Oceans 2005 - Europe*, Brest, pp. 698-701.

Augustin, JM, Dugelay, S, Lurton, X & Voisset, M 1997, 'Applications of an image segmentation technique to multibeam echo-sounder data', *OCEANS '97. MTS/IEEE Conference Proceedings*, pp. 1365-9 vol.2.

Beaudoin, JD, Hughes-Clarke, JE, Van Den Ameele, EJ & Gardner, JV 2002, 'Geometric and radiometric correction of multibeam backscatter derived from Reson 8101 systems', *Canadian Hydrographic Conference*, Canadian Hydrographic Association, Ottawa, Ontario.

Bentrem, FW, Avera, WE & Sample, J 2006, 'Estimating Surface Sediments Using Multibeam Sonar', *Sea Technology,* vol. 47, no. 6, pp. 37-40.

Blondel, P, Parson, LM & Robigou, V 1998, 'TexAn: textural analysis of sidescan sonar imagery and generic seafloor characterisation', *OCEANS '98 Conference Proceedings*, pp. 419-23 vol.1.

Brekhovskikh, L & Lysanov, Y 2001, *Fundamentals of ocean acoustics,* 3rd edn, Springer, New York, pp. 278.

Broschat, SL & Thorsos, EI 1997, 'An investigation of the small slope approximation for scattering from rough surfaces. Part II. Numerical studies', *Journal of the Acoustical Society of America,* vol. 101, no. 5, pp. 2615-25.

Burroughs, PA & McDonnell, A 1998, *Principles of geographic information systems*, Oxford University Press, pp. 356.

Canepa, G & Pace, NG 2000, 'Seafloor segmentation from multibeam bathymetric sonar', *Proceedings of the Fifth European Conference on Underwater Acoustics*, ed. ME Zakharia, Lyon, France, pp. 361-6.

Caress, DW & Chayes, DN 1995, 'New software for processing sidescan data from sidescan-capable multibeam sonars, ' *IEEE Oceans 95 Conference*, pp. 997-1000.

Chakraborty, B, Kodagali, V & Baracho, J 2003, 'Sea-floor classification using multibeam echo-sounding angular backscatter data: A real-time approach employing hybrid neural network architecture', *IEEE Journal of Oceanic Engineering,* vol. 28, no. 1, pp. 121-8.

Chotiros, NP, Boehme, H, Goldsberry, TG, Pitt, SP, Lamb, RA, Garcia, AL & Attenburg, RA 1985, 'Acoustic backscattering at low grazing angles from the ocean bottom. Part II. Statistical characteristics of bottom backscatter at a shallow water site', *The Journal of the Acoustical Society of America,* vol. 77, no. 3, pp. 975-82.

Clark, R 2002, *XTF File Format Description Document*, Triton Elics.

Dartnell, P & Gardner, JV 2004, 'Predicting seafloor facies from multibeam bathymetry and backscatter data', *Photogrammetric Engineering and Remote Sensing,* vol. 70, no. 9, pp. 1081-91.

de Moustier, CP 1986, 'Beyond bathymetry: mapping acoustic backscattering from the deep seafloor with Sea Beam', *The Journal of the Acoustical Society of America,* vol. 79, no. 2, pp. 316-31.

de Moustier, CP & Alexandrou, D 1991, 'Angular dependence of 12-kHz seafloor acoustic backscatter', *The Journal of the Acoustical Society of America,* vol. 90, no. 1, pp. 522-31.

Diaz, JVM 1999, *Analysis of multibeam sonar data for the characterization of seafloor habitats*, MEng Thesis, University of New Brunswick.

Duda, RO, Hart, PE & Stork, DG 2001, *Pattern classification*, John Wiley, New York, pp. 680.

Dunlop, J 1997, 'Statistical modelling of sidescan sonar images', *Proceedings of MTS/IEEE Oceans '97*, pp. 33-8.

Embrechts, P, Kluppelberg, C & Mikosch, T 1997, *Modelling Extremal Events*, Springer-Verlag, Berlin.

Essen, HH 1994, 'Scattering from a rough sedimental seafloor containing shear and layering', *Journal of the Acoustical Society of America,* vol. 95, no. 3, pp. 1299-310.

Fonseca, L & Calder, B 2005, 'Geocoder: An Efficient Backscatter Map Constructor', *U.S. Hydrographic Conference*, San Diego, CA, USA.

Fonseca, L, Calder, B & Wetzler, M 2006, 'Experiments for Multibean Backscatter Adjustments on the NOAA Ship Fairweather', *Oceans 2006*, IEEE, Boston, USA.

Fonseca, L, Mayer, LA & Kraft, BJ 2005, 'Seafloor characterisation through the application of AVO analysis to multibeam sonar data', *Boundary influences in high frequency, shallow water acoustics*, eds. NG Pace & P Blondel, University of Bath, UK.

Foote, KG, Chu, D, Baldwin, KC, Mayer, LA, McLeod, A, Hufnagle, LC, Jr., Jech, JM & Michaels, W 2003, 'Protocols for calibrating multibeam sonar', *The Journal of the Acoustical Society of America,* vol. 114, no. 4, pp. 2307-8.

Foster-Smith, RL & Sotheran, IS 2003, 'Mapping marine benthic biotopes using acoustic ground discrimination systems', *International Journal of Remote Sensing,* vol. 24, no. 13, pp. 2761-84.

Gallaudet, TC & de Moustier, CP 2003, 'High-frequency volume and boundary acoustic backscatter fluctuations in shallow water', *Journal of the Acoustical Society of America,* vol. 114, no. 2, pp. 707-25.

Gavrilov, AN, Duncan, AJ, McCauley, RD, Parnum, IM, Penrose, JD, Siwabessy, PJW, Woods, AJ & Tseng, Y-T 2005, 'Characterization of the Seafloor in Australia's Coastal Zone using acoustic techniques', *Proceedings of the International Conference "Underwater Acoustic Measurements: Technologies & Results"*, Crete, Greece.

Gavrilov, AN, Siwabessy, PJW & Parnum, IM 2005, *Multibeam echo sounder backscatter analysis*, Centre for Marine Science and Technology, Perth, Australia, CA3.03.

Gensane, M 1989, 'A statistical study of acoustic signals backscattered from the sea bottom', *IEEE Journal of Oceanic Engineering,* vol. 14, no. 1, pp. 84-93.

Gragg, RF, Wurmser, D & Gauss, RC 2001, 'Small-slope scattering from rough elastic ocean floors: General theory and computational algorithm', *Journal of the Acoustical Society of America,* vol. 110, no. 6, pp. 2878-901.

Haralick, RM, Shanmugam, K & Dinstein, I 1973, 'Textural features for image classification', *IEEE Transactions on Systems, Man and Cybernetics - Part C,* vol. 6, pp. 610-21.

Harris, PT, Pattiaratchi, CB, Cole, AR & Keene, JB 1992, 'Evolution of subtidal sandbanks in Moreton Bay, eastern Australia', *Marine Geology,* vol. 103, no. 1-3, pp. 225-47.

Hellequin, L, Boucher, JM & Lurton, X 2003, 'Processing of high-frequency multibeam echo sounder data for seafloor characterization', *IEEE Journal of Oceanic Engineering,* vol. 28, no. 1, pp. 78-89.

Holdgate, M 1994, 'Environmental challenges and priorities for action', *Marine Pollution Bulletin,* vol. 29, no. 6-12, pp. 258-61.

Holmes, KW, Radford, B, Van Niel, K & Kendrick, GA 2005, 'Predictive Mapping of Seafloor Substrate and Biota at Point Addiss Marine Park, Victoria', in *Research for coastal management*. CRC for Coastal Zone, Estuary and Waterway Management, Coolangatta, Queensland, Australia, 14 September 2005.

Holmes, KW, Van Niel, K, Kendrick, GA & Baxter, KJ 2006, *Designs for remote sampling: review, discussion, examples of sampling methods and layout and scaling issues*, CRC for Coastal Zone, Estuary and Waterway Management, 87.

Houziaux, J-S, Degrendele, K, Norro, A, Mallefet, J, Kerckhof, F & Roche, M 2007, 'Gravel fields of the western Belgian border, southern bight of the North Sea: A multidisciplinary approach to habitat characterisation and mapping', *2nd International Conference & Exhibition on "Underwater Acoustic Measurements: Technologies & Results"*, Crete, Greece.

Hughes Clarke, JE 1994, 'Towards remote seafloor classification using the angular response of acoustic backscatter: a case study from multiple overlapping GLORIA Data', *IEEE Journal of Oceanic Engineering,* vol. 19, no. 1, pp. 112-27.

Hughes Clarke, JE, de Moustier, CP, Mayer, LA & Wells, DE 2004, *34th Multibeam Sonar Training Course*, Ottawa, Canada.

Hughes Clarke, JE, Mayer, LA, Mitchell, NC, Godin, A & Costello, G 1993, 'Processing and interpretation of 95 kHz backscatter data from shallow-water multibeam sonars', *IEEE Oceans conference*, pp. 437-42.

Hughes Clarke, JE, Mayer, LA & Wells, DE 1996, 'Shallow-water imaging multibeam sonars: a new tool for investigating seafloor processes in the coastal zone and on the continental shelf', *Marine Geophysical Researches,* vol. 18, no. 6, pp. 607-29.

Ierodiaconou, D, Burq, S, Reston, M & Laurenson, L 2006, 'Marine habitat mapping using multibeam data, georeferenced video and image classification techniques: A case study in south-west Victoria.' *Coastal GIS*, University of Wollongong, Australia.

Isar, A, Isar, D, Moga, S, Augustin, JM & Lurton, X 2005, 'Multi-scale MAP Despeckling of SONAR Images', *Oceans - Europe* Brest, France.

Jackson, DR & Briggs, KB 1992, 'High-frequency bottom backscattering: roughness versus sediment volume scattering', *The Journal of the Acoustical Society of America,* vol. 92, no. 2, pp. 962-77.

Jackson, DR, Briggs, KB, Williams, KL & Richardson, MD 1996, 'Tests of models for high-frequency seafloor backscatter', *IEEE Journal of Oceanic Engineering,* vol. 21, no. 4, pp. 458-70.

Jackson, DR, Winebrenner, DP & Ishimaru, A 1986, 'Application of the composite roughness model to high-frequency bottom backscatter', *Journal of the Acoustical Society of America,* vol. 79, pp. 1410-22.

Jakeman, E 1988, 'Non-Gaussian models for the statistics of the scattered waves', *Advances in Physics,* vol. 37, no. 5, pp. 471-529.

Jakeman, E & Pusey, PN 1976, 'A model for non-Rayleigh sea echo', *IEEE Transactions on Antennas and Propagation,* vol. 24, no. 6, pp. 806-14.

Johnson, N, Kotz, S & Balakrishnan, N 1995, *Continuous Univariate Distributions,* vol. 2, 2nd edn, Wiley, New York, pp. 752.

Kendrick, GA, Aylward, MJ, Hegge, BJ, Cambridge, ML, Hillman, K, Wyllie, A & Lord, DA 2002, 'Changes in seagrass coverage in Cockburn Sound, Western Australia between 1967 and 1999', *Aquatic Botany,* vol. 73, no. 1, pp. 75-87.

Kennedy, P 2005, *Marmion marine park hydro acoustic field trials 2004 and 2005*, Fugro Survey Pty Ltd, pp. 33.

Kenny, AJ, Cato, I, Desprez, M, Fader, G, Schuttenhelm, RTE & Side, J 2003, 'An overview of seabed-mapping technologies in the context of marine habitat classification', *ICES Journal of Marine Science,* vol. 60, no. 2, pp. 411-8.

Kostylev, VE, Todd, BJ, Fader, GBJ, Courtney, RC, Cameron, GDM & Pickrill, RA 2001, 'Benthic habitat mapping on the Scotian Shelf based on multibeam bathymetry, surficial geology and sea floor photographs', *Marine Ecology-Progress Series,* vol. 219, pp. 121-37.

Kur'yanov, B.F. (1962), 'The scattering of sound at a rough surface with two types of irregularity', *Soviet Physics Acoustics,* 8, 252-257.

Le Chenadec, G, Bouchery, J-M, Lurton, X & Augustin, J-M 2005, 'Angular dependence of statistical distributions for backscattered signals: Modelling and application to multibeam echosounder data', *Oceans 2005*, IEEE, Brest, pp.1234.

Lurton, X 2002, *An introduction to underwater acoustics: principles and applications*, Springer-Verlag and Praxis Publishing Ltd, pp. 347.

Lurton, X, Dugelay, S & Augustin, JM 1994, 'Analysis of multibeam echo-sounder signals from the deep seafloor', *Proceedings of OCEANS '94. 'Oceans*

Engineering for Today's Technology and Tomorrow's Preservation.' pp. 213-18

Lyons, AP & Abraham, DA 1999, 'Statistical characterization of high-frequency shallow-water seafloor backscatter', *Journal of the Acoustical Society of America,* vol. 106, no. 3, pp. 1307-15.

Lyons, AP, Anderson, AL & Dwan, FS 1994, 'Acoustic scattering from the seafloor: modeling and data comparison', *The Journal of the Acoustical Society of America,* vol. 95, no. 5, pp. 2441-51.

Mackenzie, KV 1961, 'Bottom reverberation for 530 and 1030 cps sound in deep water.' *Journal of the Acoustical Society of America,* vol. 33, pp. 1498-504.

Malthus, TJ & Mumby, PJ 2003, 'Remote sensing of the coastal zone: an overview and priorities for future research', *International Journal of Remote Sensing,* vol. 24, no. 13, pp. 2805-15.

Mayer, LA 2006, 'Frontiers in seafloor mapping and visualization', *Marine Geophysical Researches,* vol. 27, pp. 7-17.

McDaniel, ST & Gorman, AD 1983, 'An examination of the composite-roughness scattering model', *Journal of the Acoustical Society of America,* vol. 73, no. 5, pp. 1476-86.

Medwin, H & Clay, CS 1998, *Fundamentals of Acoustical Oceanography,* 1st edn, Academic Press, U.S., pp. 712.

Middleton, D 1999, 'New physical-statistical methods and models for clutter and reverberation: the KA-distribution and related probability structures', *IEEE Journal of Oceanic Engineering,* vol. 24, no. 3, pp. 261-84.

Milvang, O, Bang Huseby, R, Weisteen, K & Solberg, A 1993, 'Feature extraction from backscatter sonar data', *Acoustic Classification and Mapping of the Seabed*, Institute of Acoustics, University of Bath, UK.

Mitchell, NC 1996, 'Processing and analysis of Simrad multibeam sonar data', *Marine Geophysical Researches,* vol. 18, pp. 729-39.

Mumby, PJ, Clark, CD, Green, EP & Edwards, AJ 1998, 'Benefits of water column correction and contextual editing for mapping coral reefs', *International Journal of Remote Sensing,* vol. 19, no. 1, pp. 203-10.

Novarini, JC & Caruthers, JW 1998, 'A simplified approach to backscattering from a rough seafloor with sediment inhomogeneities', *IEEE Journal of Oceanic Engineering,* vol. 23, no. 3, pp. 157-66.

Oglivy, JA 1991, *Theory of wave scattering from random rough surfaces*, IOP Publishing Ltd.

Pace, NG & Gao, H 1988, 'Swathe Seabed Classification', *IEEE Journal of Oceanic Engineering,* vol. 13, no. 2, pp. 83-90.

Parnum, IM, Gavrilov, AN & Siwabessy, PJW 2007, 'Analysis of multibeam data for the purposes of seafloor classification', *Proceedings of the Second International Conference "Underwater Acoustic Measurements: Technologies & Results"*, Crete, Greece.

Parnum, IM, Gavrilov, AN, Siwabessy, PJW & Duncan, AJ 2005, 'The effect of incident angle on statistical variation of backscatter measured using a high-frequency multibeam sonar', *Acoustics 2005: Proceedings of the Annual Conference of the Australian Acoustical Society*, ed. T McMinn, Australian Acoustical Society, Busselton, Australia, pp. 433-8.

Parnum, IM, Gavrilov, AN, Siwabessy, PJW & Duncan, AJ 2006, 'Analysis of high-frequency multibeam backscatter statistics from different seafloor habitats', *Eighth European Conference on Underwater Acoustics*, eds. SM Jesus & OC Rodriguez, Carvoeiro, Portugal, pp. 775-80.

Parnum, IM, Siwabessy, PJW & Gavrilov, AN 2004, 'Identification of Seafloor Habitats in Coastal Shelf Waters Using a Multibeam Echosounder', *Acoustics 2004*, Proceedings of the Annual Conference of the Australian Acoustical Society, Gold Coast, pp. 181-6.

Parsons, MJG, McCauley, RD, Mackie, M & Siwabessy, PJW 2006, 'Evaluation of acoustic backscatter data collected from samsonfish (*Seriola hippos*) spawning aggregations in Western Australia', *Eighth European Conference on Underwater Acoustics*, Carvoeiro Portugal.

Parsons, MJG, Parnum, IM, Siwabessy, PJW, McCauley, RD & Mackie, M 2007, 'Multi-beam visualisation of Samson Fish (*Seriola hippos*) aggregations and spawning habitats in Western Australia ', *Proceedings of the Second International Conference "Underwater Acoustic Measurements: Technologies & Results"*, Crete, Greece.

Penrose, JD 2007, 'Coastal water habitat mapping', in R Souter (ed.), *Building the bridges: seven years of Australian coastal cooperative research*, Cooperative Research Centre for Coastal Zone, Estuary and Waterway Management, pp. 75-9.

Perry, CT 2005, 'Morphology and occurrence of rhodoliths in siliciclastic, intertidal environments from a high latitude reef setting, southern Mozambique', *Coral Reefs,* vol. 24, pp. 201-7.

Pickrill, RA & Todd, BJ 2003, 'The multiple roles of acoustic mapping in integrated ocean management, Canadian Atlantic continental margin', *Ocean & Coastal Management,* vol. 46, no. 6-7, pp. 601-14.

Preston, JM 2004, 'Acoustic Classification by Sonar', *Hydro International,* vol. April, pp. 23-5.

Preston, JM & Christney, AC 2003, *Compensation of sonar image data primarily for seabed classification,* 427624.

Preston, JM, Christney, AC, Beran, LS & Collins, WT 2004, 'Statistical seabed segmentation - from images and echoes to objective clustering', *7th European Conference On Underwater Acoustics*, Delft, The Netherlands, pp. 813-6.

Preston, JM, Christney, AC, Bloomer, SF & Beaudet, IL 2001, 'Seabed classification of multibeam sonar images', *MTS/IEEE Oceans 2001 Conference*, pp. 2616-23.

Reed, TB & Hussong, D 1989, 'Digital image processing techniques for enhancement and classification of SeaMARC II side scan sonar imagery', *Journal of Geophysical Research,* vol. 94, no. B6, pp. 7469-90.

Reichelt, RE & McEwan, AD 1999, 'Australia's marine science and technology plan: an action plan for Australia's Oceans Policy', *Marine and Freshwater Research,* vol. 50, no. 8, pp. 711-6.

RESON Inc. 2002a, *Seabat 8101 operator's manual,* Version 3.02 edn, California, USA.

RESON Inc. 2002b, *SeaBat 8125 operator's manual, version 3.02*, California, USA.

Richards, JA & Jia, X 1999, *Remote sensing digital image analysis : an introduction*, Springer, New York, pp. 476.

Rinehart, R, Wright, D, Lundblad, E, Larkin, E, Murphy, J & Cary-Kothera 2004, 'ArcGIS 8.x Benthic Terrain Modeler: Analysis in American Samoa,' *Proceedings of the 24th Annual ESRI User Conference,*, San Diego, CA,.

Siwabessy, PJW 2001, *An investigation of the relationship between seabed type and benthic and bentho-pelagic biota using acoustic techniques*, PhD Thesis, Curtin University of Technology.

Siwabessy, PJW, Gavrilov, AN, Duncan, AJ & Parnum, IM 2006, 'Analysis of statistics of backscatter strength from different seafloor habitats', *Acoustics 2006*, Australian Acoustic Association, Christchurch, New Zealand, pp. 507-14.

Skene, D, Ryan, DA, Brooke, BP & Radke, L 2005, *Report on the Geomorphology and Sediments of Cockburn Sound* Geoscience Australia, Milestone Report CG4.04A.

Stanic, S & Kennedy, E 1992, 'Fluctuations of high-frequency shallow water seafloor reverberation', *Journal of the Acoustical Society of America,* vol. 91, no. 4, pp. 1967-73.

Stewart, WK 1994, 'A Neural Network Approach to Classification of Sidescan Sonar Imagery from a Midocean Ridge Area', *IEEE Journal of Oceanic Engineering,* vol. 19, no. 2, pp. 214-24.

Stewart, WK, Chu, D, Malik, S, Lerner, S & Singh, H 1994, 'Quantitative seafloor characterization using a bathymetric sidescan sonar', *IEEE Journal of Oceanic Engineering,* vol. 19, no. 4, pp. 599-610.

Talukdar, KK, Tyce, RC & Clay, CS 1995, 'Interpretation of Sea Beam backscatter data collected at the Laurentian fan off Nova Scotia using acoustic backscatter theory', *The Journal of the Acoustical Society of America,* vol. 97, no. 3, pp. 1545-58.

Trevorrow, MV 2004, 'Statistics of fluctuations in high-frequency low-grazing-angle backscatter from a rocky sea bed', *IEEE Journal of Oceanic Engineering,* vol. 29, no. 2, pp. 236-45.

Trevorrow, MV 2005, 'Volumetric multibeam sonar measurements of fish, zooplankton and turbulence', *Proceedings of the International Conference "Underwater Acoustic Measurements: Technologies & Results"*, Crete, Greece.

Tso, B & Mather, PM 2001, *Classification methods for remotely sensed data,* 1st edn, Taylor and Francis, London, pp. 332.

Turner, L, Tracey, D, Tilden, J & Dennison, WC 2004, *Where River Meets Sea: Exploring Australia's Estuaries*, CRC for Coastal Zone, Estuary and Waterway Management, Brisbane, Australia, pp. 278.

Udy, J & Levy, D 2002, *Deep seagrass and coral habitats found in Eastern Moreton Bay*, University of Queensland, Brisbane.

Urick, RJ 1983, *Principles of underwater sound,* 3rd edn, Peninsula Publishing, California, USA.

US Army Corps of Engineers 2002, 'Acoustic multibeam survey systems for deep-draft navigation projects', in *Engineering and Design - Hydrographic Surveying*, US Army Corps of Engineers, Maryland, USA, pp. 33.

Voronovich, AG 1985, 'Small-slope approximation in wave scattering by rough surfaces', *Soviet Physics JETP,* vol. 62, no. 1, pp. 65-70.

Whitmore, CE 2003, *Integration of high-resolution multibeam sonar imagery with observational data from submersibles to classify and map benthic habitats at Heceta Bank, Oregon*, MSc Thesis, Oregon State University.

Williams, KL, Jackson, DR, Thorsos, EI, Tang, D & Briggs, KB 2002, 'Acoustic backscattering experiments in a well characterized sand sediment: data/model comparisons using sediment fluid and biot models', *IEEE Journal of Oceanic Engineering,* vol. 27, no. 3, pp. 376-87.

Wilson, PS & Dunton, KH 2007, 'Seagrass acoustics: results of an experimental laboratory investigation', *Proceedings of the Second International Conference "Underwater Acoustic Measurements: Technologies & Results*, Crete, Greece.

APPENDIX A

DATA DESCRIPTION

A1. Morinda Shoal, Queensland

Table A1.1: Lines and rotation used for gridding data along with the settings of the Reson Seabat 8125 for Morinda Shoal survey.

Line numbers	BGB 7-16,30-37
Survey date	19/08/2004
Rotation of data for gridding	40°
Transmit power	205 dB re 1 µPa
Pulse length	101 µs
Receiver gain	9 dB

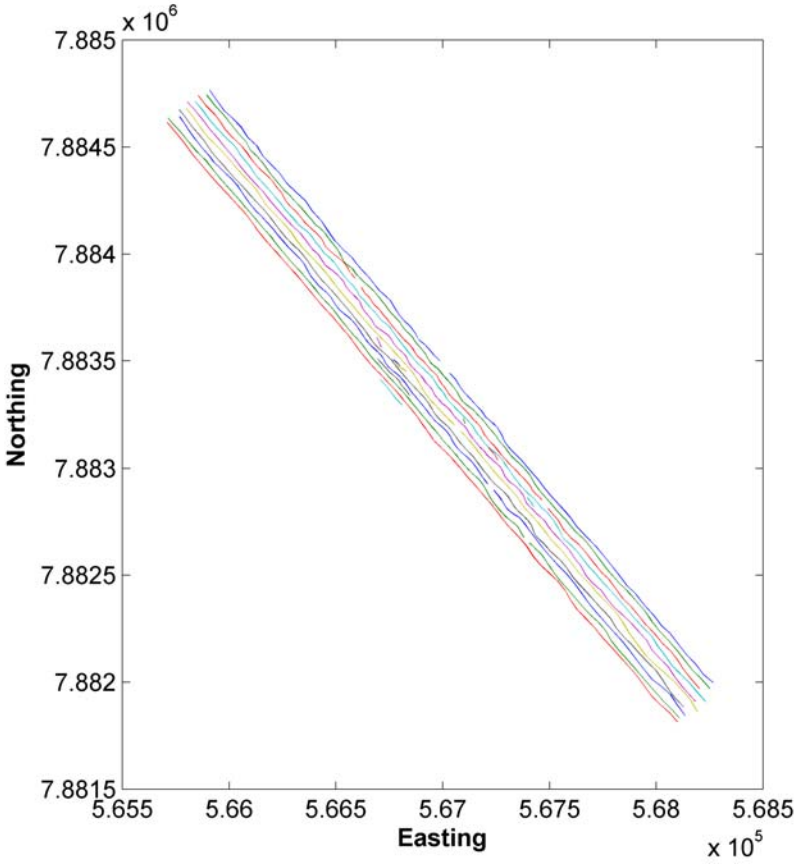

Figure A1.1: Track lines from the Morinda Shoal survey. UTM zone 55 south.

A2. Esperance Bay, Western Australia

A2.1 East of Woody Island (Data used in Chapters 4-6)

Table A2.1: Lines and rotation used for gridding data along with the settings of the Reson Seabat 8125 for east of Woody Island survey.

Line numbers	Esperance 291-310
Survey date	11/05/2005
Rotation of data for gridding	330º
Transmit power	205 dB re 1 µPa
Pulse length	101 ms
Receiver gain	9 dB

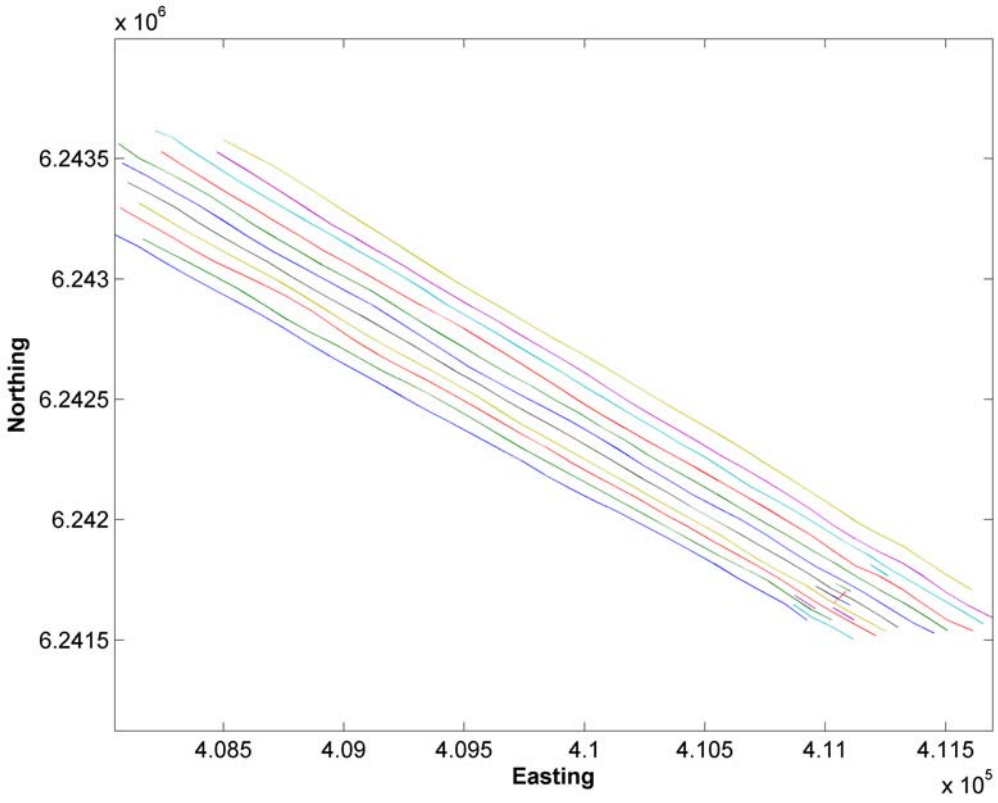

Figure A2.1: Track lines from east of Woody Island survey. UTM zone 51 south.

A2.2 North Thomas Island (Data used in Chapter 5 for angle cube explanation)

Table A2.2: Lines and rotation used for gridding data along with the settings of the Reson Seabat 8125 for north Thomas Island survey.

Line numbers	Woody 38-41
Survey date	1/11/2003
Rotation of data for gridding	None
Transmit power	205 dB re 1 μPa
Pulse length	51 ms
Receiver gain	16 dB

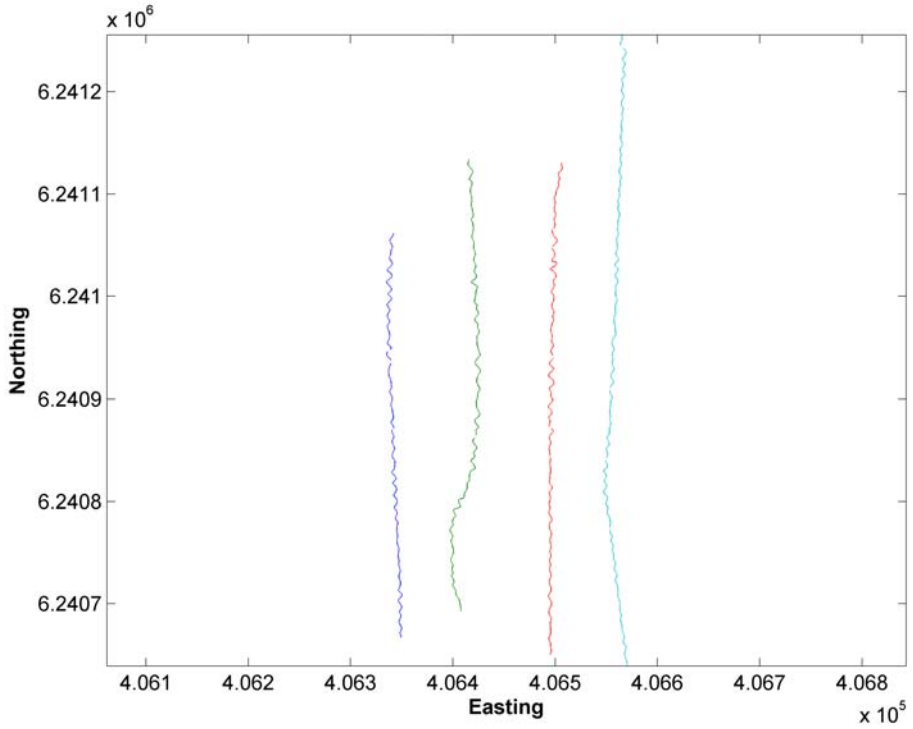

Figure A2.2: Track lines from north Thomas Island survey. UTM zone 51 south.

A2.3 Between Woody and Thomas Island (data from Chapter 4 and 5)

Table A2.3: Lines and rotation used for gridding data along with the settings of the Reson Seabat 8125 for the survey between Thomas and Woody Islands.

Line numbers	Esperance 350-361
Survey date	12/05/2005
Rotation of data for gridding	34º
Transmit power	205 dB re 1 µPa
Pulse length	101 ms
Receiver gain	7 dB

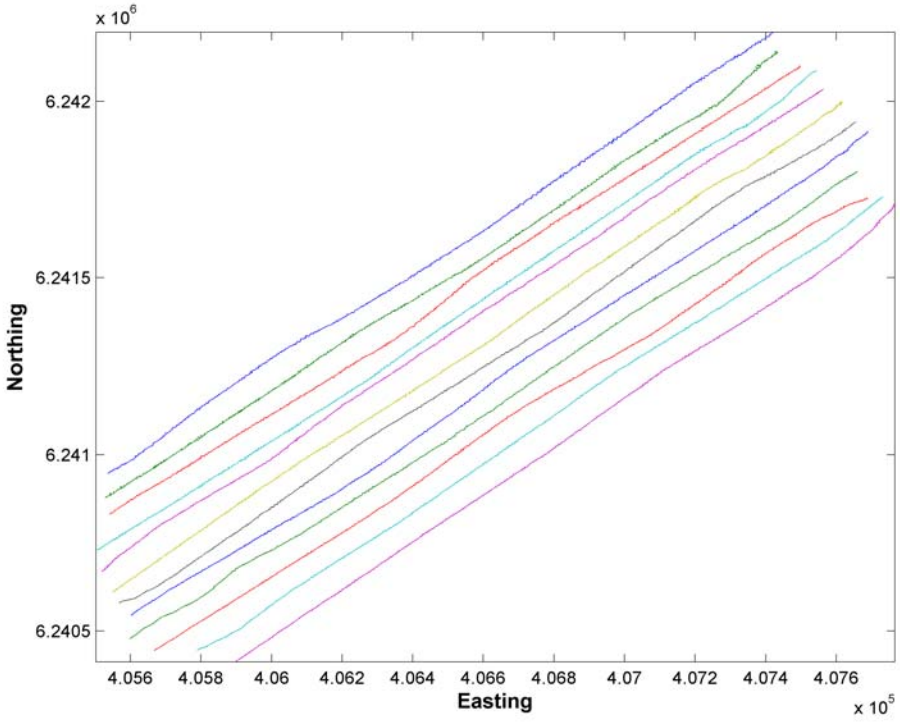

Figure A2.3: Track lines for the survey between Thomas and Woody Islands. UTM zone 51 south.

A3. Owen Anchorage, Western Australia

Table A3.1: Lines and rotation used for gridding data along with the settings of the Reson Seabat 8125 for Owen Anchorage survey.

Line numbers	Cockburn Sound 146-150
Survey date	13/07/2004
Rotation of data for gridding	None
Transmit power	205 dB re 1 µPa
Pulse length	73 ms
Receiver gain	4 dB

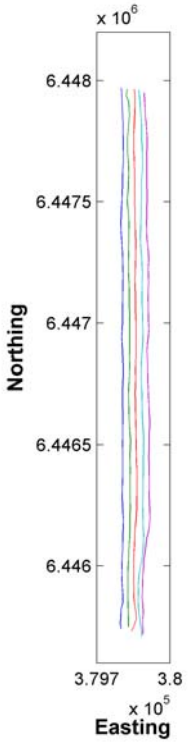

Figure A3.1: Track lines from the Owen Anchorage survey. UTM zone 50 south.

A4. Moreton Bay, Queensland

Table A4.1: Lines and rotation used for gridding data along with the settings of the Reson Seabat 8125 for Moreton Bay survey.

Line numbers	MB 92,93,95-100,102-114,121-125
Survey date	2/09/2004
Rotation of data for gridding	21°
Transmit power	205 dB re 1 µPa
Pulse length	101 ms
Receiver gain	9 dB

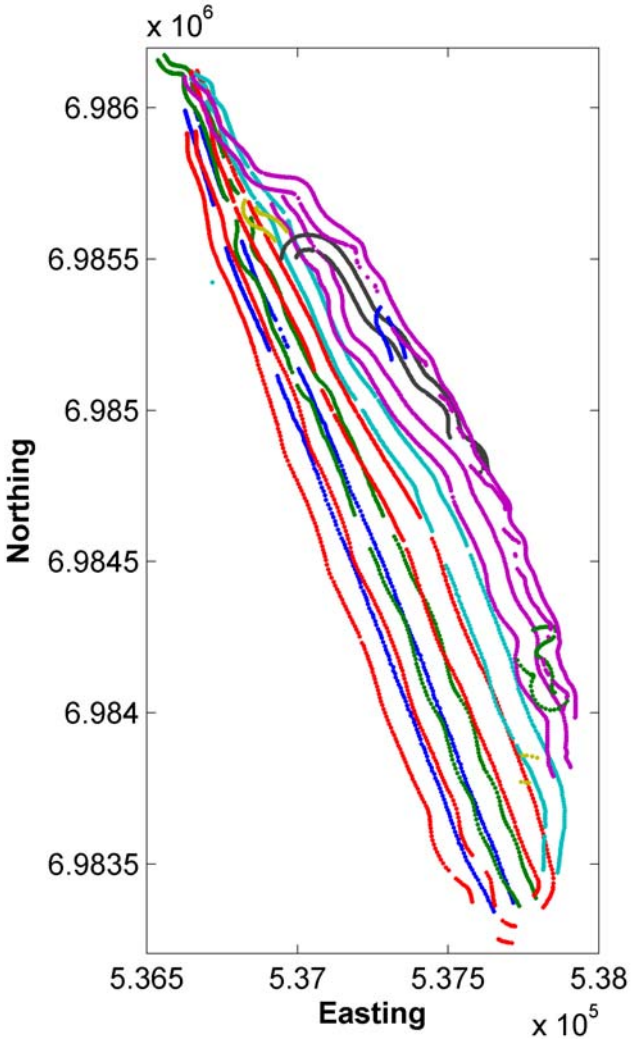

Figure A4.1: Track lines from the Owen Anchorage survey. UTM zone 56 south.

A5. Keppel Bay, Queensland

Table A5.1: Lines and rotation used for gridding data along with the settings of the Reson Seabat 8125 for Keppel Bay survey.

Line numbers	Fitzroy 71-88, 90-143, 223-225, 225-237
Survey date	24/09/2004
Rotation of data for gridding	7°
Transmit power	205 dB re 1 µPa
Pulse length	101 ms
Receiver gain	9 dB

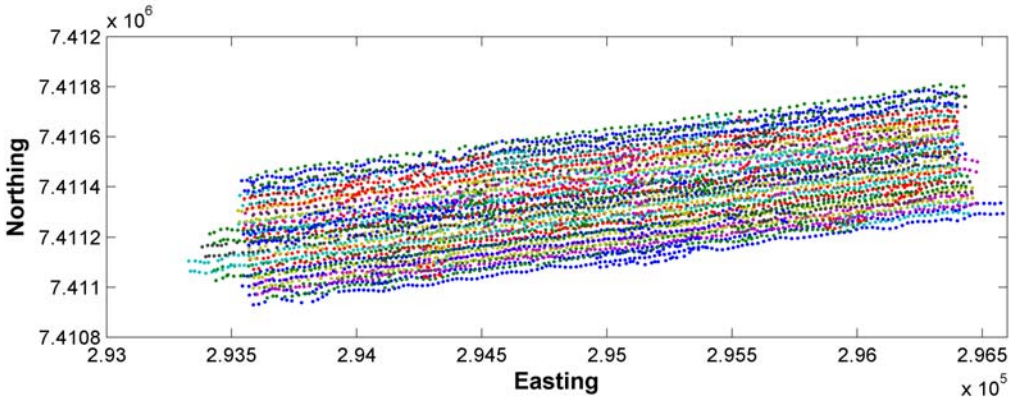

Figure A5.1: Track lines from the Keppel Bay survey. UTM zone 56 south.

APPENDIX B: THE EFFECT OF BEAM PATTERN ON BACKSCATTER INTENSITY MEASUREMENTS

The intensity of backscatter signals is proportional to the surface integral of the product of sonar transmit and receive beam patterns projected onto the seafloor surface (Clay and Medwin, 1998). For rectangular transducers, the beam patterns are commonly expressed in terms of the elevation angles in the two perpendicular directions. For multibeam sonar systems, the insonification area is limited in the along-track direction by the transmit beam width. For calculating the insonification area of narrow transmit beams, it is commonly assumed, including this study (see Chapter 2), that the spatial widow for integration is rectangular with width of $R_s*\Delta\varphi$, where R_s is the slant distance from the sonar head to the bottom and $\Delta\varphi$ is the –3-dB full width of the beam pattern. However, the actual beam pattern is not uniform within the 3-dB beam width and is not zero outside it. For rectangular transducers, the beam pattern is a sinc function of angle, if side-lobe shading is not applied. A Gaussian shape is frequently used to approximate the main lobe of beam patterns with the same width at the –3-dB level:

$$\Psi(\varphi) = \exp\left\{-\frac{\varphi^2}{2\sigma^2}\right\}, \qquad \text{(B1.1)}$$

Where: $\sigma = \left[12\log(10)/5\right]^{-1/2}\Delta\varphi$. Because $\psi(\varphi)$ is rapidly decreasing with φ when $\Delta\varphi$ is small, integration of Equation B.1.1 can formally be extended to $\pm\infty$, which gives $\left[5\pi/6\log(10)\right]^{1/2}\Delta\varphi \approx 1.066\Delta\varphi$, or a value of about 0.3 dB higher than that obtained for a rectangular window. A similar value of the error in the insonification area affected by the beam pattern was obtained by Jackson and Richardson (2007). This error can be neglected, because it is small comparing to other possible errors of measurements.

The effect of the across-track beam pattern of MBS receive beams on the backscatter energy and instantaneous intensity is much more complex, because the insonification area, from which the sonar receives the backscatter signal within any particular beam, is limited by the transmit pulse width and the footprint area of the receive beam. At small and moderate angles of incidence, the width of insonification area can be much larger than the across-track width of the receive beam footprint. At

large angles of incidence, the insonification area can be much smaller than the footprint. The relationship between the insonification area and the receive beam footprint depends on the incidence angle, pulse width and sea depth, as discussed in Chapter 2. A number of different approaches have been suggested to model the influence of insonification area on the backscatter intensity at small and moderate incidence angles, when the insonification area is larger than or comparable to the across-track width of the beam footprint (for example, see Hellequin *et. al*, 2003 and Jackson and Richardson, 2007).

To model effects of the receive beam pattern on the backscatter energy and instantaneous intensity, we will employ an approach similar to time-domain models (e.g. Jackson and Richardson, 2007), but formulated in a simplified way. For simplicity and without loss of generality, let us assume that the seafloor backscatter coefficient is unity and independent of incidence angle, and the seafloor is horizontal. In further calculation, we also ignore the transmission (spreading and absorption loss), which can be added later in the model.

The backscatter intensity is proportional to the integral $I(t_r) = \int_{r_2}^{r_1} \int_{-\pi/2}^{\pi/2} S(\theta)\Theta(\theta')\Phi(\varphi') r dr d\varphi$, where φ is azimuth, r is distance from the nadir, r_1 and r_2 are external and internal radii of the insonification area respectively, $\varphi' = \tan^{-1}(\sin\theta' \tan\varphi)$ is the longitudinal elevation angle, θ' is the transversal elevation angle, $\Phi(\varphi')$ is the longitudinal directivity pattern of the transmit beam, and $\Theta(\theta')$ is the transversal directivity pattern of the receive beams. The beam patterns are approximated by a Gaussian shape:

$$I(t_r) = \int_{r_2}^{r_1} \int_{-\pi}^{\pi} S(\theta) \exp\left\{-(\theta' - \theta_S)^2 / 2\sigma_\theta^2(\theta_S)\right\} \exp\left\{-\varphi'^2 / 2\sigma_\varphi^2\right\} r dr d\varphi,$$

where θ_S is a beam steering angle, $\sigma_\theta(\theta_S) = [5\lg(e)/3]^{1/2} \Delta\theta(\theta_S)/2$, $\Delta\theta(\theta_S)$ is the –3-dB full width of the receive beams, $\sigma_\varphi = [5\lg(e)/3]^{1/2} \Delta\varphi/2$, and $\Delta\varphi$ is the –3-dB full width of the transmit beam. After changing the integration variable to φ' and expressing r through φ', θ' and sea depth D, the integral over φ' can be approximately evaluated for small $\Delta\varphi$ and $\theta' > \Delta\varphi$:

$$I(t_r) \approx \sqrt{2\pi}\sigma_\varphi D \int_{r_2}^{r_1} S(\theta) \exp\left\{-(\theta' - \theta_S)^2 / 2\sigma_\theta^2(\theta_S)\right\} / \cos\theta' \, dr \qquad \text{(B1.2)}$$

For $\theta' > \Delta\varphi$, one can use an approximation $\theta' \approx \theta = \tan^{-1}(r/D)$. The transmitted pulse front reaches the bottom at $t_0 = D/c$ and then propagates along r with time t as $r_1 = \left[(ct)^2 - D^2\right]^{1/2}$. The trailing edge of the insonification area propagates as $r_2 = \mathrm{Re}\left[(ct - c\tau/2)^2 - D^2\right]^{1/2}$, i.e. $r_2 = 0$, when $t_0 \le t \le t_0 + \tau/2$. The backscatter signal returns to the sonar at time $t_r = 2t$, so that we can express r_1 and r_2 as a function of t_r: $r_1 = \left[(ct_r/2)^2 - D^2\right]^{1/2}$ and $r_2 = \mathrm{Re}\left[(ct_r/2 - CT/2)^2 - D^2\right]^{1/2}$. For small $\Delta\theta$, we can use only the first two terms in the power series expansion for $\tan^{-1}(r/D)$ around θ_S, and integrate Eq.B1.2 after replacing r with $r' = \dfrac{(r - D\tan\theta_S)\cos^2\theta_S}{2^{1/2} D\sigma_\theta}$, which gives:

$$I(t_r) = \pi D^2 \sigma_\theta \sigma_\varphi \cos^{-3}\theta_S \left\{ \mathrm{erf}(r')\big|_{r_1} - \mathrm{erf}(r')\big|_{r_2} \right\}. \qquad \text{(B1.3)}$$

Equation B1.3. includes only half of the whole insonification area on either port or starboard side. At near-nadir angles of beam steering, the opposite side also contributes to the backscatter signal. To include the contribution of the opposite side, we change the sign of θ_s in the expression for r' and add the second integral to Eq.B1.3, which gives:

$$I(t_r) = \pi D^2 \sigma_\theta \sigma_\varphi \cos^{-3}\theta_S \left\{ \mathrm{erf}(r')\big|_{r_1(\theta_S)} - \mathrm{erf}(r')\big|_{r_2(\theta_S)} + \mathrm{erf}(r')\big|_{r_1(-\theta_S)} - \mathrm{erf}(r')\big|_{r_2(-\theta_S)} \right\}. \qquad \text{(B1.4)}$$

Figure B1(a) shows the amplitude distortion of the backscatter signal envelope due to the influence of the receive beam pattern and insonification area for the odd beams (121 – 239) of the Reson 8125 system at sea depth of 20 m and pulse length of 100 μs. The right panel (b) shows the envelopes only for the near-nadir beams.

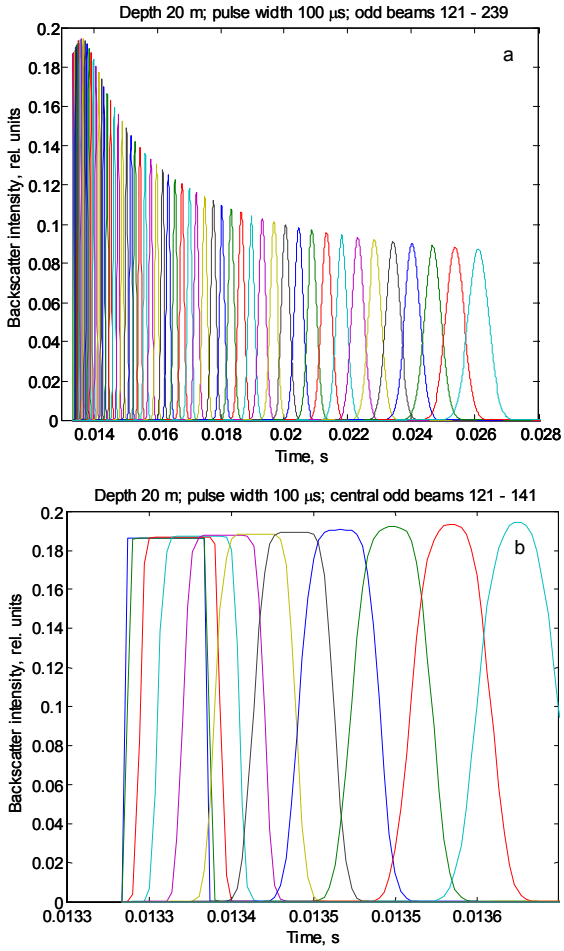

Figure B1: Distortion of backscatter signal envelope due to receive beam pattern shown for odd beams 121 – 239 (a) and 121 – 141 (b) for sea depth of 20 m and pulse width of 100 μs.

The variation of the peak backscatter intensity in each beam with the angle of incidence is shown in Figure B2 after correction for the insonification area limited by the beam footprint, as it was suggested in Chapter 2 using an ideal rectangular model for the beam pattern. As before, we ignore the transmission loss (or assume that it was fully compensated) and assume that the backscattering strength is 0 dB and independent of the incidence angle.

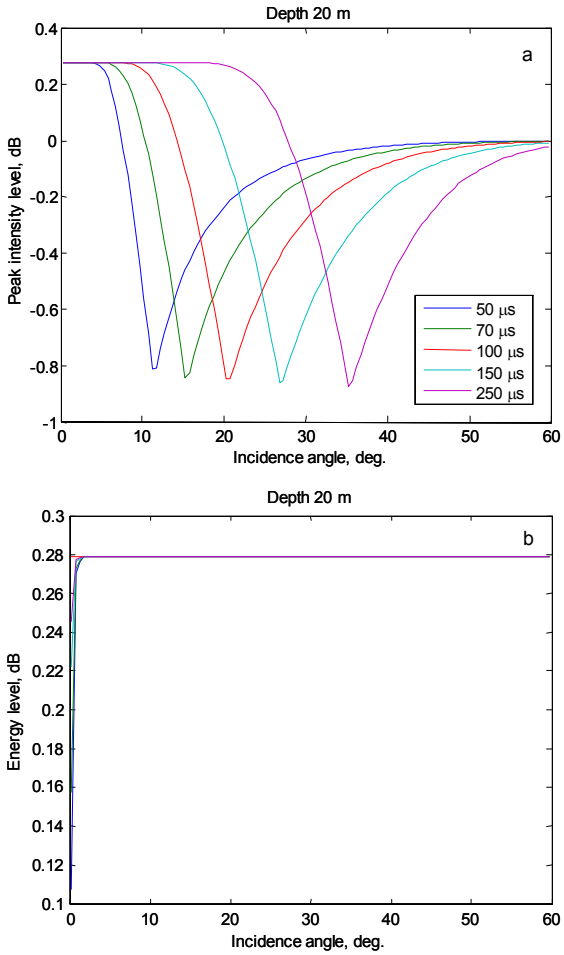

Figure B2: Angular dependence of the backscatter strength estimates derived from the peak intensity (a) and energy (b) for sea depth of 20 m and different pulse width.

As one can expect, the estimate of backscatter strength derived from the peak intensity tends to 0 dB at large incidence angles, where the across-track width of the insonification area becomes much smaller than the footprint and hence the variation of the beam pattern at its maximum within the insonification area is negligible. At small angles (but not too close to the nadir), where the footprint is much smaller than the insonification area, the estimate tends to a value of about 0.3 dB, which is the error resulted from approximation of the Gaussian beam pattern with an ideal rectangular shape. At moderate angles, where the width of insonification area is comparable to the width of the footprint, the backscatter strength obtained from the peak intensity is underestimated with the maximum error of about –0.8 dB, which

occurs because the beam pattern in this transition zone changes significantly within the insonification area.

The estimates of backscatter strength, derived from the backscatter energy normalized by the transmit pulse width and the footprint area (Figure B3), do not suffer from such angle dependent errors. An error of about 0.3 dB, resulting from the Gaussian shape of the beam pattern, is nearly constant for all angles and at all values of the pulse width. It is necessary to note, that the estimate of backscatter strength from the backscatter signal energy must be normalized by half of the transmit pulse energy, because the energy is spread on both sides. The variations of estimates at very small near-nadir angles are due to errors of numerical integration of short signals and rapidly decrease as the sampling frequency increases. In MBS systems, the signal sampling frequency is usually chosen based on a tradeoff between the spatial resolution needed and the maximum data transfer rate allowed. The sampling rate in the Reson 8125 system is about 28.5 kHz, i.e. just one or two samples for the transmit pulse of 30-ms long. This results in significant errors of integration when calculating the backscatter energy, especially at near-nadir angles, where the backscatter signals are the shortest ones. The errors of energy estimates due to discrete sampling at 28 kHz, averaged for a random timing offset (or small random fluctuations of sea depth) are shown in FigureB3 for different values of the pulse width. It's clearly seen that the backscatter strength is considerably underestimated at small angles below approximately 5 degrees, and the error of estimates increases as the pulse width decreases. Such a decrease in the estimates of backscatter strength at near-nadir angles was also observed in experimental measurements (for example, see Figure 4.5 in Chapter 4).

At a low sampling frequency, the backscatter strength derived from the peak intensity value is even more underestimated, especially at shorter transmit pulses and moderate angles of incidence, which is seen from comparing Figure B3(a) with Figure B2(a).

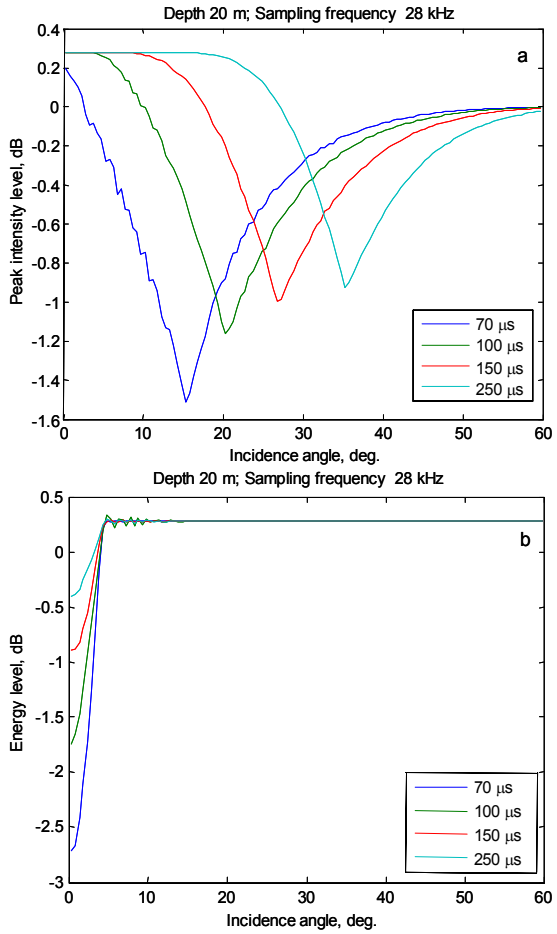

Figure B3: Angular dependence of the backscatter strength estimates derived from the peak intensity (a) and energy (b) measured at the sampling frequency of 28 kHz and different pulse width and sea depth of 20 m.

Summarising the results obtained from this analysis, one can conclude that the effect of the beam pattern on the backscatter strength estimates derived from backscatter energy and normalized by the footprint area is fairly small and similar for all angles. The total error of estimates is expected to be about 0.6 dB resulting from both along-track and across-track shapes of the transmit and receive beam patterns. The main source of errors appearing significant at near-nadir angles of incidence is a relatively slow sampling rate. The only way to reduce such errors is to operate the sonar at wider transmit pulses. The estimates of backscatter strength from the peak intensity contain larger errors. These errors are substantially angle-dependent and result from both the finite width of insonification area and finite sampling rate.

APPENDIX C: ACRONYMS

To assist the reader this appendix contains a list of the different acronyms used throughout the thesis.

ADC	Analogue to Digital Conversion
APL	Applied Physics Laboratory
ASC	Acoustic Seabed Classification
AUV	Autonomous Underwater Vehicle
AVO	Angle Versus Offset
CLT	Central Limit Theorem
CMST	Centre for Marine Science and Technology
CRC	Cooperative Research Centre
CWHM	Coastal Water Habitat Mapping
CV	Coefficient of Variation
FC	Fisher Criterion
GLCM	Grey-Level Co-occurrence Matrix
LDA	Linear Discriminate Analysis
MAP	Maximum A Posteriori
MBS	Multibeam Sonar
MSP	Method of Small Peturbation
PCA	Principal Component Analysis
RMS	Root Mean Square
ROV	Remotely Operated Vehicle
SNR	Signal to Noise Ratio
SSA	Small Slope Approximation
TVG	Time Varied Gain